DISSERTATION

CLASSIFICATION AND QUANTIFICATION OF TRMM RADAR OBSERVATIONS

Submitted by

Basim Zafar

Department of Electrical and Computer Engineering

In partial fulfillment of the requirements

For the Degree of Doctor of Philosophy

Colorado State University

Fort Collins, Colorado

Summer 2005

COLORADO STATE UNIVERSITY

April 15, 2005

WE HEREBY RECOMMEND THAT THE DISSERTATION PREPARED UNDER OUR SUPERVISION BY BASIM JAMEEL ZAFAR ENTITLED CLASSIFICATION AND QUANTIFICATION OF TRMM RADAR OBSERVATIONS BE ACCEPTED AS FULFILLING IN PART REQUIREMENTS FOR THE DEGREE OF DOCTOR OF PHILOSOPHY.

Committee on Graduate Work

Adviser

Department Head

ABSTRACT OF DISSERTATION

CLASSIFICATION AND QUANTIFICATION OF TRMM RADAR OBSERVATIONS

A better knowledge of precipitation types and their radar reflectivity structures is important for interpretation of space-borne radar observations as well as microphysical processes for improving satellite precipitation algorithms. The differences in microphysics, or drop size distributions lead to different reflectivity rain rate relationships for convective and stratiform clouds. While this approach is simple for convective/stratiform classification to rain profiles and suitable for estimating profiles of latent heating, it does not address a variety of problems. Raindrop size distributions can vary widely within the convective and stratiform categories themselves. Research that goes further into classifying precipitation profiles can bridge this gap.

The fundamental observation of space-borne radar is the vertical profile. All inferences and classifications must start there. Classifying rainfall by the three-dimensional structure of its reflectivity field offers the potential to reduce both random and systematic errors in raindrop size distributions assumed in rainfall retrievals. This research attempts to address the specific and unique problems that exist in the field of space-borne radar observation of precipitation profiles on a global scale. The difficulty in modeling the precipitation profile can be attributed to the lack of validated data on a global scale to guide this work. It is likely that long-term research will be required to

fully develop the concepts introduced in this work. This effort only takes the first step in defining such an outline. Extensive experimental verification in a wide range of regions is required to validate the usability of new derived techniques.

The main goal of this research is to use the vertical structure of the observed radar reflectivity field, in an information theoretic framework, to extend rain-type classification beyond convective/stratiform separation and to define a natural classification for radar reflectivity profiles that can eventually be related to microphysical variability of precipitation profiles. The classification of precipitation type to convective/stratiform rain type from space-borne precipitation radar observation and 2-dimensional wavelet analysis is first introduced in this research. Subsequently this dissertation includes the study of the classification of the self-organizing map of TRMM-PR rain profiles on a global scale, the global study of bright band structure as well as the study of the variability of raindrop size distribution.

Basim Zafar
Electrical and Computer Engineering Department
Colorado State University
Fort Collins, Co 80523
Summer 2005

ACKNOWLEDGEMENTS

First of all, I would like to thank God for everything. I also would like to thank all the people who helped me during this work. I am especially thankful to my advisor, Dr. V. Chandrasekar, for his kindness, support, guidance and encouragement during my graduate study. Also, I would like to thank Dr. V. Bringi, Dr. D. Lile and Dr. P. Mielke for agreeing to be on my thesis committee and reviewing my thesis.

I would like also to extend my gratitude to the crew at the Radar and Communication Lab at Colorado State University for the help given to me during the various stages of my thesis. I would like to express my sincere thanks to Dr. Wanyu Li, Dr. Ahmad Khogeer and Dr. Ayman Fayoumi for their friendship and for their help during this project.

I would like also to thank my parents, brother and sisters for their love and support while I was far away from home. Finally, I would like to thank my wife, Hanaa Alaama, my daughter, Afnan, and my son, Rayyan, for all their love, support and encouragement over the years and while doing my thesis.

TABLE OF CONTENTS

LIST OF TABLES

LIST OF FIGURES

CHAPTER 1

INTRODUCTION

1.1 INTRODUCTION

Remote and in-situ observations from ground and space show that precipitation field exhibit high spatial variability. The small-scale variability of precipitation has implications for the better understanding of weather, climate, and hydrological processes [1]. An understanding of the vertical structures of precipitating systems is important because the structures imply differences in rainfall rates and have an impact on global atmospheric circulation [18]. A better understanding of the vertical structures of precipitation is important for understanding satellite precipitation algorithms, and for the microphysical processes, including latent heating release [3][4][5]. Our current knowledge of characteristics of precipitation on a global scale, such as distributions of different precipitation types and vertical structures of precipitation, is still mostly based on ground-based and a limited extent on space-based observations [2].

Observation of the vertical profile of precipitation over the global tropics is a key objective of the Tropical Rainfall Measuring Mission (TRMM). TRMM is the first mission dedicated to observing and understanding tropical rainfall and its effects on global climate. The primary instruments on the TRMM satellite for measuring precipitation are the Precipitation Radar (PR), the TRMM Microwave Imager (TMI), and the Visible and Infrared Scanner (VIRS). The Precipitation Radar (PR) is the first space-

borne instrument designed to provide three-dimensional maps of the storm structure and to obtain rainfall measurements over land as well as over oceans. Such measurements should yield very valuable information on the intensity and distribution of rain, rain type, storm depth, and height at which snow melts into rain. Estimates of the heat released into the atmosphere at different heights based on these measurements can be helpful for improving models of global atmospheric circulation [8][9][10].

Rain can be classified as either convective or stratiform regions that further can be described by different mean vertical motion distributions and growth mechanisms [6]. Large horizontal reflectivity gradients, strong vertical motions, and high rainfall rate often characterize convective precipitation. Smaller horizontal reflectivity gradients, weaker vertical motions, and lower rain rates, on average, characterize stratiform precipitation. The occurrence of a bright band typically indicates stratiform precipitation

Bright Band (BB) has perhaps been one of the most widely known radar signatures for a long time. Extensive research documenting various features of bright bands has been reported in the literature. BB is denoted by a sharp increase in the vertical profile of reflectivity [21]. In the BB region, there is an increase in the dielectric constant as hydrometeors melt, and this results in an increase in the backscatter. When reflectivity measurements of precipitation are contaminated by bright band, surface rainfall overestimations can be as large as a factor of 10 [51]. In addition to affecting precipitation estimated by radar, proper identification of melting-layer heights can be useful for understanding precipitation types and surface temperature [20][58]. Davies 1992 in [59] showed that there is a relationship between the bright band area and the background rainfall. Therefore, several attempts have been made to identify the bright

band and account for its impact on surface rainfall estimates since the 1950s [21][51][52][53][54][55][56][57]. An understanding of the vertical structure of the BB region is important because it holds extensive information on the type of precipitation and its variability. In addition, a better understanding of the vertical structures of the BB region and its radar reflectivity structures is important for understanding microphysical processes of stratiform precipitation.

Specific attenuation in precipitation is mainly due to absorption at high frequencies and is proportional to the volume of rain. The reflectivity of rain profile is relative to the sixth power of raindrop sizes. A physical explanation of the variability in the k - Z relation can be provided with the normalized raindrop size distributions (DSD). To retrieve the parameters of the DSD, the relation between specific attenuation and reflectivity is used. The differences in the microphysics for convective and stratiform clouds may affect drop size distribution (DSD) and lead to different reflectivity-rain rate relationships [7]. Therefore, knowledge of the convective-stratiform distribution is very important. Even though this approach is appropriate for estimating vertical profiles of latent heating, it is not enough to constrain DSDs. That is because the DSDs vary widely within the convective and stratiform types themselves [11].

1.2 BACKGROUND RESEARCH AND LITERATURE REVIEW

The large-scale spatial variability of precipitation over different regions around the globe and the efforts to classify the precipitation observation vertical profiles has been extensively documented in the literature. The results and the approach of the literature are presented in this section.

1.2.1 Regional Studies

Many authors study the precipitation systems of diurnal and seasonal variability as well as the variability between oceanic and continental systems. Berg et al. [12] have studied rainfall system differences between the East and West Pacific. Varma et al. and Pokhet et al. [13][14] have examined the rain variability over the Indian subcontinent. Differences in oceanic and continental precipitation are also reported by a number of researchers [15][16].

The diurnal and seasonal variability of the vertical structure of precipitation systems in different regions based on TRMM-PR data was documented in [18][2][12]. In [17], the diurnal and seasonal variability of the vertical structure of storms in Africa was studied using five years of TRMM-PR data. Precipitation radar data derived from the TRMM satellite were used in [2] to study the precipitation characteristics over East Asia, focusing on mid-latitude land and ocean (the East China Sea and the South China Sea). The analysis of vertical structures of precipitations in [2] illustrates the significant difference between convective and stratiform rains, regardless of the location and the season. In [12], a comparison of the structure of precipitation systems between selected East and West Pacific regions along the inter-tropical convergence zone was conducted using a combination of satellite observations. That scheme includes vertical profile retrievals from the TRMM-PR. The comparison in that study shows that the structure of precipitation systems and the rainfall climate regimes between the East and West Pacific Ocean exhibit seasonal and inter-annual variability.

The study in [19] combines both TRMM-PR and Lightning Imaging Sensor (LIS) data to examine the vertical structures of tropical precipitation across a broad spectrum of

locations in the global tropics. The TRMM-PR reflectivity data was utilized to produce seasonal mean precipitation ice-water contents. The characterization of the pixel-scale variability of precipitation is an importance factor for the developing rain retrieval method. In [1], an attempt is made to understand the pixel-scale variability of precipitation from a global perspective through two attributes; namely fractional rain cover and conditional probability distribution function of the precipitation. The global variability of these two attributes is investigated separately for convective and stratiform rain type using three years of data from TRMM-PR.

1.2.2 Melting Layer

Many studies have been conducted to understand the characteristics of the melting layer on different scales since the 1950s [21]. Because of these field experiments, the microphysical features of the melting layer are well established. The behavior of the melting-layer altitude in stratiform precipitation suggests a close relationship between surface temperature and the melting-layer altitude [20]. A 14-month climatological study of the altitude of the melting layer in stratiform precipitation is conducted in [20], using reflectivity data from TRMM-PR. The monthly mean fields of the melting layer altitude are computed over the entire domain covered by the TRMM satellite. This study also shows that the seasonal cycle is more obvious over land than ocean. Further, it shows that the largest seasonal variability tends to occur at higher latitudes and over land. Likewise, it demonstrates that mean melting layers over oceanic regions are narrower and better defined than over land. Finally, the study shows that the region centered at the equator does not exhibit a pronounced annual cycle because the seasonal differences of both sides tend to be averaged over the domain.

1.2.3 Convective/Stratiform Rain Type

The characteristics of convective and stratiform rain rates have received significant attention since the launch of TRMM [22][24]. A study across the tropics using TRMM-PR indicates that stratiform precipitation accounts for 73% of the area covered by rain and 40% of the total rain amount. The ratio of the convective rain rate to the stratiform rain rate is 4.1, on average, at the horizontal resolution of the PR data [24]. The research in [24] shows that the ocean environment appears more efficient in the production of stratiform precipitation. In addition, the study shows that factors such as wind shear and the relative humidity of the large-scale environment can also affect the production of stratiform rain.

1.2.4 Classification of the Vertical Profile

Cluster analysis of the vertical profile of reflectivity from TRMM-PR data demonstrates that automated typing of radar vertical columns, which retains vertical structure information, is achievable [26]. The spatial-temporal frequencies of occurrence of these profiles provide a multi-parameter description of the realized convective spectrum. The author of [26] suggests that the objective regime identification is useful in algorithm development, ground validation, satellite retrieval, data assimilation, and empirical or theoretical studies of convective response to environmental forcing.

Regardless of the fact that radar observations in rain show considerable variety in the shape of echoes and in the resulting vertical reflectivity profiles, Fabry in [25] grouped the various reflectivity profiles in rain into five classes to study the vertical profile of reflectivity and precipitation. These five classes of vertical reflectivity profiles cause different difficulties for the estimation of surface rainfall.

1.2.5 Drop Size Distribution

In an attempt to study the relationships between the microphysics of precipitating cloud systems and their radar reflectivity patterns, the analysis in [11] shows that classifying rainfall by the three-dimensional structure of its reflectivity field offers a potential to reduce both random and systematic errors in DSDs assumed in rainfall retrievals. An algorithm to defining rain types was developed in [11]. The algorithm uses the following eight variables: near-surface reflectivity, slopes between the surface and 2 km, 2-4 km, 4-6 km, and 6-8 km, the ratio of the maximum reflectivity in the profile to that at the surface, the highest altitude with a radar echo above 20 dBZ, and the mean horizontal gradient in surface reflectivity between the pixel and its eight nearest neighbors. This study also shows that differences between easterly and westerly regime rainfall remain even after classification. The technique presented in [11] provides a template for future rain type classification schemes in determining DSD. Thus, it is equally as valuable to assess both the mean and standard deviation of DSDs assigned to a rain type class as it is to verify the retrieved rainfall rate. The necessity for focusing the validation program on improving the confidence in the DSDs assigned to each rain type that represents a larger fraction of global rainfall was proposed in [11].

1.3 GENERAL DESCRIPTION OF THE PROBLEM

A better knowledge of precipitation types and their radar reflectivity structures is important for interpretation of space-borne radar observations as well as microphysical processes for improving satellite precipitation algorithms. The differences in microphysics, or drop size distributions lead to different reflectivity rain rate relationships for convective and stratiform clouds. While this approach is suitable for

convective/stratiform classification to rain profiles and suitable for estimating profiles of latent heating, it does not address a variety of problems. Raindrop size distributions can vary widely within the convective and stratiform categories themselves. Research that go further into classifying precipitation profiles with regard to the variety of raindrop size distributions can bridge this gap.

The fundamental observation of space-borne radar is the vertical profile. All inferences and classifications must start there. Classifying rainfall by the three-dimensional structure of its reflectivity field offers the potential to reduce both random and systematic errors in raindrop size distributions assumed in rainfall retrievals. Rain type classification provides a means for exporting raindrop size distributions deduced from polarimetric radars to those without polarization capability, such as the Tropical Rainfall Measuring Mission Precipitation Radar (TRMM-PR), by assigning each vertical profile the properties of its appropriate rain-type. This research attempts to address the specific and unique problems that exist in the field of space-borne radar observation of precipitation profiles on a global scale. As this area of study is still growing, new and creative techniques are needed. The difficulty in modeling the precipitation profile can be attributed to the lack of validated data on a global scale to guide this work. It is likely that long-term research will be required to fully develop the concepts introduced in this work. This effort only takes the first incremental step in defining such an outline. Extensive experimental verification in a wide range of regions is required to validate the usability of new derived techniques.

The main goal of this research is to use the vertical structure of the observed radar reflectivity field in an information theoretic framework to extend rain-type classification

beyond convective/stratiform separation and to define a natural classification for radar reflectivity profiles that can eventually be related to the microphysical variability of precipitation.

1.4 OBJECTIVES OF THE RESEARCH

The following points summarize the objectives of the research. This section groups the tasks according to their major goals.

- Classification of precipitation type to convective/stratiform rain type from space-borne precipitation radar observation and 2D wavelet analysis.
    - Examine the current algorithm used in TRMM-PR.
    - Study the processes that may need improvement in the current algorithm.
    - Develop a multiresolution analysis algorithm based on 2D wavelet analysis to do the rain type classification for the observation of the vertical profile using TRMM-PR.
    - Evaluate the proposed convective/stratiform classification algorithm and compare it with the current algorithm used in TRMM-PR and coincident ground radar observations.
- Study the classification of the self-organizing map of TRMM-PR on a global scale.
    - Through analysis, demonstrate the choice of the resolution of the vertical profile between sampling at 250 m and 125 m.
    - Compare and contrast the self-organizing map with clustering analysis.
    - Develop an algorithm for the self-organizing map that provides classification of vertical profiles of reflectivity.

- Classify the vertical profile of reflectivity of precipitation data over the globe with variable granularity.
- Study the natural separation results of the vertical profile of reflectivity classification on different sizes of the self-organizing map.
- Study results of the vertical profile of reflectivity classification in different topographies.
- Study the seasonal variation of the vertical profile of reflectivity classification.
- Study the vertical profile of reflectivity for different rain types.
- Study differences of the vertical profile of reflectivity classification in the East and West Pacific Ocean.

- Global study of bright band structure as observed from TRMM-PR.
  - Define the process that will determine the bright band region properties.
  - Develop a technique that provides classification of the vertical profile of reflectivity in the bright band region using a self-organizing map.
  - Study the climatological behavior of the bright band structure on a global scale utilizing a statistical approach.
  - Study results of the bright band region profile classification in different topographies.
  - Study the seasonal variation of the bright band region profile classification.
  - Study differences of the bright band region profile classification in East and West Pacific Ocean.
- Study the variability of raindrop size distribution around the globe
  - Evaluate the technique of space-borne radar to derive the parameters of

raindrop size distribution.

- Study the statistical characteristics of raindrop size distribution parameters retrieved around the globe classified into various categories such as convective, stratiform and other types of classifications using TRMM-PR data.
- Generate the monthly maps of the raindrop size distribution around the globe using the TRMM-PR based raindrop size distribution retrieval algorithms.

CHAPTER 2

TRMM SYSTEM AND DATA CHARACTERISTICS

2.1 INTRODUCTION

The Tropical Rainfall Measuring Mission (TRMM) is the first mission to measure precipitation quantitatively from space. TRMM is dedicated to observing and understanding the tropical rainfall and its effects on global climate. TRMM is a joint mission between NASA and the Japan Aerospace Exploration Agency (JAXA). The primary instruments on the TRMM satellite for measuring precipitation are the Precipitation Radar (PR), the TRMM Microwave Imager (TMI), and the Visible and Infrared Scanner (VIRS).

The Precipitation Radar (PR) is the first space-borne instrument designed to provide three-dimensional maps of storm structures and to obtain rainfall measurements over land as well as over oceans. Such measurements yield very valuable information on the intensity and the distribution of rain, rain type, storm depth, and height at which snow melts into rain. Estimates of the heat released into the atmosphere at different heights based on these measurements can be used to improve models of global atmospheric circulation.

2.2 SYSTEM DESCRIPTION

The TRMM-PR records energy reflected from precipitation and surface targets. The

PR is a 128-element active phased array system operating at 13.8 GHz. The PR electronically scans from right to left, looking in the flight direction across the ground track of the satellite every 0.6 seconds, with horizontal resolution at the ground of 4.3 km and a swath width of 215 km (Figure 1).

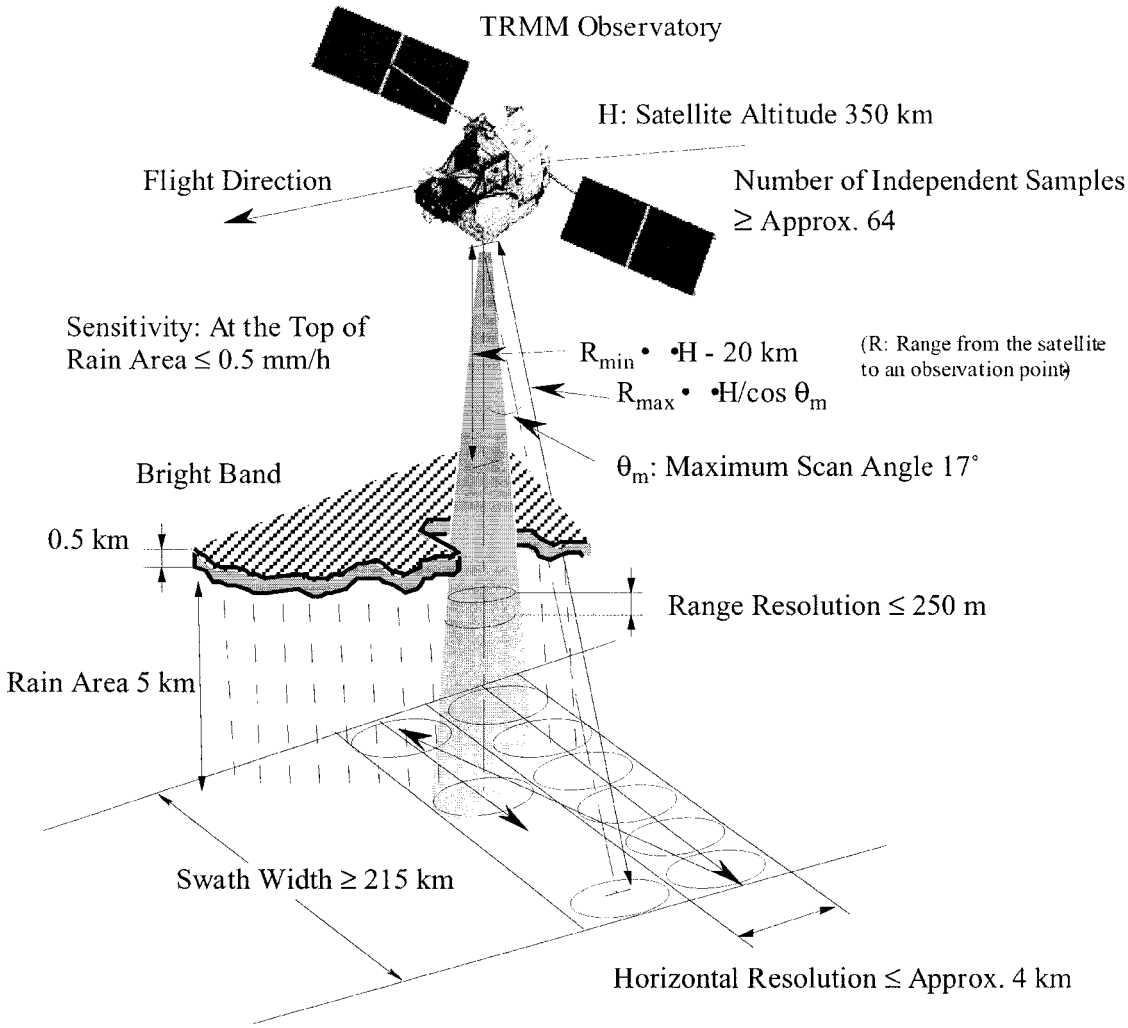

Figure 2-1. The observation concept of the PR (adopted from PR Instruction Manual [27]).

Each PR scan contains 49 rays sampled over an angular sector of 34 degrees. For any given ray, the instrument begins recording samples at a fixed distance from the satellite

and records a certain number of samples along the ray. The complex scan geometry is represented in Figure 2. The starting distance and the number of samples are different for each ray. Rays other than the nadir ray also sample below the ground surface. The purpose of this extension below the surface is to clearly detect the location of the surface. One of TRMM-PR's most important features is the ability to provide vertical profiles of rain and snow from the surface up to a height of about 20 km.

The PR is able to detect fairly light rain rates down to 0.7 mm/h. At intense rain rates, where the attenuation effects can be strong, new methods of processing have been developed that help correct for this effect. The Precipitation Radar is able to separate out rain echoes for vertical sample sizes of about 250 m when looking straight down. Data points in the vertical are saved in the normal sample, as shown in Figure 3. The mirror is contained in the normal sample. A subset of the remaining data points is saved in two oversamples: the surface oversample and the rain echo oversample. Both oversamples have a spacing of 250 m along a ray, but a region with both normal sample and oversample has a spacing of 125 m. The PR determines which levels to save in the oversamples based on its on-board determination of the surface bin. No data are saved as oversample in rays 1-10 and 40-49. Five levels are saved from rays 11-39 in the surface oversample. If the PR detects the surface in an oversample bin, the surface oversample is centered on the detected surface. If, on the other hand, the PR detects the surface in a normal sample bin, 3 oversample bins are above and 2 oversample bins are below the detected surface. In addition, 28 levels (immediately above the surface oversample) are saved from rays 20-30 in the rain echo oversample. The TRMM-PR will carry out all these measurements while using only 224 watts of electric power. The TRMM satellite

has a circular non-synchronous orbit with an altitude of approximately 350 km. This orbit allows the TRMM satellite to pass over each part of the surface of the earth at a different local time daily. Precipitation radar parameters are listed in Table 2–1.

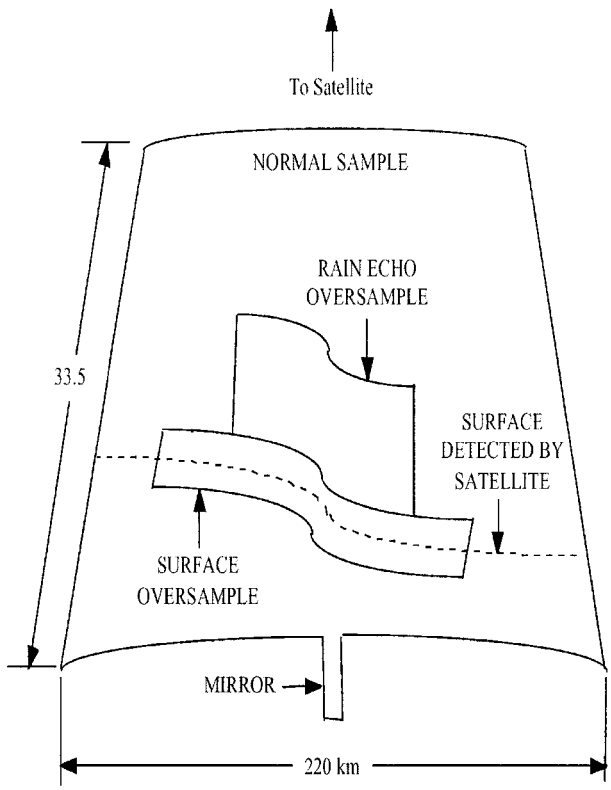

Figure 2-2. PR scan geometry (adopted from ICS [28]).

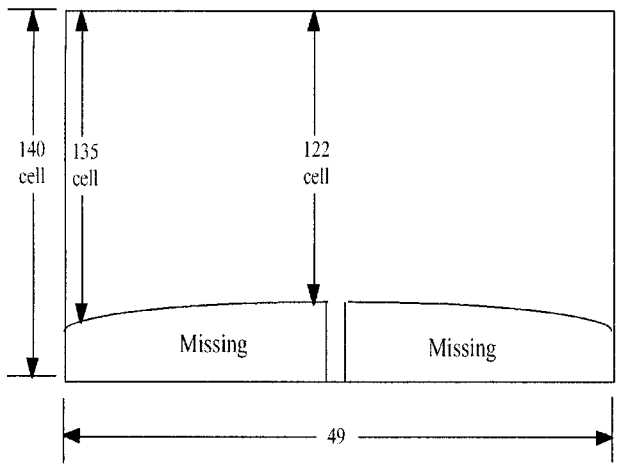

Figure 2-3 Normal sample data array (adopted from ICS [28]).

Table 2–1. Precipitation radar parameters (adopted from PR Instruction Manual [27]).

Radar Type	Active phased-array radar
Frequency	13.796 GHz and 13.802 GHz (Two-Channel frequency agility)
Swath Width	About 215 km
Observable Range	Over 20 km
Range Resolution	250 km
Horizontal Resolution	4.3 km (nadir)
Sensitivity	S/N per pulse $\geq$ 0 dB for 0.5 mm/h rain at rain top
Independent Samples	64
Data Rate	93.5 kbps
Weight	465 kg
Power	213 watts
Antenna Type	128-element slotted wave guide array antenna
Beam Width	0.71° x 0.71°
Aperture	2.1 m x 2.1 m
Scan Angle	±17°
Gain	About 47.4 dB
Transmitter Type	SSPA & LNA (128 channels)
Peak Power	Over 700 W
Pulse Width	1.6 μsec x 2 ch
Pulse Repetition Frequency	2776 Hz
Dynamic Range	About 81.5 dB

2.3 DESCRIPTION OF TRMM MEASUREMENT

The TRMM Science Data and Information System (TSDIS) processes TRMM data from the Precipitation Radar, the TRMM Microwave Imager, and the Visible and Infrared Scanner into data products oriented toward measuring rainfall in the tropics. Most TRMM data products are written using Hierarchical Data Format (HDF). This section summarizes the data products for Precipitation Radar. More details on these data products are found in the six volumes of the Interface Control Specification (ICS) [28]. TRMM data products are listed in Table 2–2.

Table 2–2. TRMM Products for PR, TMI and VIRS (adopted from PR Instruction Manual [27]).

Sensor	Processing Level	Product	Scene Unit	Data Volume
PR	1B21	Calibrated Received Power	1 orbit (16/day)	149 MB
	1C21	Radar Reflectivity	1 orbit (16/day)	149 MB
	2A21	Normalized Radar Surface Cross Section	1 orbit (16/day)	10 MB
	2A23	PR Qualitative	1 orbit (16/day)	13 MB
	2A25	Rain Profile	1 orbit (16/day)	241 MB
	3A25	Monthly Statistics of Rain Parameter	Global Map (Monthly)	40 MB
	3A26	Monthly Rain Rate using a Statistical Method	Global Map (Monthly)	9.3 MB
TMI	1B11	Brightness Temperature	1 orbit (16/day)	14 MB
	2A12	Rain Profile	1 orbit (16/day)	97 MB
	3A11	Monthly Oceanic Rainfall	Global Map (Monthly)	53 MB
VIRS	1B01	Radiance	1 orbit (16/day)	92 MB

2.3.1 LEVEL-1B

The PR Level-1B product, 1B-21, PR Power, contains calibrated PR powers in 3-dimensional arrays whose dimensions are scan, ray, and range bin. Power is written in three arrays: normal sample, surface oversample, and rain oversample. Values of -32734 and -32767 denote missing data. The vertical spacing is 250 m for the normal sample. If the surface oversample and rain oversample are combined with the normal sample, the result is 125 m vertical spacing in limited regions.

2.3.2 LEVEL-1C

The PR Level-1C product, 1C-21, PR Reflectivity, has the same format as 1B-21, with 3 changes: the variable in the Normal Sample, Surface Oversample, and Rain Oversample is reflectivity (dBZ) in IC-21. Figure 4 shows the structure of 1C-21.

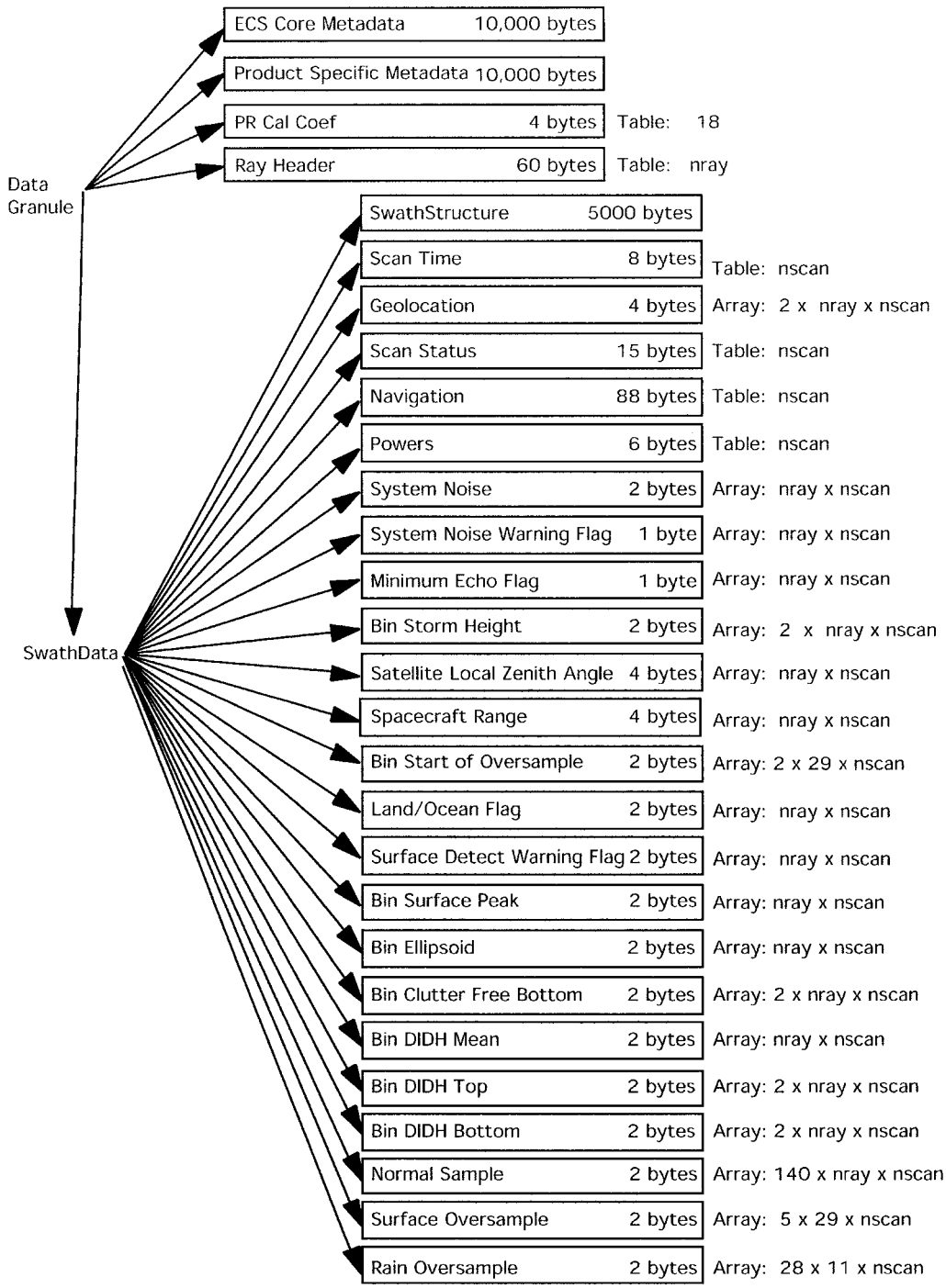

Figure 2-4. PR 1C-21 Structure (adopted from ICS [28]).

2.3.3 LEVEL-2A

The PR Level-2A product, 2A-21, 2A-23 and 2A-25, where:

- 2A-21, Surface Cross Section, computes the normalized surface cross section. If rain is present, it will also compute path attenuation and its associated reliability factor. Figure 5 shows the structure of the 2A-21 product in terms of component objects and their sizes.

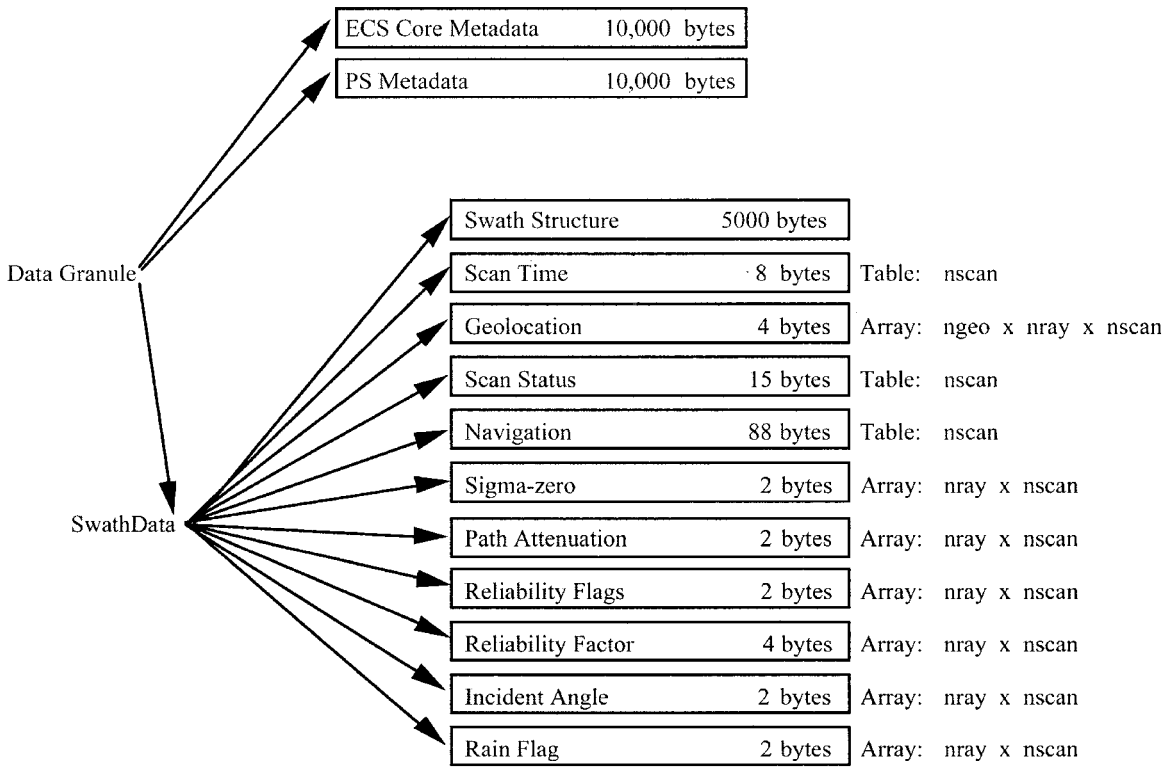

Figure 2-5. PR 2A21 Structure (adopted from ICS [28]).

- 2A-23, PR Qualitative, produces a "Rain/No-rain" flag. If rain is present, this algorithm will detect the bright band, determine the heights of the bright band and the storm, and classify rain types. Figure 6 shows the structure of the 2A-23 product in terms of component objects and their sizes.

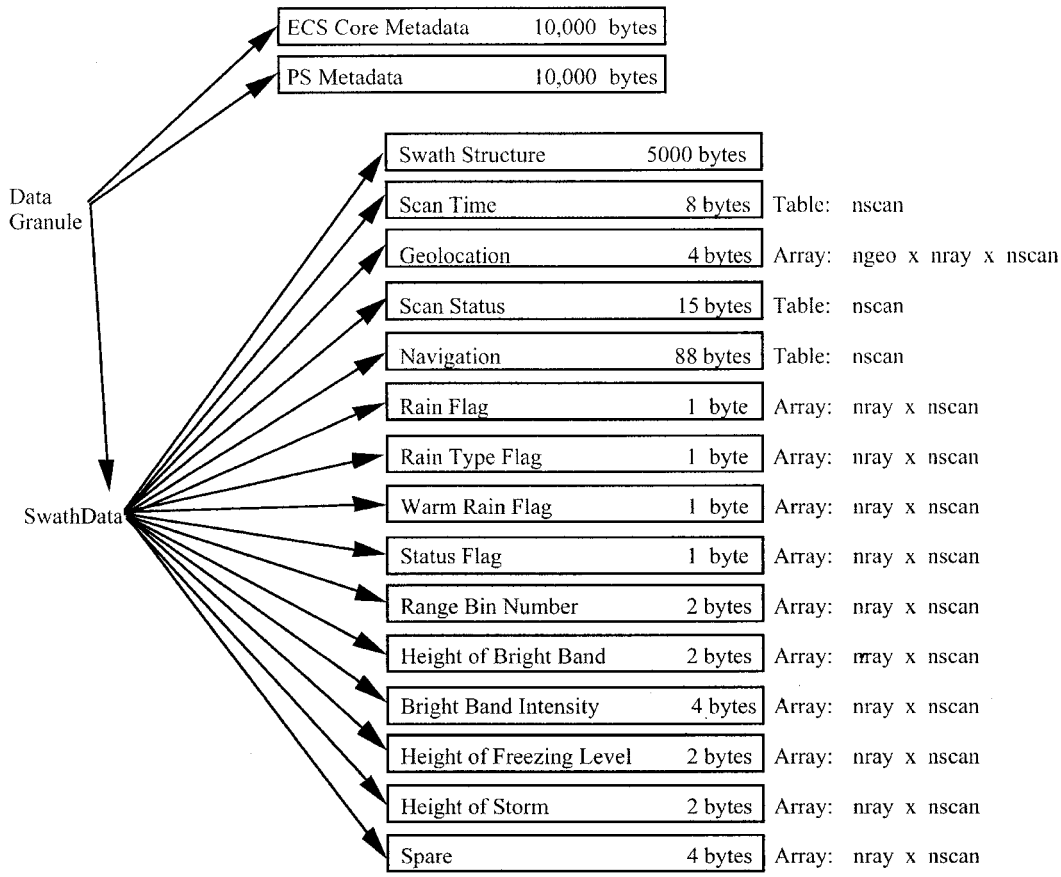

Figure 2-6. PR 2A-23 Structure (adopted from ICS [28]).

- 2A-25, PR Profile, produces an estimate of vertical rainfall rate profile for each radar beam. The rainfall rate estimate is given at each resolution cell of the PR radar. To compare with ground-based radar data, the attenuation-corrected profile is also given. The average rainfall rate between the two pre-defined altitudes is calculated for each beam position. Other output data include parameters of relationships, integrated rain rate of each beam, range bin numbers of rain layer boundaries, and many intermediate parameters. Figure 7 shows the structure of the 2A-25 product in terms of component objects and their sizes.

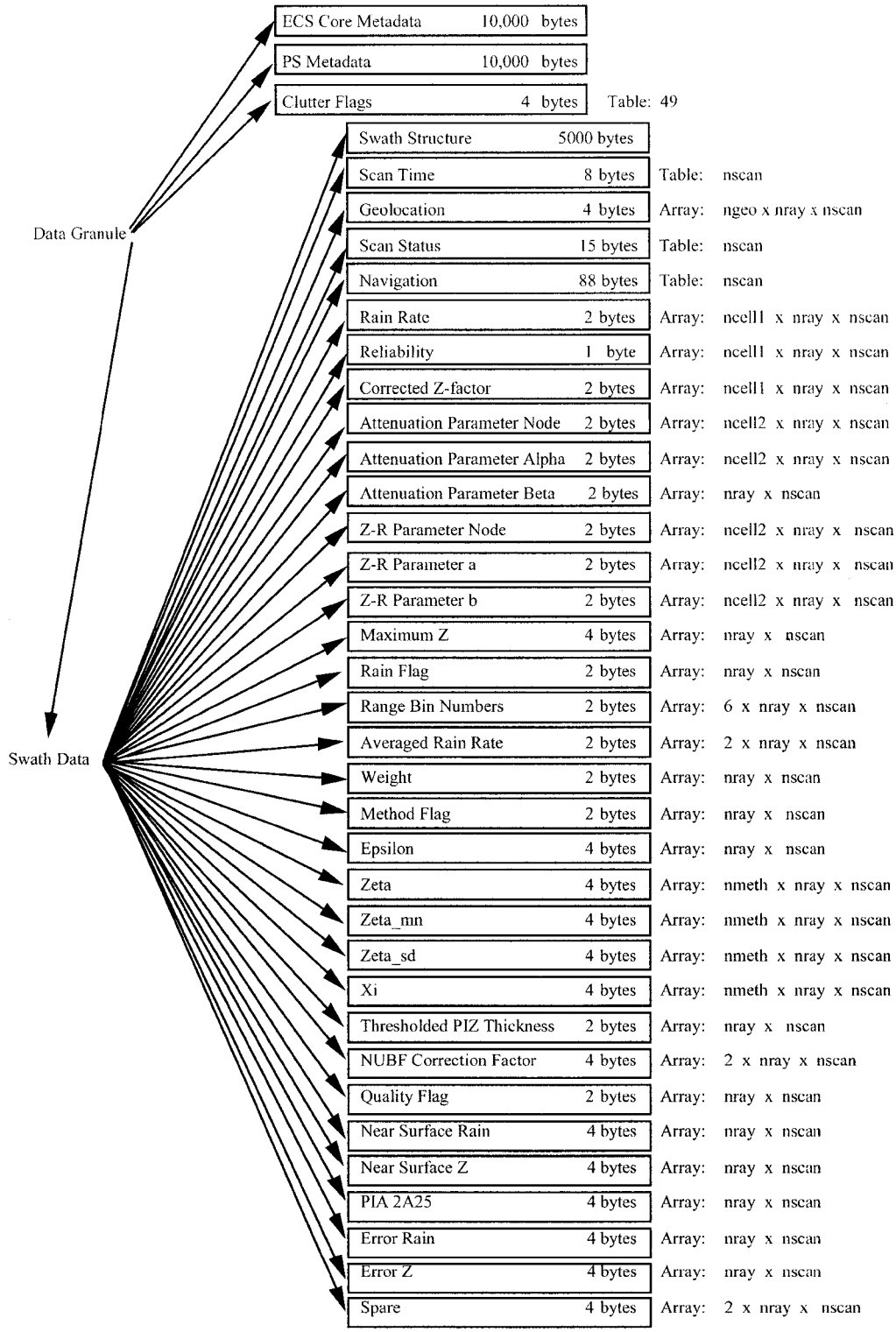

Figure 2-7. PR 2A-25 Structure (adopted from ICS [28]).

2.3.4 LEVEL-3A

The PR Level-3A product, 3A-25 and 3A-26, where:

- 3A-25, PR Rainfall, contains 5° x 5° and 0.5° x 0.5° latitude/longitude monthly statistics of PR measurements. The statistics include means, standard deviations, sample sizes, histograms, and correlation coefficients. The PR measurements include rainfall, reflectivity, Path-Integrated Attenuation (PIA), storm height, bright band height, snow-ice layer, and the Non-Uniform Beam Filling (NUBF) correction.
- 3A-26, Surface Rain, computes the distribution of rainfall on a 5° x 5° grid on a monthly basis. The output products are calculated at three fixed heights (2, 4, and 6 km) and for path-averaged rain rates. 3A-26 also computes fitting parameters for cumulative probability functions of rain rate as a function of 20 rain categories and 6 thresholds.

2.4 GROUND VALIDATION PROGRAM

The TRMM science team suggested having 10 ground validation (GV) sites, representing a reasonable variety of tropical rain regimes, in place at the time of TRMM launch [30]. The TRMM-PR program focused on four of the highest priority sites, i.e., Florida, Kwajalein, Australia, and Texas, Due to the extremely high volume of raw data as well as logistical difficulties in obtaining and quality controlling data from radars, rain gauges and disdrometers, Figure 2-8 indicates the actual distribution of the TRMM validation sites and primary sites [29][30].

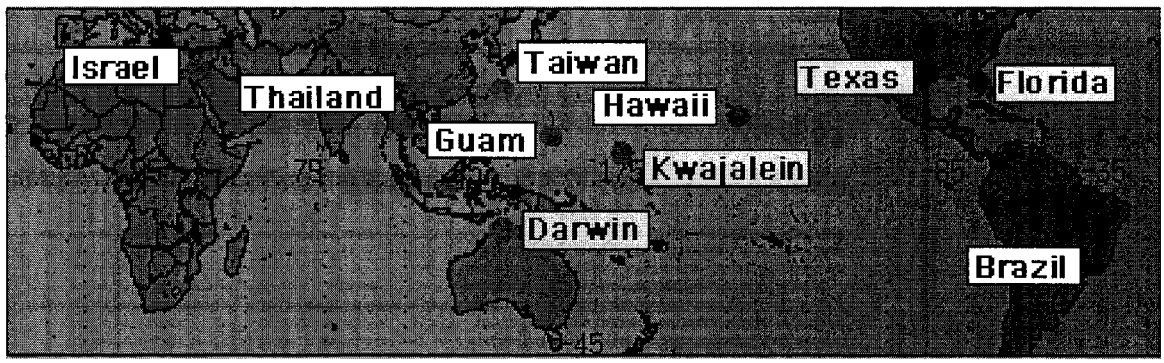

Figure 2-8. Worldwide distribution of TRMM ground validation sites.

2.4.1 TRMM-GV AND TRMM-PR

The prime goal of TRMM is "evaluation of the four-dimensional structure of latent heating in the tropical atmosphere" [31]. The goals of TRMM control the TRMM Ground Validation work. The GV program operates several ground validation sites on a continual basis while the TRMM is in orbit. These sites provide a climatological sample of the aspects of precipitation represented by the TRMM objective. Each operational GV site is equipped with Doppler radar instrumented for precipitation measurements and a network of surrounding rain gauges. The resolution of the operational GV site radar data is ~2 km in the horizontal. The slant range resolution (along a radar beam) is < 1 km. Interpolation of the slant-range data to a Cartesian grid yields a vertical resolution of ~0.5-2 km in the vertical, depending on horizontal distance from the radar.

The basic spatial resolutions of the TRMM-PR (4 km horizontally and 250 m vertically) and of the operational GV site radars fundamentally limit the comparisons between the TRMM satellite data and the GV site data. Since the operational GV site data have considerably greater horizontal resolution than do the TRMM satellite data, the operational GV data provide the better picture of the horizontal texture of the

precipitation. The PR will detect only that precipitation which has radar reflectivity of 17 dBZ or greater. The operational GV site radars will detect echoes down to 0 dBZ or less. This greater sensitivity means the GV radars will give a more complete picture of the precipitation. The operational GV radars provide a much better indication of the distribution of ice-phase precipitation particles. The PR has a wavelength of about 2 cm, which is highly attenuated, especially by melting snow particles. The GV radars have wavelengths of 10 cm, which suffer very little attenuation. The high attenuation rates of the PR complicate direct inter-comparison of reflectivities measured by the PR and operational GV radar viewing the same targets. Because of the measurement differences, the products based on the operational GV site data will be stand-alone products that will fully address all of the TRMM goals for a particular site. In this way, the GV site constitutes the best possible comparison data set for the TRMM satellite data.

Both the TRMM satellite and the TRMM-GV sites will produce estimates of areas of convective and stratiform precipitation, vertical structure of radar reflectivity, and rain maps. However, both the TRMM satellite measurements and the GV site measurements are subject to large uncertainties of sampling, instrumentation, and theoretical interpretation of the data. The fundamental philosophy of the TRMM-GV program recognizes that the TRMM-GV provides an independent estimate, at some locations, of the same quantities estimated by TRMM-PR. The closer the estimates from GV sites and PR are to agreement, the greater the confidence will be in both estimates. It is not possible to attach accurate error bars to either the GV products or the satellite data products. However, the degree of agreement between the two types of products will lend confidence to the combined TRMM science achievements [30].

CHAPTER 3

CLASSIFICATION OF PRECIPITATION TYPE FROM SPACE-BORNE PRECIPITATION RADAR DATA AND 2D WAVELET ANALYSIS

3.1 INTRODUCTION

Classification of precipitation into convective and stratiform type is one of the products of the Tropical Rainfall Measuring Mission (TRMM) data. This classification was introduced to understand how precipitation relates to heating of the tropical atmosphere. Large horizontal reflectivity gradients, strong vertical motions, and high rainfall rate often characterize convective precipitation. Smaller horizontal reflectivity gradients, weaker vertical motions, and lower rain rates characterize stratiform precipitation. The presence of a bright band typically indicates a stratiform region. Separation of tropical precipitation into convective and stratiform components is one of the major objectives of the TRMM Precipitation Radar.

Ideally, vertical motion data could be used to differentiate between convective and stratiform rainfall, but because such data are not available from space-borne radar, other methods that use only radar reflectivity observations should be used. The TRMM-PR rain classification algorithm (2A-23) uses two different methods for classifying rain type; one is the vertical profile method (V-method) and the other is the horizontal pattern method (H-method) [32].

The one-dimensional wavelet analysis based on vertical profile has been successfully used to classify rain types [71]. The convective/stratiform classification algorithm using one-dimensional wavelet analysis is limited by the information content of each single vertical profile and its variability. However, the TRMM-PR provides the three-dimensional reflectivity structure of precipitation. The two-dimensional wavelet analysis has the ability to study the complete vertical and horizontal planes simultaneously at different resolution levels. Therefore, it is easer to search for features of convective/ stratiform precipitation at those planes.

This chapter introduces a two-dimensional wavelet-based algorithm to further expand upon the success of the convective/stratiform algorithm using vertical profiles only. This algorithm analyzes the structure of reflectivity fields of precipitation in both horizontal and vertical planes. Figure 3-1 is a schematic diagram that shows the horizontal, vertical, as well as cross-track and long-track directions for the TRMM-PR observation. The rain type is determined by analyzing the wavelet coefficients of each plane. A new algorithm is developed based on this analysis. In addition the new algorithm introduces a technique to potentially improve the horizontal method used in the TRMM-PR 2A-23 algorithm using the wavelet analysis.

3.2 TRMM PRECIPITATION RADAR RAIN-TYPE ALGORITHM

TRMM-PR rain classification (2A-23) algorithm uses two different methods for classifying rain type; one is the vertical profile method (V-method) and the other is the horizontal pattern method (H-method) [33]. Both methods classify rain into three categories: stratiform, convective, and other. 2A-23 outputs a unified rain type.

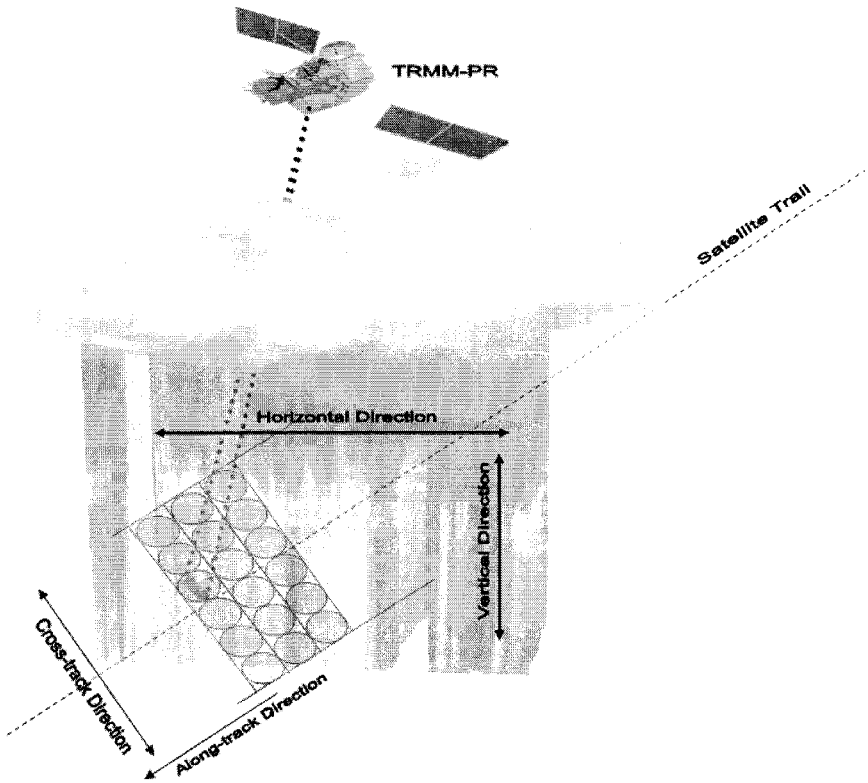

Figure 3-1. Schematic diagram showing the horizontal, vertical as well as cross-track and long-track direction for the TRMM-PR.

The main objectives of 2A-23 can be summarized as follows:

- Classify rain type into three categorizes: stratiform, convective, and other.
- Detect the bright band (BB) in the vertical profiles and determine the bright band height and the bright band peak reflectivity.
- Detect the warm rain.
- Output a "rain/no-rain" flag.
- Compute the estimated height of freezing level.
- Output storm top height.

3.2.1 V-METHOD

Vertical Profile Method (V-method) [32] begins its classification by detecting the existence of bright band in the vertical profile. If the bright band is detected then the profile classifies as stratiform rain type. The V-Method, in the next step, classifies the convective rain type region, which is characterized by a strong radar echo. The profile is classified as "other" if the algorithm failed to classify the profile as either a stratiform or convective rain type.

Bright band detection is carried out by peak search in the rain region of the vertical profile. The peak search is made on a vertical plane of one scan of data. The first stage of peak detection uses the following spatial filter:

$$\begin{vmatrix} -1 & -1 & -1 \\ +2 & +2 & +2 \\ -1 & -1 & -1 \end{vmatrix}$$

The spatial filter is based on the second derivative of reflectivity (Z) with respect to the range from the satellite. Since the spatial filter uses 3 adjacent angle bins of the data, the first bright band detection can miss the bright band; e.g., when peaks are out of phase. Hence, bright band detection is done once again on the same vertical plane of one scan data profiles.

The spatial filter is applied to the linear scale of Z, but not to the logarithmic (dB) value of Z, which makes the peak search very close to a search of the maximum value of Z in the rain region on a vertical plane of one scan of data.

When the output of the spatial filter exceeds a given threshold, it is concluded that a candidate for the bright band peak is detected. When the following conditions are satisfied, it is concluded that the bright band is detected [32]:

- Bright band has a clear peak.
- The height of bright band (HBB) must be close to freezing height (within 2.5 km).
- Above the height of bright band, the value of the profile reflectivity decreases significantly.
- The height of bright band appears at almost the same height (within 0.65 km in one vertical plane).
- With these conditions, the algorithm can discriminate between the bright band peak and a fictitious peak of convective precipitation, which occurs due to a strong attenuation on the radar signal of the TRMM-PR (whose frequency is 13.8 GHz).

The height of freezing height is computed using the following equation:

$$HFH = \frac{T_{surf}}{T_{lapse}} \tag{1}$$

where T_{surf} is the climatological surface temperature, and the lapse rate of the temperature (T_{lapse}) is assumed to be 6.0°/km. When the bright band is detected, it is easy to compute the bright band height using the information concerning range and local zenith angle. After the detection of bright band, the V-method goes on to classify precipitation type. The outline of the determination of precipitation type is as follows [32]:

- When bright band exists, rain is basically classified as stratiform.
- When bright band is not detected, and the maximum reflectivity value at a given angle bin exceeds 39 dBZ, rain is classified as convective.

- The "other" type is defined as not stratiform and not convective rain type.

The stratiform type of precipitation classified by the V-method depends on the detection of bright band. If bright band detection fails, then the V-method automatically classifies the precipitation type as either "convective" or "other" even if the rain is actually stratiform.

3.2.2 H-METHOD

The horizontal pattern method (H-method) classifies rain into three categories: stratiform, convective, and other. The H-method is based on the University of Washington convective/stratiform separation method [33], which examines the horizontal pattern of Z at a given height, where Z has a 2 km horizontal resolution. In the 2A-23 algorithm, the following modifications are made to be suitable for TRMM-PR [32]

- Instead of examining the horizontal pattern of reflectivity (Z) at a given height, a horizontal pattern of the maximum of Z along the range for each antenna scan angle below freezing height (minus 1 km margin) is examined.
- Parameters are changed so that they may be suitable for the TRMM data with 4.3 km horizontal resolution.
- The "other" type of rain is introduced to handle noise, as well as cases in which a clear decision cannot be made.
- The detection of convective rain is made first.

Convective cell region centers are identified when the difference (ΔZ) between the reflectivity of an individual grid point and the local background reflectivity (the average of the radar reflectivity factor of nonzero radar echoes within a radius of 11 km around the grid point) exceeds a convective center criterion. Once the convective centers have

been identified, grid points within a certain radius of the convective center are classified as convective. The ΔZ is given by this equation:

$$\Delta Z = \begin{cases} 10, & Z_{bg} < 0 \\ 10 - Z_{bg}^2, & 0 \le Z_{bg} < 42.43 \\ 0, & Z_{bg} \ge 42.43 \end{cases} \quad (2)$$

Rain type for a convective center is convective, and rain type for the pixels nearest to the convective center is also convective. In the H-method, if rain type is not convective and if the rain echo is certain to exist, the rain type is stratiform. In the H-method, rain type is "other" if the radar echoes are possibly noise. This means that by the H-method the "other" type includes noise and cloud.

3.2.3 Unified Rain Type

The 2A-23 algorithm outputs a unified rain type that depends on the V-method and the H-method. Unified rain type is expressed by 2 digits. The first digit indicates the rain type (1: stratiform, 2: convective, 3: other), and the last digit indicates a level of confidence, which decreases as the number increases. The unification of precipitation types in Table 3–1 uses the strong points of each method.

Table 3–1 Unification of precipitation type.

V-method	H- method	Unified Type
Stratiform	Stratiform	Stratiform
Stratiform	Other	Stratiform
Other	Stratiform	Stratiform
Stratiform (BB Certain)	Convective	Stratiform
Convective	Convective	Convective
Other	Convective	Convective
Convective	Other	Convective
Convective	Stratiform	Convective
Stratiform (BB not Certain)	Convective	Convective
Other	Other	Other

3.2.4 CONVECTIVE/STRATIFORM PRODUCT AT GROUND VALIDATION PROGRAM

The TRMM Ground Validation program operates several ground validation radar sites (GV) to provide a climatological sample of the aspects of precipitation represented by the TRMM objectives. The basic principle of the TRMM-GV program is that the GV program can produce an independent estimation of all TRMM products and comprise the best possible comparison data set for the TRMM satellite data. For each satellite overpass of a TRMM-GV site, both GV and PR maps indicate the locations of convective and stratiform precipitation.

For the sake of comparison, a map is made showing the convective/stratiform pixels on the PR map overlaid on a map showing the convective/stratiform pixels of the GV map. In general, the operational GV radar will show a much larger region of rain because the PR has low sensitivity (17 dBZ minimum detectable signal). A comparison of GV-based and PR-based convective/stratiform designations may be done only within the region where both radars show precipitation. A further complication in comparing the GV-based and PR-based convective/stratiform maps is that the horizontal resolution of the PR is 4 km, while that of the GV radar map has a resolution of 2 km. This difference in GV and PR resolution must be accounted for the comparison when determining the degree of agreement between GV-based and PR-based convective/stratiform designations. The GV team adopted the Steiner et al. [33] method for producing rain type classification (2A-54) product. The 2A-54 product by TRMM-GV program is an instantaneous map in Cartesian coordinates with 2 km horizontal resolution that identifies the surface precipitation as either convective or stratiform.

The fundamental philosophy of the TRMM-GV program recognizes that the TRMM-GV program provides an independent estimate at certain locations of the same quantities estimated by TRMM-PR. The closer the estimates are to agreement, the greater the confidence will be in all estimates. The uncertainties in instrumentation, sampling, and theoretical interpretation make it impossible to attach accurate error bars to either the GV data products or the PR data products.

3.3 WAVELET TRANSFORM ANALYSIS OF PR RANGE PROFILES

3.3.1 INTRODUCTION

Space-borne radar measurements exhibit extensive variability in the vertical and horizontal directions. The convective/stratiform structures are studied in terms of these variabilities. Bright band is seen as a sharp increase in the reflectivity of narrow vertical extent. In an informational sense, these variations or the change in the reflectivity at bright band region can be considered as a singularity. The convective core of the precipitation radar image has higher reflectivity than the surrounding background and larger variability in the horizontal direction. Wavelet transform is well suited for analyzing spatial variabilities at different scales as well as detecting singularities. An algorithm based on wavelet analysis is developed in this chapter for both scale decomposition as well as singularity detection.

Multiresolution analysis [34] using wavelets analysis is used to address this problem. The sharp changes in the profile, or "high frequency", can be detected at the first resolution level of the multiresolution analysis of wavelet transform. As we go to the second or third level the multiresolution analysis can detect changes over a large scale or

"lower frequency." In this research, quadratic spline wavelet [34] is used for this analysis because of its compact support and its ability to detect singularity in the data.

3.3.2 MULTIRESOLUTION ANALYSIS OF WAVELET TRANSFORM

The original resolution of the signal needs to be fixed in any attempt to detect the singularity in signal. In order to keep the original sampling frequency, the wavelets in the context of multiresolution analysis can be written as

$$\psi_{j,k}(t) = \frac{1}{\sqrt{2}}\psi\left(\frac{t-k}{2^j}\right) \tag{3}$$

and the scaling functions can be written as

$$\phi_{j,k}(t) = \frac{1}{\sqrt{2}}\phi\left(\frac{t-k}{2^j}\right) \tag{4}$$

The multiresolution relationships for non-orthogonal wavelets in the Fourier domain can be expressed as [34]

$$\hat{\phi}(\omega) = \frac{1}{\sqrt{2}}\hat{h}\left(\frac{\omega}{2}\right)\hat{\phi}\left(\frac{\omega}{2}\right) \tag{5}$$

and

$$\hat{\psi}(\omega) = \frac{1}{\sqrt{2}}\hat{g}\left(\frac{\omega}{2}\right)\hat{\phi}\left(\frac{\omega}{2}\right) \tag{6}$$

Similarly, the approximated signal $a_{j+1,k}$ and detail signal $D_{j+1,k}$ can be computed using these multiscale relationships through low-pass filter h and high-pass filter g. The approximated and detail signals are determined by

$$a_{j+1,k} = a_j * \bar{h}_j(k), \tag{7}$$

and

$$d_{j+1,k} = a_j * \bar{g}_j(k). \tag{8}$$

respectively.

The approximated signal at level $(j+1)$ can be calculated by inserting $(2j-1)$ zeros between each sample of the low-pass filter h and performing the discrete convolution between a_j and the resulting filter. The detail signal at level $(j+1)$ can be computed in a similar way using the high-pass filter g. The signals at higher levels of decomposition provide information with large details.

In order to reconstruct signals at lower levels of decomposition, the dual scaling function $\tilde{\phi}(t)$ and dual wavelet $\tilde{\psi}(t)$ can be defined. For an orthonormal wavelet basis, the basis and its dual are the same [34]. The multiscale relationships for the dual scaling function $\tilde{\phi}(t)$ and the dual wavelet $\tilde{\psi}(t)$ exist in the Fourier domain as

$$\hat{\tilde{\phi}}(\omega)=\frac{1}{\sqrt{2}}\hat{\tilde{h}}\left(\frac{\omega}{2}\right)\hat{\tilde{\phi}}\left(\frac{\omega}{2}\right) \tag{9}$$

and

$$\hat{\tilde{\psi}}(\omega)=\frac{1}{\sqrt{2}}\hat{\tilde{h}}\left(\frac{\omega}{2}\right)\hat{\tilde{\psi}}\left(\frac{\omega}{2}\right) \tag{10}$$

where $\tilde{h}$ is called the low-pass reconstruction filter, and $\tilde{g}$ is called the high-pass reconstruction filter. The reconstructed signal $a_{j,k}$ are then computed as

$$a_{j,k}=\frac{1}{2}\left(a_{j+1}*\tilde{h}_j(k)+d_{j+1}*\tilde{g}_j(k)\right) \tag{11}$$

Using Equation 11, the approximated signal $a_{j,k}$ can be reconstructed by first inserting $(2j-1)$ zeros between each sample of the reconstruction filters $\tilde{h}$ and $\tilde{g}$ and then adding together the discrete convolution between a_{j+1} and the resulting low-pass dual filter and the convolution between d_{j+1} and the resulting high-pass dual filter.

This algorithm is suitable for applications in which the exact location of the wavelet decomposition is important, such as singularity detection and certain approximation

problems because the number of data and the location of each point are preserved across scales during the analysis.

3.3.3 Decomposition and Reconstruction Algorithms in Two Dimensions

The two-dimensional wavelet transform can be computed with a separable extension of the one-dimensional decomposition algorithm [35]. Figure 3-2 demonstrates the decomposition of the original reflectivity field into "Approximate" coefficients, and "Horizontal," "Vertical," and "Diagonal" details coefficients. The one dimension of original image (i.e., image rows) is first filtered with a one-dimensional filter and then the other dimension of the resulting signals (i.e., image column) is filtered with another one-dimensional filter. The wavelet transform is computed on an image by repeating this process for different resolutions.

The schematic diagram in Figure 3-3 demonstrates the reconstruction of the original image from its "Approximate" and "details" coefficients. One dimension of the "Approximate" and details images is filtered with a one-dimensional filter; then, the other dimension of the resulting images is filtered with another one-dimensional filter. The resulting images will be the Approximation (*A*), Horizontal details (*H*), Vertical details (*V*) and Diagonal details (*D*), which will reconstruct the original image when added together. Therefore, this methodology can be viewed as an extension of the classification of rain type using one-dimensional wavelet analysis.

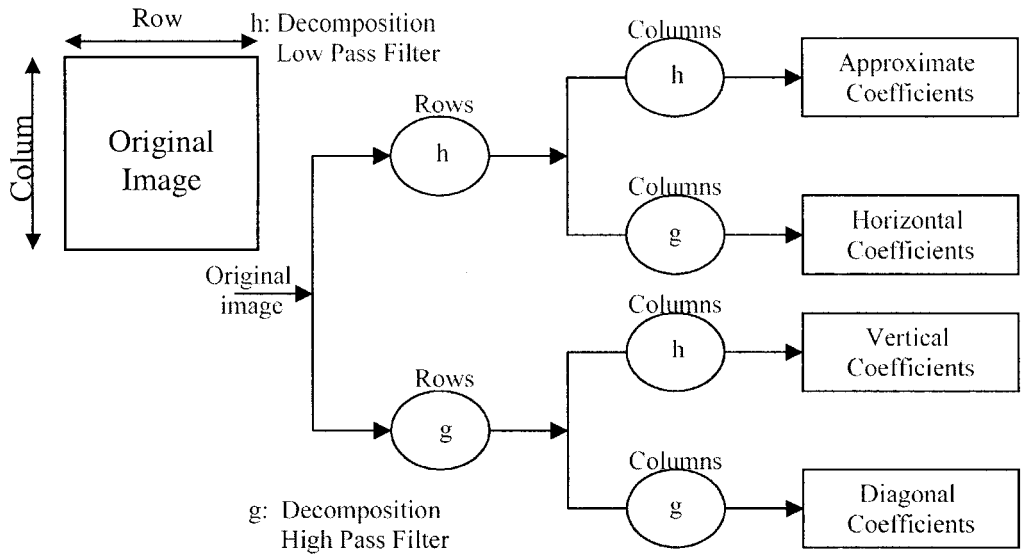

Figure 3-2. The diagram shows the multiresolution analysis using 2-D wavelet transform. The two-dimensional reflectivity field decomposition into "Approximate" coefficients and "Vertical," "Horizontal," and "Diagonal" coefficients is shown. In order to get these coefficients, the rows (one dimension of the image) go through the low-pass filter and high-pass filter. Subsequently, the columns of the results go through another decomposition with low- and high-pass filters

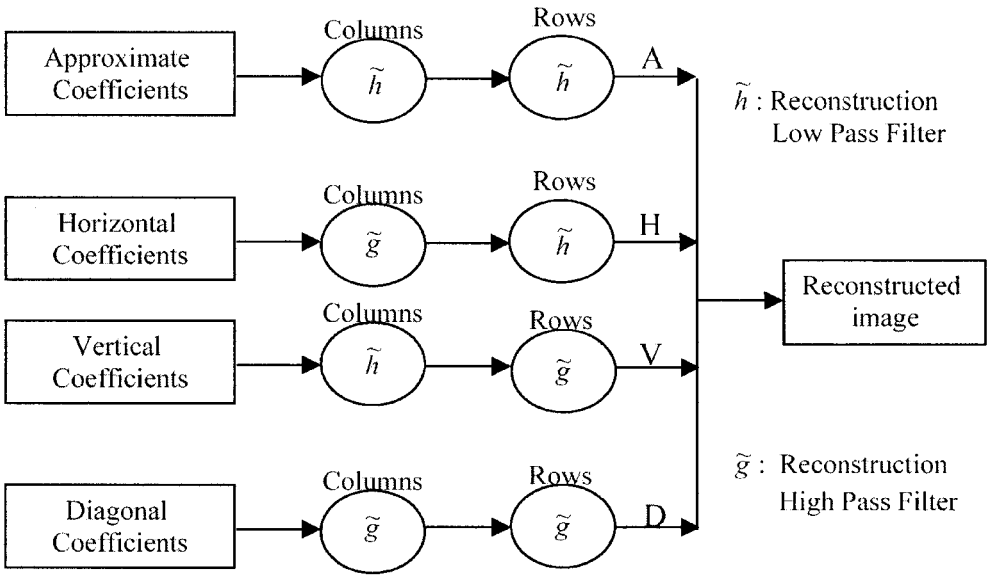

Figure 3-3. This diagram shows how the multiresolution analysis using 2-D wavelets is used for reflectivity field in reconstruction. The columns and the rows, the two dimensions of the image, go in two stages through reconstruction via low and high filters. The details A, V, H, and D are added together to get the original image.

3.3.4 Quadratic Spline Wavelet for Singularity Detection

If a wavelet is chosen as the first derivative of a smoothing function, any function whose integral is equal to one and asymptotically reaches zero, and if the first and the second derivative of the function exists, then the local maxima of the absolute value of the wavelet transform can be used to detect the occurrence of singularities [35][37]. A quadratic spline wavelet with compact support, which is shown in Figure 3-4, is used in the proposed algorithm to classify precipitation type. The quadratic spline is suitable for detecting singularity in the data [36]. The quadratic spline wavelet is given by

$$\psi(t)=\begin{cases} 2(t+1)^2 & -1 \le t < -1/2 \\ -4t(t+1)-2t^2 & -1/2 \le t < 0 \\ -4t(1-t)-2t^2 & 0 \le t < 1/2 \\ -2(t-1)^2 & 1/2 \le t < 1 \end{cases} \tag{12}$$

The filter coefficients of quadratic spline wavelet are given in Table 3–2 [34]

Table 3–2. Filter coefficients for the spline wavelet.

k	h(k)	$\tilde{h}$ (k)	g(k)	$\tilde{g}$ (k)
2				0.03125
1	0.125	0.125		0.21875
0	0.375	0.375	-0.5	0.68750
1	0.375	0.375	0.5	0.68750
2	0.125	0.125		0.21875
3				0.03125

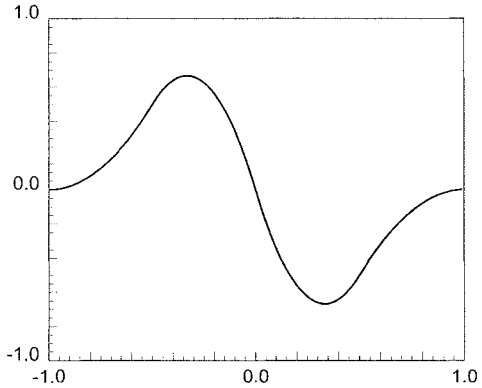

Figure 3-4. Quadratic spline wavelet from [35].

3.4 ALGORITHM DEVELOPMENT FOR PRECIPITATION TYPE CLASSIFICATION

The development of the rain type classification algorithm, which is based on the two-dimensional wavelet transform technique, is described in this section. The two-dimensional wavelet transform analysis decomposes the signal to "Approximate" coefficients, and "Horizontal," "Vertical," and "Diagonal" details coefficients. In this proposed algorithm, the reconstructed "Vertical" (V), and "Horizontal" (H) details shown in Figure 3-3 are used. Figure 3-5 shows the wavelet decomposition of the reflectivity field into V and H details through a storm observed by TRMM-PR. A_1, A_2, and A_3 are the approximation for the original signal at resolution levels 1, 2 and 3. V_1, V_2, and V_3 are the vertical details for the original signal at resolution levels 1, 2 and 3. H_1, H_2, and H_3 are the horizontal details for the original signal at resolution levels 1, 2 and 3. If we add *A1 to* H_1, V_1, and D_1, we will get the original image. We will also get A_1 if we add A_2 to H_2, V_2, and D_2. Similar inferences can be applied to level three.

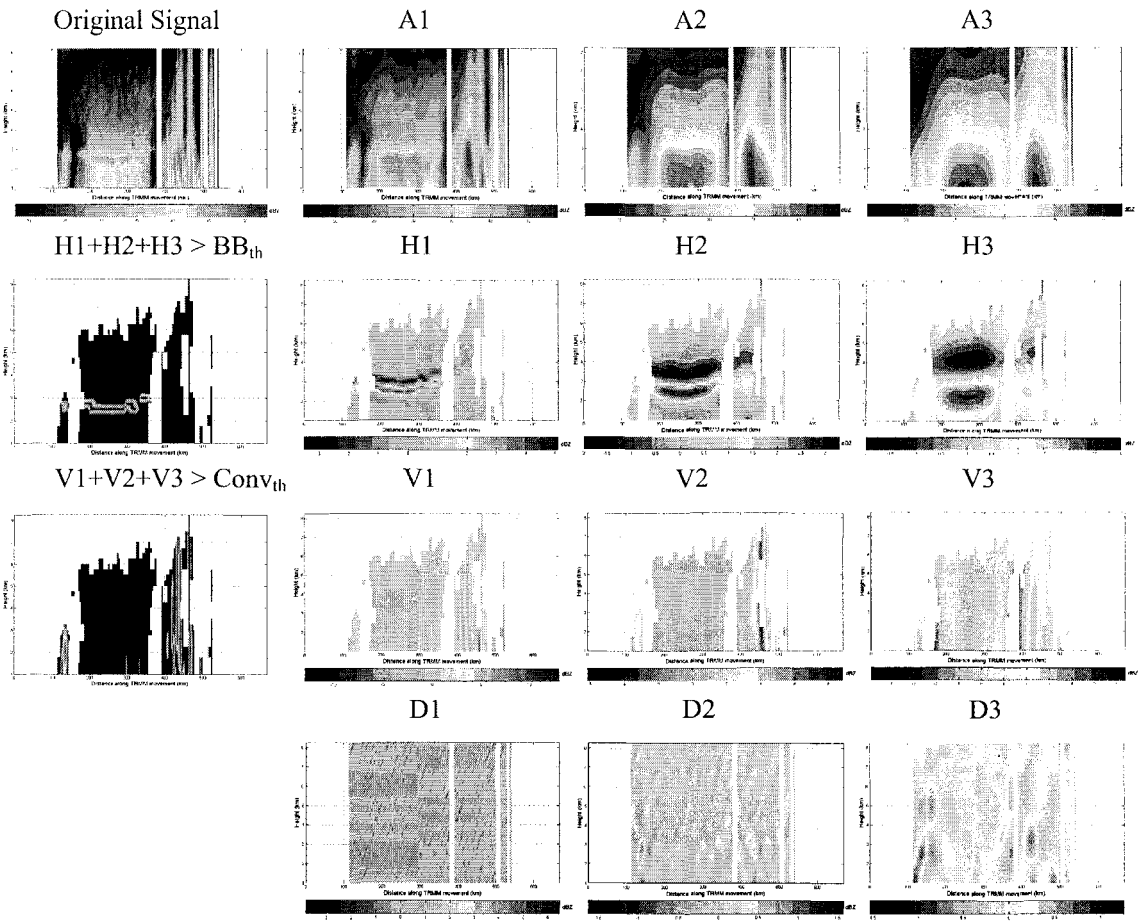

Figure 3-5. The wavelet analysis of the vertical profile of reflectivity of precipitation data decomposed on 3 resolution levels. Ai , Hi, and Vi are the Approximate coefficients, Horizontal coefficients and Vertical coefficients at the resolution level i. The summation of H1, H2, and H3 is introduced to show the ability to detect bright band using the horizontal details. Similarly, the figure that shows the summation of the vertical coefficients $V_1+V_2+V_3$ is introduced to demonstrate the potential of using these coefficients to detect the convective regions. Conv_th is the convective threshold while BB_th is the BB threshould.

The proposed algorithm uses four steps for classifying rain types. The algorithm first tries to detect the bright band by analyzing the horizontal details of the multiresolution analysis of the two-dimensional wavelet transform. If bright band is detected, then the profile is classified as stratiform with bright band. In the next two steps, the convective regions of the rain are classified based on the vertical details of wavelet analysis and a modified version of TRMM-PR 2A-23 H-method algorithm. During the last step, the

profiles not identified as bright bands or convective are classified as stratiform. Figure 3-6 shows the flowchart that outlines the convective stratiform classification algorithm based on the multiresolution analysis of two-dimensional wavelet transform. The details of each step are described in the following sections.

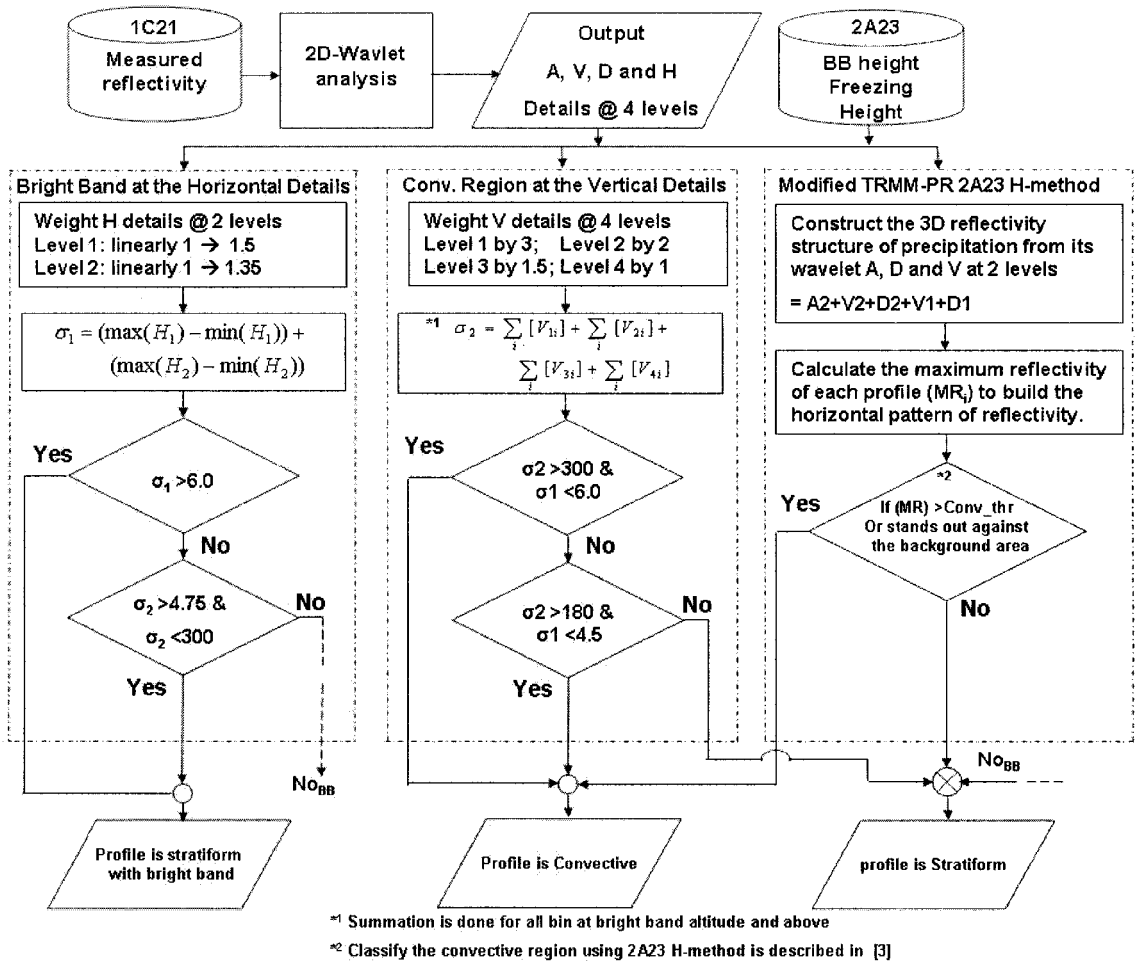

Figure 3-6. The flowchart of the procedure of convective stratiform classification algorithm based on the 2D wavelet transform analysis. The algorithm first detects the BB using the H details. Then the classification of the convective region is done using the vertical details and a modified version of the H-method..

3.4.1 BRIGHT BAND AT THE HORIZONTAL DETAILS

The analysis based on the horizontal details of the vertical profile can be summarized as follows:

- By using the ground as the reference, we can see that there is a rapid increase in reflectivity value from below the bright band. This is seen as a large positive value in the horizontal details of the analyzed reflectivity field. The plots of H_1 and H_2 in Figure 3-5 show high positive value at bright band altitude.
- The value of the reflectivity in the vertical profile decreases above the altitude of the bright band. This can be seen as a large negative value in the horizontal details of the reflectivity field. The plots of H_1 and H_2 at Figure 3-5 show high negative value at the area above bright band height.
- Bright band peaks occur at approximately at the same altitude from ground within a storm. The horizontal details of the two-dimensional wavelet analysis tend to detect the similarities in the horizontal direction within a small variation with altitude from ground. The plots of H_1 and H_2 in Figure 3-5 show similarity in the horizontal details at the same altitude from ground.
- In order to minimize spurious signals, a window of size 2 km on either side of freezing height is chosen to search for the bright band region.

To detect the bright band at each vertical profile, the sum of the difference between the maximum and minimum of the horizontal details of two resolution levels at bright band window is calculated as

$$\sigma_1 = (max\,(H_1) - min\,(H_1)) + (max\,(H_2) - min\,(H_2)) \qquad (13)$$

As the TRMM-PR scans off nadir, the vertical profile of reflectivity for stratiform precipitation with bright band tends to be less sharp than the profile near the nadir ray. In order to use the same threshold off-nadir as well as near nadir rays, the horizontal details (H_1 and H_2) are weighted at the first resolution level by a factor of 1 near nadir, and 1.75 off nadir at ray 49 and a linearly varying value in between. At the second resolution level, the horizontal details are weighted by a factor of 1 near nadir and 1.35 off nadir at ray 49 and a linearly varying value in between. The weighting factor is larger in the first level because the horizontal details at the first level detect the sharp changes while at the second level they detect wider ones. The weighting factor is determined by examining many profiles with bright band at nadir and off nadir.

If the difference value (σ_1) exceeds a threshold of value 6, then the bright band is detected and the rain profile is stratiform. But if the difference value is less than 6 and more than 4.75, then the algorithm will wait until examination of the vertical details of the profile to make a decision. This is done to ensure that the evidence of the existence of bright band is thoroughly examined, and not potentially contaminated by the features of the convective region, as there are some overlaps between the two regions. The threshold value 6 was determined experimentally by analyzing a large volume of bright band data. The profile will be classified as stratiform with bright band if the sum of the vertical details (σ_2, described in the following) is small.

3.4.2 Convective Region and the Vertical Details

The convective rain type region can be viewed as a region with high reflectivity compared to its surrounding area in the vertical cut of the reflectivity profile. Similar to the detection of bright band using the horizontal details described in the previous section,

the vertical details of the two-dimensional wavelet analysis of the vertical section is used to detect the convective region. The sum of the vertical details is calculated at each vertical resolution at each bin at bright band height and above, as in the following equation

$$\sigma_2 = \sum_{i=1}^{4} \sum_{j=1}^{n} a_i V_{ij} \qquad (14)$$

Where V_{ij} is the vertical details of the multiresolution analysis of the 2D plane of the reflectivity field at cross-track direction at resolution level i and bin j; n varies from the index of the bright band up to storm top; a_i is the weighting factor. If bright band altitude is unknown, then the altitude of 0.5 km below freezing height is used. The vertical details are weighted at different resolution levels with different values. First resolution level is weighted by 3, second resolution level is weighted by 2, third resolution level is weighted by 1.5, and the fourth resolution level is weighted by 1. The weighting factor is introduced to weight the lower scale more than the higher ones to effectively detect convective storms.

This method is used to ensure that the bright band detection based on the horizontal details does not detect a false bright band. If the value of σ_2 exceeds a threshold of 300 and the horizontal details in the first step did not exceed 6, then the corresponding profile is perceived to be convective. Also, if the value is more than 180 and the horizontal details in the first step did not exceed 4.75, the profile will be classified as convective.

3.4.3 Improvement to TRMM-PR 2A-23 H-method Algorithm.

As mentioned before, the convective rain type region can be viewed as an area with high reflectivity compared to its surrounding area. This technique has been used to

distinguish the convective rain region from the stratiform rain region by examining the storm horizontal pattern of reflectivity [33]. In order to avoid including bright band peak reflectivity, the 2A-23 H-method uses the maximum reflectivity value of the vertical profile below the freezing height with a 1 km margin to build the storm horizontal pattern of reflectivity. Due to the uncertainty in determining the freezing height in some regions around the globe and due to the very low freezing height in other areas, the reflectivity of the bright band peak in some cases can be wrongly used when calculating the horizontal pattern of reflectivity.

The current procedure can be improved in two areas. Currently, the local maximum of reflectivity is only calculated at a limited height that is below the freezing height with a 1 km margin. This will limit choosing the real maximum value of vertical profile of reflectivity outside this limited area and may lead to misclassification of some convective rain type as stratiform rain type. Secondly, when the algorithm erroneously picks a bright band peak, the vertical profile may be classified as convective. The technique using the two-dimensional wavelet analysis proposes a solution to these problems by the following three steps:

- The reflectivity field is decomposed using the two-dimensional wavelet analysis at 2 levels.
- The reflectivity field after that is reconstructed from its "Approximate" (*A*), "Vertical" (*V*) and "diagonal" (*D*) details.
- The convective rain region is classified by examining the reconstructed horizontal pattern of reflectivity using the same algorithm proposed for the H-method in [33].

The "Horizontal" details (H_1 and H_2) that may carry bright band characteristics are not included in rebuilding the reconstructed reflectivity field. This will help in calculating the horizontal pattern of reflectivity for a storm without interference from bright band region reflectivity. Also, the search for maximum reflectivity value along the vertical profile is extended up to storm top height when building the horizontal pattern of reflectivity. Using these steps will allow detection of the precise maximum reflectivity value in the vertical section that excludes bright band contamination.

3.5 DATA ANALYSIS AND ASSESSMENT

A comparison between the decisions from the convective stratiform classification algorithm based on the 2-Dimensional Wavelet Analysis method (2D-WA) and those of TRMM-PR (2A-23) algorithm is done for 30 different cases from different regions around the globe. The precipitation type product (2A-54) of the TRMM Ground Validation (GV) program from validation sites around the globe, namely, Melbourne, Florida; Houston, Texas; Darwin, Australia; and Kwajalein, Marshall Islands are used in most cases for comparison. The detailed analysis for five of those cases is presented here in detail.

3.5.1 CASE STUDY: AUGUST 26, 2001 (LATITUDE: -33.05°, LONGITUDE: -58.32°).

This is an ideal case that shows the potential of the proposed algorithm. In this case, the V-method of 2A-23 misses detecting the bright band region that occurs at low altitude at off nadir vertical profiles. On the other hand, the H-method of 2A-23 when building the horizontal pattern of reflectivity includes the reflectivity of the bright band region in its calculation of the maximum reflectivity value. This leads to rain type

misclassification. Figure 3-7 shows the location of the storm. The horizontal pattern for the reflectivity at 2 km above the ground level is shown in Figure 3-8. The TRMM-PR 2A-23 H-method algorithm is compared against bright-band observations detected by the V-method. Errors in detecting the bright band at the vertical method may make it difficult to make the correct decision on the 2A-23 algorithm. The proposed algorithm based on the modified H-method described in the previous section removes the horizontal details of the wavelet analysis of the reflectivity profile (bright band region), which leads to better use of the horizontal method without interference from the bright band region.

Figure 3-9 and Figure 3-10 show the maximum reflectivity before and after removing the horizontal details. Figure 3-11 and Figure 3-12 show the convective region "without the surrounding area labeled as convective" as classified by the modified H-method and the original method. The original method has more convective regions than the modified method. In some cases, the modified H-method tends to increase the area of the convective region when calculating maximum reflectivity at all heights of the vertical profile of reflectivity, which increases the chance of having a larger value of maximum reflectivity.

Figure 3-13 and Figure 3-14 show the value of the maximum sum of the horizontal details and the maximum sum of the vertical details. To detect bright band and classify the convective region, those values are compared against a threshold as described.

The decision maps of 2A-23, one-dimensional wavelet analysis descried in [71], and 2D-WA algorithm are shown in Figure 3-15-Figure 3-17. As shown the decision map of 2A-23, the inference has more convective regions at the edge of the storm far from the nadir ray. The algorithm based on one-dimensional wavelet analysis detected more bright

band at off-nadir ranges. The one-dimensional algorithm is based on a point-wise vertical profile, and horizontal continuity is not enforced explicitly. This may result in slightly noisy images. This problem is solved by going to 2D wavelet analysis.

Figure 3-18 shows the total of 3 levels of horizontal details at a vertical cut from the top of the storm toward the ground at 252 km along the TRMM movement. It is clear from this figure that the bright band region exists in the middle of the storm as well as at the edges, but with different resolutions. The multiresolution analysis using a two-dimensional wavelet is tuned to detect both the sharp bright band and the weak one. It should be noted that the presence of a bright band implies stratiform precipitation. In summary, the two-dimensional analysis improves further the performance of the one-dimensional analysis presented before in [71] as well as the 2A-23 decision.

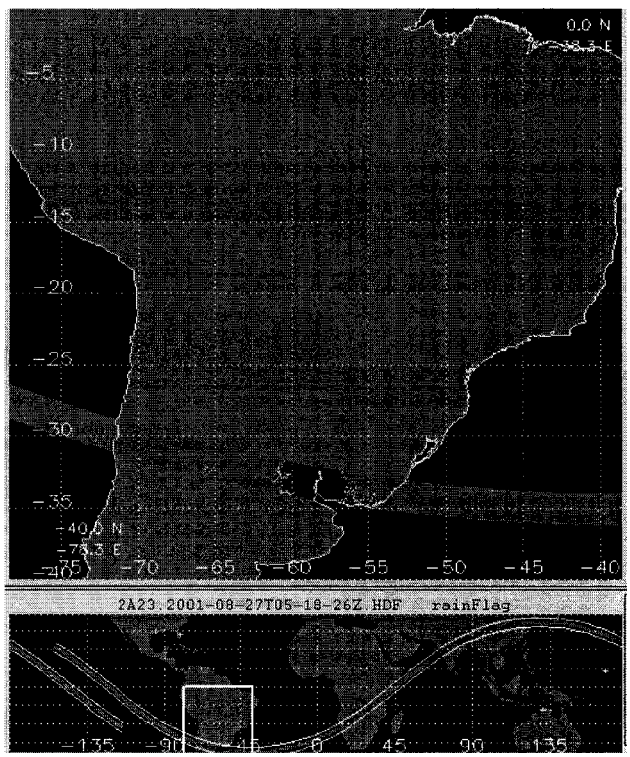

Figure 3-7. Location of the storm for case study of August 26, 2001, over South America.

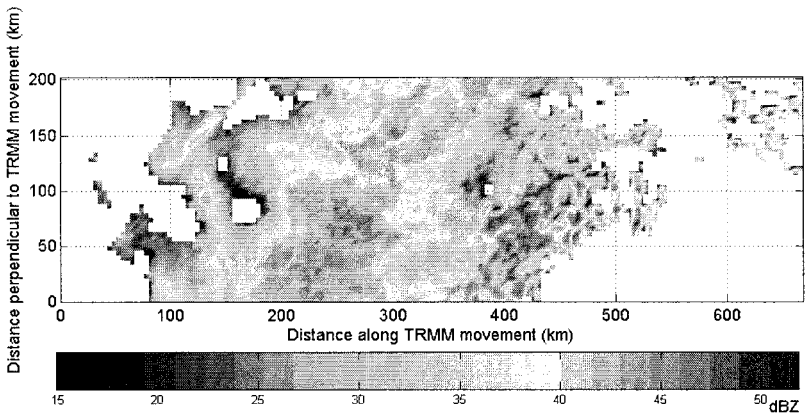

Figure 3-8. Reflectivity map of the storm at 2 km above the ground for case study of August 26, 2001.

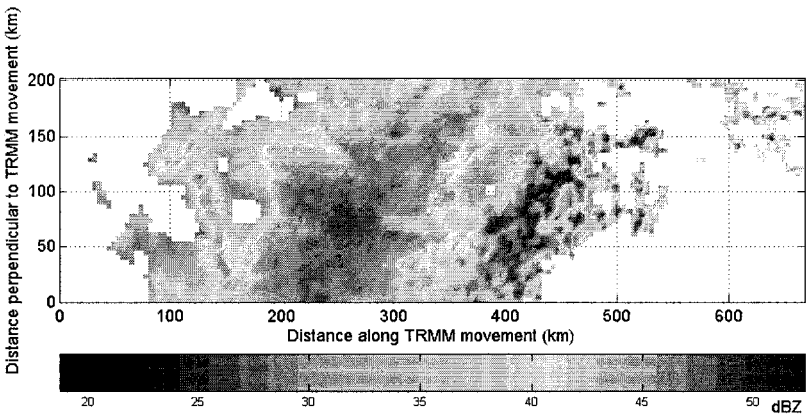

Figure 3-9. Maximum reflectivity at each vertical profile for case study of August 26, 2001.

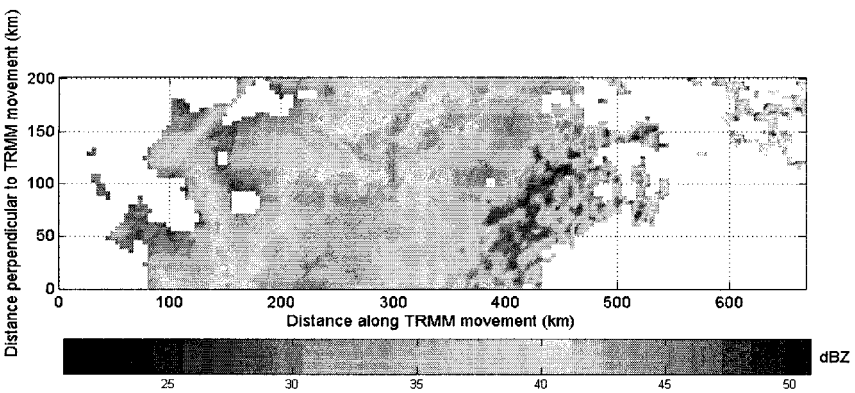

Figure 3-10. Maximum reflectivity at each vertical profile after removing the horizontal details for case sudy of August 26, 2001. It shows the convective area is not affected by this procedure while the stratiform area has decreased in the reflectivity value.

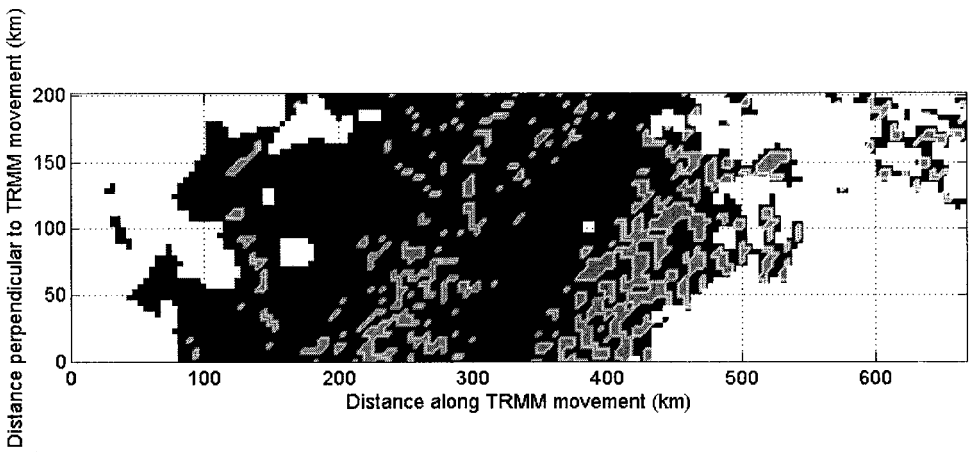

Figure 3-11. Decision map for case study of August 26, 2001, using the modified H-method. Red indicates convective region while blue indicates stratiform region.

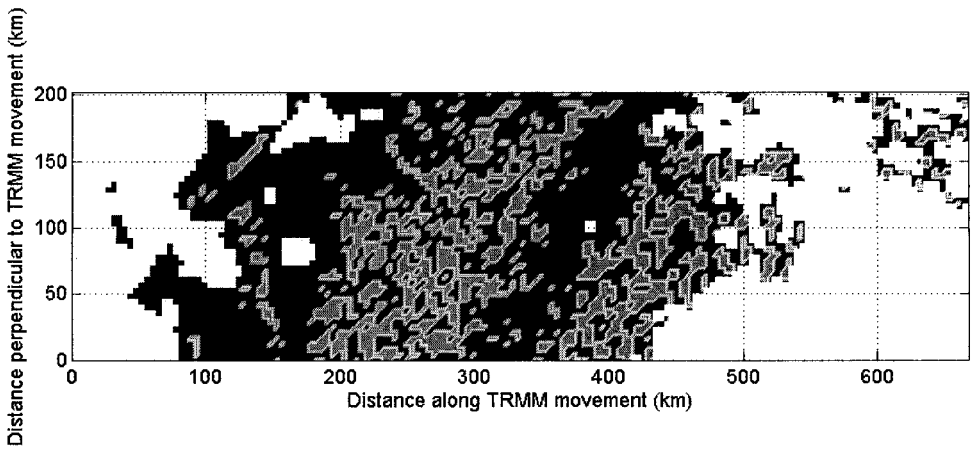

Figure 3-12. Decision map for case study of August 26, 2001, using 2A-23 H-method. Red indicates convective region while blue indicates stratiform region.

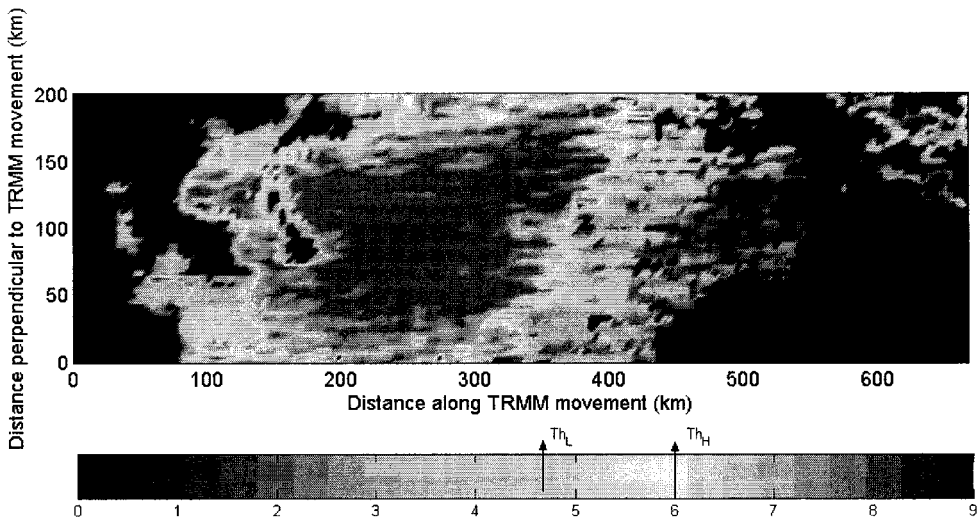

Figure 3-13. The maximum of the sum of the horizontal details at each profile for the study of August 26, 2001. The high value indicates that the profile mostly has stratiform with bright band and the low value indicates that the profile mostly has no bright band.

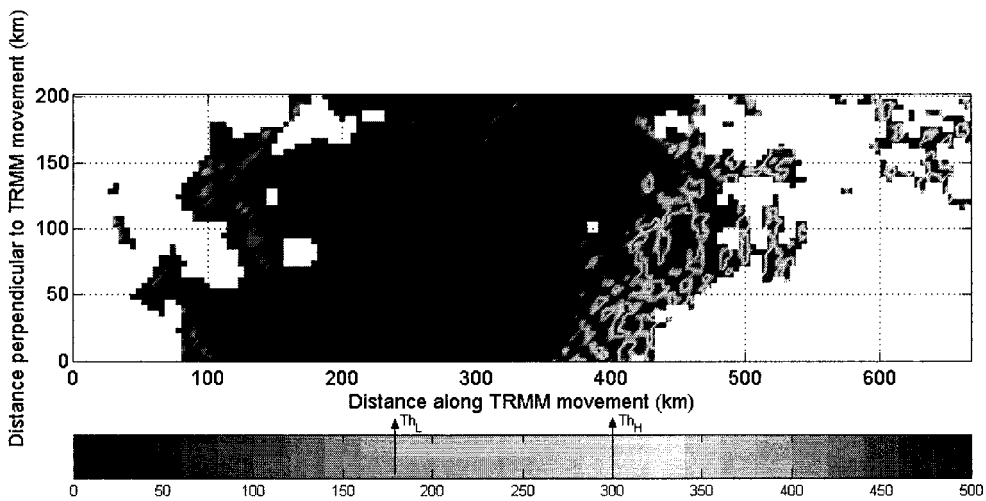

Figure 3-14. The maximum of the sum of the vertical details of the wavelet analysis of the vertical profile that was used for convective region classification for the study of August 26, 2001. The high value indicates that the profile is mostly convective.

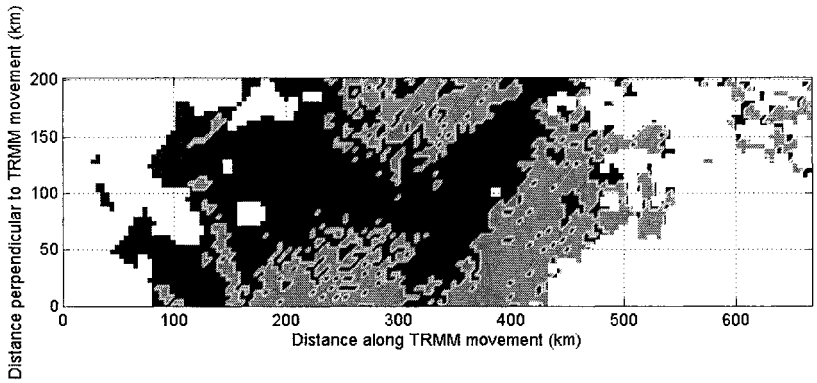

Figure 3-15. Decision map for case study of August 26, 2001, using the TRMM-PR (2A-23) algorithm. Red indicates convective region while blue indicates stratiform region.

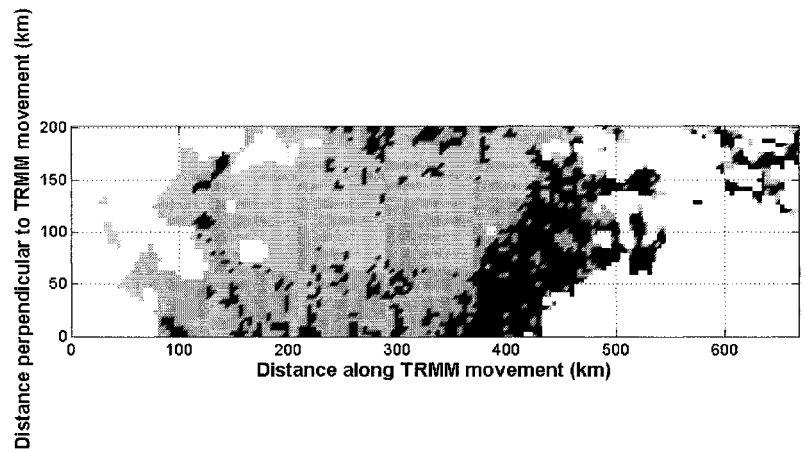

Figure 3-16. Decision map for case study of August 26, 2001, using the 1D wavelet analysis algorithm described in [71]. Red indicates convective region while blue indicates stratiform region.

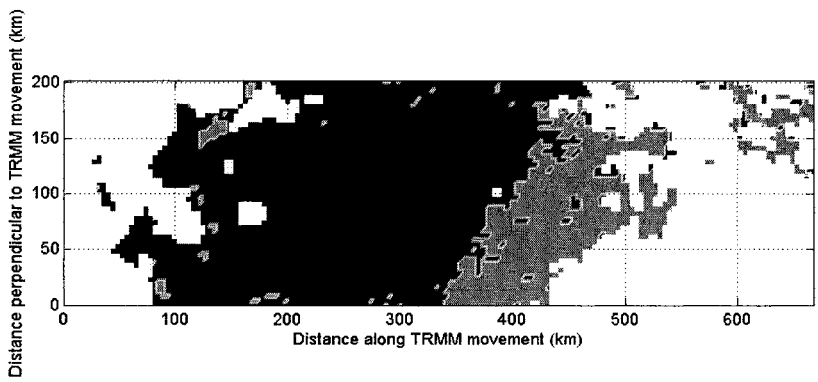

Figure 3-17. Decision map for case study of August 26, 2001, using the 2D wavelet analysis (2D-WA). Red indicates convective region while blue indicates stratiform region.

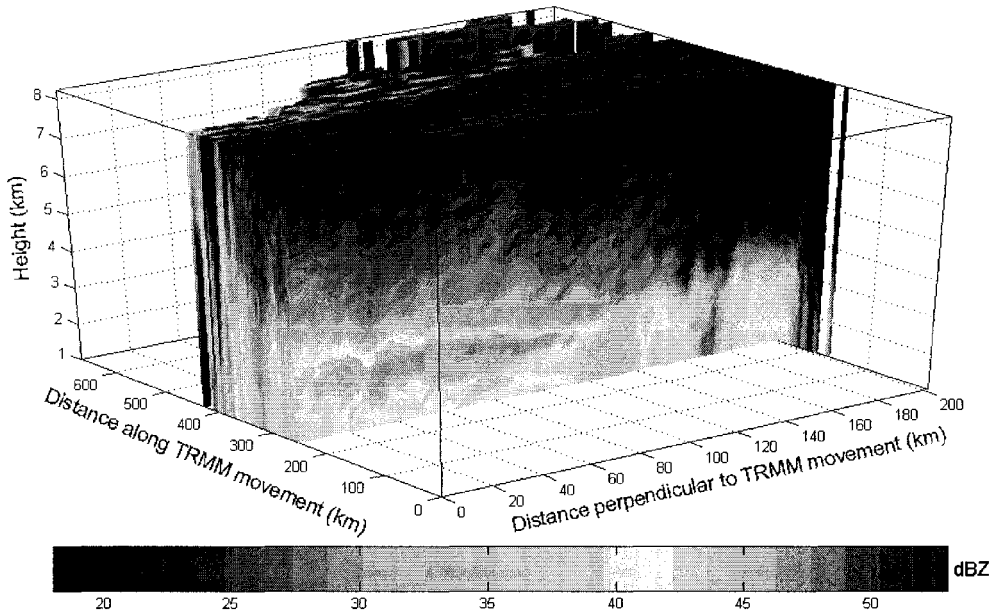

Figure 3-18. Reflectivity range profile at 252 km along the TRMM movement for case study of August 26 , 2001.

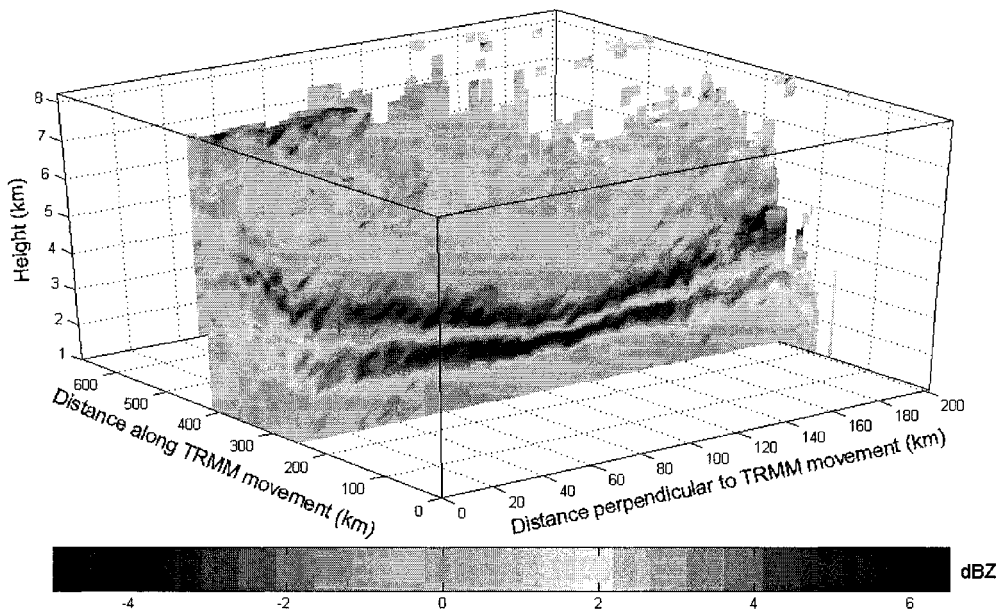

Figure 3-19. The sum of the horizontal details of 3 resolutions levels at 252 km along the TRMM movement for case study of August 26, 2001. The bright band is sharper near nadir than off-nadir rays. Positive value indicates increase in reflectivity value while negative value indicates decrease in reflectivity value.

3.5.2 CASE STUDY: DECEMBER 09, 1998 (LATITUDE: -12.97°, LONGITUDE: 130.73°).

In this case Hurricane Thelma, which developed from a weak tropical disturbance in the Arafura Sea, is classified as to convective/stratiform rain type. This storm system is classified as a category 5. Figure 3-20 shows the location of the storm at the north region of Australia. The visible light image and the horizontal reflectivity pattern at 2 km above the ground height are shown in Figure 3-21 and Figure 3-22. The two decisions of the 2A-23 algorithm and 2D-WA are shown in Figure 3-23 and Figure 3-24. By examining the vertical cut from the top of the storm toward the ground at 100 km along the TRMM movement for reflectivity profile and 50 km perpendicular to the TRMM movement [Figure 3-25-Figure 3-26], it is clear that the 2D-WA algorithm comes with more reasonable decisions for this case.

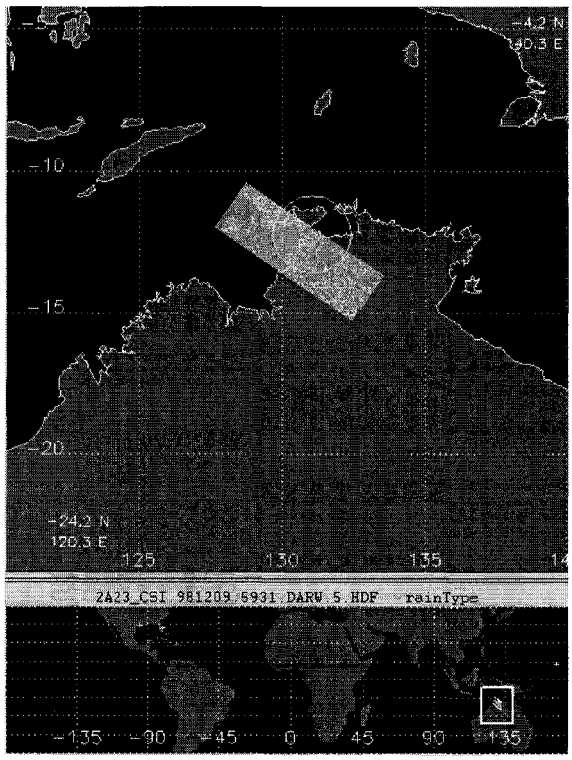

Figure 3-20. The storm location for the case study of December 9, 1998, over north Australia.

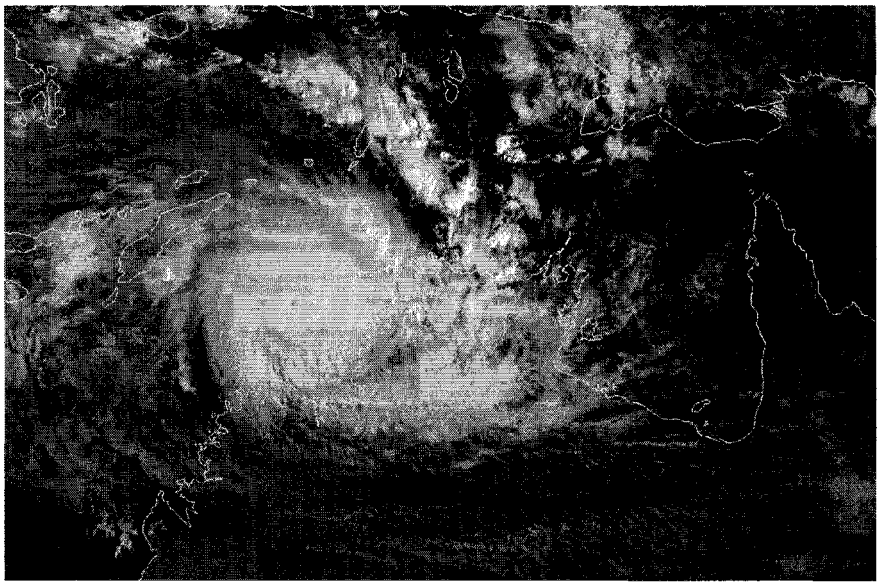

Figure 3-21. The visible light image of the storm for the case study of December 9, 1998, over North Ausraila.

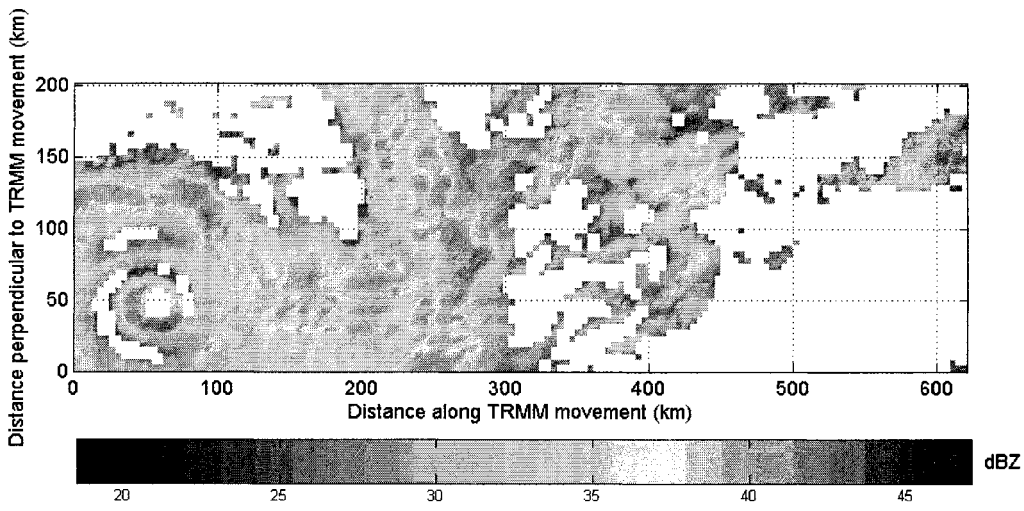

Figure 3-22. The storm reflectivity at 2 km above the ground for the case study of December 9, 1998.

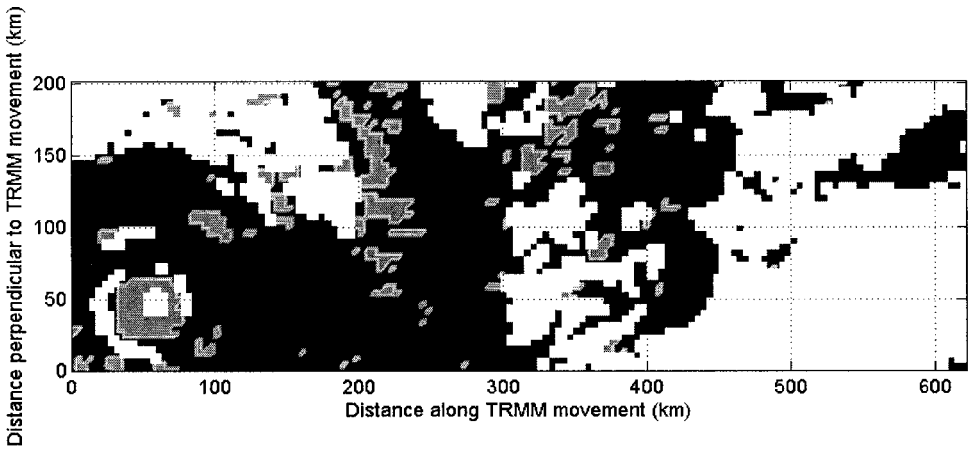

Figure 3-23. The decision map for the case study of December 9, 1998, using the 2D-WA algorithm. Red indicates convective region while blue indicates stratiform region.

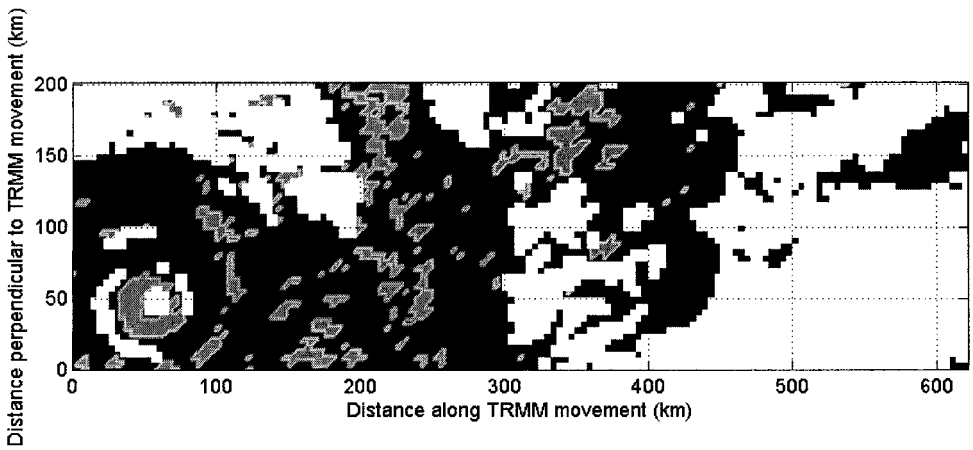

Figure 3-24. The decision map for the case study of December 9, 1998, using the TRMM-PR (2A-23) algorithm. Red indicates convective region while blue indicates stratiform region.

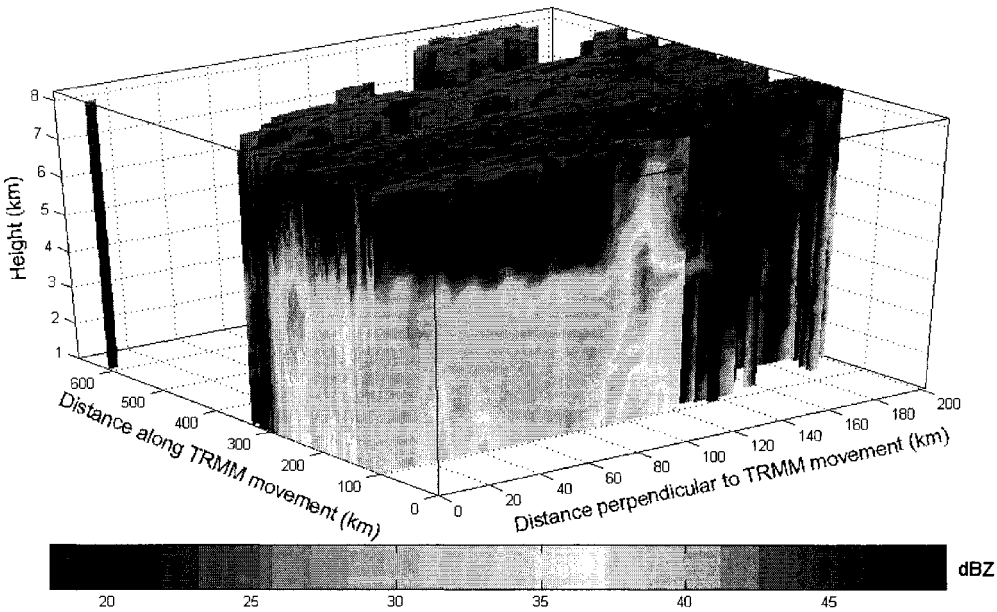

Figure 3-25. The reflectivity range profile at 100 km along the TRMM movement for the case study of December 9, 1998.

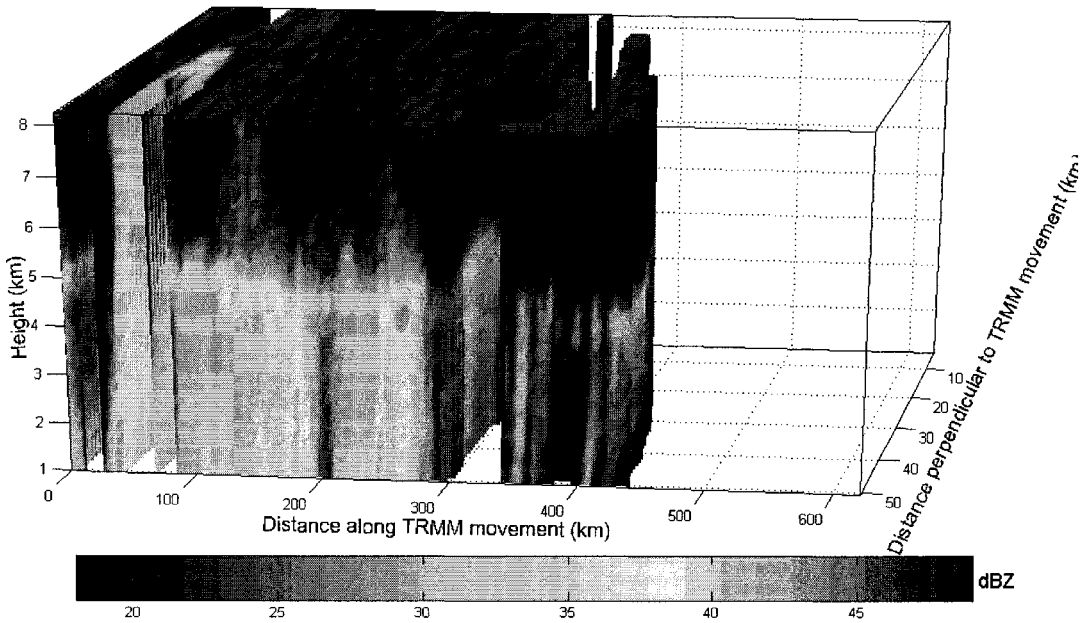

Figure 3-26. The reflectivity range profile at 50 km perpendicular to the TRMM movement for the case study of December 9, 1998.

3.5.3 CASE STUDY: COMPARISON WITH GV SITES DECISION

The TRMM-GV program operates several ground validation sites to provide ground observation of precipitation over different climatological regions. For each satellite overpass of a TRMM-GV site, both GV and PR maps indicate the locations of convective and stratiform precipitation. In general, the GV radar will show a larger region of rain because the PR has lower sensitivity. The horizontal resolution of the PR is about 4 km, while that of the GV radar map has a resolution of 2 km. The GV sites adopted the algorithm of [33] for producing a rain type classification product. The basic objective of the TRMM-GV program is that it can produce an independent product and provide reference data for comparison. If the two estimates are in agreement, the confidence will be higher in all estimates.

The convective stratiform classification product (2A-54) of the TRMM-GV program from four validation sites around the globe (Melbourne, Florida; Houston, Texas; Darwin, Australia; and Kwajalein, Marshall Islands) were evaluated. Figure 3-27-Figure 3-42 show the reflectivity at 2 km above the ground height, the classification decision of the TRMM-GV 2A-54, the classification decision of the TRMM-PR 2A-23 and the classification decision of the 2D-WA algorithm over the Melbourne, Florida; Houston, Texas; Darwin, Australia; and Kwajalein, Marshall Islands TRMM-GV sites. It should be noted that the ground validation observations were rotated and plotted to align with the local coordinate system formed with axis along the TRMM-PR orbit. The PR scan area is used as the boundary of the ground radar data to simplify the comparison.

A cursory inspection of those figures shows that the 2D-WA decision and the TRMM-GV 2A-54 as well as the 2A-23 decision are all similar. For this image, the percentage of convective region was 28% for 2A-23, 36% for the 2D-WA algorithm, and 34.5% for 2A-54, showing a good agreement of the composition.

It should be noted that TRMM-GV program provides an independent estimation at certain locations. The closer the estimates are to agreement, the greater the confidence is in all the estimates. In some cases, the proposed method (2D-WA) tends to increase the area of convective region because the calculation of the maximum reflectivity is done at all heights of the vertical profile.

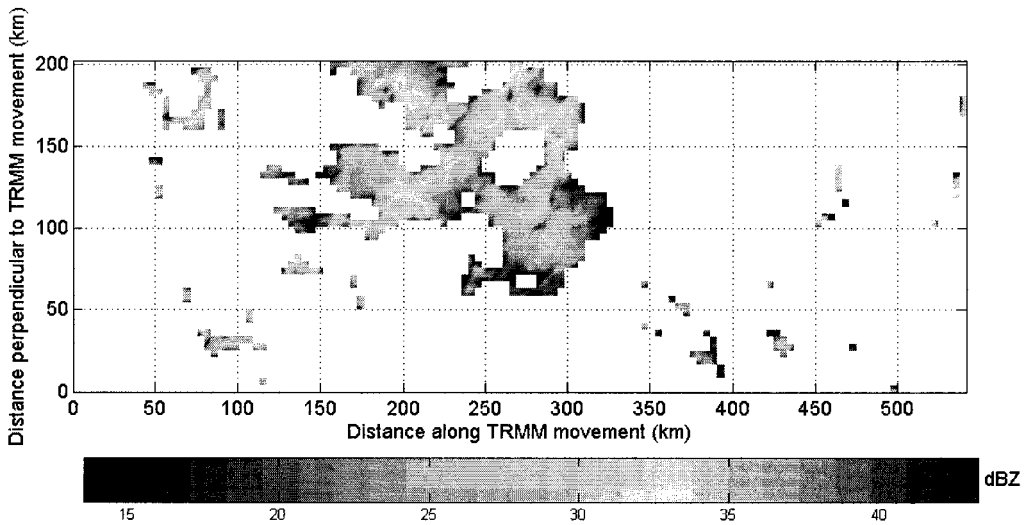

Figure 3-27. The storm reflectivity at 2 km above the ground of the case study of of August 21, 1999.

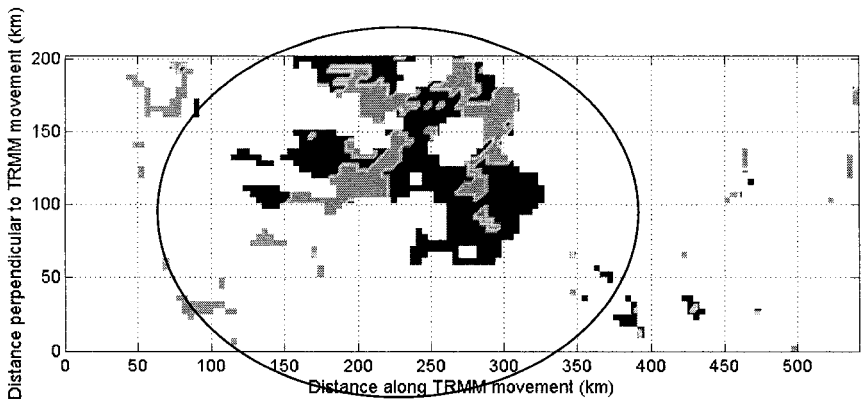

Figure 3-28. The decision map for the case study of August 21, 1999, using the 2D-WA . Red indicates convective region while blue indicates stratiform region.

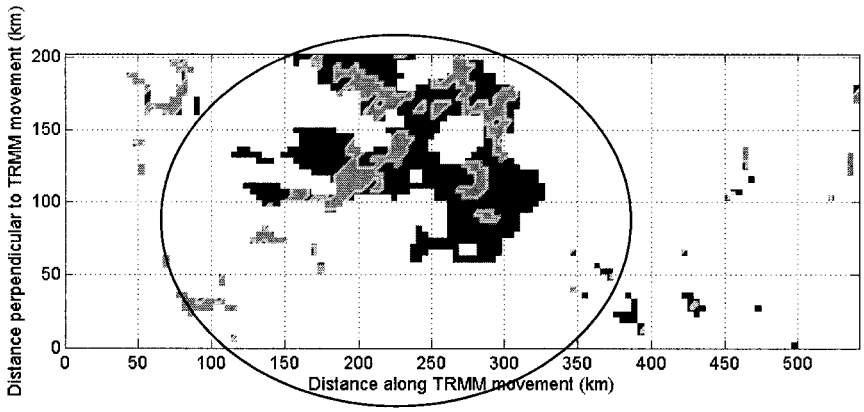

Figure 3-29. The decision map for the case study of August 21, 1999, using the TRMM-PR (2A-23) algorithm. Red indicates convective region while blue indicates stratiform region.

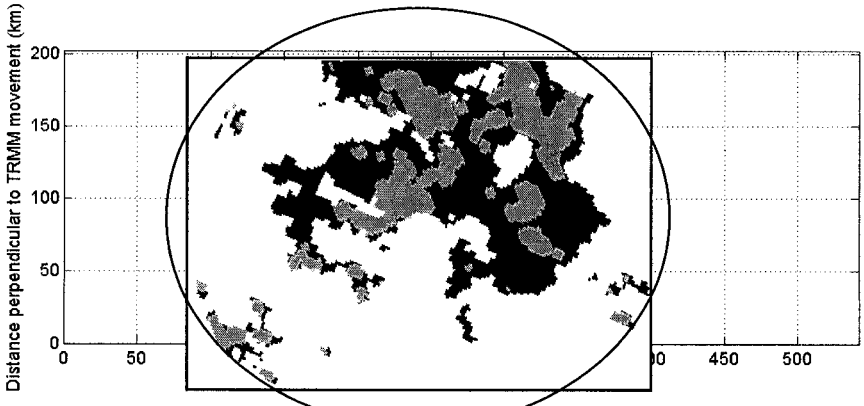

Figure 3-30. The decision map for the case study of August 21, 1999, over Melborne, Florida using the 2A-54 algorithm. Red indicates convective region while blue indicates stratiform region.

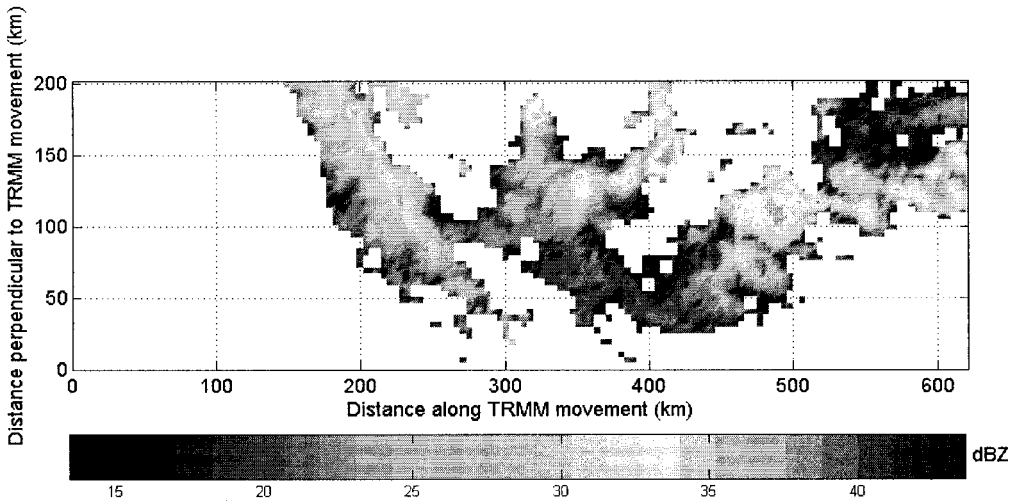

Figure 3-31. The storm reflectivity at 2 km above the ground for the case study of March 29, 1999.

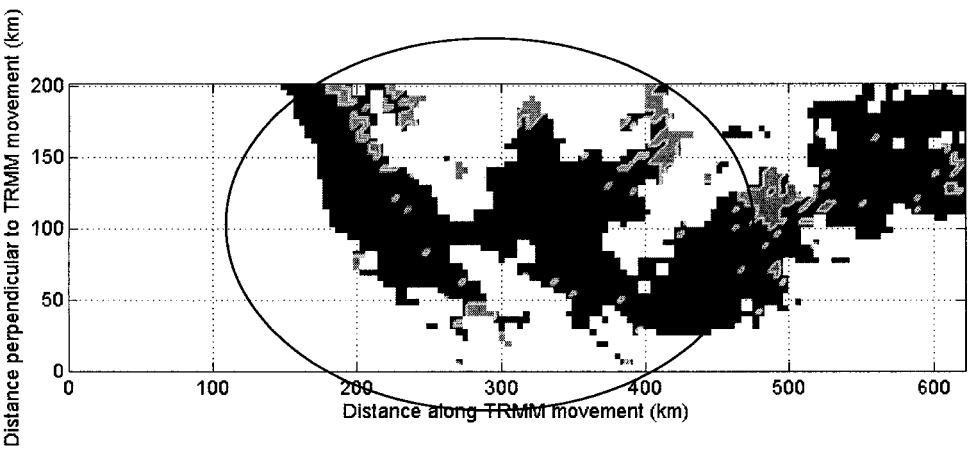

Figure 3-32. The decision map for the case study of March 29, 1999, using the 2D-WA algorithm. Red indicates convective region while blue indicates stratiform region.

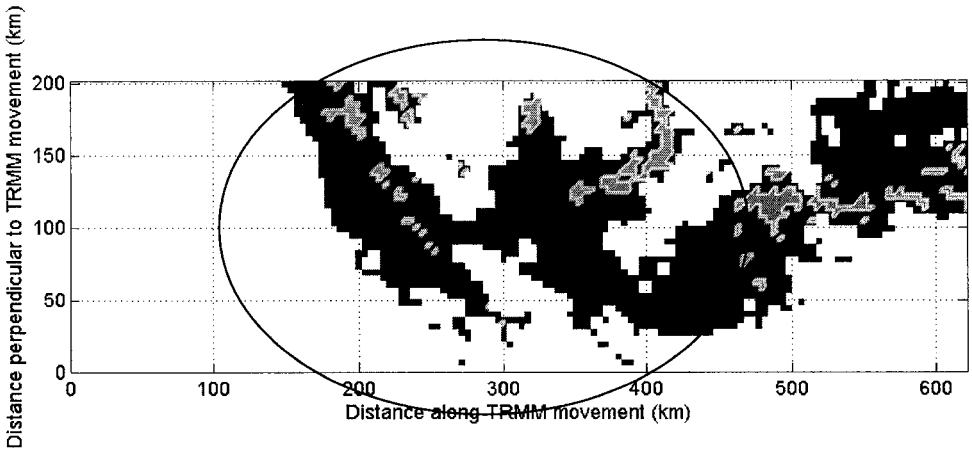

Figure 3-33. The decision map for the case study of March 29, 1999, using the TRMM-PR (2A-23) algorithm. Red indicates convective region while blue indicates stratiform region.

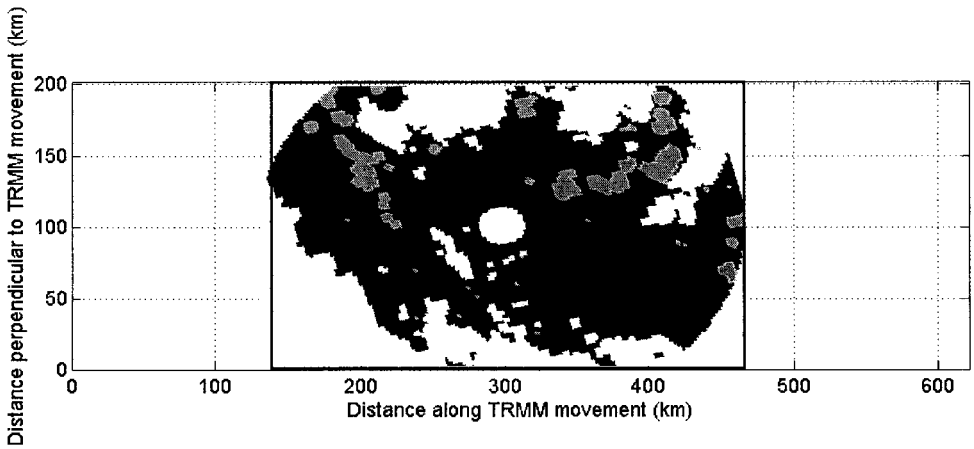

Figure 3-34. The decision map for the case study of March 29, 1999, over Houston, Texas using the 2A-54 algorithm. Red indicates convective region while blue indicates stratiform region.

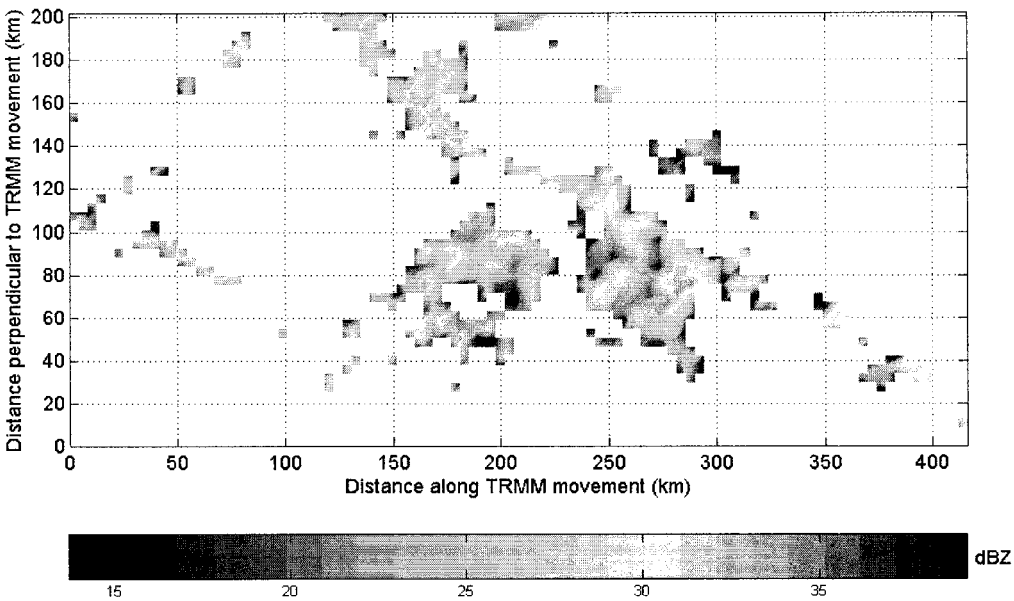

Figure 3-35 The reflectivity of the storm at 2 km above the ground for the case study of January 17, 2000.

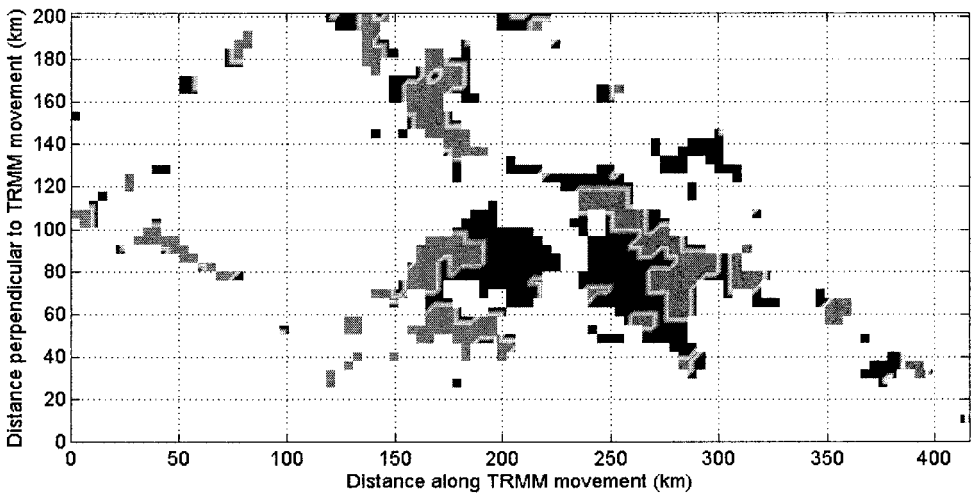

Figure 3-36. The decision map for the case study of January 17, 2000, using the 2D-WA algorithm. Red indicates convective region while blue indicates stratiform region.

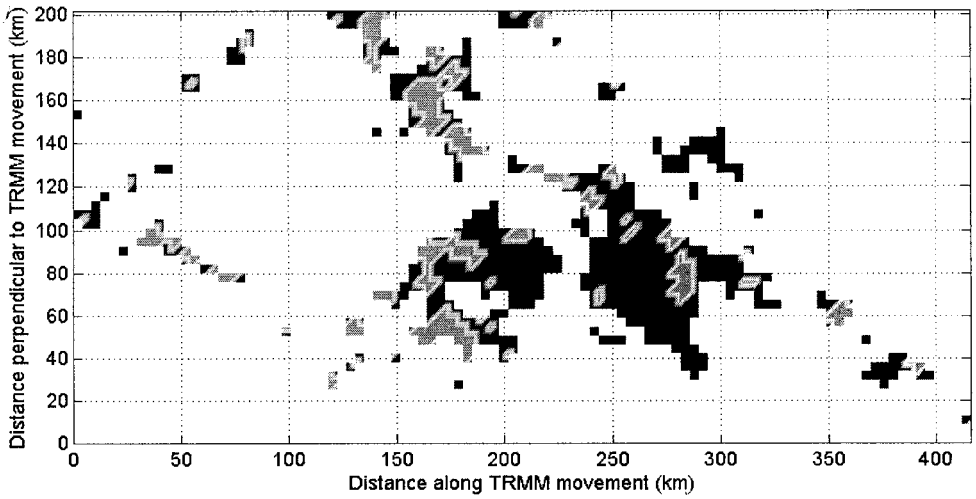

Figure 3-37. The decision map for the case study of January 17, 2000 using the TRMM-PR (2A-23) algorithm. Red indicates convective region while blue indicates stratiform region.

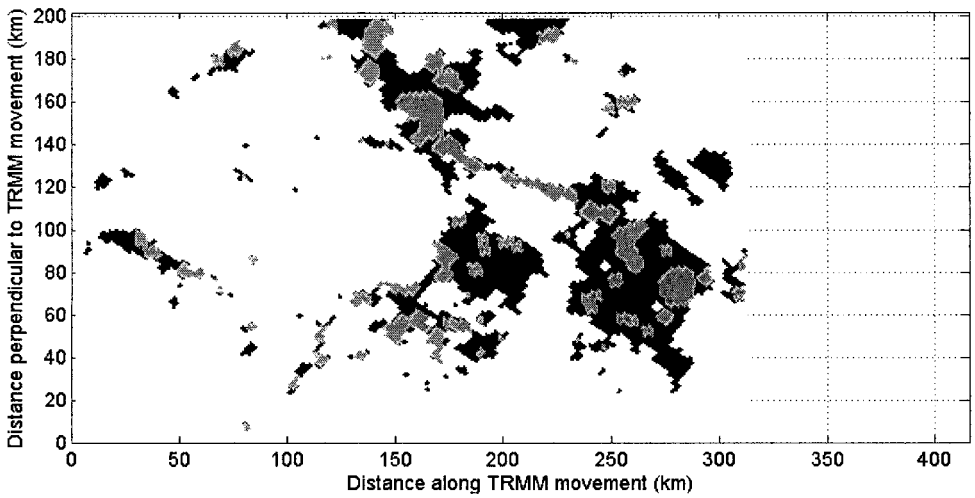

Figure 3-38. The decision map for the case study of August 21, 1999, over Kwajalein using the 2A-54 algorithm. Red indicates convective region while blue indicates stratiform region.

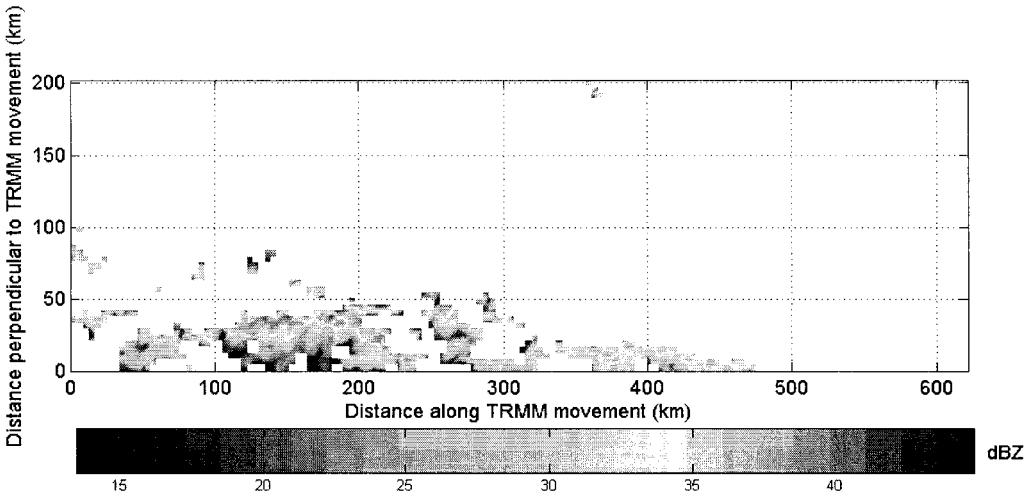

Figure 3-39. The reflectivity of the storm at 2 km above the ground for the case study of January 28, 1998.

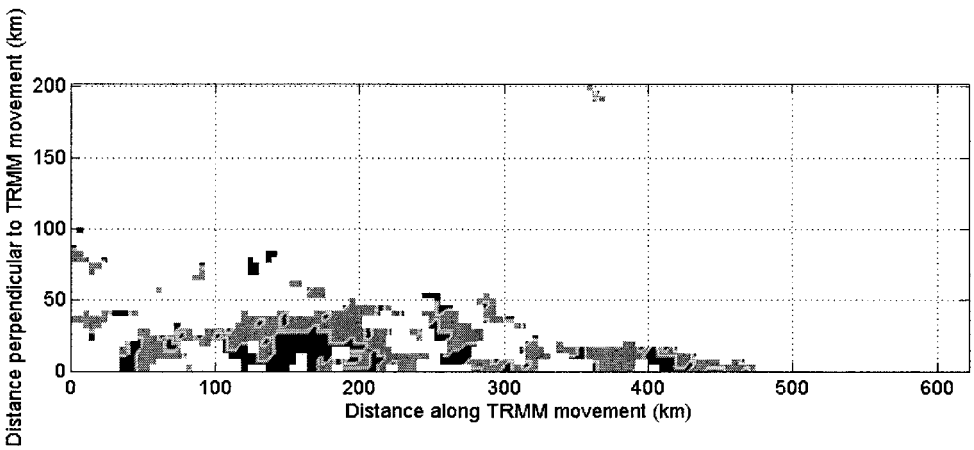

Figure 3-40. The decision map for the case study of January 28, 1998, using the 2D-WA . Red indicates convective region while blue indicates stratiform region.

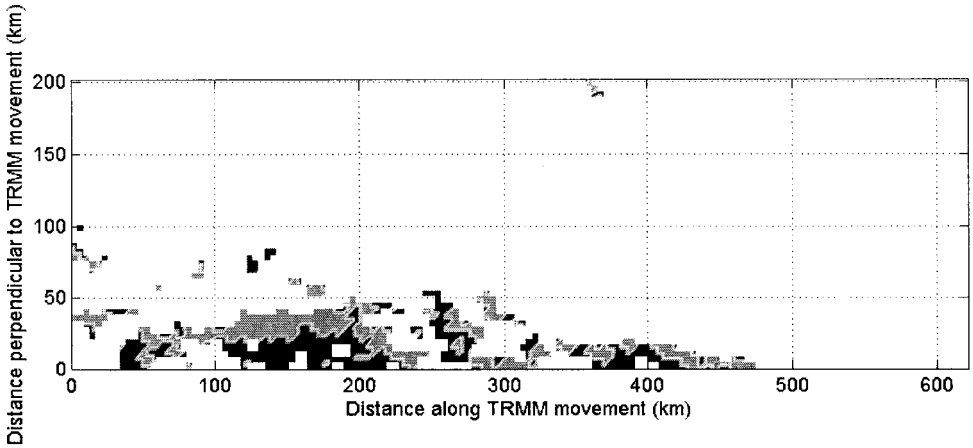

Figure 3-41. The decision map for the case study of January 28, 1998, using the TRMM-PR (2A-23) algorithm. Red indicates convective region while blue indicates stratiform region.

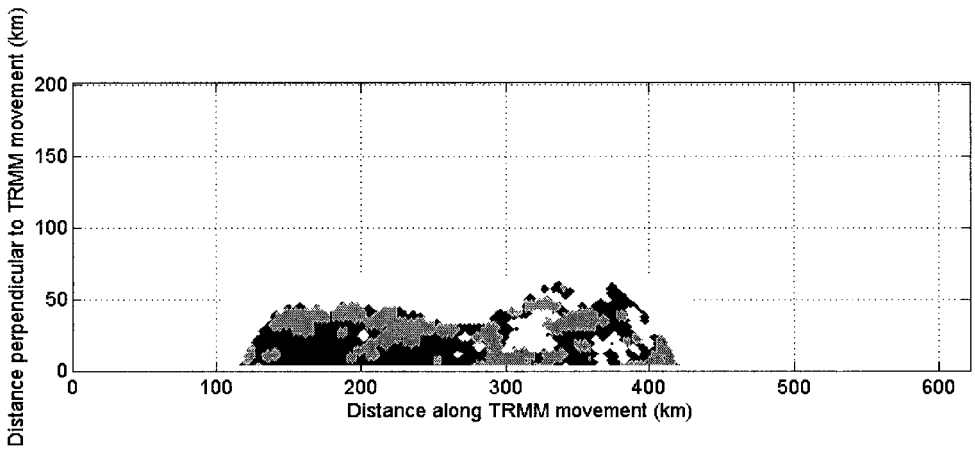

Figure 3-42. The decision map for the case study of January 28, 1998, over Darwin, Australia using the 2A-54 algorithm. Red indicates convective region while blue indicates stratiform region.

3.6 GLOBAL COMPARISON

Quantitative evaluations of the inter-comparison for the 30 cases that have 61,793 rain profiles are summarized in Table 3–3 and Table 3–4. Table 3–3 shows the comparison of convective and stratiform rain type classification between the 2D-WA method and the 2A-23 method. The results in Table 3–3 show that both methods are in agreement 84.4% of the time. The 2A-23 method classified about 77.8% of the observations as stratiform, where the 2D-WA algorithm identifies 72.2% of the data as stratiform. This slight difference is essentially the difference between the two algorithms. The increase in the percentage of convective region detected by 2D-WA is expected since it calculates the maximum value of reflectivity up to storm top height in the H-method.

Table 3–4 shows the comparison of the bright band detection between the two algorithms for the 30 cases. In general, the two algorithms agree 78.5% of the time. However, individually, the 2D-WA method detects bright band 54.4% of the time whereas 2A-23 detects bright band 40.9% of the time. This difference is expected since it was shown that the 2D-WA method detects more bright band in the vertical profile than is detected by the 2A-23 algorithm. While these are limited results, the 30 case studies were picked independently during a 4 year period over different geographical regions and are expected to be representative of the comparison trend between the two algorithms.

Table 3–3. The rain classification comparison summary between 2A-23 algorithm and 2D-WA algorithm.

Rain Type Method	Stratiform 2A-23	Convective 2A-23	Total % number of profiles
Stratiform	67.2%	5.0%	72.2%
2D-WA	41515	3103	44618
Convective	10.6%	17.2%	27.8%
2D-WA	6555	10620	17175
Total %	77.8%	22.2%	100%
# of rays	48070	13723	61793

Table 3–4. The bright band comparison summary between 2A-23 algorithm and 2D-WA algorithm.

BB/NO BB Method	BB 2A-23	No BB 2A-23	Total % number of profiles
BB	36.9%	17.5%	54.4%
2D-WA	22788	10828	33616
No BB	4.0%	41.6%	45.6%
2D-WA	2474	25703	28177
Total %	40.9%	59.1%	100%
# of rays	25262	36530	61793

3.7 CONCLUSION

Precipitation type classification and bright band detection are two results produced by the TRMM-PR program. The precipitation type is currently classified as convective or stratiform based on the spatial variability of the TRMM precipitation radar reflectivity patterns as well as the presence of bright band. Alternative algorithms for rain type classification as well as bright band detection are developed based on the two-dimensional wavelet analysis. It is shown that the 2D-WA method performs better for bright band detection, especially for bright band at low altitudes. A qualitative comparison of the rain type classification with simultaneous ground radar results show that both the 2A-23 and 2D-WA algorithms compared well with the ground radar classification. With respect to the data analyzed for bright band detection, the two algorithms agreed 78.5% of the time. 2D-WA classifies 54.4% of the cases as bright band, whereas 2A-23 classifies 40.9% of the cases as bright band. This difference is attributed to the fact that that 2A-23 lacks some of the low altitude or weak bright bands.

This study is only a comparison study and hence should not be interpreted as an evaluation of the 2A-23 algorithm. While classifying rain type, the two algorithms agree 84.4% of the time. In terms of rain type classification, 2A-23 deems 77.8% of the observations as stratiform whereas 2D-WA deems them as stratiform 5.6% lower. This

decrease in classification of stratiform types by 2D-WA and increased detection in bright band can be attributed to the use of maximum reflectivity at all heights after removing the horizontal details instead of using maximum reflectivity below freezing height (minus 1 km margin). While these are limited results, the 30 case studies were picked independently during a 4-year period over different geographical regions and are expected to be representative of the comparison trend between the two algorithms. A combination of the 2A-23 and 2D-WA decision is likely to produce better detection of bright band and rain type classification.

CHAPTER 4

SELF-ORGANIZING MAP OF SPACE-BORNE PRECIPITATION RADAR RAIN PROFILES ON A GLOBAL SCALE

4.1 INTRODUCTION

Precipitation exhibits extensive spatial variability. An understanding of the vertical structure of precipitating systems is important because it implies differences in the rainfall rate and it also has an impact on the global atmospheric circulation [18]. A better understanding of the vertical structures of precipitation is also important for improving satellite precipitation algorithm and understanding microphysical processes including latent heating release [3][4][5]. Observation of the vertical profile of precipitation over the global tropics is a key objective of the Tropical Rainfall Measuring Mission (TRMM). TRMM Precipitation Radar (PR) produces high resolution vertical profiles of precipitation. Various published research efforts have shown that extensive information about the type of storm is contained in the vertical structure.

This chapter looks into the problem of classifying global precipitation radar profiles using the self-organizing maps (SOM) technique that can extend rain-type classification beyond the convective/stratiform rain type separation. The SOM forms a non linear mapping of the data into a two-dimensional map grid. The SOM can be used as an exploratory data analysis tool for generating hypotheses about the relationships of the profiles, and eventually as a function of the vertical profile. Reflectivity observation data

of the vertical rain profile obtained from TRMM-PR is classified with a SOM algorithm. The methodology is demonstrated by computing SOMs for one year of TRMM-PR data around the globe. The organization structure is visualized by the SOM method, and the organized structures are characterized in terms of radar reflectivity profile properties. Subsequently, the data are summarized in a new way that is used to compare the reflectivity observation data from different regions around the globe as well as different seasons.

4.2 SELF-ORGANIZING MAPS AND CLASSIFICATION OF THE VERTICAL PROFILE OF REFLECTIVITY

Classifying the reflectivity observation of vertical rain profile (VPR) can help us extract useful information that can be used to discover new precipitation properties. Classification of large VPR observational data sets over the globe using a SOM is used also to summarize the data in a new way that can be useful in comparing different vertical rain profiles. This may lead to the discovery of unsuspected relationships between the classes of the VPR and other climatological parameters. Dealing with classification of VPR problems requires a large amount of background work, namely: problem specification, preparation of the data, and interpretation of the results with a priori knowledge.

4.2.1 SELF-ORGANIZING MAP

The self-organizing map is an unsupervised learning neural network which forms a nonlinear mapping of data to a two-dimensional map grid [38]. It has been widely used in different engineering applications [38][39][40][41].

A SOM consists of neurons organized on a regular low-dimensional grid. Each neuron is represented by d-dimensional weight vector, $m = [m_1 \ldots\ldots m_d]$, where d equals the dimension of the input vectors. The neurons are connected to adjacent neurons by a neighborhood relation which dictates the structure of the map. The structure of the SOM used in this research is shown in Figure 4-1. The SOM training algorithm updates the best matching unit (BMU) and its topological neighbors on the map. The region around the BMU is pulled toward the presented training sample as shown in

Figure 4-2. At the end, the neurons will become orders on the output grid [42]. The batch and sequential algorithm are used in the training SOM. The batch algorithm is much faster than the sequential algorithm, and the results of the batch algorithm are typically just as good or even better.

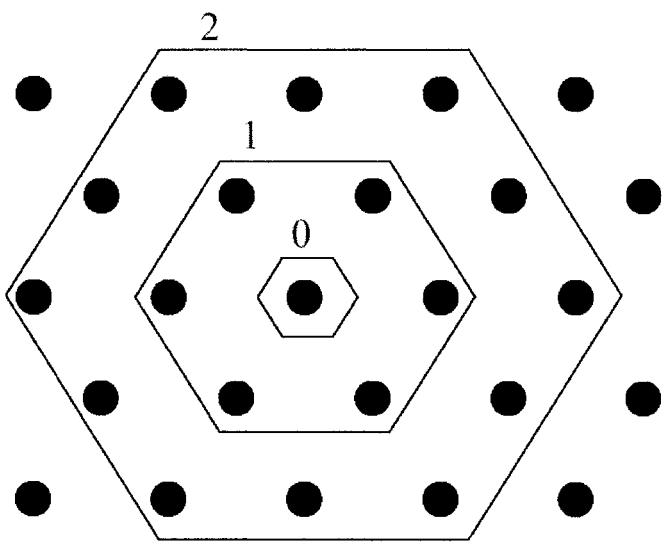

Figure 4-1. The hexagonal lattice structure of SOM with discrete neighborhood (size 0, 1 and 2) of the centermost unit.

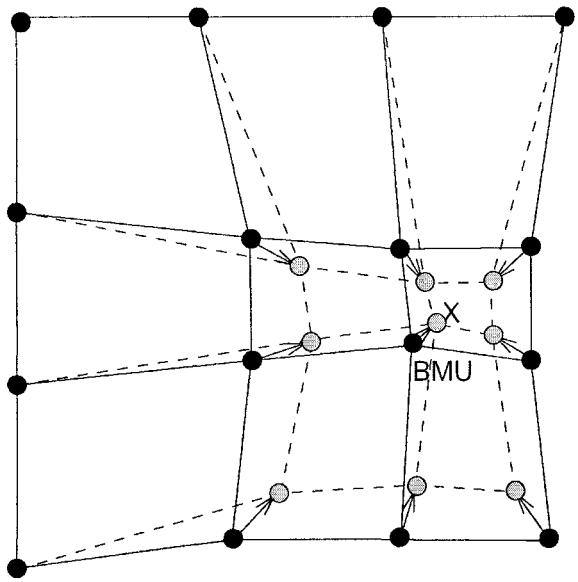

Figure 4-2. Updating the best matching unit (BMU) and its neighbors toward the input sample marked with x. The solid and dashed lines correspond to situation before and after updating, respectively.

4.2.2 SOM SEQUENTIAL ALGORITHM

A SOM sequential algorithm is trained iteratively where the input data vectors are presented to the algorithm one at a time in a random order. For each input vector x, the BMU is determined as

$$\|x - m_b\| = \min_i \{\|x - m_i\|\} \tag{15}$$

Usually, Euclidean distance is used as a measure of the similarity. To calculate the distance between vectors with missing data, the algorithm excludes these values from the distance calculation. For that the missing value contribution to the calculation of the distance is zero. Because the same data are ignored in each distance calculation, this is a valid solution [43]. The distance measure after these changes can be written as

$$\|x - m_b\|^2 = \sum_{k \in K} (x_k - m_k)^2 \tag{16}$$

where k is the set of known (not missing) variables of sample vector x. x_k and m_k are

k^{th} components of the sample and weight vectors. In the next step, the prototype vectors are updated.

The BMU and its topological neighbors are moved closer to the input vector in the input space. The update rule for the prototype vector of unit is

$$m_i(t+1) = m_i(t) + \alpha(t)h_{ci}(t)[x - m_i(t)] \tag{17}$$

where t denotes time. $x(t)$ is an input vector drawn from the input data set at time t. $h_{ci}(t)$ is the neighborhood kernel around the winner unit c and $\alpha(t)$ is the learning rate. The Gaussian neighborhood function [Figure 4-3] is mostly used in this type of problem. The Gaussian neighborhood function can be written as

$$h_{ci}(t) = \exp(-\frac{\|r_i - r_c\|^2}{2\sigma(t)^2}) \tag{18}$$

The SOM training is usually performed in two phases. In the first phase, a relatively large initial learning rate and neighborhood radius are used. In the second phase, both learning rate and neighborhood radius are small right from the beginning. This procedure first tunes the SOM approximately to the same space as the input data and then fine-tunes the map. The error function of the SOM in the case of a discrete data set and fixed neighborhood function can be shown to be [44]

$$E = \sum_{i=1}^{N}\sum_{j=1}^{M} h_{cj}\|x_i - m_j\|^2 \tag{19}$$

where N is number of training samples, and M is the number of map units

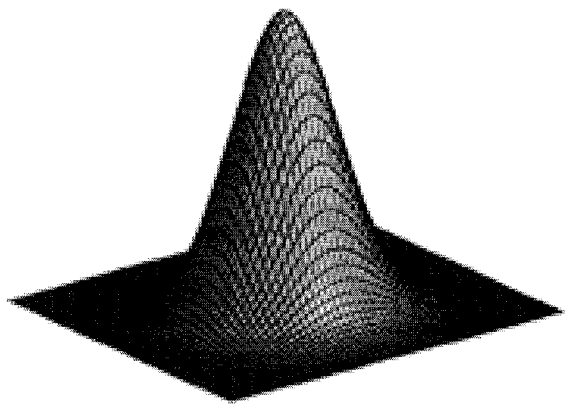

Figure 4-3. Gaussian neighborhood function in 2-dimensional map grid.

4.2.3 SOM BATCH ALGORITHM

A SOM Batch algorithm is a parameter-free and very fast version of a SOM [45]. At each step of the algorithm, all the input data vectors are simultaneously used to update all the model vectors. In each training step, the data set is partitioned according to the Voronoi regions of the map weight vectors. The Voronoi region of a particular point P is that region on the plane where P is the closest point of all points in S, where S is a set of points in that plane. For points on a plane, the Voronoi regions will always be bounded by line segments positioned halfway between pairs of points. The new weight vectors of the SOM are calculated after, then, as

$$m_i(t+1) = \frac{\sum_{j=1}^{n} h_{ic}(t) x_j}{\sum_{j=1}^{n} h_{jc}(t)} \tag{20}$$

where c is the index of the BMU of the data sample of x_j. The new weight vector is a weighted average of the data samples, where the weight of each data sample is the neighborhood function value $h_{ic}(t)$ at its BMU. Missing values are simply ignored in

calculating the weighted average. In the batch algorithm, the learning rate function used in the sequential algorithm is no longer used, but the width of the neighborhood is monotonically decreased during the learning.

4.3 REFLECTIVITY OBSERVATION OF THE VERTICAL RAIN PROFILE AND SOM

The rain reflectivity observation data using TRMM-PR is used as input for the SOM algorithm. Careful preparation of the data is necessary in any classification algorithm. The rain reflectivity observation data from TRMM-PR was already described in Chapter 2. However, some additional discussion concerning practical aspects of the input data to SOM are given below.

- Missing data: The TRMM-PR reflectivity observation data of the vertical rain profile may not be available in all heights. This may be due to noise in the data. It is also not uncommon that a radar data set contains invalid measurement values. These invalid measurement values need to be avoided in any attempt to classify the data set. One of the solutions that may overcome this problem is to interpolate the data vectors with such values. But this approach is not always reasonable because the interpolation may not be correct due to the high number of missing data in some profiles. However, using the available data vector value to find the best matching unit for each profile and exclude the missing values from the distance calculation has been demonstrated as a valid solution [43].
- Noise: The radar measurements are corrupted by a measurement noise. The SOM algorithm is robust even when the data set is noisy [47]. Since each model vector of the SOM is a weighted average of the data vectors in the Voronoi set of the map unit

and the neighboring map units, noise is reduced and does not usually constitute a major problem in SOM classification.

- Profile length: The number of points at each profile represents the length of the input vector to the SOM algorithm. For most cases, the profile length of the data is not fixed. Proper classification with the SOM is achieved by fixing the length of all profiles. To solve this problem, the points after the end of the profile have to change from missing value or noise to a small value. Using this small value will allow the algorithm to classify different profiles with large different lengths into different classes and classify different profiles with small different lengths into the same class.
- Reference: In any classification process, the choice of the reference point depends on the problem in hand. The rule in choosing the reference point of the data is controlled by the interesting data region.
- Resolution: the resolution of the vertical profile may affect the result of SOM classification if it is too low. In addition, if the resolution of the vertical profile is too high, the process of SOM classification will be slow. An experimental test of SOM classification data with two different resolutions (250 m and 125 m) shows that the result of SOM classification for both resolutions is almost identical (Figure 4-4). The 250m resolution profile is chosen because it is less time consuming.
- "Other" rain type: The input data for the SOM classification algorithm have TRMM-PR 2A-23 rain flag "Certain." Ten percent of the data with "Certain" rain flag have a type "other" rain type. Figure 4-5 shows that the profile data with type "other" mostly contain noise. For that reasons the vertical rain profile with rain type "other" is excluded from our data set.

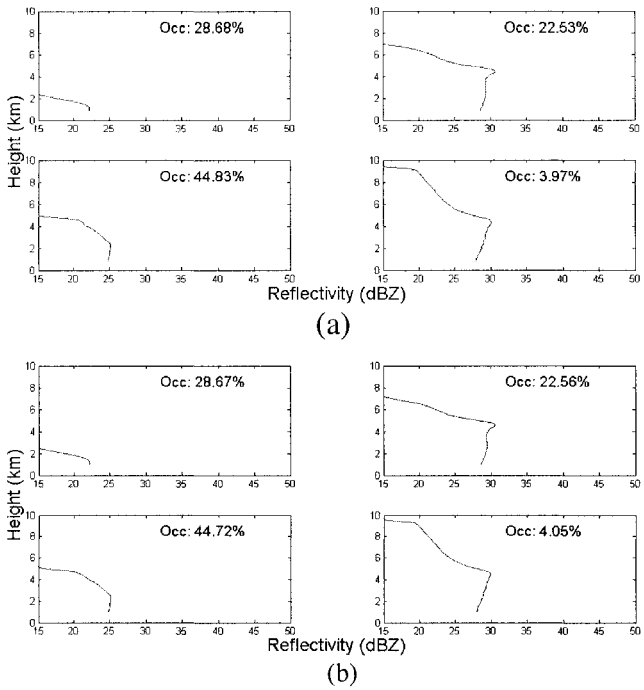

Figure 4-4. The (2X2) profiles of the SOM classification technique results using reflectivity observation data of the vertical rain profile over E-Pacific Ocean for the month of July 2000 using (a) vertical resolution of 125 m (b) vertical resolution of 250 m.

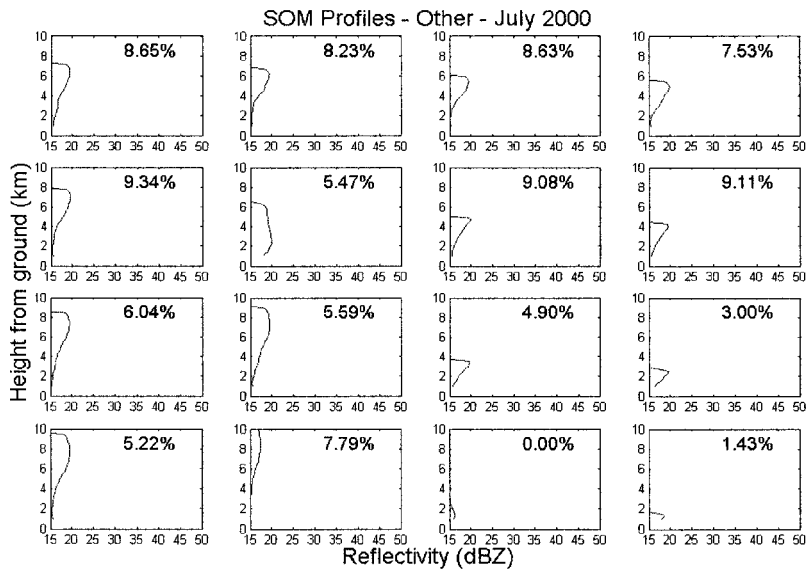

Figure 4-5. The (4X4) profiles of the SOM classification technique results for reflectivity observation data of the vertical rain profile with rain type "other."

4.4 K-MEANS CLUSTERING AND SOM

Clustering is used to reduce large data by grouping data with similar profiles into the same class. K-means clustering is very closely related to the SOM algorithm. K-means partitions data observations into k clusters. K-means creates a single level of clusters and it is suitable to cluster large data.

The data observation is treated in k-means clustering as it has a position in space. K-means partitions the data to include the points within same class to be as close as possible to each other and as far as possible to other points. Each cluster has its own member objects and defines by its centroid. The centroid for each cluster is average of all objects in that cluster. The sum of distances from each object to its cluster centroid over all clusters is minimized using k-means iterative algorithm. In this algorithm the objects moves between clusters until the sum cannot be decreased any more. The final result is a well-separated clusters.

K-means clustering is very closely related to the SOM algorithm. In k-means clustering the criterion function is the average squared distance of the data items from their nearest cluster centroids [72],

$$E_k = \sum \left\| x_k - m_{c(x_k)} \right\|^2, \tag{21}$$

Where $c(x_k)$ is the closest centroid index to x_k. One possible algorithm for minimizing the cost function begins by initializing a set of k cluster centroids denoted by m_i, $i = 1,\ldots, k$. The positions of the m_i are then adjusted iteratively by first assigning the data samples to the nearest clusters and then recalculate the centroids. The iteration is stopped when E does not change markedly any more.

4.4.1 RELATION OF SOM TO K-MEANS CLUSTERING:

The cost function of the SOM is the same as the k-means clustering algorithm tries to minimize. The difference is that in the SOM the distance of each input from all of the reference vectors instead of just the closest one is taken into account, weighted by the neighborhood kernel. As a result, the SOM functions as a k-means clustering algorithm if the width of the neighborhood is set to zero [42].

Although the k-means clustering algorithm and the SOM are very closely related, the way of using them in data mining are probably different. In the k-means clustering algorithm the number k of clusters should be chosen according to the number of clusters there are in the data, whereas in the SOM the number of reference vectors can be chosen to be much larger, irrespective of the number of clusters [42]. The cluster structures will become visible on the special displays. The results of k-means clustering algorithm are compared with the results of SOM with size (2X2) and (4X4) in the next section.

4.5 CLASSIFICATION USING SOM

In this section, the reflectivity observation of the vertical rain profile from TRMM-PR is used as an input data to the SOM classification technique. The data consist of around 20 million vertical profiles collected during the year 2000. Each profile has 41 bins, which represent the TRMM-PR observation reflectivity for rain profile from ground height up to 10 km above ground with 250 m vertical resolution. Eleven rays of each radar scan, which represent nadir ray ±5 rays, are examined.

The SOM algorithm uses the batch training algorithm that is available through the SOM toolbox [46]. All SOM algorithm maps were linearly initialized. The maps were trained in two phases: a rough training with large initial neighborhood width equal to map

size and a fine-tuning phase with small initial neighborhood width. The neighborhood width of the SOM decreased linearly to 0, e.g, for clustering the data. The Gaussian neighborhood function is used. The training epoch's lengths of the two phases were 20 times and 50 times the product of the two elements of the map size. The SOM classification technique for a large data set requires huge amounts of memory. In addition, the complexity of the algorithm increases exponentially with the number of map units in SOM. Thus, training huge maps is time-consuming and should be processed in machines with large RAM memory and high clock speed processor.

4.5.1 Case Study: Global Study of VPR using TRMM-PR Data for Year 2000

The classification algorithm using SOM is applied on the reflectivity observation of vertical rain profile data during the year 2000 on a global scale. The input data to the SOM algorithm were collected during the operation of TRMM-PR from the period January 1st 2000 to December 31st 2000. The data consist of 20 million profiles. The data are classified using a SOM of size (1X2), (2X2), (4X4) and (10X10). This classification will help us to understand the natural separation of the VPR of the data set in view of the current convective/stratiform rain type classification.

4.5.1.1 SOM classification of size (1X2)

Figure 4-6 shows the (1X2) SOM classification results of the reflectivity observation of the vertical rain profile collected using TRMM-PR during the year 2000 around the globe. SOM performs a natural separation for the entire data set into two types. The first class, which represents 70.17% of the entire data set, has a maximum reflectivity of 22.5 dBZ and a storm top height of 3.35 km above sea level. The second class, which represents 29.83% of the entire data set, has a maximum reflectivity of 32.75 dBZ and a

storm top height of 6.62 km above sea level.

The average profiles of the same data set classified into two data sets, one with stratiform rain type and the other with convective rain type, are shown in Figure 4-7 (a)-(b), respectively. By looking to the figures (Figure 4-6-Figure 4-7), it can be noticed that the average profile for the stratiform rain type data set is close in shape to the first class (1, 1) of the global SOM classification. The average profile for the convective rain type data set is close in shape to the second class (1, 2) of the SOM classification. Seventy-five percent of all profiles with stratiform rain type fall in the first class (1, 1) of the SOM of the entire data set and 62% of all profiles with convective rain type fall in the second class (1, 2). Using the data for the rain rate near the ground provided by the TRMM-PR (2A-25) algorithm, the first class is responsible for 27.1% of all rain while the second class is responsible for 72.9% of all rain. The results are summarized in Table 4–1.

Table 4–1. The percentage of each SOM class, average rainfall, stratiform rain type, and convective rain type for (1X2) SOM classification results classes.

Class	Occurrence	Rainfall	Stratiform	Convective
(1,1)	70.17%	27.1%	76% S 92%	38% C 8%
(1,2)	29.83%	72.9%	24% S 70%	62% C 30%

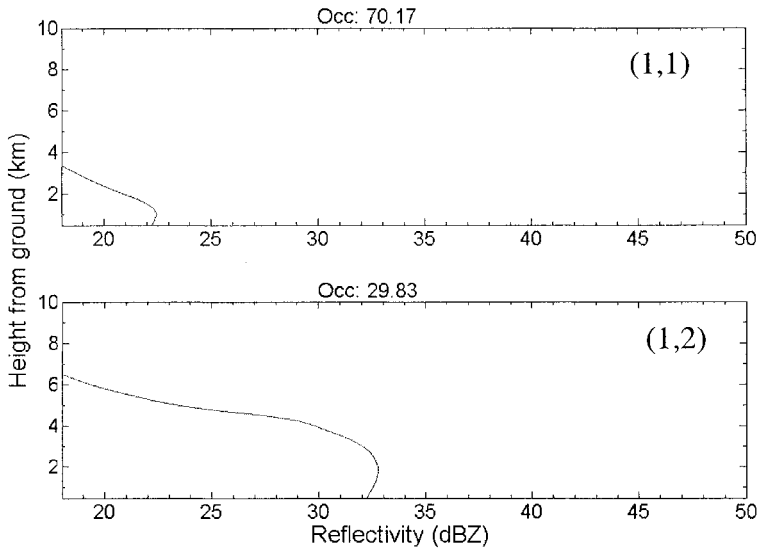

Figure 4-6. The (1X2) SOM classification results for reflectivity observation of vertical rain profile collected using TRMM-PR during the year 2000 around the globe. Occ is the percentage of the data set that belong to this class from the entire data set.

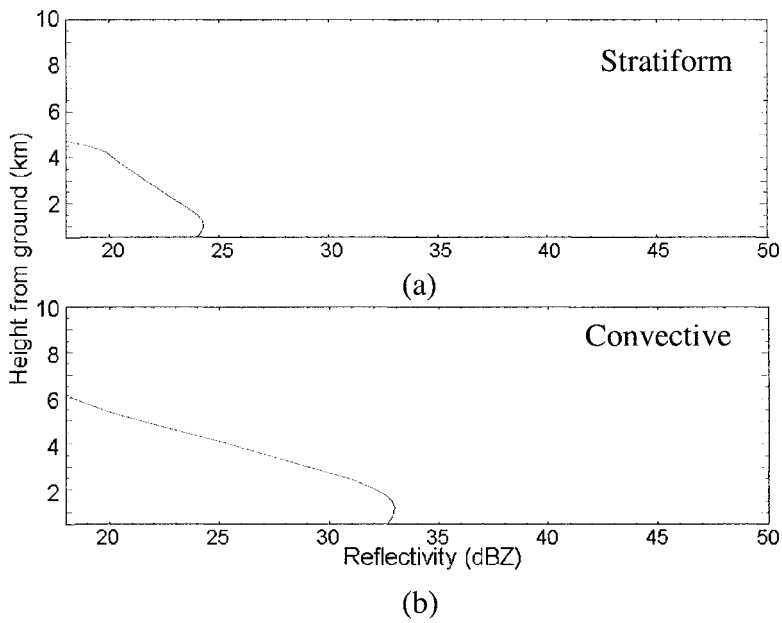

Figure 4-7. The average profile of reflectivity observation of vertical rain profile collected using TRMM-PR during the year 2000 around the globe for (a) profiles with stratiform rain type and (b) profiles with convective rain type.

4.5.1.2 SOM classification of size (2X2)

To extend our study of the reflectivity observation data of the vertical rain profile, (2X2) SOM classification results are shown in Figure 4-8. Figure 4-9 (a) shows the (1X2) SOM of the stratiform rain type profiles, while Figure 4-9 (b) shows the (1X2) SOM of the convective rain type profiles. Figure 4-8 and Figure 4-9 show that the shape of the two classes of the (1X2) SOM of the stratiform profiles are very similar to classes (1, 1) and (2, 1) of the (2X2) SOM of the entire data set. In addition, the two classes of the (1X2) SOM of the convective profiles is very similar in shape to the classes (1, 2) and (2, 2) of the (2X2) SOM of the entire data set. The percentage of each class, average rainfall, stratiform rain type, and convective rain type for (2X2) SOM classes for the entire data set is summarized in Table 4–2. The figures of (1X2) and (2X2) SOM show that the entire data set is classified naturally to classes that carry the themes of the profiles of stratiform rain type and the profiles of convective rain type.

Table 4–2. percentage of occurrence, rainfall, stratiform and convective rain type for the classes of SOM of size 2X2.

Class	Occurrence	Rainfall	Stratiform	Convective
(1,1)	46.15%	10.6%	51.8% S 96%	11.9% C 4%
(1,2)	22.50%	24.3%	21.9% S 83%	26.3% C 17%
(2,1)	22.05%	19.1%	20.7% S 81%	30.1% C 19%
(2,2)	9.29%	46.0%	5.6% S 52%	31.6% C 48%

The k-means clustering algorithm is also applied on the same data set to compare its results with SOM. The results of the k-means clustering are shown in Figure 4-10. It is clear that the vertical structure of k-means clustering classes are the same as the vertical

structure of the SOM classification technique classes that are shown in Figure 4-8 . The percentage of each class is very similar. This result is expected since the SOM functions as a K-means clustering algorithm if the width of the neighborhood is set to zero.

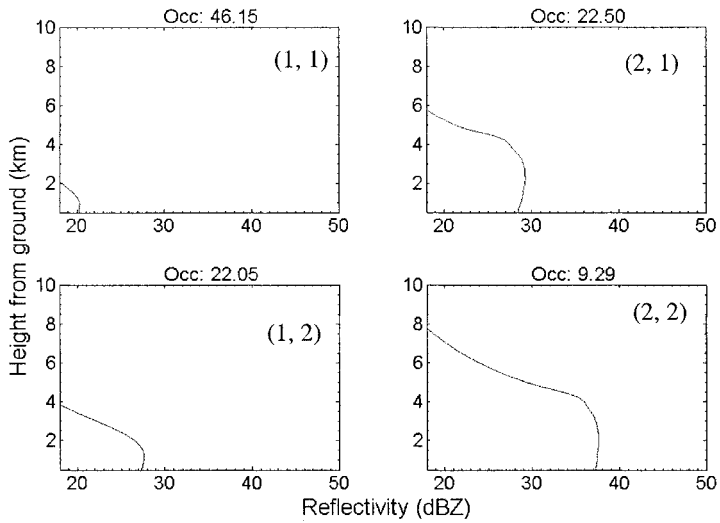

Figure 4-8. The (2X2) SOM classification results for reflectivity observation of vertical rain profile collected using TRMM-PR during the year 2000 around the globe. Occ is the percentage of the data set that belong to this class from the entire data set

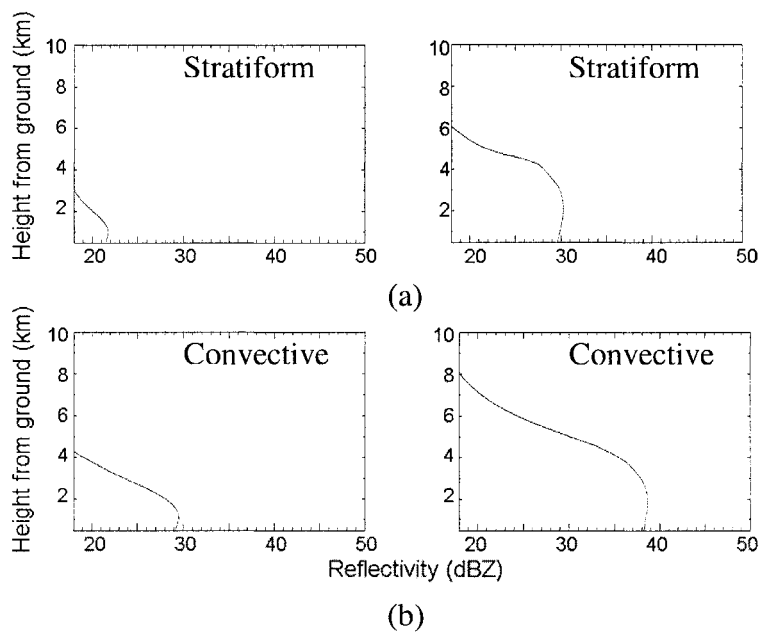

Figure 4-9. (1X2) SOM results for (a) stratiform rain type profiles for year 2000 data and (b) convective rain type profiles for year 2000 data.

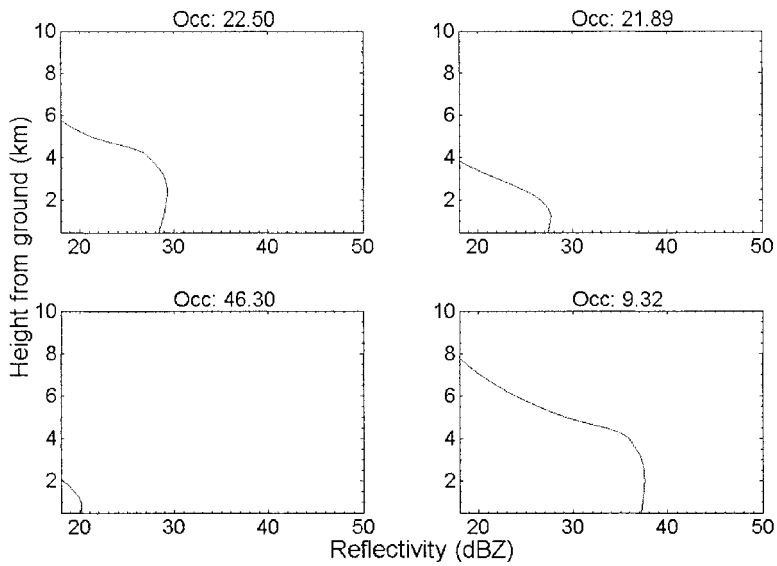

Figure 4-10. The K-means clustering results for reflectivity observation of vertical rain profile collected using TRMM-PR during the year 2000 around the globe using k=4. Occ is the percentage of the data set that belong to this cluster from the entire data set

4.5.1.3 SOM classification of size (4X4)

The SOM of size (4X4) for the entire data set is shown in Figure 4-11. The percentage of occurrence, rainfall, rain type for the classes of SOM of size 4X4 for the entire data set is summarized in Table 4–3. In general, stratiform and convective rain type profiles have different characteristics. Large horizontal reflectivity gradients, strong vertical motions, and high rainfall rate often characterize convective precipitation. Smaller horizontal reflectivity gradients, weaker vertical motions, and lower rain rates characterize stratiform precipitation. The presence of a bright band typically indicates a stratiform region. For that reason, it is difficult to study those classes if each class consists of a percentage of stratiform and convective rain type, which is the case in Figure 4-11.

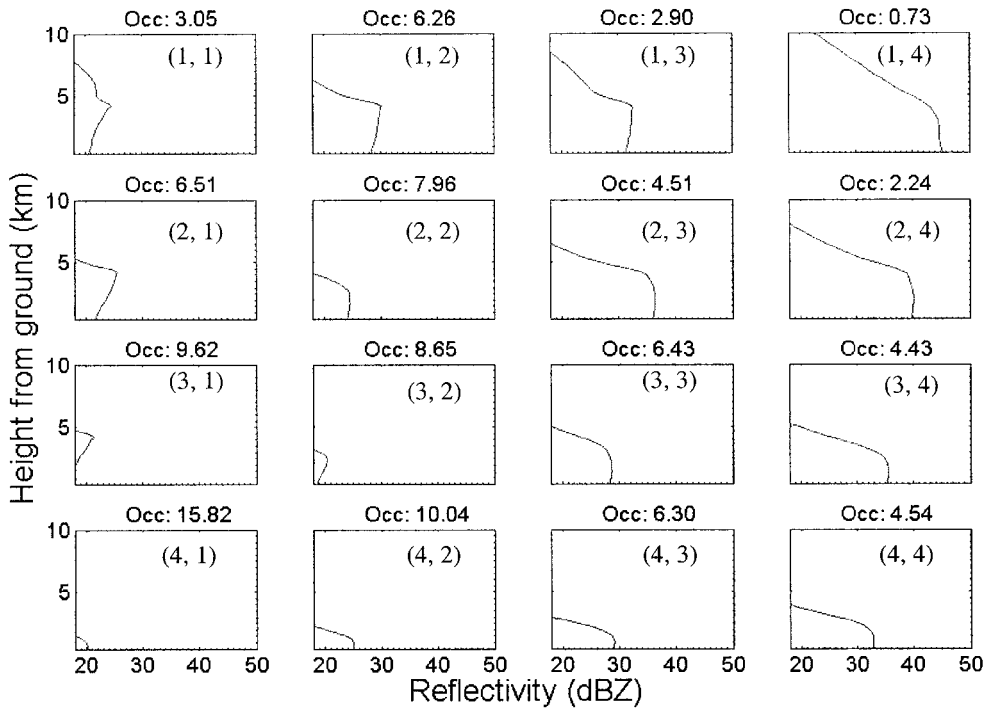

Figure 4-11. The (4X4) SOM classification result for reflectivity observation of the vertical rain profile collected using TRMM-PR during the year 2000 around the globe. Occ is the percentage of the data set that belong to this class from the entire data set.

Table 4–3. The percentage of occurrence, rainfall, stratiform and convective for the classes of (4X4) SOM.

Class	Occurrence (%)	Rainfall (%)	Stratiform (%)	Convective (%)
(1,1)	3.05	0.78	3.35	1.29
(1,2)	6.26	5.25	6.54	4.56
(1,3)	2.90	4.23	2.59	4.80
(1,4)	0.73	11.60	0.03	4.95
(2,1)	6.51	1.86	7.29	1.78
(2,2)	7.96	3.34	8.56	4.33
(2,3)	4.51	14.06	3.34	11.66
(2,4)	2.24	15.57	0.86	10.59
(3,1)	9.62	0.98	11.01	1.18
(3,2)	8.65	1.40	9.56	3.12
(3,3)	6.43	5.37	6.49	6.07
(3,4)	4.43	12.55	2.99	13.14
(4,1)	15.82	3.57	17.97	2.77
(4,2)	10.04	4.91	10.81	5.41
(4,3)	6.30	6.26	5.50	11.17
(4,4)	4.54	8.25	3.11	13.19

The k-means clustering algorithm is also applied on the same data set to compare its results with SOM. The results of the k-means clustering are shown in Figure 4-12. It is clear that the vertical structure of k-means clustering classes are the same as the vertical structure of the SOM classification technique classes that are shown in Figure 4-11. The percentage of each class is very similar for each class. The only different between the SOM classification technique and k-means clustering algorithm is that the SOM forms a non linear mapping of the data into a two-dimensional map grid and the classes will become orders on the output grid. This make the cluster structures become visible on the special displays at the output. At the rest of this work the SOM classification technique will used to cluster the data because it is ability to show data cluster structures in the large size classes.

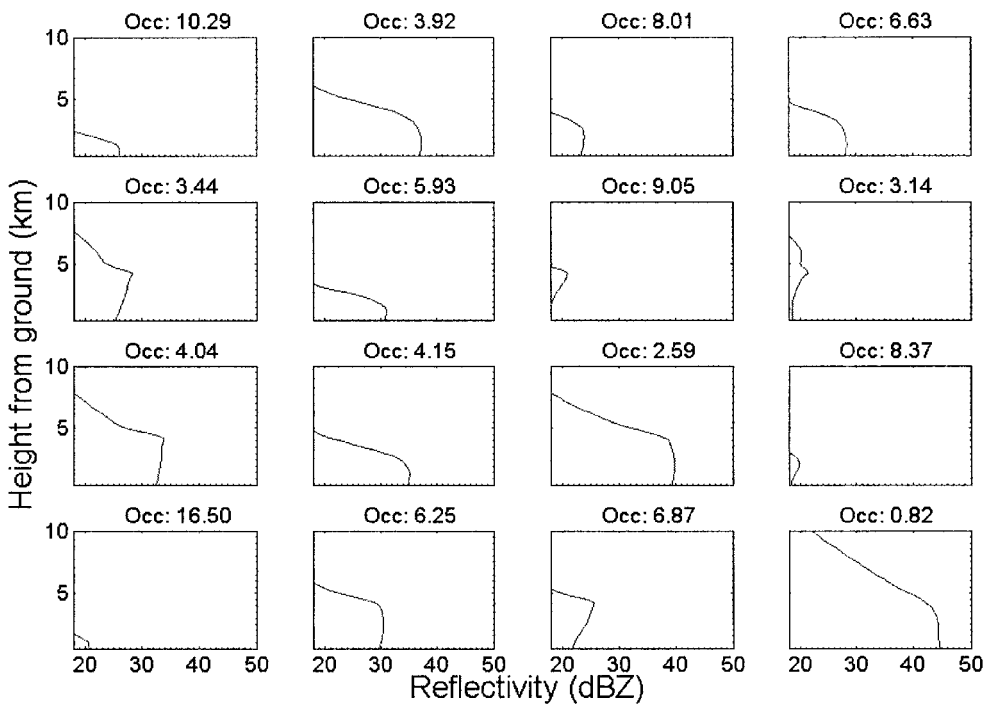

Figure 4-12. The k-means clustring result for reflectivity observation of the vertical rain profile collected using TRMM-PR during the year 2000 around the globe using k = 16. Occ is the percentage of the data set that belong to this class from the entire data set.

4.5.1.4 SOM classification of size (10X10) and classes global map

The SOM of size (10X10) for the entire data set is shown in Figure 4-13. The normalized percentage of occurrence, rainfall percentage, average rainfall rate, and land, ocean occurrence percentage for the classes of SOM of size 10X10 are summarized in Table 4–3. The results show that there are some classes that occur mostly over and there are some classes that musty occur over oceans. For example class number (1, 10) occurs mostly over land with percentage of 90%. The class number (10, 8) occurs mostly over ocean with percentage of 74%.

The global maps showing the location of occurrence of these two classes are shown in Figure 4-14 and Figure 4-15. Figure 4-16-Figure 4-22 show the global map for classes (1, 9), (2, 8), (2, 10), (3, 10), (9, 1), (10, 1) and (10, 10). It clear from these figures that there are some classes that tends to happens over certain location more than other location.

Rain type classification using SOM and the class's global map provides a means for exporting DSDs deduced from polarimetric radars in land to those without polarization capability over ocean by assigning each pixel properties of the appropriate profile class. It also helps in determine the best location to build new polarimetric radars that can use to study many rain profile classes.

It might be thought that increasing the number of classes by increasing the SOM size would help to separate the classes of each rain type. This solution will not work for two reasons. First, we would have a large number of classes where it would be difficult to study the differences in all the classes. Second, each rain type has different characteristics that need to be studied separately at different heights from the ground.

For that reason in next chapters, the study of VPR will use the SOM method on profiles of stratiform rain type and convective rain type separately.

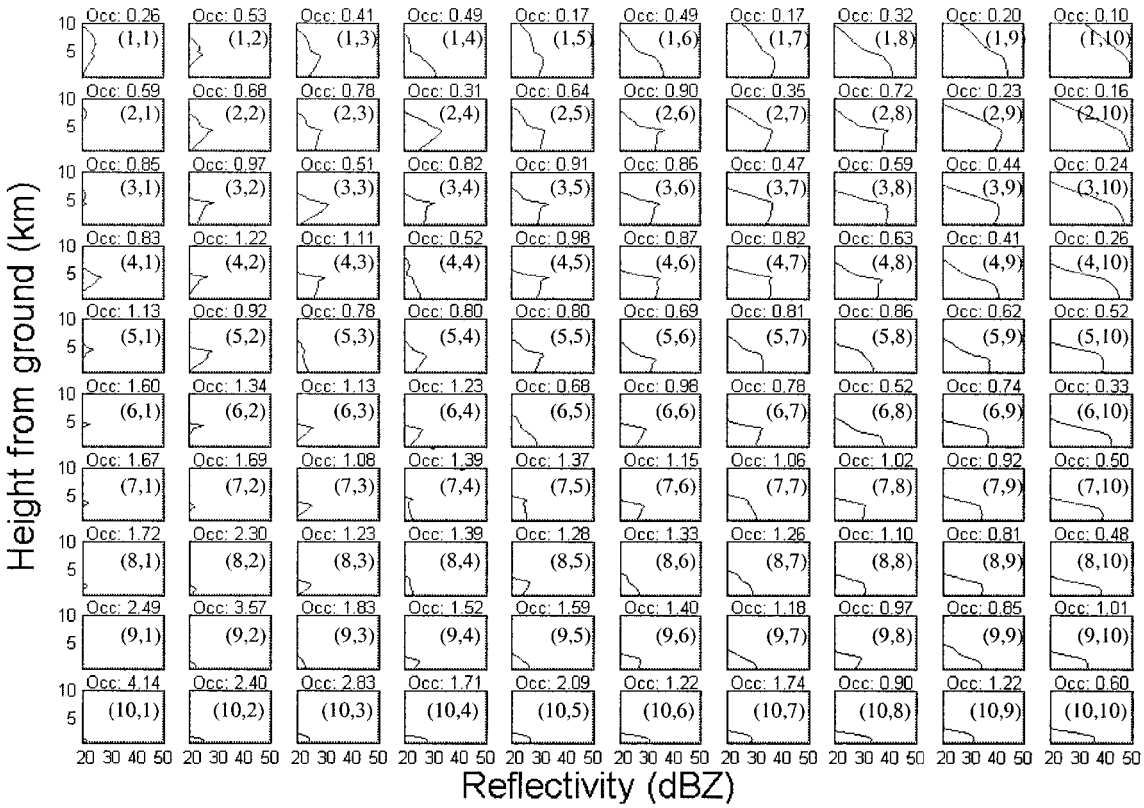

Figure 4-13. The (10X10) SOM classification results for reflectivity observation of vertical rain profile collected using TRMM-PR during the year 2000 around the globe. Occ is the percentage of the data set that belong to this class from the entire data set

Table 4–4. The normalized percentage of occurrence, rainfall percentage, average rainfall rate, and land, ocean occurrence percentage for the classes of SOM of size 10X10

Class	Occ	Land %	Ocean %	Rain %	R_{ave}
(1,1)	0.26	75	25	0.04	0.4
(1,2)	0.53	61	39	0.06	0.29
(1,3)	0.41	68	32	0.15	0.98
(1,4)	0.49	64	36	0.63	3.37
(1,5)	0.17	73	27	0.2	3
(1,6)	0.49	67	33	1.33	7.14
(1,7)	0.17	72	28	0.6	9.13
(1,8)	0.32	67	33	**2.47**	**19.87**
(1,9)	0.2	78	22	**2.44**	**31.45**
(1,10)	0.1	90	10	**2.36**	**61.27**
(2,1)	0.59	61	39	0.08	0.38
(2,2)	0.68	56	44	0.14	0.53
(2,3)	0.78	55	45	0.38	1.27
(2,4)	0.31	57	43	0.15	1.24
(2,5)	0.64	61	39	0.59	2.43
(2,6)	0.9	42	58	1.27	3.7
(2,7)	0.35	57	43	0.67	4.97
(2,8)	0.72	47	53	**2.13**	7.78
(2,9)	0.23	64	36	1.29	**14.81**
(2,10)	0.16	79	21	**3.96**	**64.64**
(3,1)	0.85	51	49	0.09	0.28
(3,2)	0.97	40	60	0.27	0.73
(3,3)	0.51	54	46	0.11	0.56
(3,4)	0.82	39	61	0.44	1.42
(3,5)	0.91	44	56	0.71	2.04
(3,6)	0.86	41	59	0.94	2.87
(3,7)	0.47	46	54	0.98	5.45
(3,8)	0.59	51	49	**2.36**	**10.42**
(3,9)	0.44	54	46	**2.29**	**13.51**
(3,10)	0.24	71	29	**4.96**	**53.92**
(4,1)	0.83	54	46	0.08	0.25
(4,2)	1.22	44	56	0.15	0.32
(4,3)	1.11	50	50	0.49	1.15
(4,4)	0.52	62	38	0.25	1.23
(4,5)	0.98	44	56	0.74	1.98
(4,6)	0.87	54	46	1.31	3.95
(4,7)	0.82	43	57	1.92	6.09
(4,8)	0.63	63	37	1.37	5.75
(4,9)	0.41	67	33	**2.48**	**15.83**
(4,10)	0.26	68	32	**3.79**	**38.16**
(5,1)	1.13	48	52	0.1	0.23
(5,2)	0.92	58	42	0.14	0.39
(5,3)	0.78	55	45	0.24	0.82
(5,4)	0.8	60	40	0.26	0.84
(5,5)	0.8	62	38	0.54	1.78
(5,6)	0.69	52	48	0.74	2.82
(5,7)	0.81	63	37	1.21	3.92
(5,8)	0.86	45	55	1.53	4.65
(5,9)	0.62	56	44	1.86	7.91
(5,10)	0.52	60	40	**2.3**	**11.54**
(6,1)	1.6	34	66	0.11	0.18
(6,2)	1.34	54	46	0.1	0.2
(6,3)	1.13	62	38	0.12	0.28
(6,4)	1.23	61	39	0.29	0.61
(6,5)	0.68	53	47	0.55	2.11
(6,6)	0.98	61	39	0.41	1.09
(6,7)	0.78	60	40	0.71	2.4
(6,8)	0.52	47	53	1.79	9.04
(6,9)	0.74	55	45	**2.06**	7.29
(6,10)	0.33	50	50	**2.65**	**21.25**
(7,1)	1.67	57	43	0.13	0.21
(7,2)	1.69	53	47	0.16	0.25
(7,3)	1.08	60	40	0.12	0.29
(7,4)	1.39	51	49	0.35	0.66
(7,5)	1.37	51	49	0.51	0.98
(7,6)	1.15	56	44	0.54	1.23
(7,7)	1.06	47	53	1	2.46
(7,8)	1.02	55	45	0.9	2.31
(7,9)	0.92	51	49	1.73	4.93
(7,10)	0.5	43	57	**2.17**	**11.46**
(8,1)	1.72	46	54	0.17	0.26
(8,2)	**2.3**	42	58	0.43	0.49
(8,3)	1.23	53	47	0.22	0.46
(8,4)	1.39	58	42	0.37	0.7
(8,5)	1.28	55	45	0.41	0.83
(8,6)	1.33	53	47	0.68	1.34
(8,7)	1.26	50	50	0.94	1.95
(8,8)	1.1	48	52	1.1	2.62
(8,9)	0.81	42	58	1.53	4.93
(8,10)	0.48	32	68	1.89	10.2
(9,1)	**2.49**	24	76	0.3	0.32
(9,2)	**3.57**	32	68	0.85	0.62
(9,3)	1.83	55	45	0.49	0.7
(9,4)	1.52	42	58	0.44	0.77
(9,5)	1.59	52	48	0.76	1.25
(9,6)	1.4	45	55	0.69	1.28
(9,7)	1.18	48	52	1.21	2.69
(9,8)	0.97	45	55	0.58	1.57
(9,9)	0.85	46	54	1.61	4.97
(9,10)	1.01	36	64	1.64	4.23
(10,1)	**4.14**	21	79	0.92	0.58
(10,2)	**2.4**	29	71	0.95	1.04
(10,3)	**2.83**	35	65	0.95	0.88
(10,4)	1.71	25	75	1.05	1.61
(10,5)	**2.09**	32	68	1.04	1.31
(10,6)	1.22	23	77	1.26	2.7
(10,7)	1.74	33	67	1.23	1.84
(10,8)	0.9	25	75	1.48	4.32
(10,9)	1.22	31	69	1.29	2.78
(10,10)	0.6	26	74	1.56	6.83

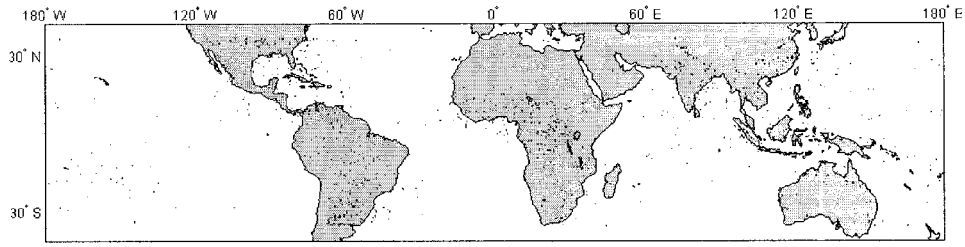

Figure 4-14. Global map shows the location of occurrence for class (1, 10). The plots are restricted to the latitudes of ±37°, coinciding with the coverage of TRMM-PR. Each pixel in the plot is 0.5°X 0.5° area.

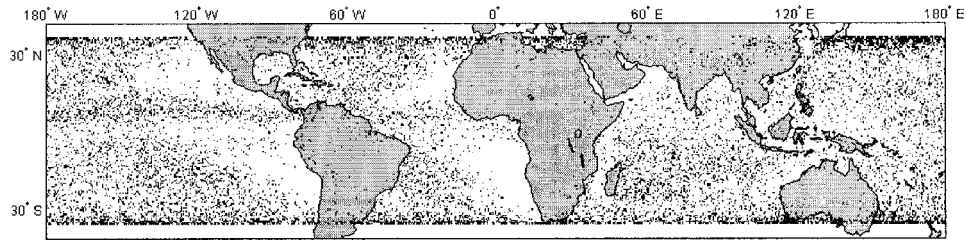

Figure 4-15. Global map shows the location of occurrence for class (10, 8). The plots are restricted to the latitudes of ±37°, coinciding with the coverage of TRMM-PR. Each pixel in the plot is 0.5°X 0.5° area.

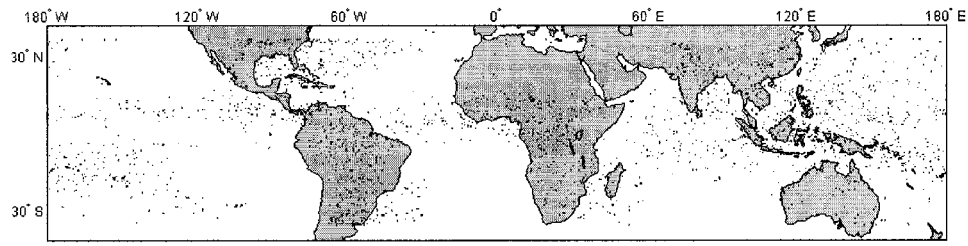

Figure 4-16. Global map shows the location of occurrence for class (1, 9). The plots are restricted to the latitudes of ±37°, coinciding with the coverage of TRMM-PR. Each pixel in the plot is 0.5°X 0.5° area.

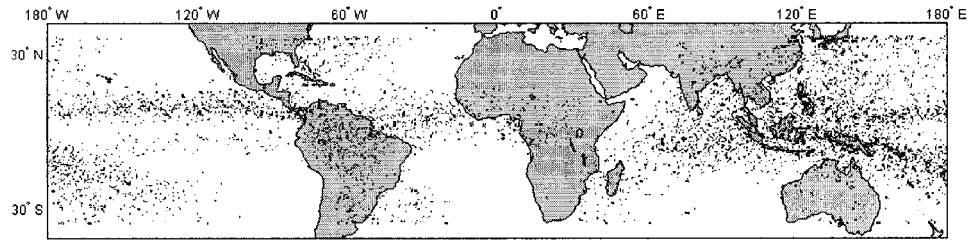

Figure 4-17. Global map shows the location of occurrence for class (2, 8). The plots are restricted to the latitudes of ±37°, coinciding with the coverage of TRMM-PR. Each pixel in the plot is 0.5°X 0.5° area.

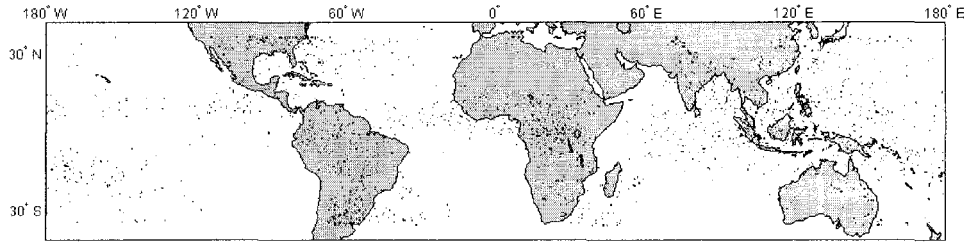

Figure 4-18. Global map shows the location of occurrence for class (2, 10). The plots are restricted to the latitudes of ±37°, coinciding with the coverage of TRMM-PR. Each pixel in the plot is 0.5°X 0.5° area.

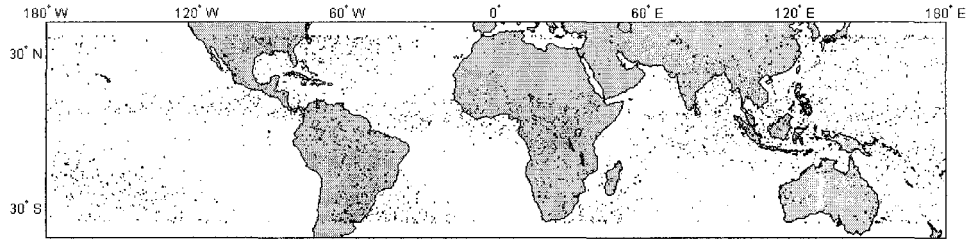

Figure 4-19. Global map shows the location of occurrence for class (3, 10). The plots are restricted to the latitudes of ±37°, coinciding with the coverage of TRMM-PR. Each pixel in the plot is 0.5°X 0.5° area.

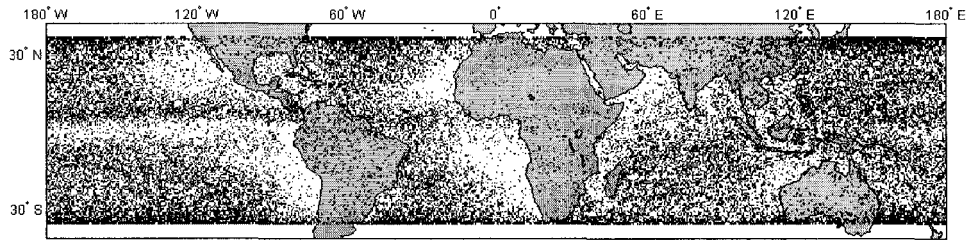

Figure 4-20. Global map shows the location of occurrence for class (9, 1). The plots are restricted to the latitudes of ±37°, coinciding with the coverage of TRMM-PR. Each pixel in the plot is 0.5°X 0.5° area.

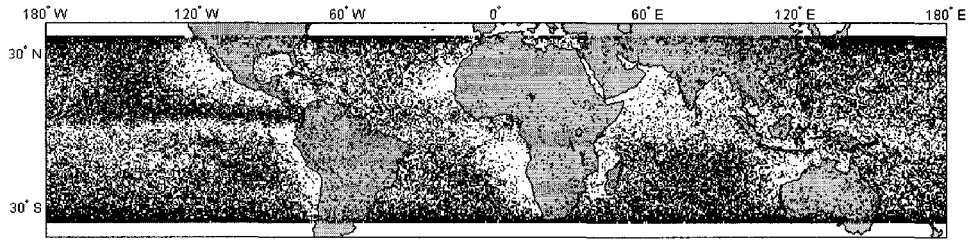

Figure 4-21. Global map shows the location of occurrence for class (10, 1). The plots are restricted to the latitudes of ±37°, coinciding with the coverage of TRMM-PR. Each pixel in the plot is 0.5°X 0.5° area.

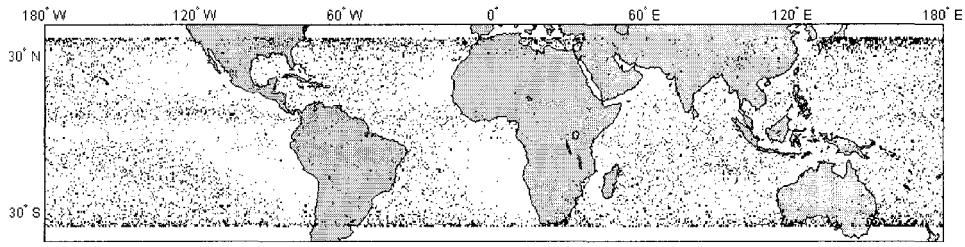

Figure 4-22. Global map shows the location of occurrence for class (10, 10). The plots are restricted to the latitudes of ±37°, coinciding with the coverage of TRMM-PR. Each pixel in the plot is 0.5°X 0.5° area.

CHAPTER 5

GLOBAL STUDY OF BRIGHT BAND STRUCTURE AS OBSERVED FROM SPACE-BORNE PRECIPITATION RADAR

5.1 INTRODUCTION

Bright band (BB) has been perhaps one of the most widely known radar signatures for a long time. Extensive research has been reported in the literature documenting various features of bright bands. BB is denoted by a sharp increase in the vertical profile of reflectivity [21]. In the BB region, there is an increase in the dielectric constant as hydrometeors melt, which results in an increase in the reflectivity backscatter. When reflectivity measurements of precipitation are contaminated by bright band, surface rainfall overestimations can be as large as a factor of 10 [51]. In addition to affecting precipitation estimated by radar, proper identification of melting-layer heights can be useful for understanding precipitation types and surface temperature [20][58]. Davies 1992 in [59] showed that there is a relationship between the bright band area and the background rainfall. Several attempts have been made to identify the bright band and account for its impact on surface rainfall estimates since the 1950s [21][51][52][53][54][55][56][57].

An understanding of the vertical structure of the BB region is important because it holds extensive information on the types of precipitation and their variability. A better understanding of the vertical structures of BB region and its radar reflectivity structure is

important for understanding microphysical processes of stratiform precipitation.

Observation of the vertical profile of precipitation over the global tropics is an important objective of the Tropical Rainfall Measuring Mission (TRMM). TRMM precipitation Radar (PR) produces high-resolution vertical profiles of precipitation that are suitable for the study of BB region structure. A Self-Organizing Map (SOM) analysis of the vertical profile of reflectivity from TRMM-PR data can be used to classify the BB region vertical profiles [67].

The study in this chapter presents a SOM classification technique to identify the characteristics of the region of the BB from TRMM-PR vertical profile measurements for one year on a global scale. Subsequently, the SOM classification data are summarized in a new way that can be useful in comparing the vertical profile of reflectivity from different regions around the globe as well as different seasons.

5.2 DATA ANALYSIS USING SOM

Bright band is caused by several factors related to the physical characteristics of melting hydrometeors. The level where frozen aggregates melt completely to rain and rain particle fall velocities increase marks the bottom of this layer. The technique developed using a SOM identifies the top and bottom of the melting layer, which permits calculation of the thickness of the melting layer. The definition of upper and lower boundary is similar to that used by [50].

The proposed algorithm relies on the shape of the VPR of TRMM-PR data near the top and bottom of the melting layer. The diagram illustrating the various features that are extracted from VPR data in the BB region is shown in Figure 5-1. The BB region top

height (h_{top}) is defined as the height at which the curvature in log (Z) is the maximum. The resulting height should be much closer to the height where melting starts. A similar criterion is used to find the height of the BB region bottom (h_{bot}). Once the bright band boundaries are determined, the peak in the BB reflectivity (Z_{peak}) and its height (h_{peak}) are easily found. Related quantities such as the bright band thickness (BB_{th}) and BB sharpness index are likewise easily derived. The bright band sharpness index (δ) is defined as $\Delta Z_{BB}/BB_{th}$, where ΔZ is defined as $((Z_{peak}-Z_{rain})+(Z_{peak}-Z_{snow}))/2$. The snow reflectivity (Z_{snow}) is defined as the reflectivity at the BB top height (h_{peak}). Finally, the rain reflectivity (Z_{rain}) is measured at 125 m (or one range sample) below the BB bottom height (h_{bot}).

The BB parameters calculation will be affected by the measurement fluctuations and the missing data in radar observation vertical profile. To be able to calculate the curvature of the VPR of the BB region at the top and the bottom of the BB peak, the vertical profile should be a smooth curve with no missing data. Any attempt to smooth the curve of each profile will suffer from different types of error based on the type of problem. The SOM classifies all profiles to a limited number of profiles. Each model vector of the SOM classification result is a weighted average of the data vectors of the map unit and its neighboring map units, with a smooth curve output profile. These make it easy to calculate the BB parameters from these centroid profiles.

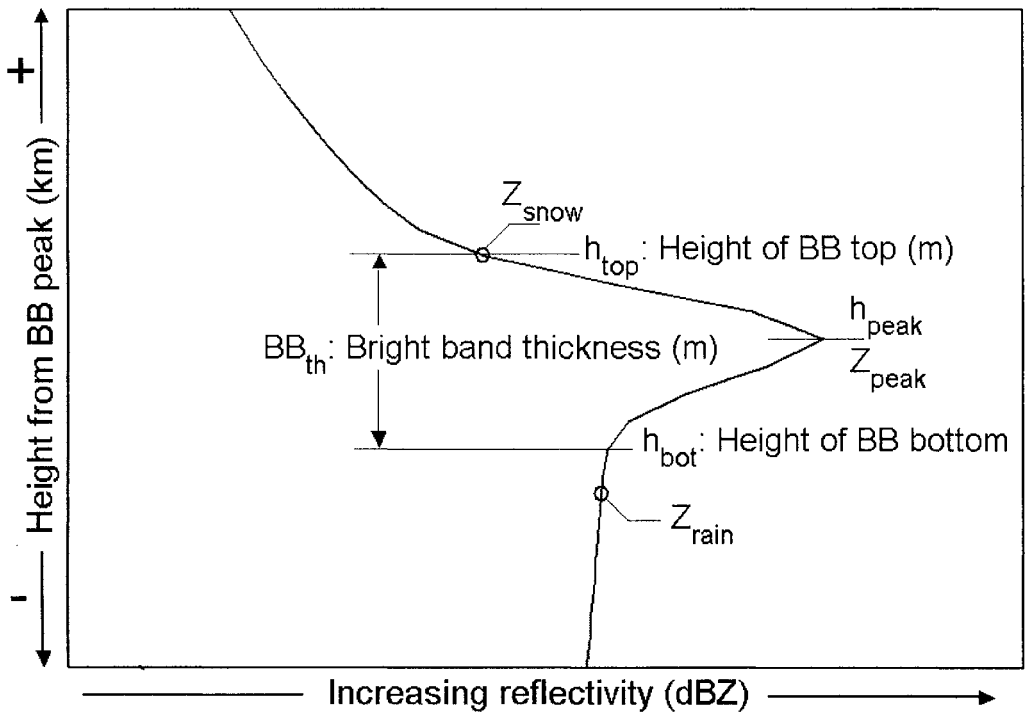

Figure 5-1. The diagram that illustrrates the various features extracted from VPR data in the BB region. The solid curve shows a typical VPR from SOM classification result.

5.2.1 GLOBAL STUDY

A SOM classification algorithm is used to analyze the BB region reflectivity structure of stratiform rain type profiles collected during the year 2000. The data are collected over the global and ordered using two reference point, the ground height and the BB height above ground. Figure 5-2 shows the result of (2X2) SOM classification of rain profiles with ground height as a reference point.

Figure 5-3 shows the same thing using BB height as a reference point. In Figure 5-2, the characteristics of the BB region described in the previous section are not clear because the BB peak occurs at a different height from the ground. In Figure 5-3, the characteristics of the bright band region are clearer and can be calculated for each SOM classification class.

Therefore, we will study the characteristics of the BB region using data with the BB height as the reference point. Figure 5-3 shows the BB thickness and the percentage of occurrence for each class for global observation data for year 2000. Class (1,1), which represents the average of 30.37% of the entire data, has 500 m BB thickness and 26 dBZ BB peak reflectivity. Class (2,2), which represents the average of 14.36% of the entire data, has 875 m BB thickness and 40 dBZ BB peak reflectivity.

The same things are done using data from each month of year 2000 separately. The SOM result is shown in Figure 5-4. It is clear from the figure that the reflectivity structure of all months in the year 2000 is almost the same. The main difference is in the BB height which will be discussed later. This means that the reflectivity structure of the BB region has no seasonal differences.

To calculate the BB thickness and BB sharpness index, the number of classes of the SOM classification algorithm has to be large enough. The size of (10X10) the SOM is used to calculate the BB thickness and BB sharpness index. The SOM result is shown in Figure 5-5.

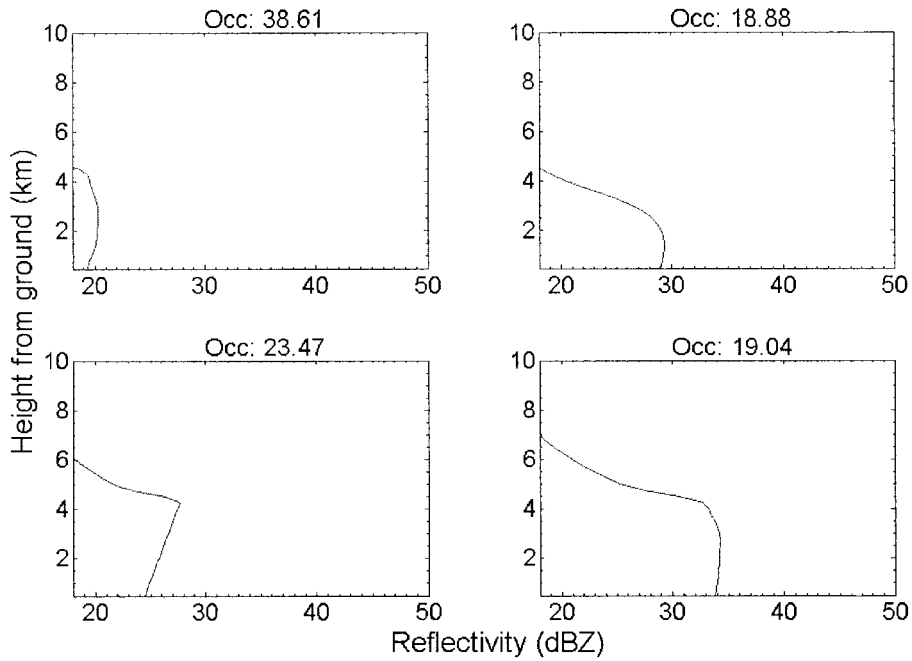

Figure 5-2. The (2X2) SOM classification results using VPR of stratiform rain type with BB collected using TRMM-PR during the year 2000 around the globe. Ground height is used as data refrence point.

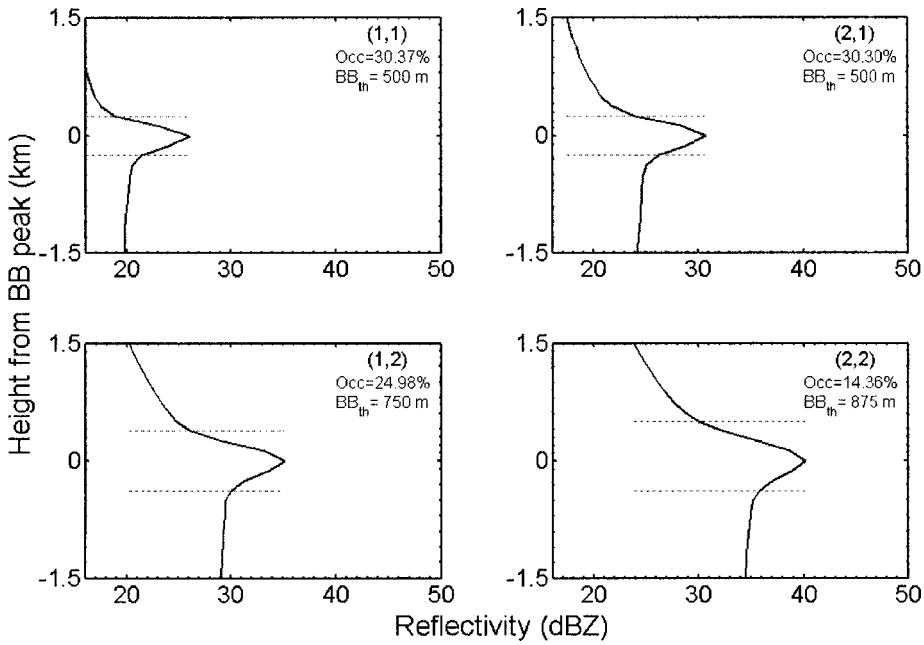

Figure 5-3. The (2X2) SOM classification results using VPR of stratiform rain type with BB collected using TRMM-PR during the year 2000 around the globe. BB height is used as data refrence point. Occ: the percentage of occurance for this class in entire dataset. BB_{th}: BB thickness in meters.

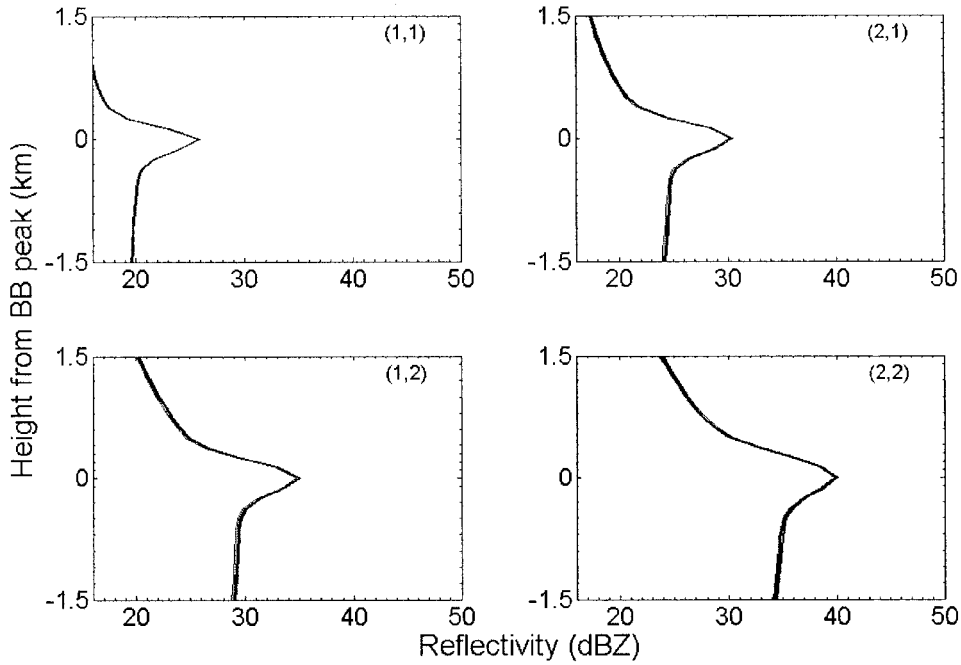

Figure 5-4. The (2X2) SOM classification results using VPR of stratiform rain type with BB collected using TRMM-PR for data of each month of year 2000 separately.

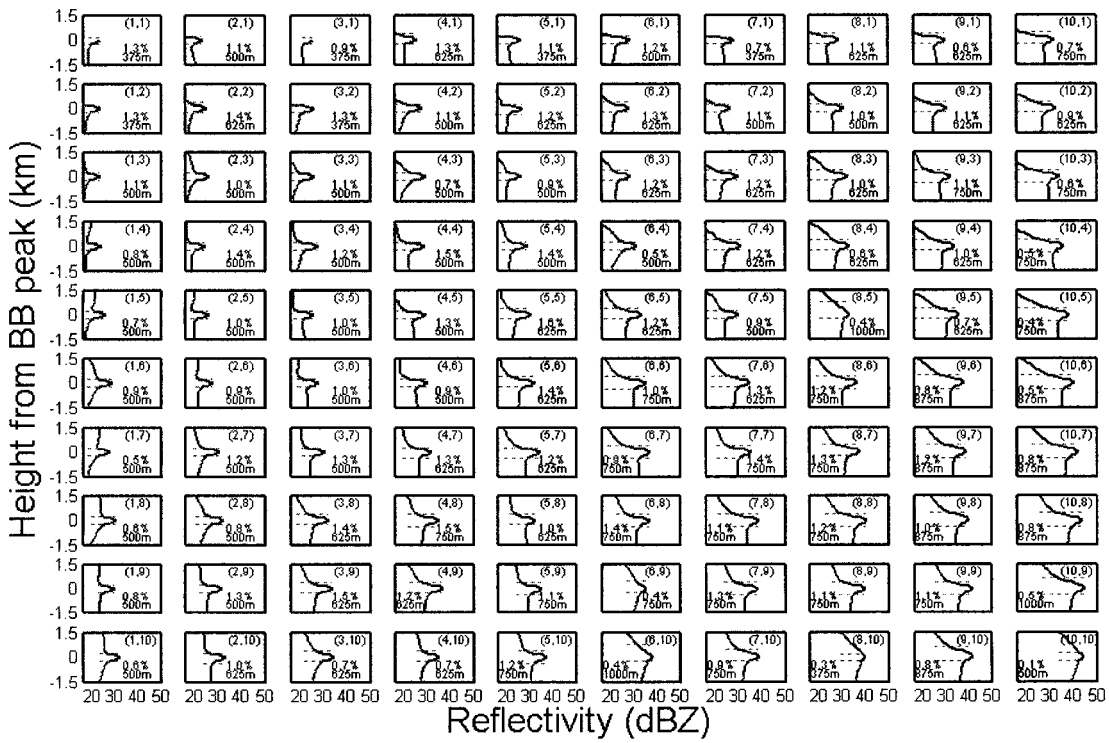

Figure 5-5. The (10X10) SOM classification result using VPR of stratiform rain type with BB collected using TRMM-PR during the year 2000 around the globe. BB height is used as data refrence point.

The histogram of the bright band thickness using the (10X10) SOM classification result of year 2000 data is shown in Figure 5-6. The bright band thickness has an average value of 610 m. The histogram of bright band sharpness index of year 2000 data is shown in Figure 5-7. Bright band sharpness index has an average value of 10.54 dBZ/km. The scatter plot of the bright band thickness vs. the rain reflectivity for stratiform rain type with BB profiles of year 2000 data is shown in Figure 5-8. The scatter plot of reflectivity of BB peak vs. rain reflectivity of stratiform rain type with BB profiles of year 2000 data is shown in Figure 5-9. Both of the figures show that BB thickness and BB peak reflectivity increase with the increase of rain reflectivity, which is an expected result.

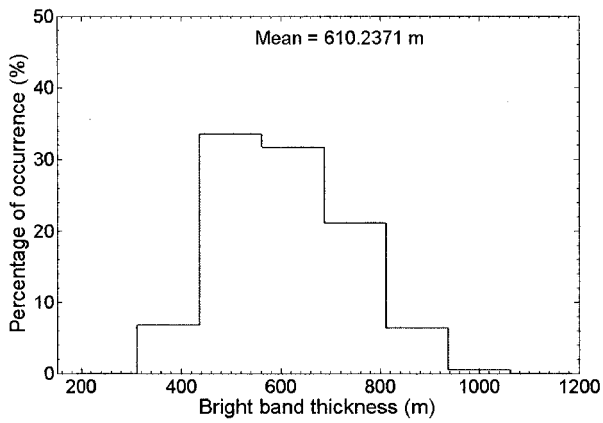

Figure 5-6. The histogram of the bright band thickness using (10 X10) SOM classificaton results of year 2000 data around the globe.

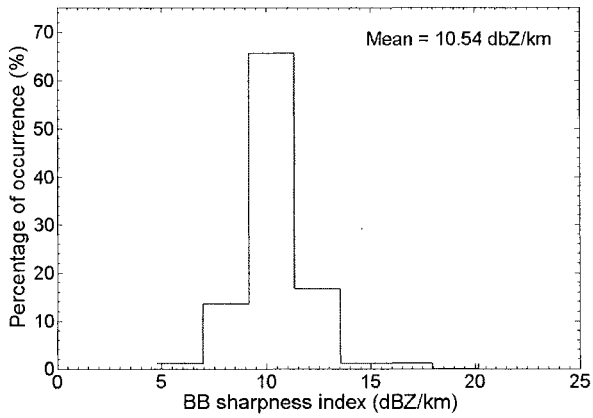

Figure 5-7. The histogram of the bright band sharpness index using (10 X10) SOM classification result of year 2000 data around the globe.

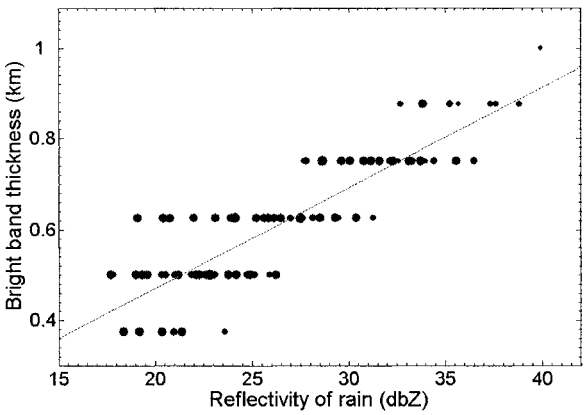

Figure 5-8. The scatter plot of the bright band thickness vs. the rain reflectivity using (10 X10) SOM classification result of the year 2000 data around the globe.

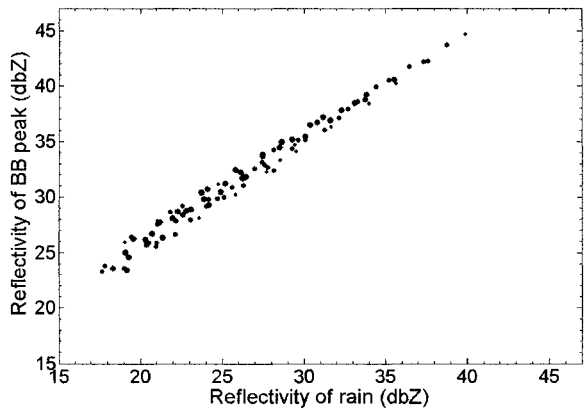

Figure 5-9. The scatter plot of the reflectivity of BB peak vs. the rain reflectivity using (10 X10) SOM classification result of the year 2000 data around the globe.

Figure 5-10 (a) shows the histogram and the average value of the bright band peak height from sea level during all months of the year 2000. Figure 5-10(b) shows the monthly mean value for bright band peak height from sea level of all months of the year 2000 and the average for nadir ray during the year 2000. The average of each month changes very closely around the mean because data are distributed over the northern and southern hemispheres. Figure 5-11 (a) shows the histogram and the average of the height of storm top from the sea level of all months of the year 2000 profiles. Figure 5-11 (b) shows the monthly mean value for storm top height from sea level of the year 2000 and the average using the nadir ray only during the year 2000.

The average of each month changes very closely around the mean. Figure 5-12 (a) shows the histogram and the average of BB peak reflectivity of all months of the year 2000. Figure 5-12 (b) shows the monthly mean value for BB peak reflectivity of all months of the year 2000 and the same average using the nadir ray only during the year 2000. The mean value of BB peak reflectivity of year 2000 profiles for nadir ray is larger than the monthly average. This happened due to the smear of the vertical profile data while radar scans off nadir.

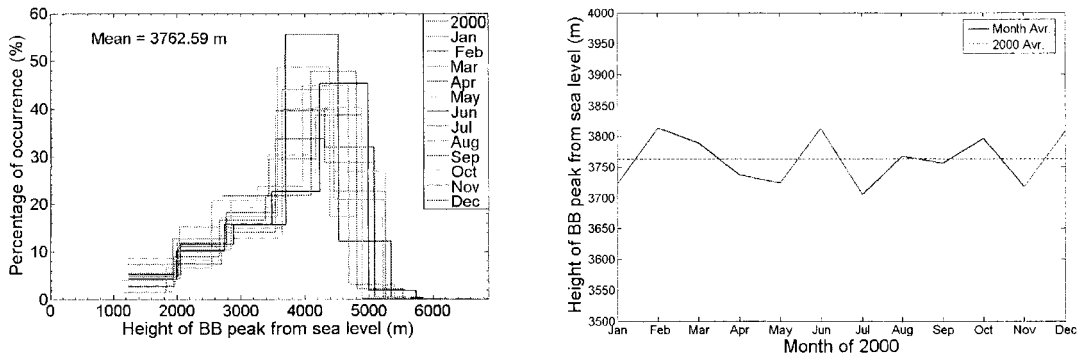

(a) (b)

Figure 5-10. (a) The histogram and the average of the bright band peak height from sea level for all months of the year 2000 (b) The mean value for bight band peak height from sea level of all months for the year 2000 and the same average using the nadir ray only during the year 2000.

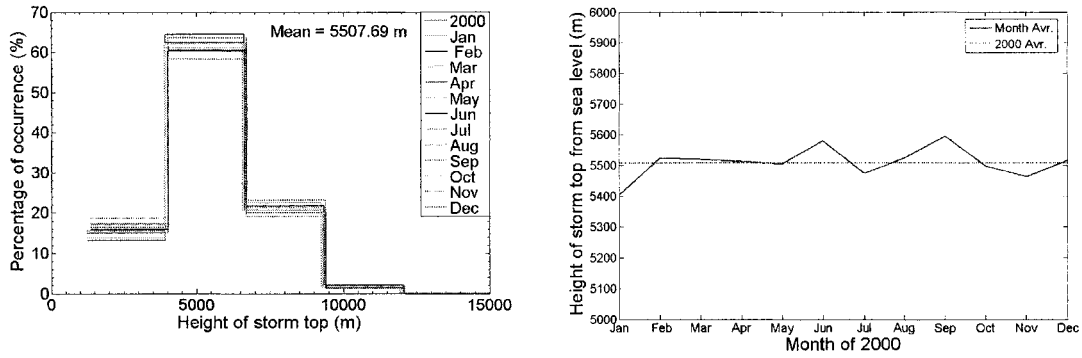

(a) (b)

Figure 5-11. (a) The histogram and the average of storm top height from sea level for all months of the year 2000 (b) The mean value for storm top height from sea level of all months of the year for 2000 and the average during year 2000.

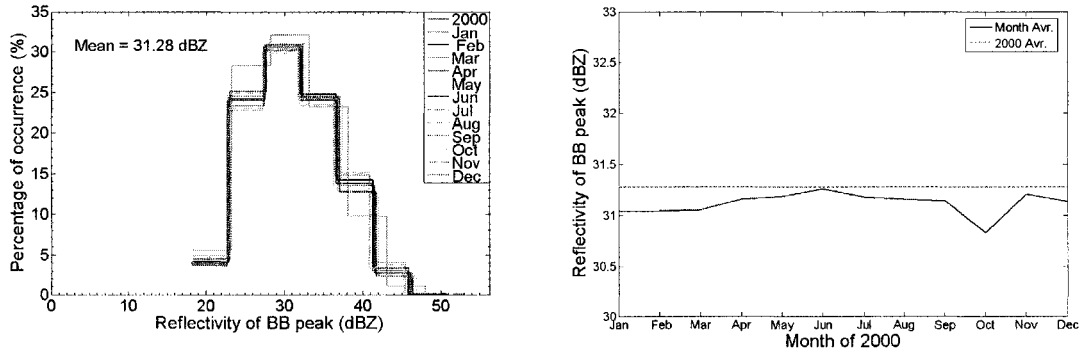

(a) (b)

Figure 5-12. (a) The histogram and the average of reflectivity of BB peak for all months of the year 2000. (b) The mean value for reflectivity of BB peak for all months of the year of 2000 and the same average using the nadir ray only during the year 2000.

5.2.2 Northern and Southern Hemisphere Differences

Satellite-based retrievals offer the only source of large-scale precipitation observations over the northern and the southern hemispheres. Using TRMM-PR data and SOM, we attempt to investigate the properties of the BB region over the northern and the southern hemispheres. Many studies have examined differences in the structure of the BB region in stratiform precipitation between both areas. In this section, a brief comparison of BB region properties over the northern and southern hemispheres is introduced.

Figure 5-13 shows that there are no differences in SOM classification classes for rain profiles over the northern and southern hemispheres for year 2000. Figure 5-14 shows the same things for the months of January, April, August, and November of year 2000. Figure 5-14 shows just a small difference in the reflectivity structure under BB peak height during the months of January and August. The histogram of bright band peak height from sea level for year 2000 and the months of January, April, August, and November of year 2000 are shown in Figure 5-15 and Figure 5-16. Figure 5-16 (a) and (c) show that there is a difference in the bright band peak height from sea level over the northern and the southern hemispheres during the months of January and August. This difference can cause the small difference in reflectivity structure under the height of the BB peak in the months of January and August in Figure 5-14 (a) and (c). Figure 5-17-Figure 5-24 show the histogram of the storm top height, the bright band peak reflectivity, the BB thickness, and the BB sharpness index for the year 2000 and for the months of January, April, August, and November of year 2000. From all figures, it appears that though there are slight differences, the differences are marginal and do not have an effect on the reflectivity structure of the SOM of both cases.

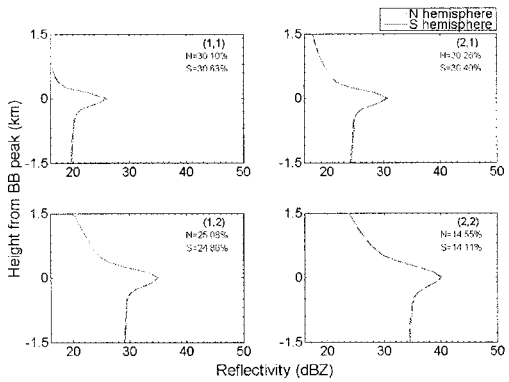

Figure 5-13. The (2X2) SOM for data profiles over northern and southern hemispheres. N is the total percentage of profiles over the northern hemisphere and S is the total percentage of profiles over the southern hemisphere.

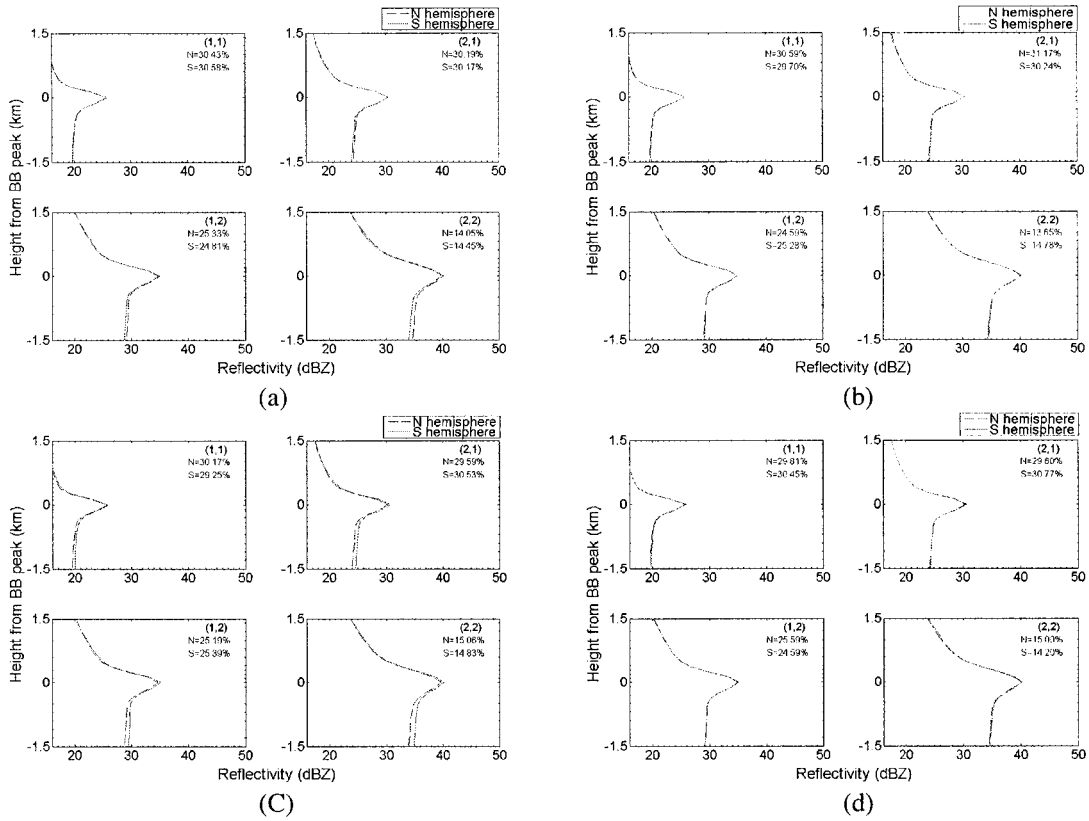

Figure 5-14. The (2X2) SOM for data profiles over the northern hemisphere and southern hemisphere for the months of (a) January 2000, (b) April 2000, (c) August 2000, and (d) November 2000.

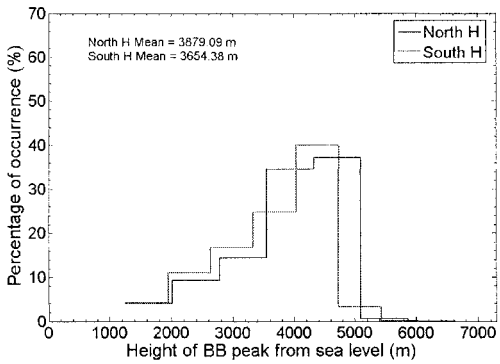

Figure 5-15. The histogram and the average value of the bright band peak height from sea level of year 2000 data profiles over the northern and southern hemispheres.

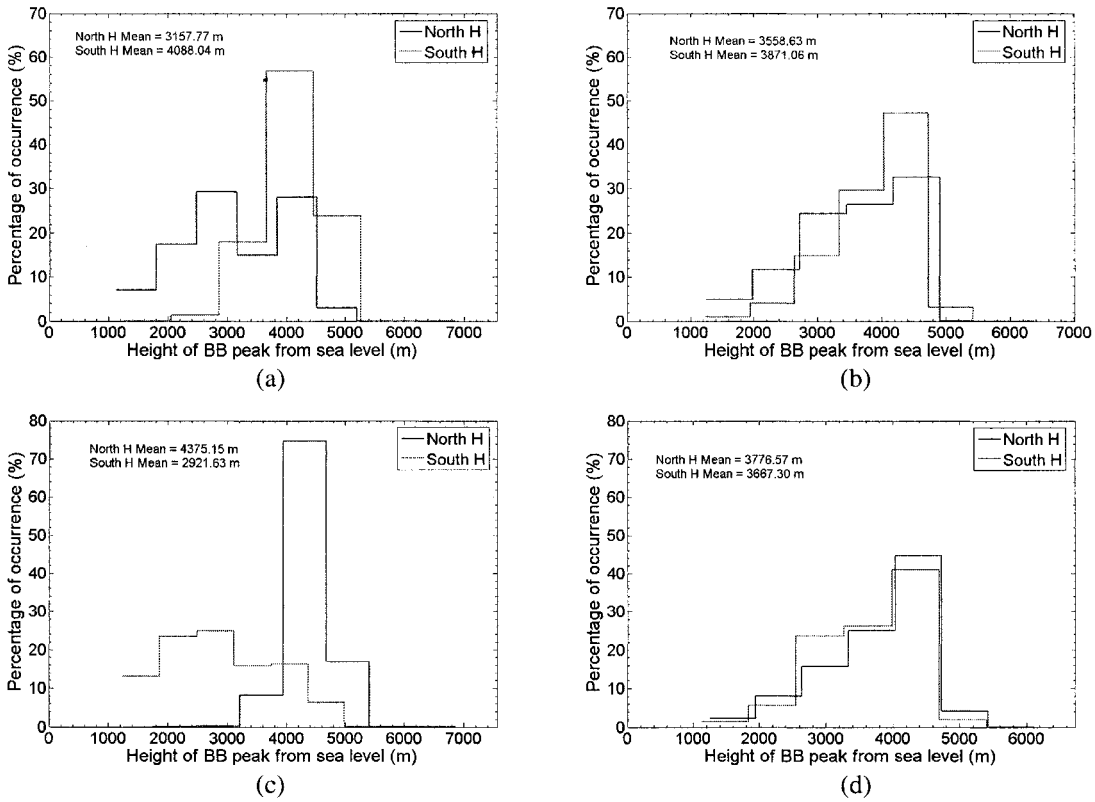

Figure 5-16. The histogram and the average value of bright band peak height from sea level over the northern and southern hemispheres for data profiles of the months of (a) January 2000, (b) April 2000, (c) August 2000, and (d) November 2000.

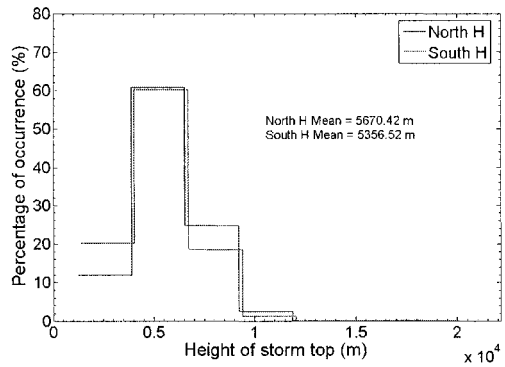

Figure 5-17. The histogram and the average value of storm top height of the year 2000 over the northern and southern hemispheres.

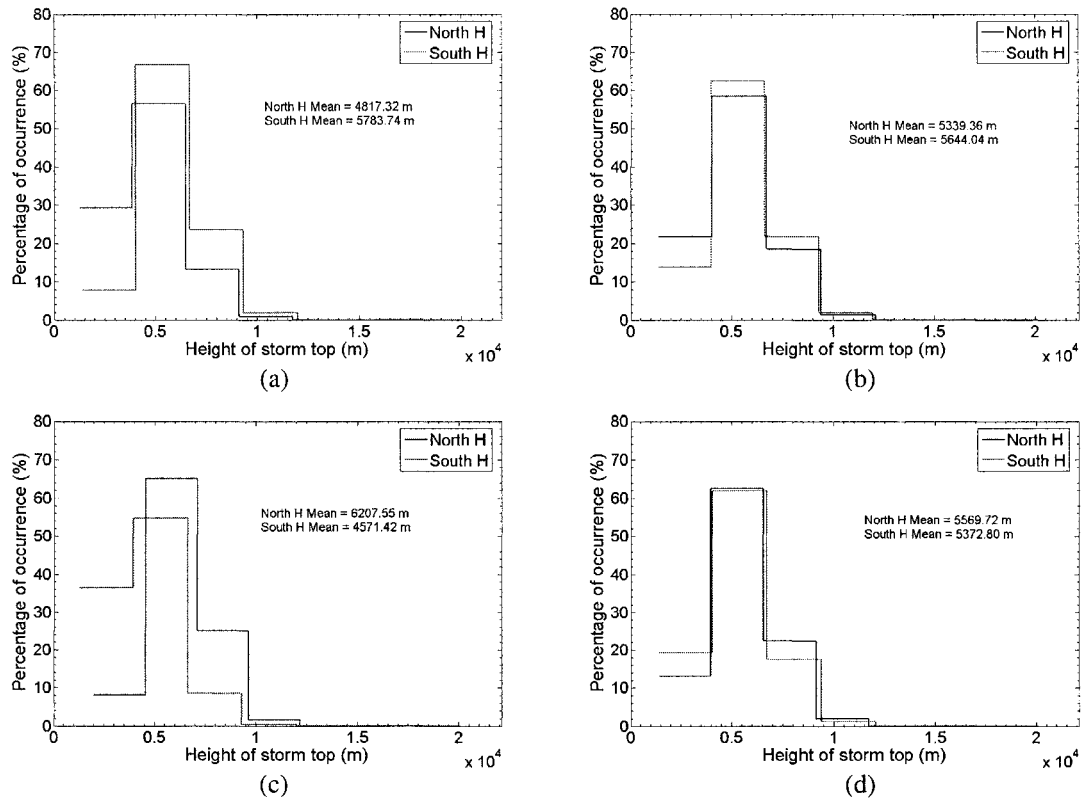

Figure 5-18. The histogram and the average value of storm top height over the northern and southern hemispheres for the months of (a) January 2000, (b) April 2000, (c) August 2000, and (d) November 2000.

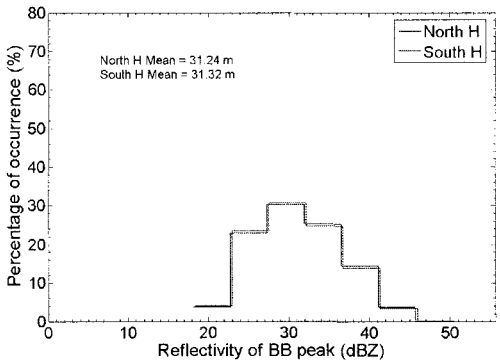

Figure 5-19. The histogram and average value of BB peak reflectivity of the year 2000 data profiles over the northern and southern hemispheres.

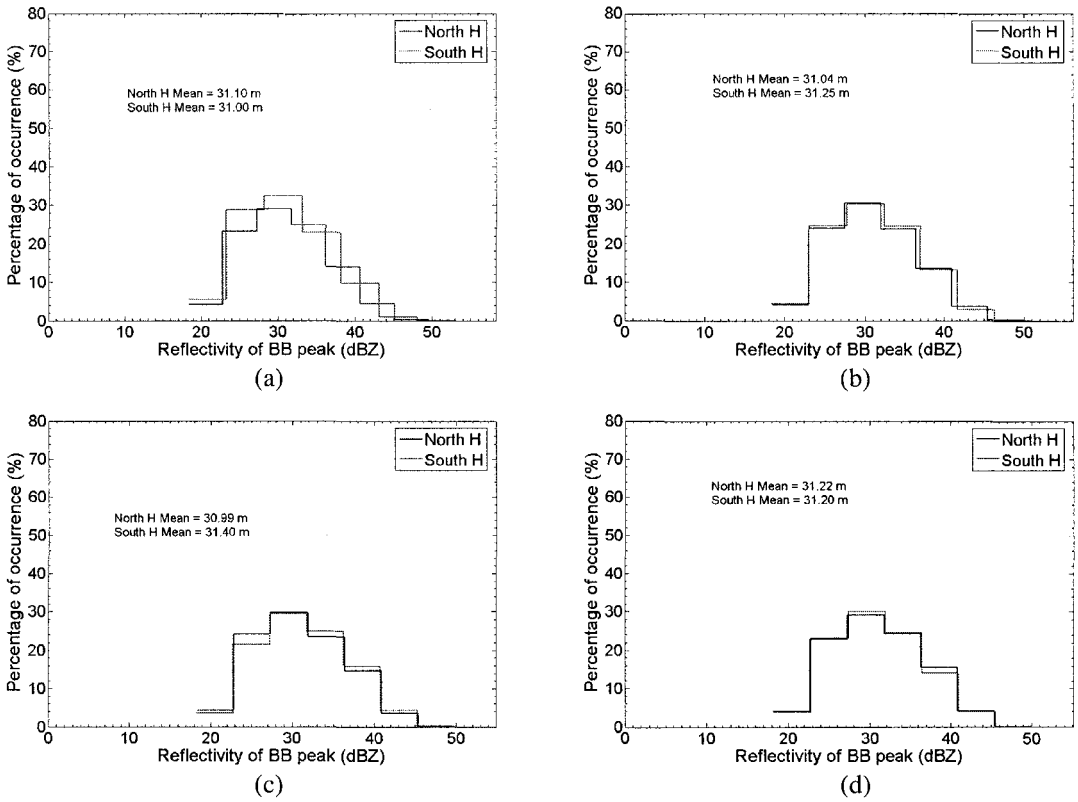

Figure 5-20. The histogram and the average value of BB peak reflectivity over the northern and southern hemispheres for the months of (a) January 2000, (b) April 2000, (c) August 2000, and (d) November 2000.

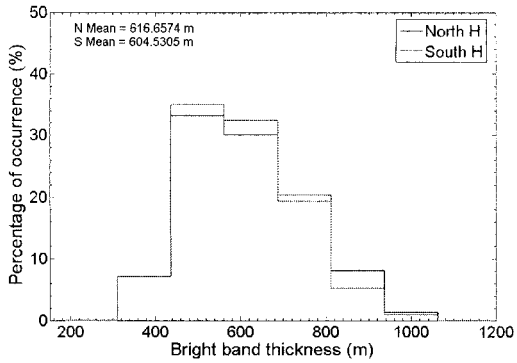

Figure 5-21. The histogram and the average value of bright band thickness of the year 2000 data profiles over the northern and southern hemispheres.

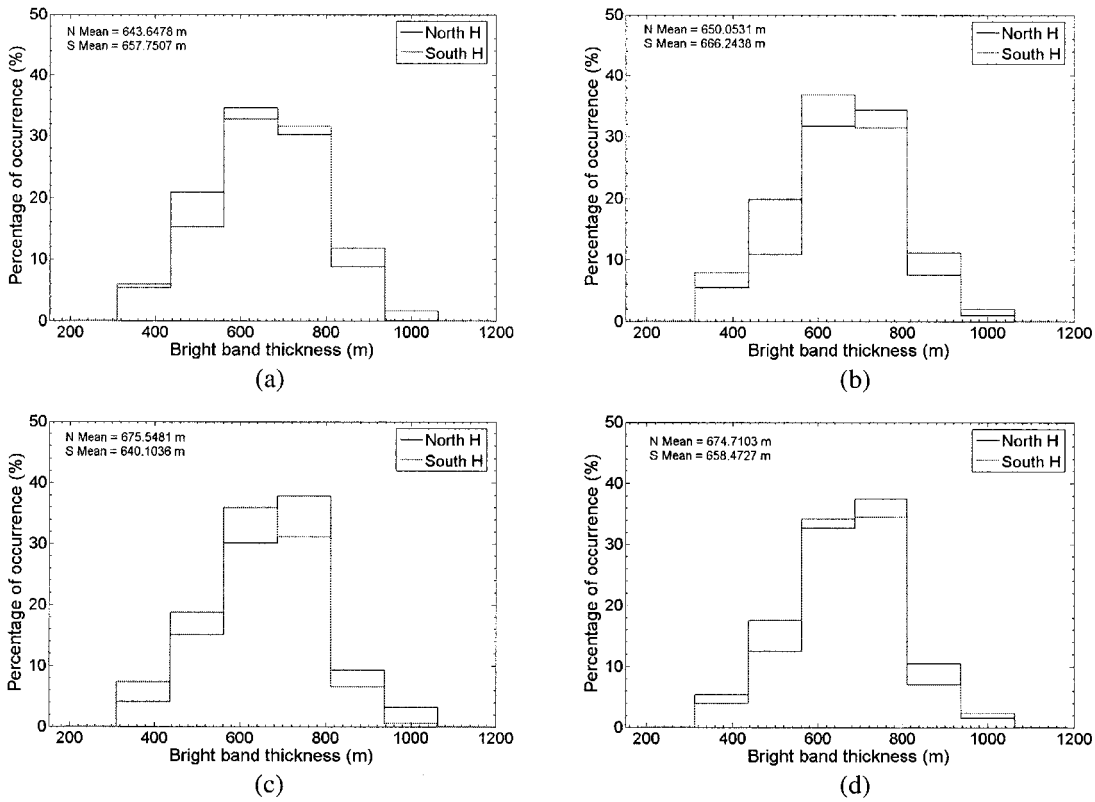

Figure 5-22. The histogram and the average value of bright band thickness over the northern and southern hemispheres for the months of (a) January 2000, (b) April 2000, (c) August 2000, and (d) November 2000.

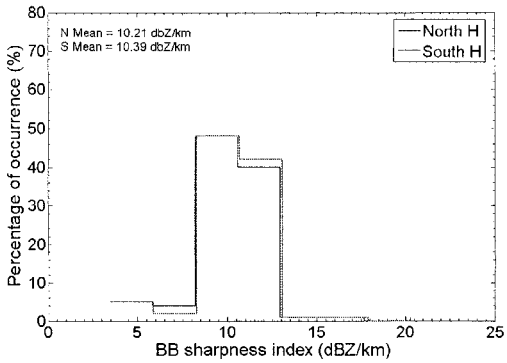

Figure 5-23. The histogram and the average value of bright band sharpness index of the year 2000 data profilers over the northern and southern hemispheres.

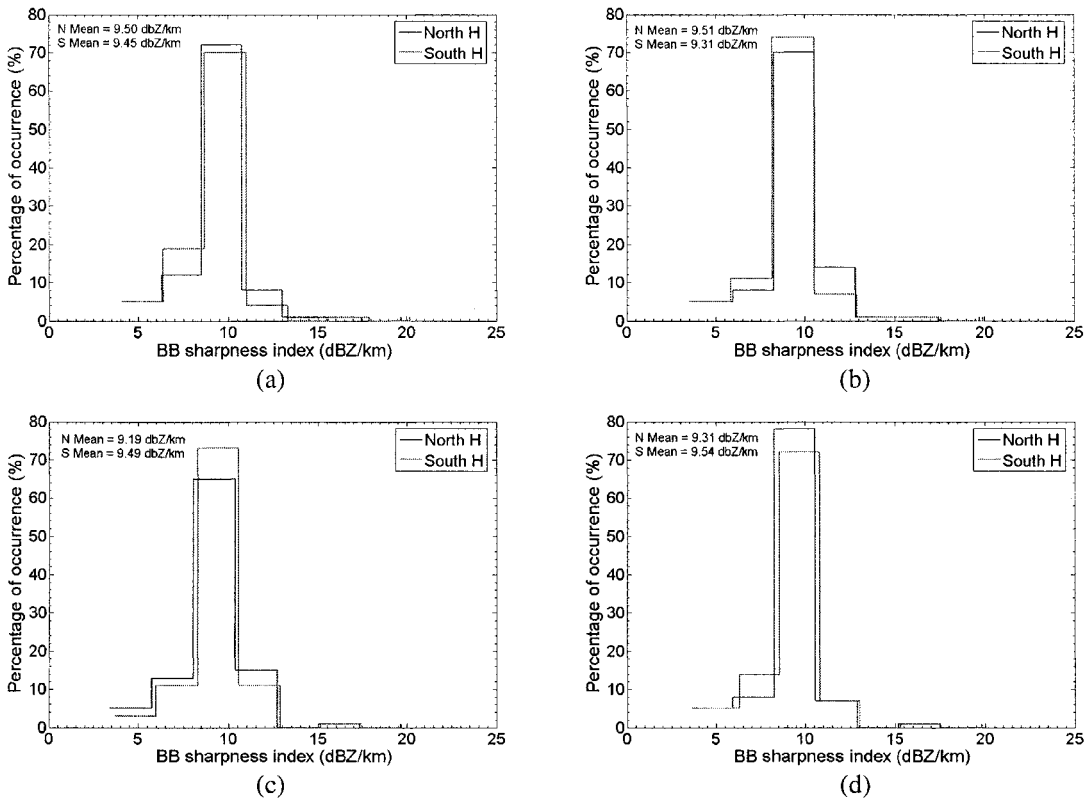

Figure 5-24. The histogram and the average value of bright sharpness index over the northern and southern hemispheres for the months of (a) January 2000, (b) April 2000, (c) August 2000, and (d) November 2000.

5.2.3 Northern (0°N - 10°N) and Southern Hemispheres (0°S - 10°S) Differences Near the Equator.

Using vertical structure of rain systems observed using TRMM-PR, we attempt to investigate the properties of BB region over the northern (0° N to 10°N latitude) and southern hemispheres (0°S to 10°S latitude). Figure 5-25 shows no difference in SOM classification classes for year 2000 data profiles over northern and southern hemispheres in that region. Figure 5-26 shows the same things for the months of January, April, August , and November of year 2000.

The histogram of bright band peak height from sea level during the year of 2000 and for the months of January, April, August, and November of year 2000 is shown in Figure 5-27 and Figure 5-28. Figure 5-28 shows that there is virtually no difference in the bright band peak height from sea level during the months of January and August.

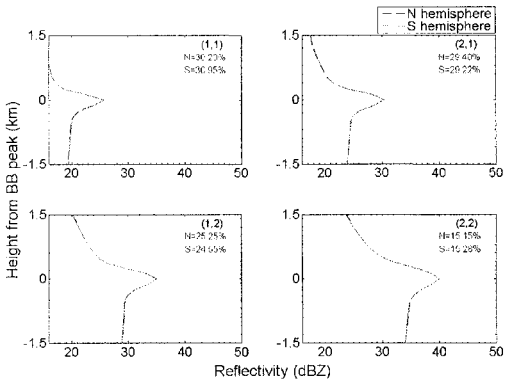

Figure 5-25. The (2X2) SOM for stratiform with BB rain type reflectivity observation collected over the northern (0°N - 10°N) and southern hemispheres (0°S - 10°S). N is the total percentage of profiles over (0°N - 10°N) and S is the total percentage of profiles over (0°S - 10°S).

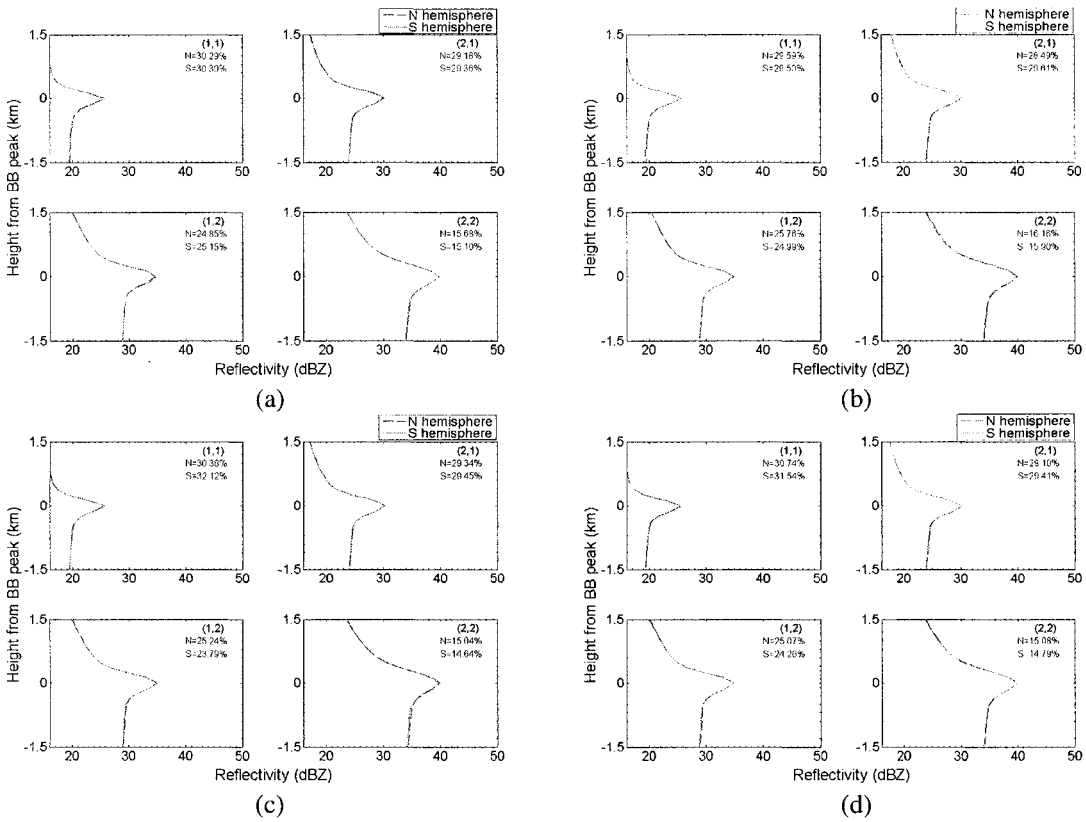

Figure 5-26. The (2X2) SOM for stratiform with BB rain type reflectivity observation collected over the northern (0°N - 10°N) and southern hemispheres (0°S - 10°S) for the months of (a) January 2000, (b) April 2000, (c) August 2000, and (d) November 2000.

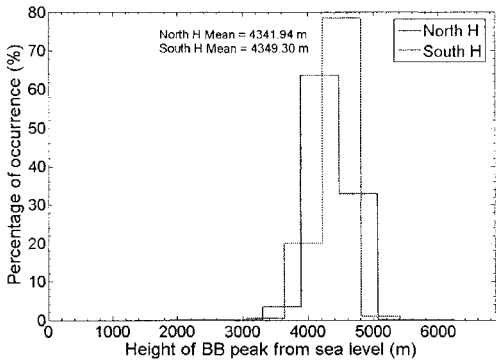

Figure 5-27. The histogram of bright band peak over the northern (0°N - 10°N) and southern hemispheres (0°S - 10°S) for the year 2000.

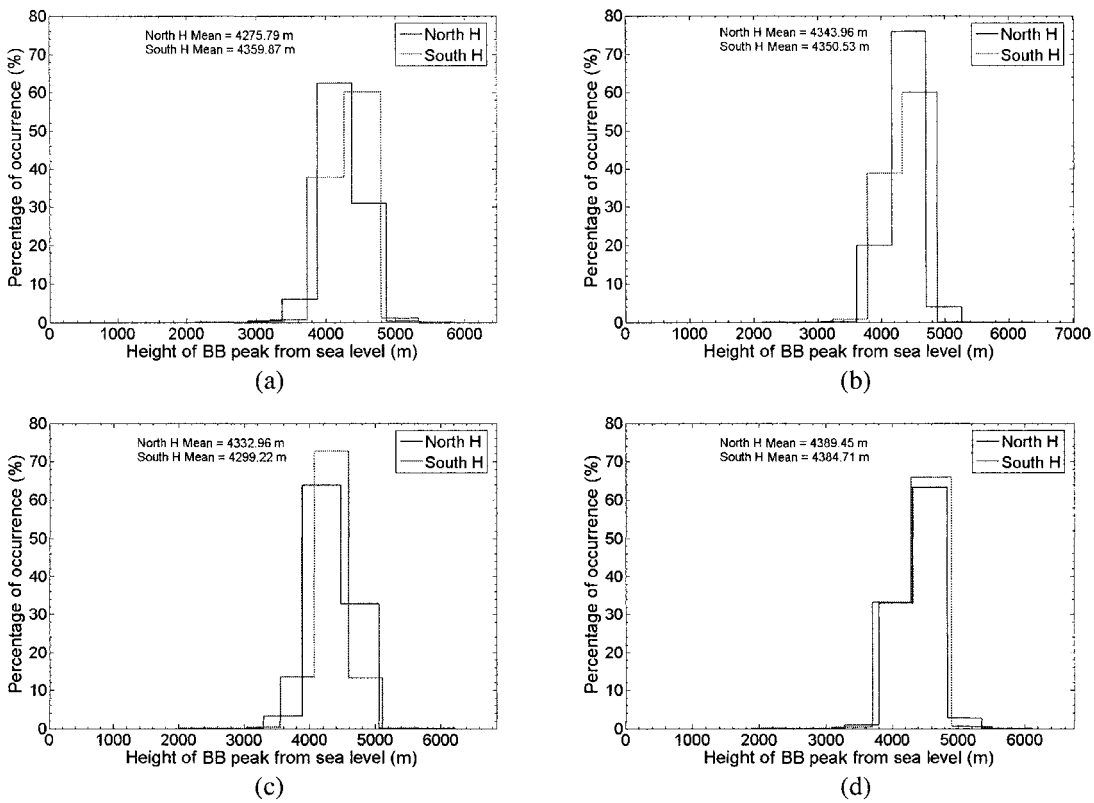

Figure 5-28. The histogram of bright band peak over the northern (0°N - 10°N) and southern hemispheres (0°N - 10°N) for the months of (a) January 2000, (b) April 2000, (c) August 2000, and (d) November 2000.

5.2.4 Northern (20°N - 37°N) and Southern Hemispheres (20°S - 37°S) Differences Far from the Equator.

Using the vertical structure of rain systems observed using TRMM-PR, we attempted to investigate the properties of the BB region over the northern (20° N to 37°N latitude) and the southern hemispheres (20°S to 37°S latitude). Figure 5-29 shows that there is no difference in the SOM BB reflectivity structure classes over the northern and southern hemispheres. Figure 5-30 shows that there was a small difference in the reflectivity structure under the BB peak height during the months of January and August 2000. The histogram of bright band peak height from sea level during the year of 2000 and for the months of January, April, August, and November of 2000 is shown in Figure 5-31 and Figure 5-32. Figure 5-32 shows that there is a large different in bright band peak height from sea level during the months of January and August. This difference can cause the small difference in reflectivity structure under the height of the BB peak in the months of January and August in Figure 5-30 (a) and (c).

Figure 5-33 and Figure 5-34 show the histogram of storm top height from sea level during the year of 2000 and for the months of January, April, August, and November of 2000. There is a large difference in the storm top height from sea level during the months of January and August, but this did not affect the reflectivity structure of SOM classes above the bright band peak height. Figure 5-35-Figure 5-40 show the histogram of bright band peak reflectivity, the BB thickness, and the BB sharpness index for the year 2000 for the months of January, April, August, and November of 2000. From all figures, it appears that though there are slight differences, the differences are marginal and do not have an effect on the reflectivity structure of the SOM of both cases.

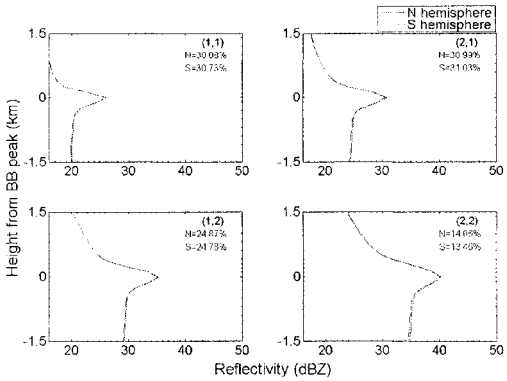

Figure 5-29. The (2X2) SOM for stratiform with BB rain type reflectivity observation collected over the northern (20°N - 37°N) and southern hemispheres (20°S - 37°S). N is the total percentage of profiles over (20°N - 37°N) and S is the total percentage of profiles over (20°S - 37°S).

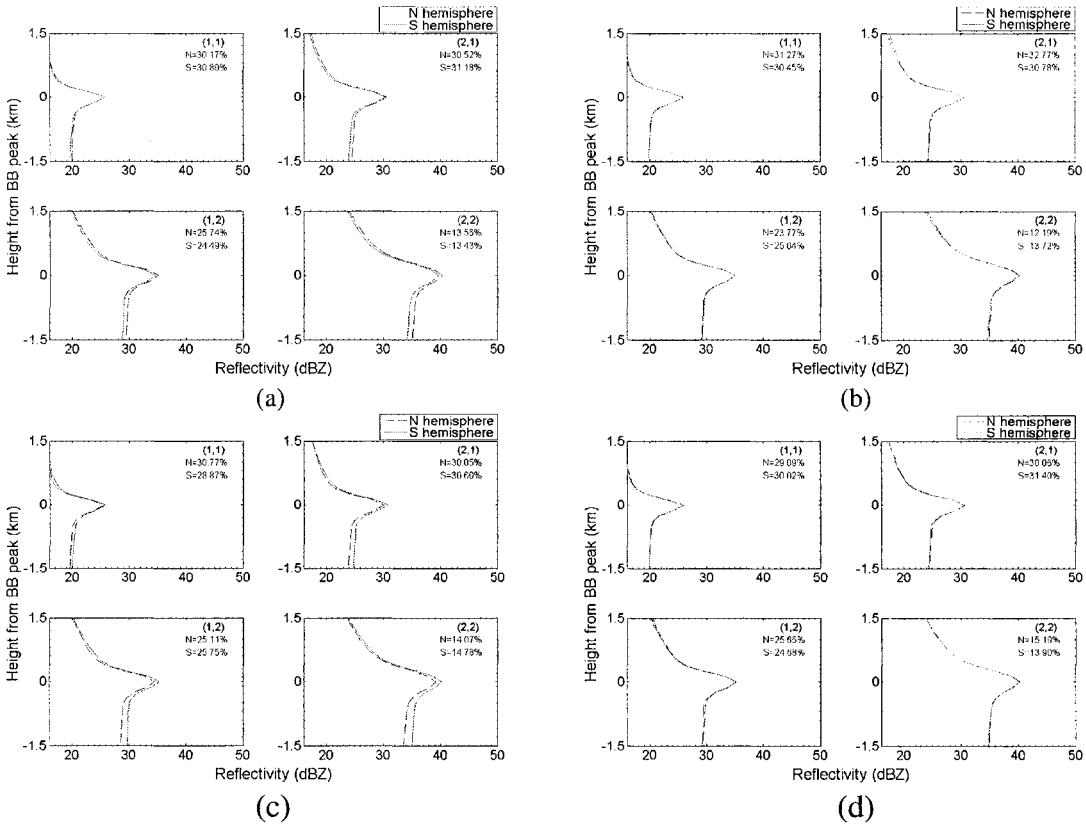

Figure 5-30 The (2X2) SOM for Stratiform with BB rain type reflectivity observation collected over the northern (20°N - 37°N) and southern hemispheres (20°S - 37°S) for the months of (a) January 2000, (b) April 2000, (c) August 2000, and (d) November 2000.

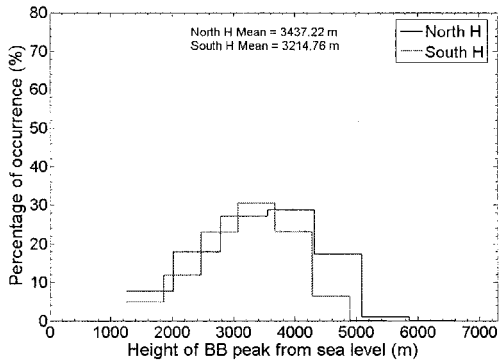

Figure 5-31. The histogram of bright band peak over the northern (20°N - 37°N) and southern hemispheres (20°S - 37°S) for year 2000.

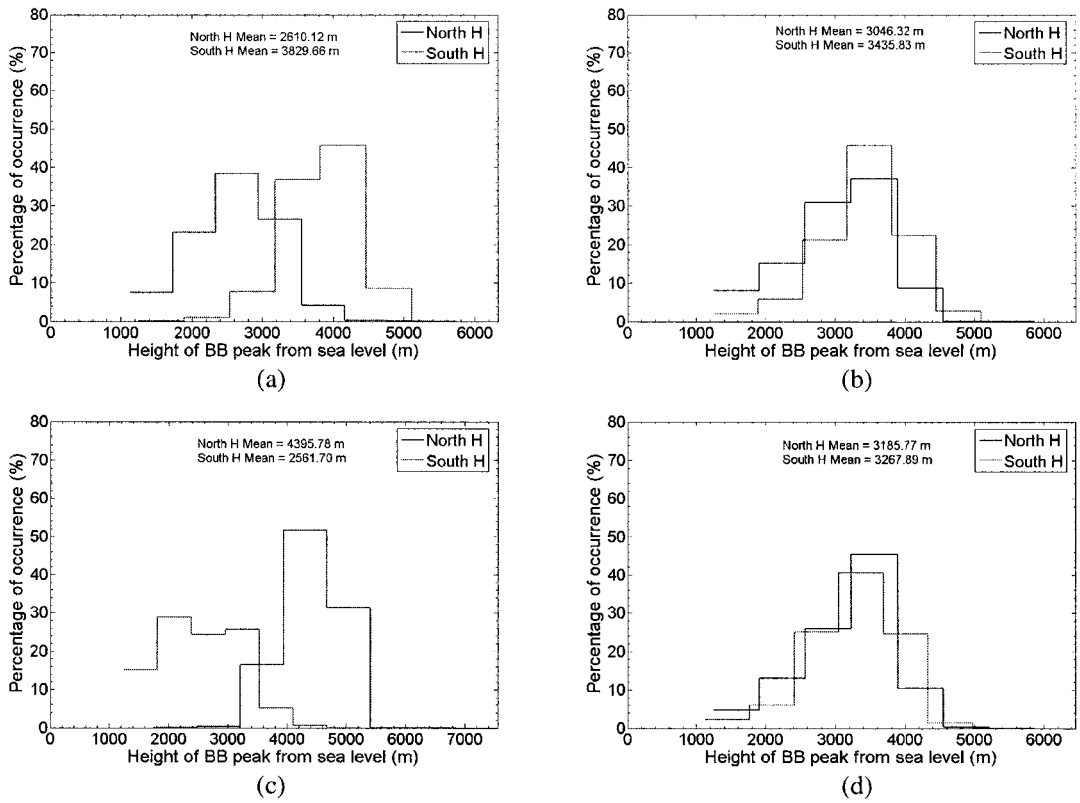

Figure 5-32. The histogram of bright band peak over the northern (20°N - 37°N) and southern hemispheres (20°N - 37°N) for the months of (a) January 2000, (b) April 2000, (c) August 2000, and (d) November 2000.

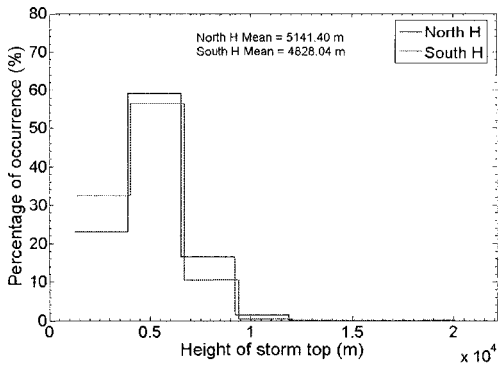

Figure 5-33. The histogram of storm top over the northern (20°N - 37°N) and southern hemisphere (20°S - 37°S) for year 2000.

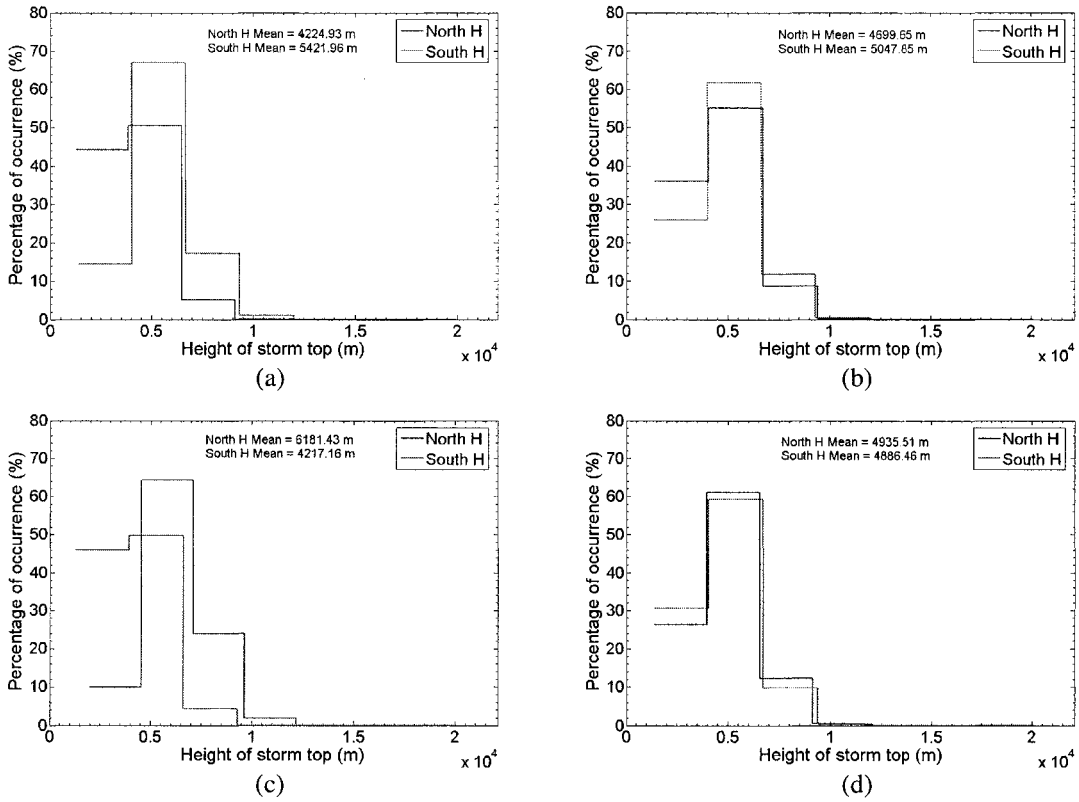

Figure 5-34. The histogram of storm top over the northern (20°N - 37°N) and southern hemispheres (20°N - 37°N) for the months of (a) January 2000, (b) April 2000, (c) August 2000, and (d) November 2000.

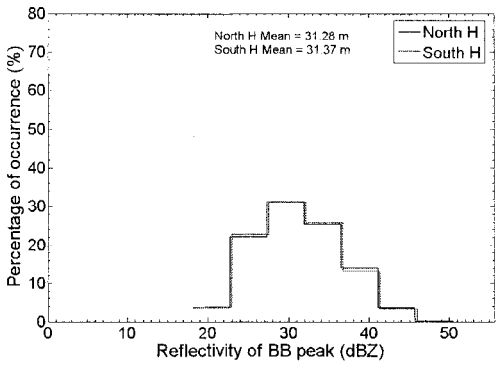

Figure 5-35. The histogram of BB peak reflectivity over the northern (20°N - 37°N) and southern hemispheres (20°S - 37°S) for year 2000.

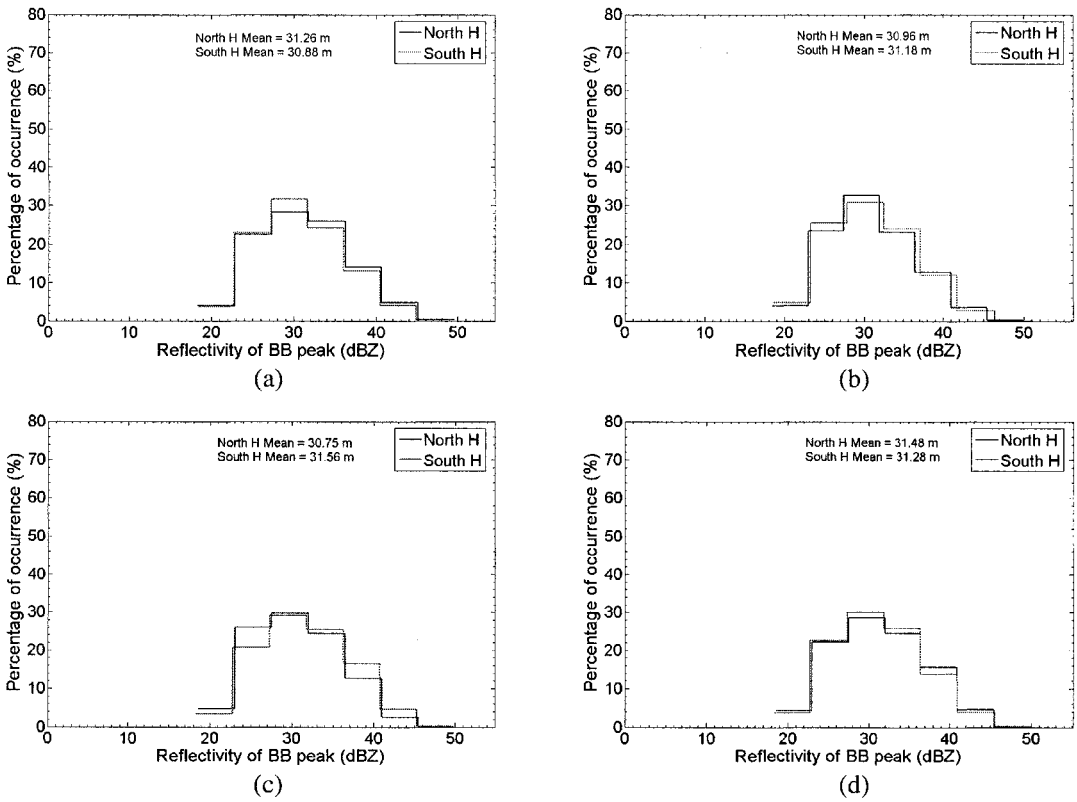

Figure 5-36. The histogram of reflectivity of bright band peak over the northern (20°N - 37°N) and southern hemispheres (20°N - 37°N) for the months of (a) January 2000, (b) April 2000, (c) August 2000, and (d) November 2000.

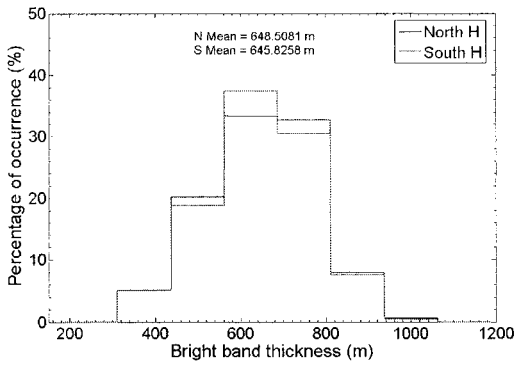

Figure 5-37. The histogram of bright band thickness over the northern (20°N - 37°N) and southern hemisphere (20°S - 37°S) for year 2000.

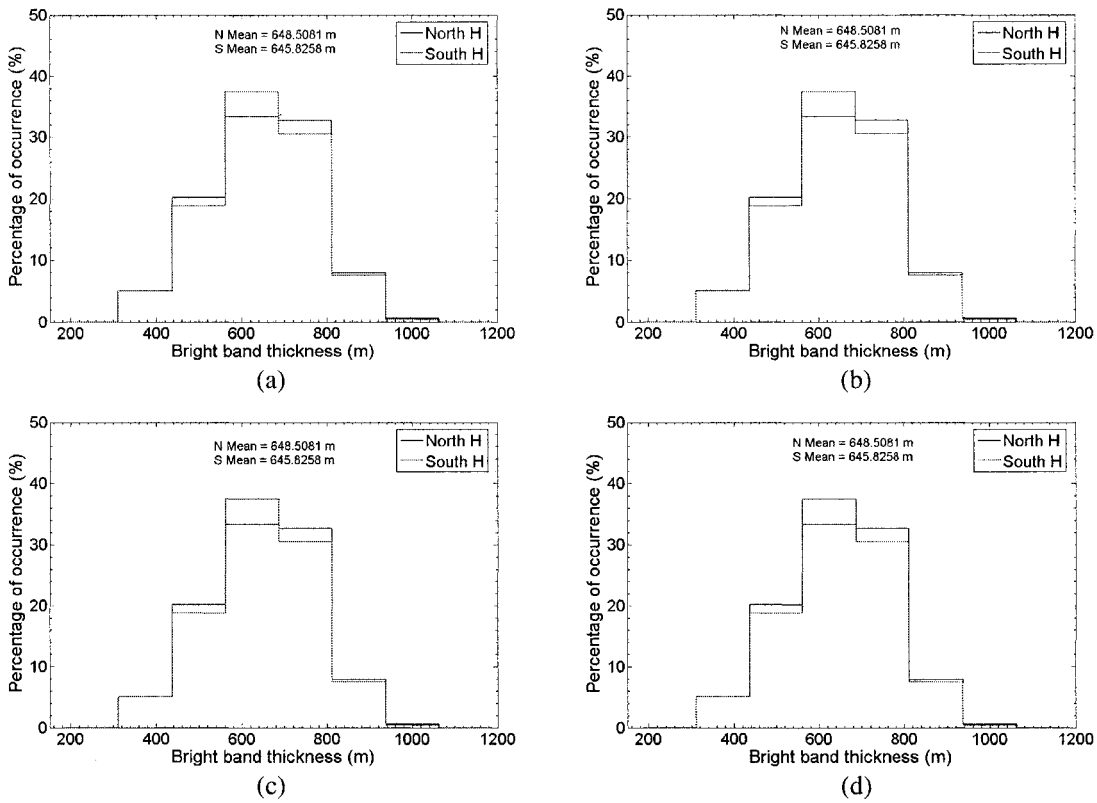

Figure 5-38. The histogram of bright band thickness over the northern (20°N - 37°N) and southern hemispheres (20°N - 37°N) for the month of (a) January 2000, (b) April 2000, (c) August 2000, and (d) November 2000.

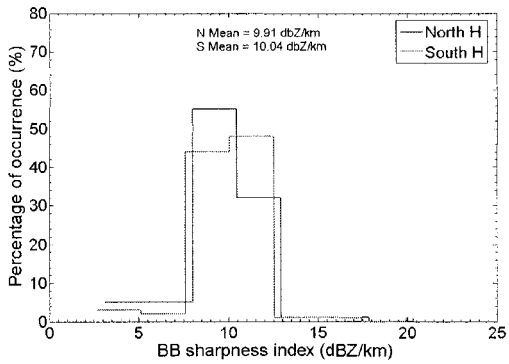

Figure 5-39. The histogram of bright band sharpness index over the northern (20°N - 37°N) and southern hemispheres (20°S - 37°S) for year 2000.

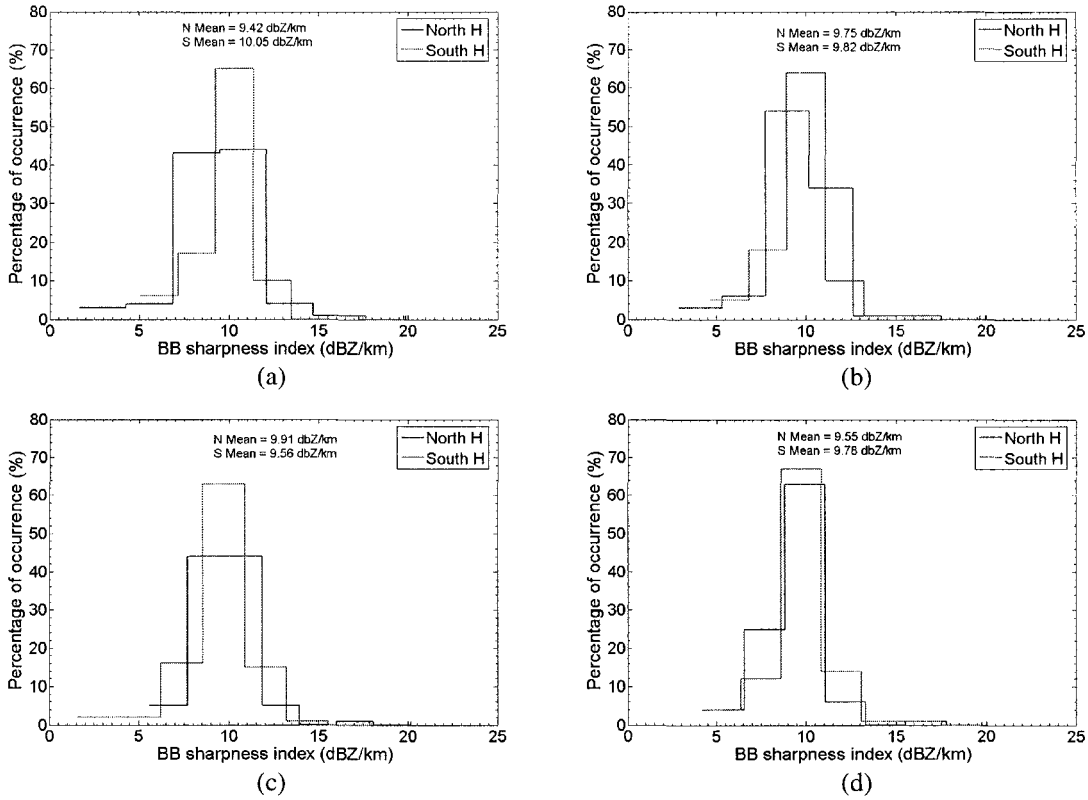

Figure 5-40. The histogram of bright band sharpness index over the northern (20°N - 37°N) and southern hemispheres (20°N - 37°N) for the months of (a) January 2000, (b) April 2000, (c) August 2000, (d) November 2000.

5.2.5 LAND AND OCEAN DIFFERENCES

Similar to Northern/Southern hemispheres analysis, there has been a perception that possibly bright band region reflectivity structures over land regions are different than over Oceans. However, a similar analysis using BB height as the reference point for the input data for the SOM algorithm was done for data collected during the year 2000.

Figure 5-41 shows that there is no difference of SOM BB reflectivity structure classes over land and over ocean for year 2000. Figure 5-42 shows the same results for the months of January, April, August, and November of year 2000. Figure 5-42 shows a small difference in reflectivity structure under the BB peak height during the months of January and August and above the height of the BB peak during all months of year 2000.

The histogram of bright band peak height from sea level during the year 2000 and for the months of January, April, August, and November of year 2000 is shown in Figure 5-43 and Figure 5-44. Figure 5-44 shows that there is a difference in the bright band peak height from sea level over land and over oceans during the months of January and August of year 2000. This difference can cause the small difference in reflectivity structure under the height of the BB peak in the month of January and August in Figure 5-42 (a), (c).

Figure 5-45 and Figure 5-46 show the histogram of the storm top height from sea level during the year 2000 and for the months of January, April, August, and November of year 2000. Even though there is a large difference in the storm top height from sea level during the months of January and August, we cannot say it is the cause of the small difference above bright band peak height in the land/ocean classes. This because in the previous section we show that even though there are large differences in the storm top height between the northern and southern hemispheres, this did not affect the reflectivity

structure above the BB peak height. Figure 5-47- Figure 5-52 show the histogram of the bright band peak reflectivity, the BB thickness, and the BB sharpness index for the year 2000 and for the months of January, April, August, and November of year 2000.

From all figures, it appears that though there are slight differences, the differences are marginal and do not have an effect on the reflectivity structure of the SOM of both cases. The analysis demonstrates that the bright band properties are almost similar over land and ocean.

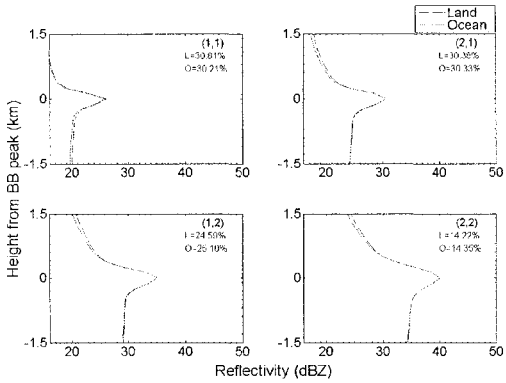

Figure 5-41. The (2X2) SOM for stratiform with BB rain type reflectivity observation collected over land (L) and over ocean (O).

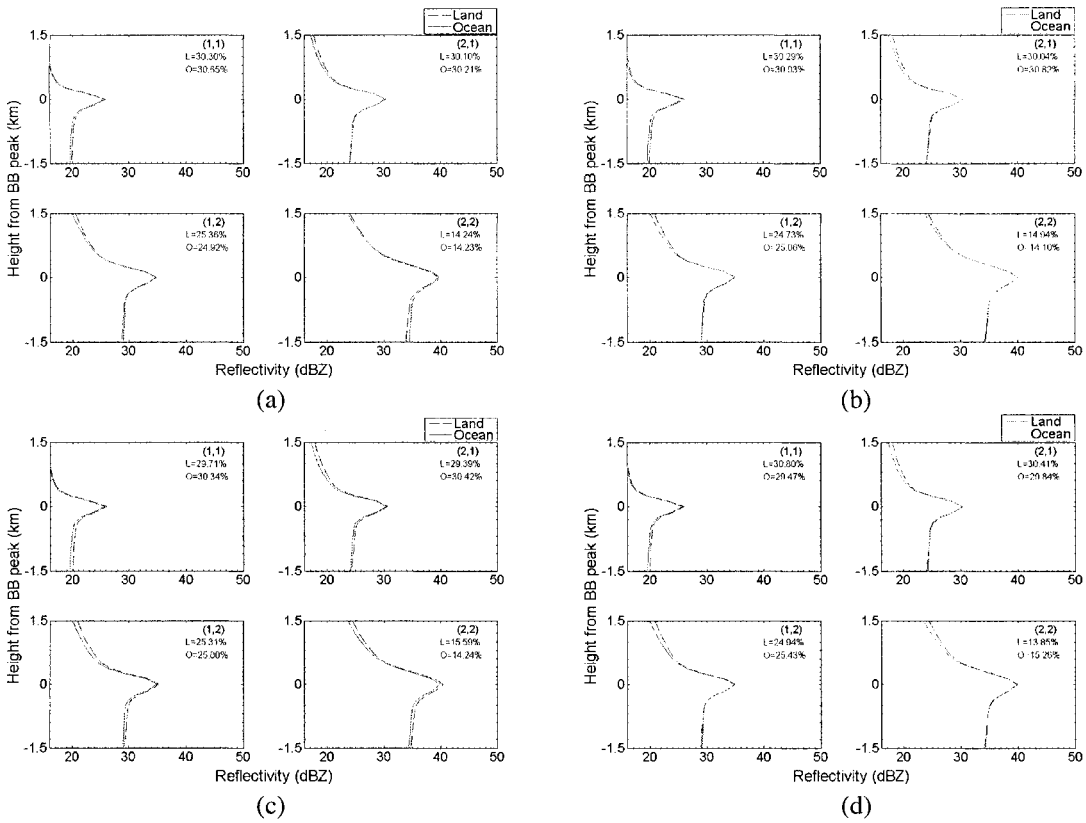

Figure 5-42. The (2X2) SOM for stratiform with BB rain type reflectivity observation collected over land (L) and over ocean (O) for the months of (a) January 2000, (b) April 2000, (c) August 2000, and (d) November 2000.

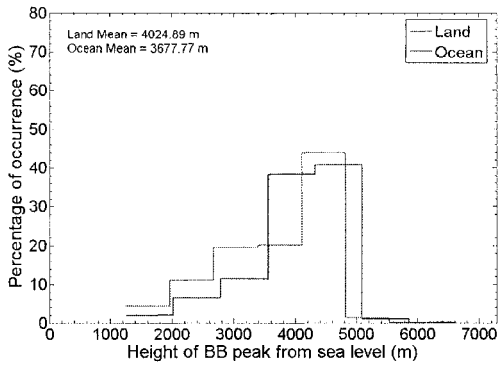

Figure 5-43. The histogram of bright band peak height from sea level of the year 2000 over land (L) and over ocean (O).

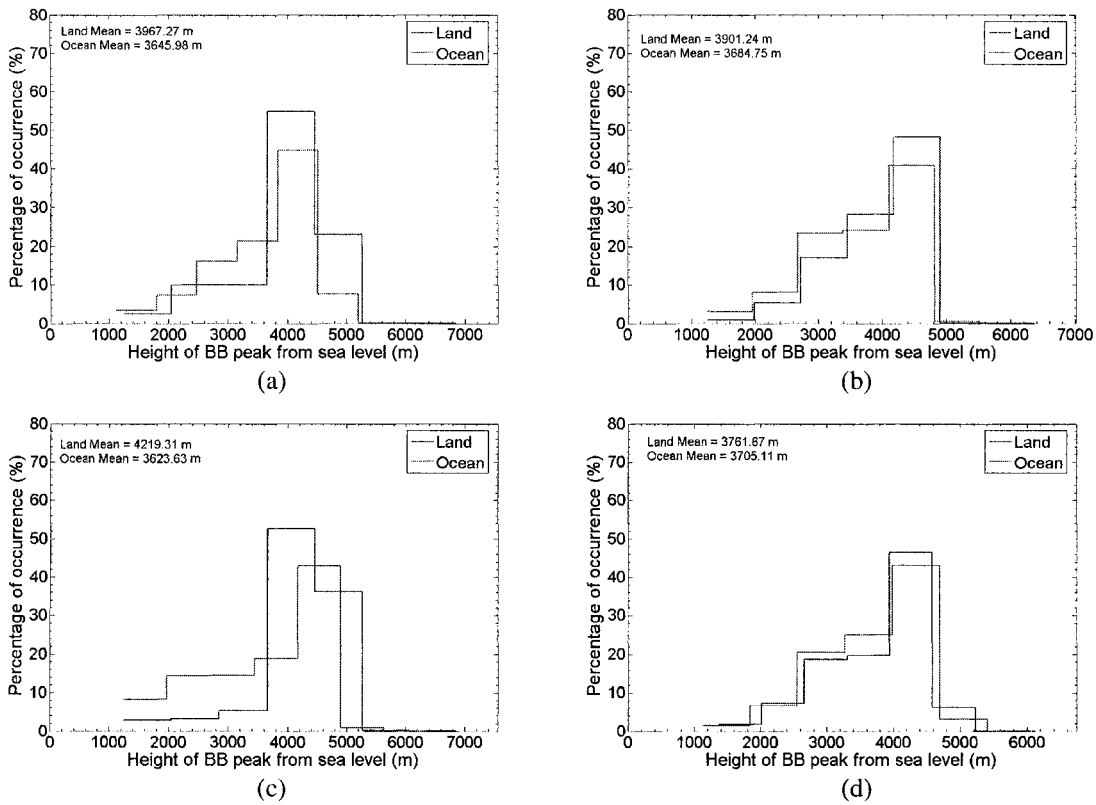

Figure 5-44. The histogram of bright band peak height from sea level over land (L) and ocean (O) for the months of (a) January 2000, (b) April 2000, (c) August 2000, and (d) November 2000.

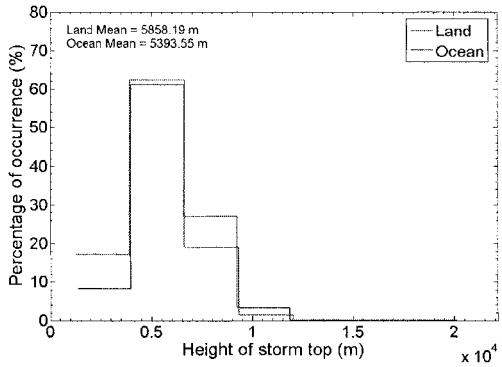

Figure 5-45. The histogram of storm top height of the year 2000 over land (L) and over ocean (O).

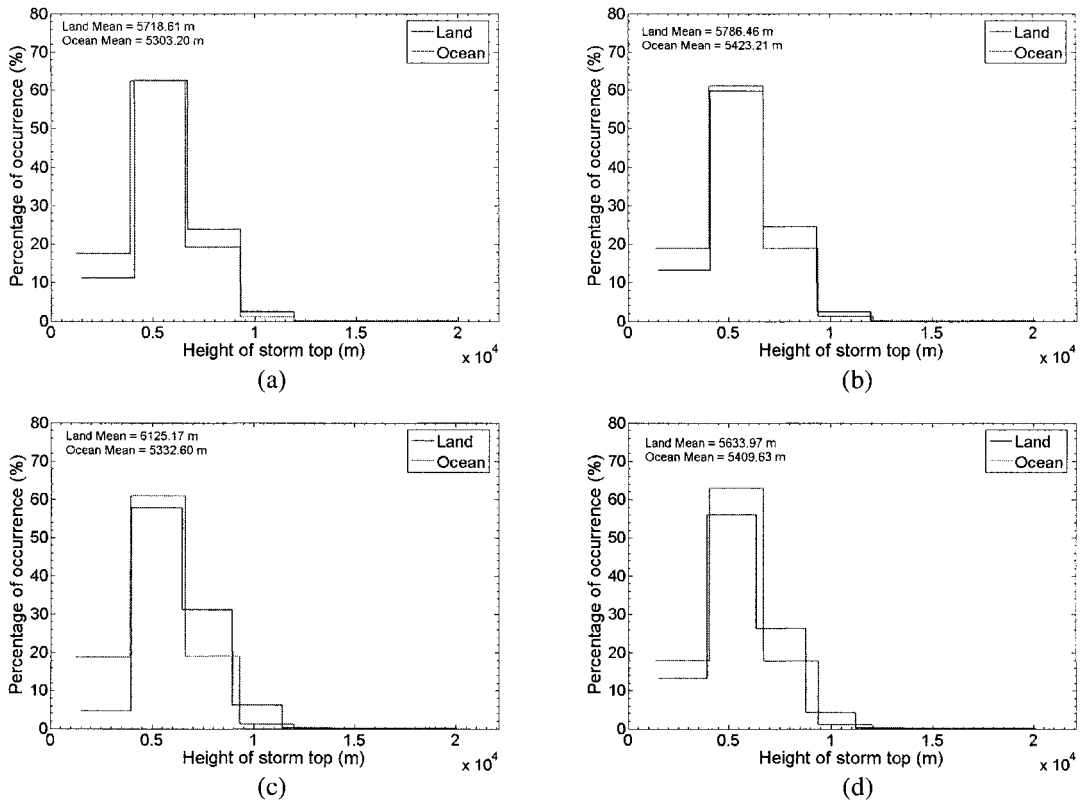

Figure 5-46. The histogram of storm top height over land (L) and over ocean (O) for the months of (a) January 2000, (b) April 2000, (c) August 2000, and(d) November 2000.

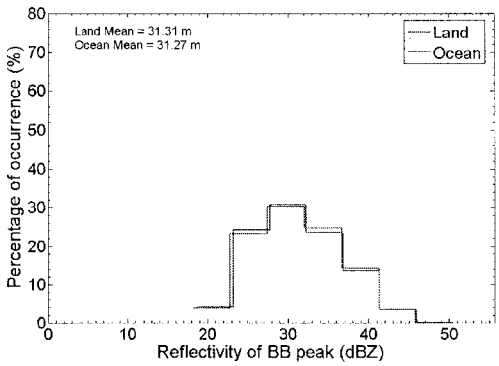

Figure 5-47. The histogram of reflectivity of BB peak of the year 2000 over land (L) and over ocean (O).

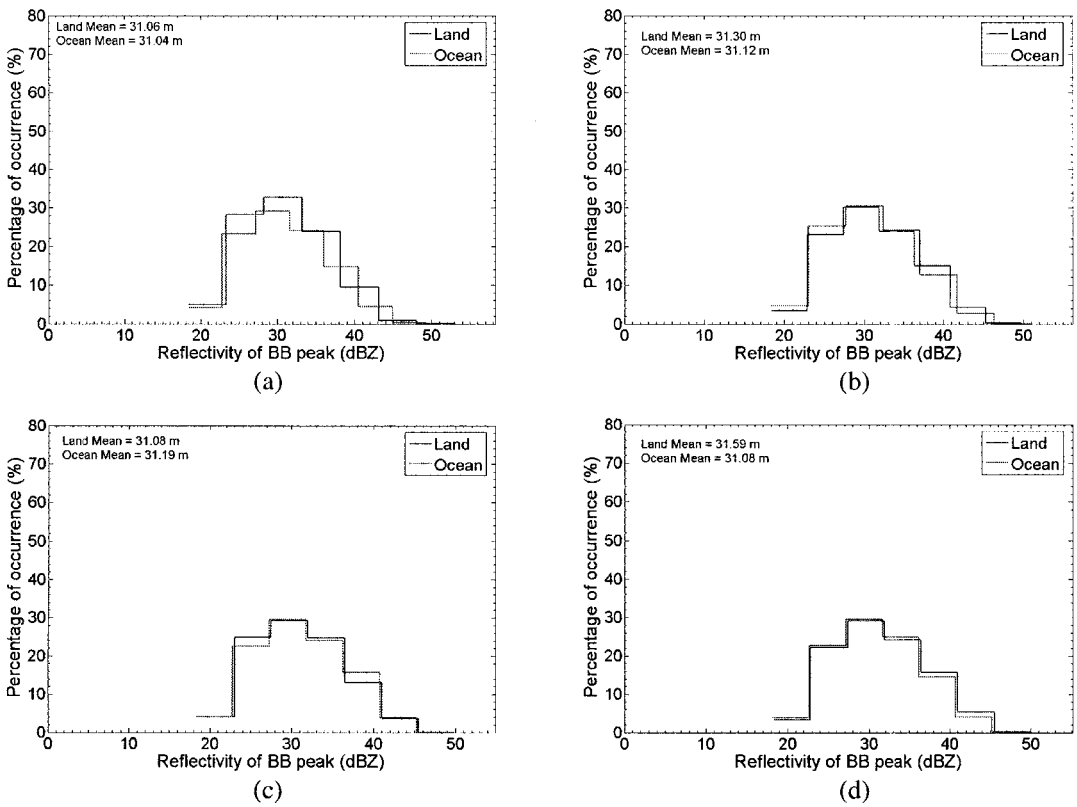

Figure 5-48. The histogram of reflectivity of BB peak over land (L) and over ocean (O) for the months of (a) January 2000, (b) April 2000, (c) August 2000, and (d) November 2000.

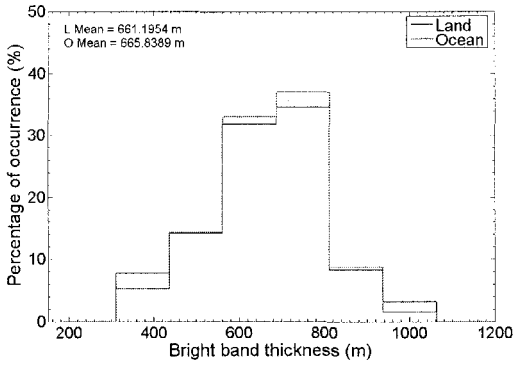

Figure 5-49. The histogram of the bright band thickness of the year 2000 over land (L) and over ocean (O).

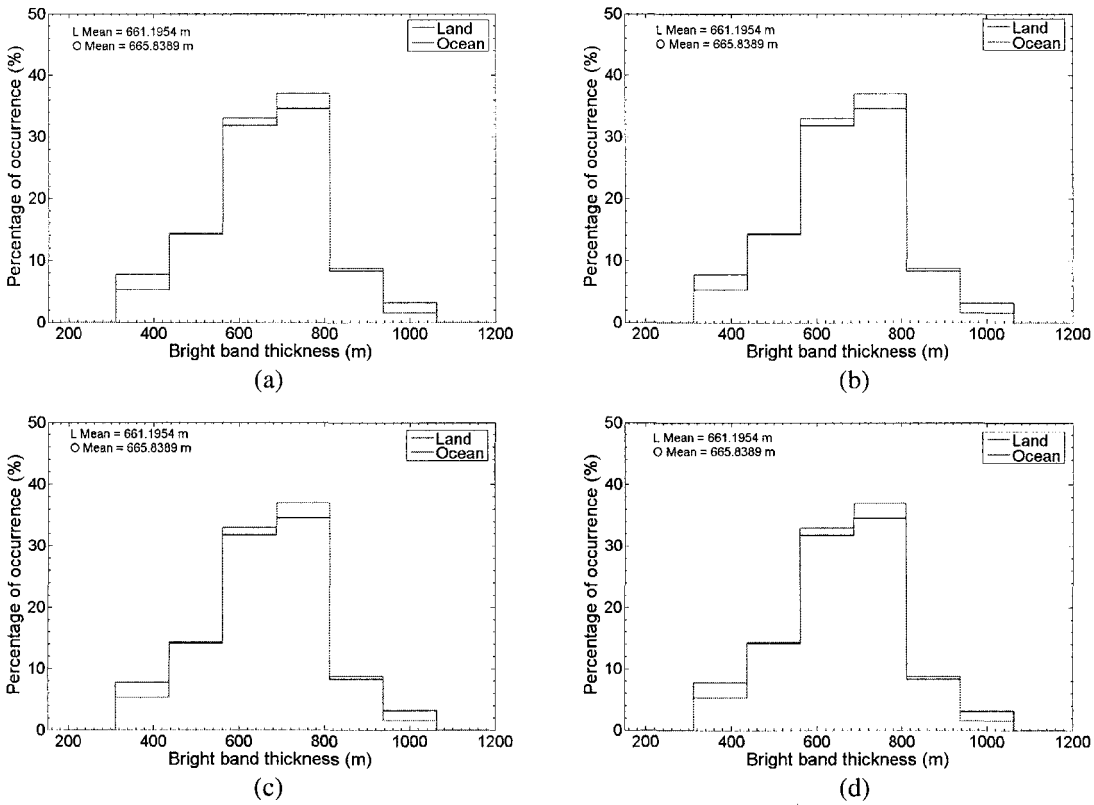

Figure 5-50. The histogram of the bright band thickness over land (L) and over ocean (O) for the months of (a) January 2000, (b) April 2000, (c) August 2000, (d) November 2000.

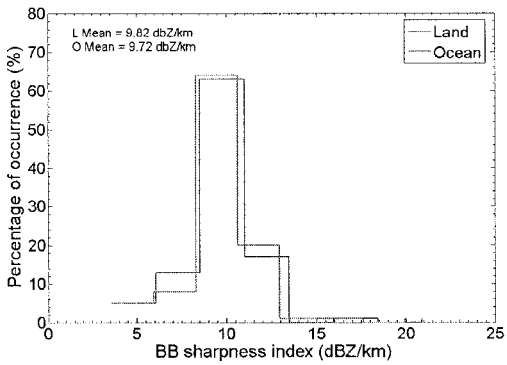

Figure 5-51. The histogram of bright band sharpness index of the year 2000 over land (L) and over ocean (O).

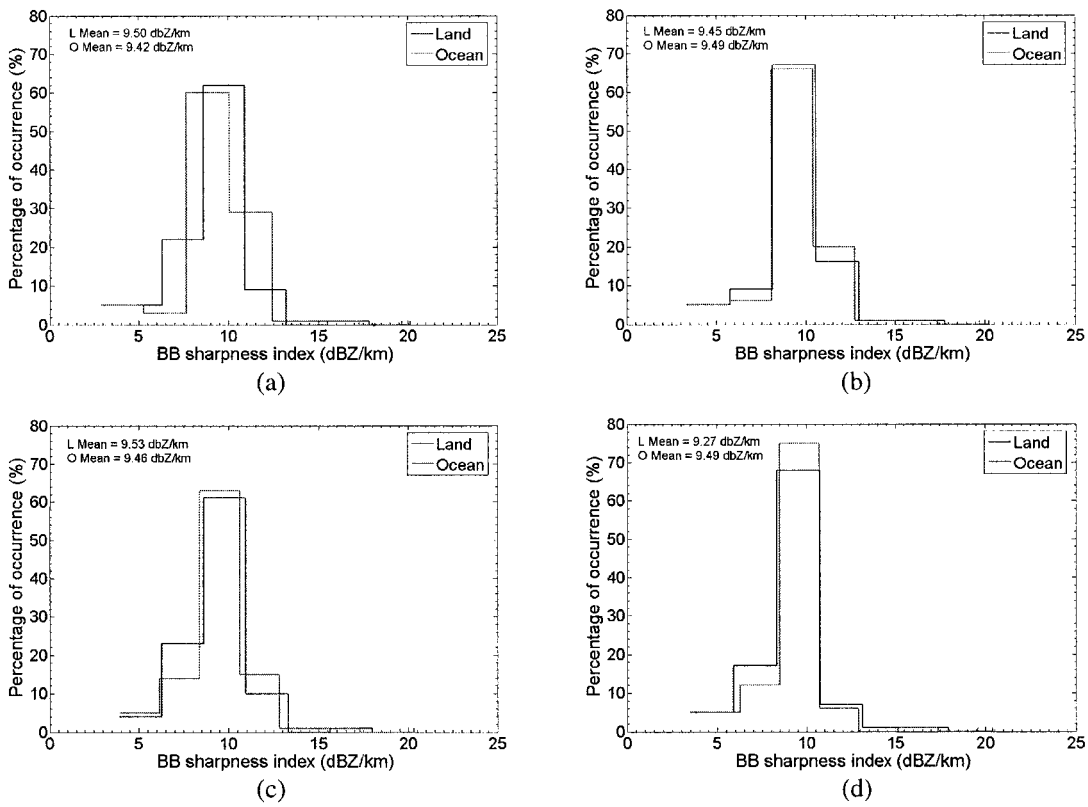

Figure 5-52. The histogram of bright sharpness index over land (L) and over ocean (O) for the month of (a) January 2000, (b) April 2000, (c) August 2000, and (d) November 2000.

5.2.6 East and West Pacific Ocean Differences

Satellite-based retrievals offer the only source of large-scale precipitation observations over oceans. Using vertical structure of rain systems observed with the PR from TRMM, we attempt to investigate the properties of BB data over the East and West Pacific Ocean. Many studies have examined differences in the structure of the BB region in stratiform precipitation between the tropical East and West Pacific [12][70].

Figure 5-53 shows that there is no difference of the SOM BB reflectivity structure classes over the East and West Pacific Ocean for year 2000. Figure 5-54 shows the same things for the months of January, April, August, and November of year 2000 with no difference in reflectivity structure between the East and West Pacific Ocean. Figure 5-55-Figure 5-64 show the histogram of the bright band peak height, the storm top height, the bright band peak reflectivity, the BB thickness and the BB sharpness index for the months of January, April, August, and November of year 2000.

From all figures, it appears that although there are slight differences, the differences are marginal and do not have an effect on the reflectivity structure of the SOM of both cases. The analysis demonstrates that the bright band properties are similar for the East and West Pacific Ocean.

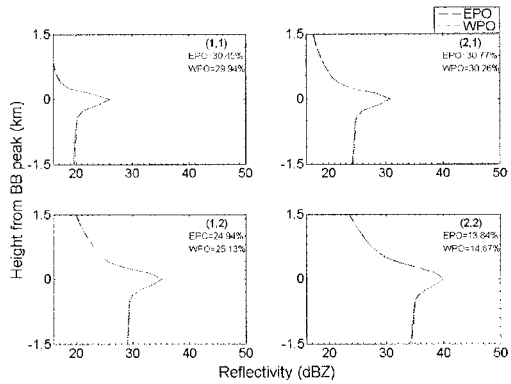

Figure 5-53. The (2X2) SOM for stratiform with BB rain type reflectivity observation collected over the East Pacific Ocean (EPO) and Weat Pacific Ocean (WPO).

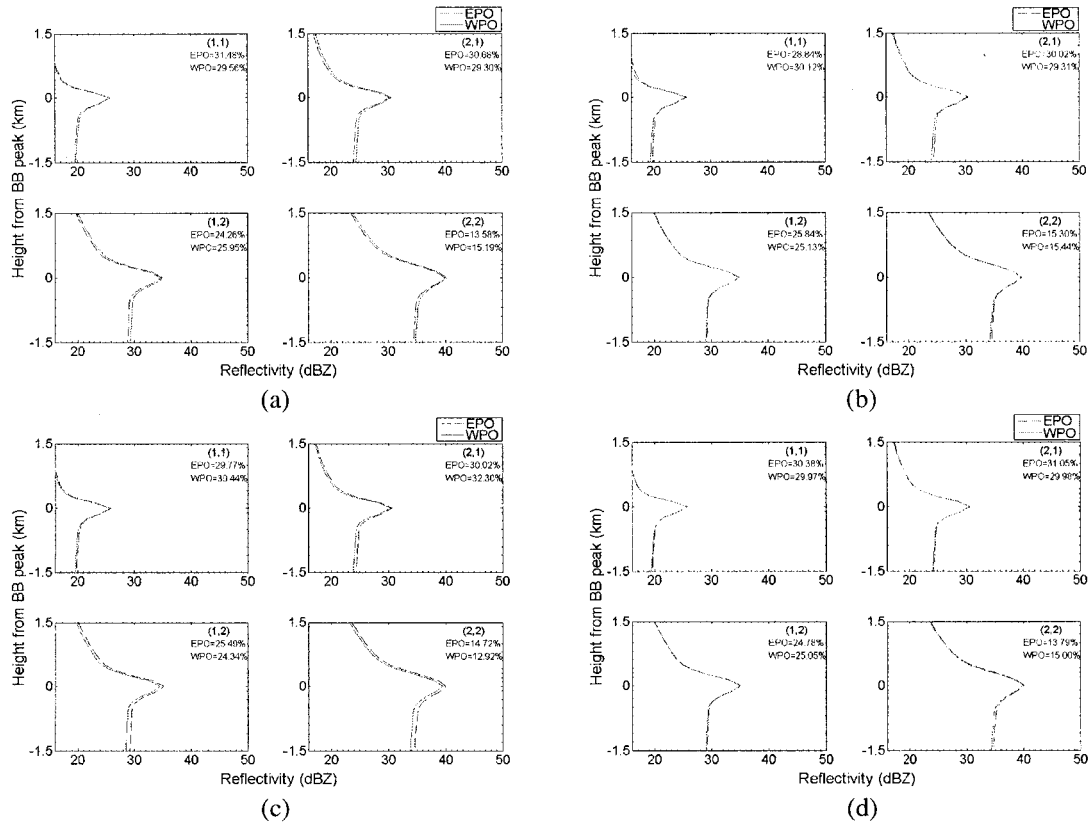

Figure 5-54. The (2X2) SOM for Stratiform with BB rain type reflectivity observation collected over the East Pacific Ocean (EPO) and Weat Pacific Ocean (WPO) for the months of (a) January 2000, (b) April 2000, (c) August 2000, and (d) November 2000.

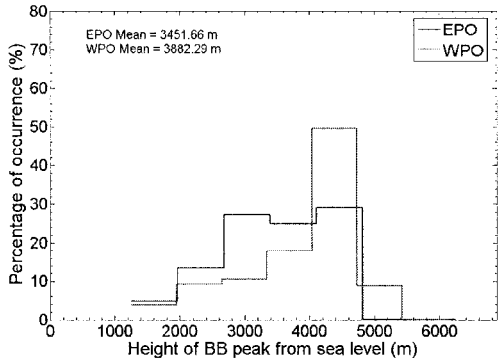

Figure 5-55. The histogram of bright band peak height of the year of 2000 over the East Pacific Ocean (EPO) and Weat Pacific Ocean (WPO).

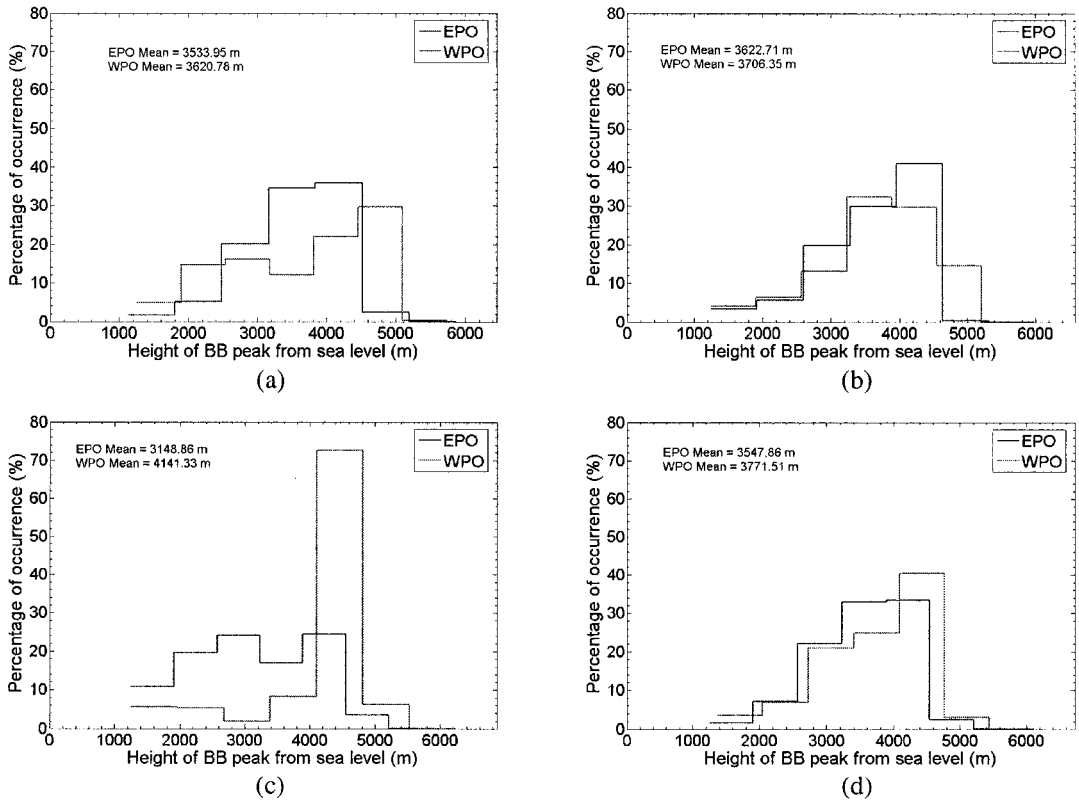

Figure 5-56 The histogram of bright band peak height from sea level over the East Pacific Ocean (EPO) and West Pacific Ocean (WPO) for the months of (a) January 2000, (b) April 2000, (c) August 2000, and (d) November 2000.

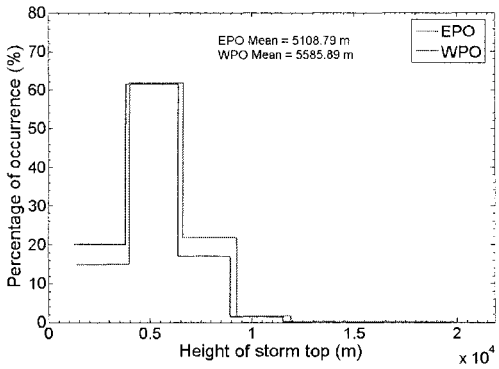

Figure 5-57. The histogram of storm top height of year 2000 over the East Pacific Ocean (EPO) and West Pacific Ocean (WPO).

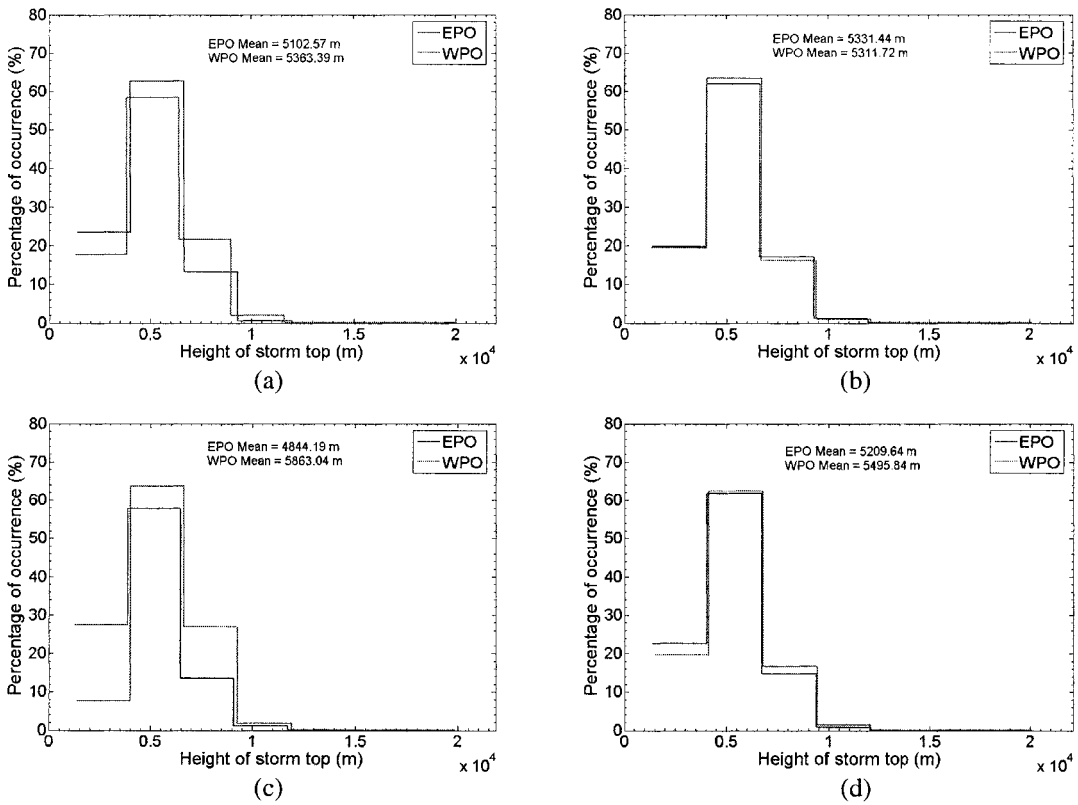

Figure 5-58. The histogram of storm top height over the East Pacific Ocean (EPO) and West Pacific Ocean (WPO) for the months of (a) January 2000, (b) April 2000, (c) August 2000, and (d) November 2000.

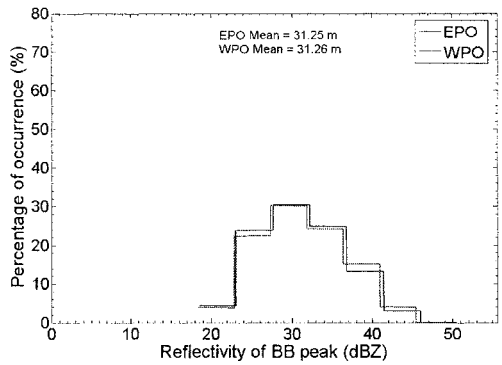

Figure 5-59. The histogram of reflectivity of BB peak of the year 2000 over the East Pacific Ocean (EPO) and West Pacific Ocean (WPO).

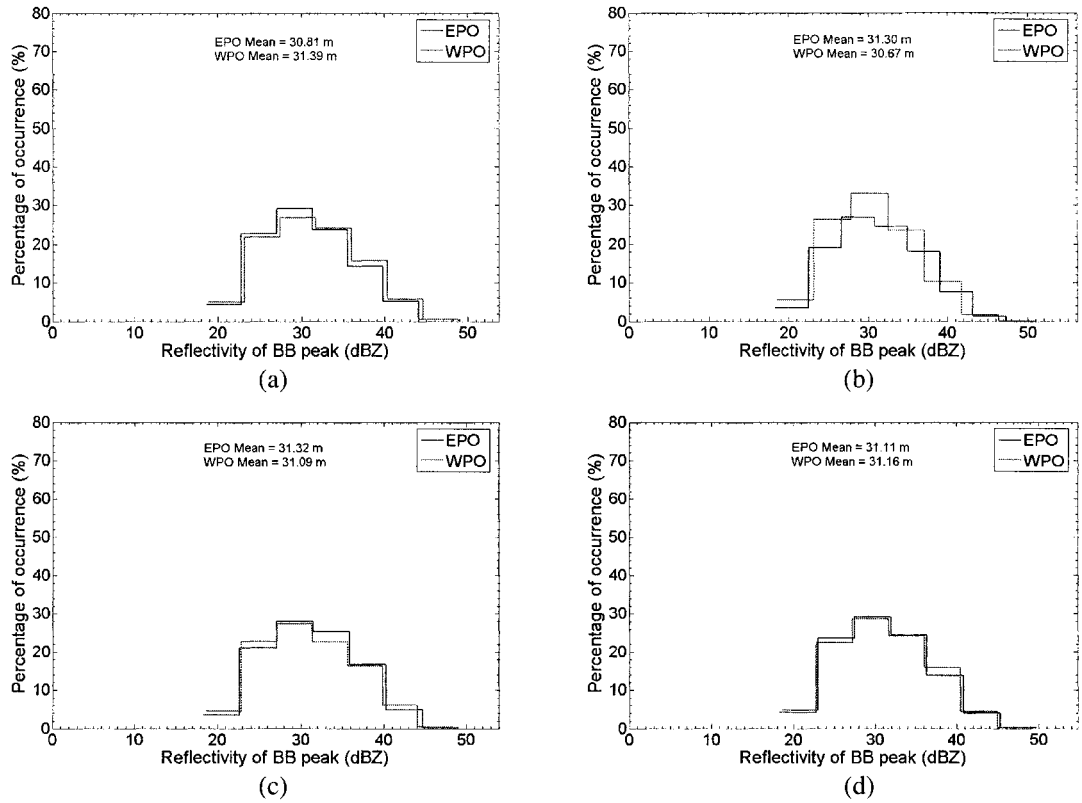

Figure 5-60. The histogram of reflectivity of BB peak over the East Pacific Ocean (EPO) and West Pacific Ocean (WPO) for the months of (a) January 2000, (b) April 2000, (c) August 2000, and (d) November 2000.

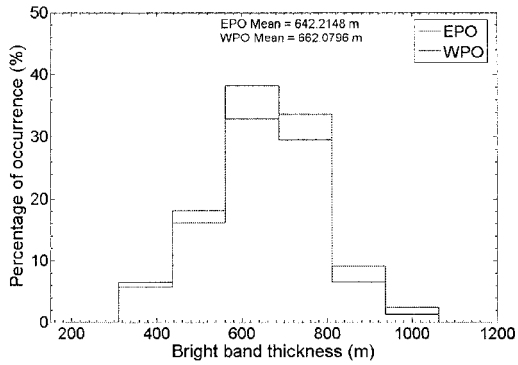

Figure 5-61. The histogram of bright band thickness of the year 2000 over the East Pacific Ocean (EPO) and West Pacific Ocean (WPO).

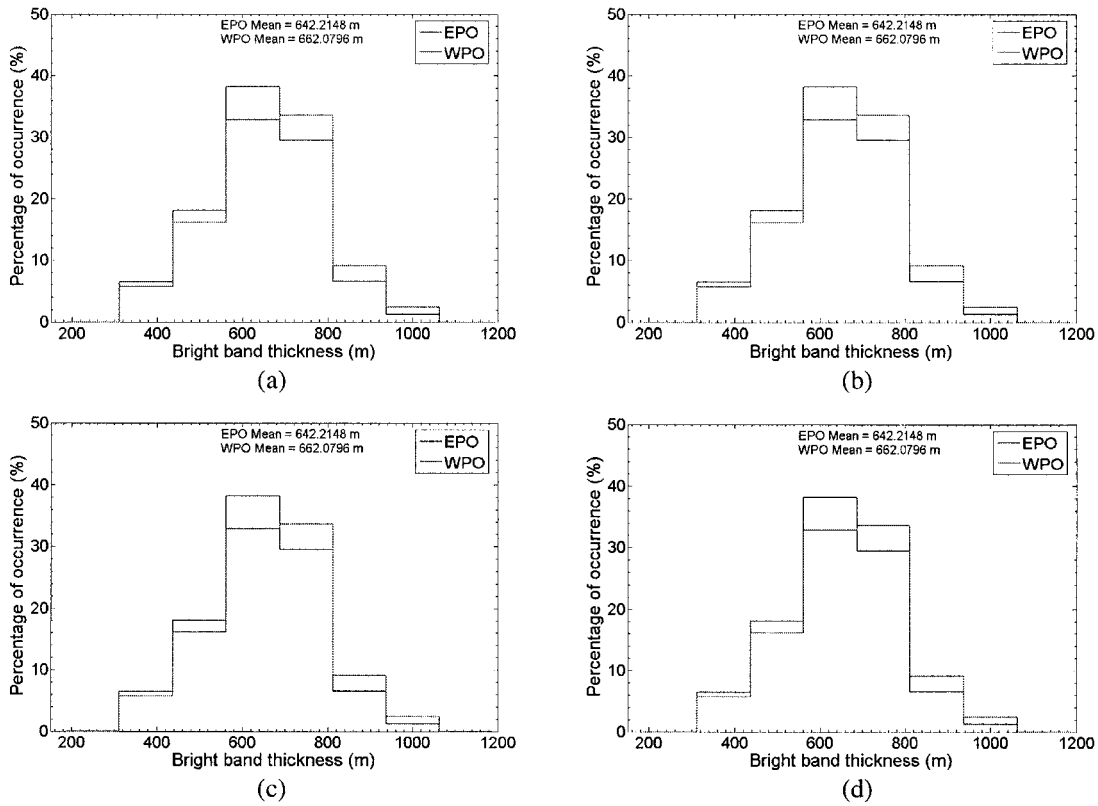

Figure 5-62. The histogram of bright band thickness over the East Pacific Ocean (EPO) and West Pacific Ocean (WPO) for the months of (a) January 2000, (b) April 2000, (c) August 2000, and (d) November 2000.

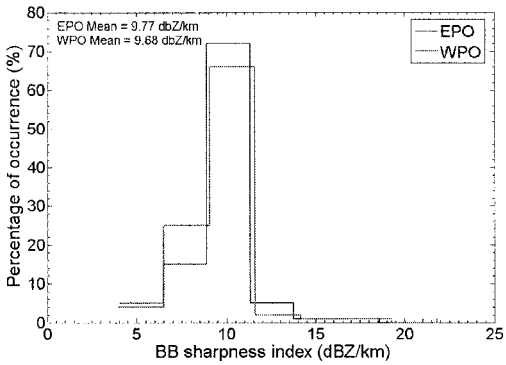

Figure 5-63. The histogram of bright band sharpness index of the year 2000 over the East Pacific Ocean (EPO) and West Pacific Ocean (WPO).

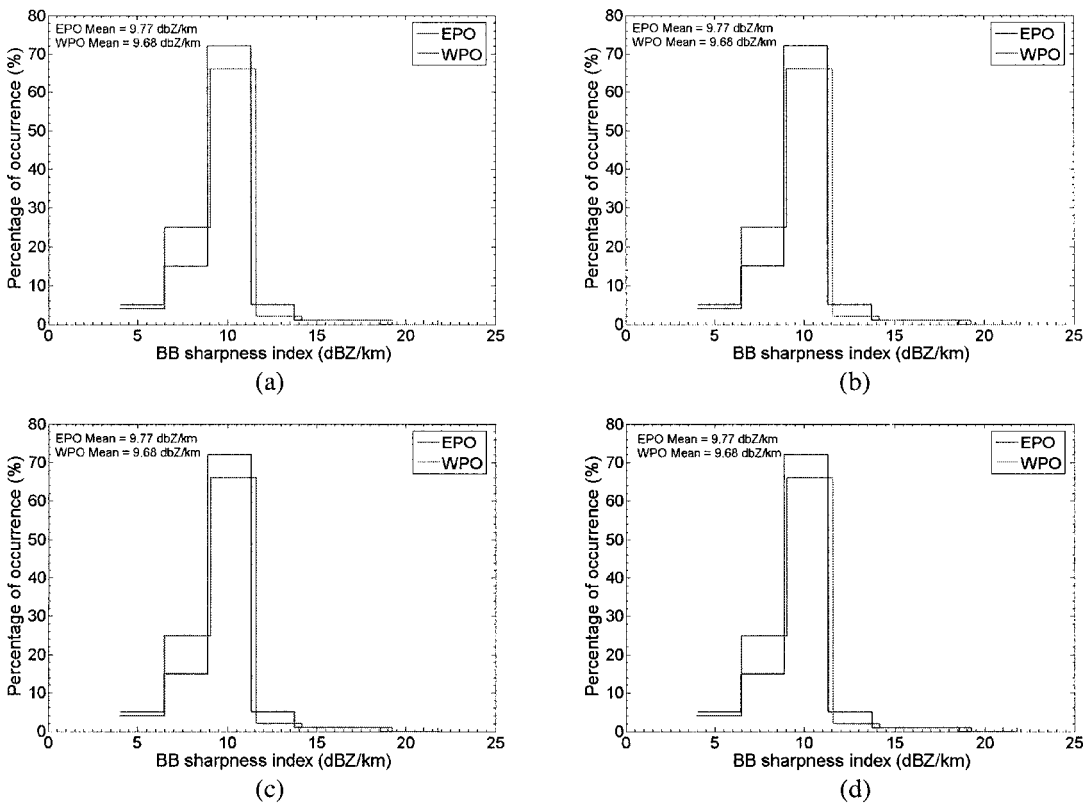

Figure 5-64. The histogram of bright sharpness index over the East Pacific Ocean (EPO) and West Pacific Ocean (WPO) for the months of (a) January 2000, (b) April 2000, (c) August 2000, and (d) November 2000.

5.3 CONCLUSION

A classification of vertical profiles of the bright band region of reflectivity from radar observations obtained by TRMM-PR using a self-organizing map is presented. The classification is used to build statistics of bright band profile characteristics in terms of bright band peak height, storm top height, bright band peak reflectivity, bright band thickness, and bright band sharpness index. The results presented in the paper show that while bright band height varies widely, the BB thickness and sharpness do not vary around the globe. There is no seasonal variation. The height of bright band may have a small effect on the reflectivity structure below the BB peak height. There are small differences above BB height between land and ocean due to the differences in their topology.

CHAPTER 6

GLOBAL STUDY OF CONVECTIVE RAIN-TYPE REFLECTIVITY STRUCTURE AS OBSERVED FROM SPACE-BORNE PRECIPITATION RADAR

6.1 INTRODUCTION

A better knowledge of the precipitation types and their radar reflectivity structures is important for understanding cloud dynamics and microphysical processes, including latent heating release, and for improving satellite precipitation algorithms. The differences in microphysics affect drop size distribution and lead to different reflectivity rain rate relationships for convective and stratiform clouds. While this approach is suitable for estimating vertical profiles of latent heating simple convective/stratiform clouds, it is not enough to address a variety of problems [23]. DSDs can vary widely within the convective and stratiform categories themselves. Recent research and proper approaches that go deeply in classifying precipitation profiles with regard to the variety of DSDs can bridge this gap.

The fundamental observation of the space-borne radar is the vertical profile. Classifying rainfall by the structure of its reflectivity field offers the potential of reducing both random and systematic errors in DSDs assumed in the rainfall retrievals. Rain type classification provides a means for exporting DSD deduced from polarimetric radars to those without polarization capability, such as the TRMM-PR, by assigning each vertical

profile the properties of the appropriate rain type.

Convective storms are identified with strong vertical velocity fields, small area horizontal dimension, and high rainfall rates [68]. Convective rain type storms are not the same around the globe. The authors in [24] show that there are weaker convective rain rates over ocean than over land. The goal of this chapter is to use the SOM classification algorithm to define a natural classification for the vertical structure profiles of the observed radar reflectivity field of convective rain type storms that potentially correspond to the microphysical variability of precipitation.

6.2 DATA CLASSIFICATION USING SOM

In this chapter, the reflectivity vertical profile with convective precipitation type from TRMM-PR are used. The data in this case consist of around 2 million vertical profiles collected during the year 2000. Each profile has 41 bins, which represent the reflectivity from the ground height up to 10 km above ground with a vertical resolution of 250 m. The data used in this research consist of 11 rays, which represent Nadir ray ±5 rays at each radar scan.

The SOM algorithm used in this chapter was trained with the batch training algorithm [46]. All maps were linearly initialized. The maps were trained in two phases: a rough training with a large initial neighborhood width equal to map size minus one, and a fine-tuning phase with a small initial neighborhood width. The neighborhood width of the SOM decreased linearly to zero, for clustering the data. The training epoch's lengths of the two phases were 20 times and 50 times the product of the two elements of the map size.

Classification using SOM for a large data set requires huge amounts of memory and the complexity increases exponentially with the number of map units. Thus, training huge maps is time-consuming and should be processed in machines with large RAM memory and high clock speed processors.

6.2.1 Case Study: Global Study of Convective VPR for Year 2000

The classification result of the convective rain type profiles for year 2000 using the (2X2) SOM algorithm is shown in Figure 6-1. Figure 6-2 shows the classification using the data collected each month separately from January, April, August, and November of the year 2000. The percentage of occurrences, the DSD parameters, and the percentage of occurrences over land as well as over ocean for these classes are listed in Table 6–1.

The percentage of occurrence for convective rain type profiles is 77% over ocean and 23% over land. The first class (1,1) has the lowest rainfall rate average, with a value equal to 2.74 mm/hr and it has the smallest D_o of all classes. This class occurs mostly over the ocean, with a percentage of 85%. The calculated value for the average N_w for classes (1,1), (1,2) and (2,1) is almost the same, with values around 4.305. The average D_o for the first 3 classes varies from 0.86 mm for the 1st class to 1.27 mm for the 2nd class and 1.09 mm for the 3rd class. The differences in D_o values are due to the differences in the reflectivity structure for these classes. The fourth class (2,2) has the highest average rainfall rate and D_o value. This class occurs over land more than other classes do. This gives an indication that the storms over land tend to have heavier rain rates than storms over oceans do. This issue will be investigated in the next section.

The seasonal variation of the classes of the SOM in Figure 6-2 is very small. This indicates that there is no seasonal variation for the convective profiles around the globe.

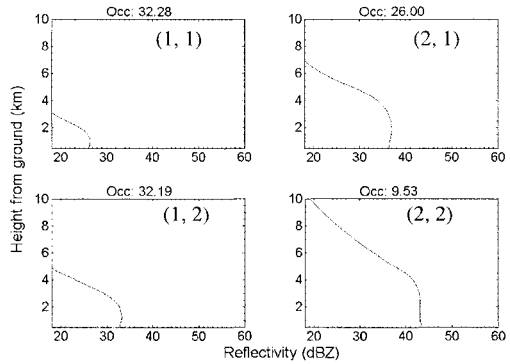

Figure 6-1. The (2X2) SOM classification result for the convective rain type reflectivity observation collected using TRMM-PR during the year 2000 around the globe. Occ is the percentage of the data set that belong to this class from the entire data set.

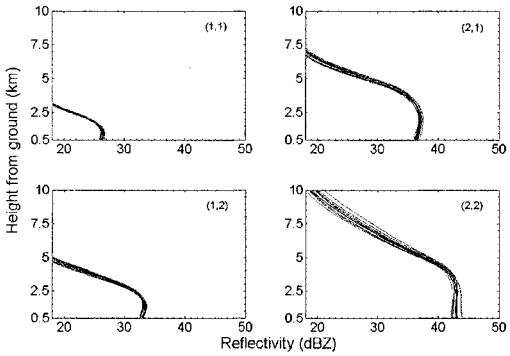

Figure 6-2. The (2X2) SOM classification result for the convective rain type reflectivity observation collected using TRMM-PR during the 12 months of year 2000 around the globe.

Table 6–1. Percentage of occurrences, D_o, N_w, rainfall rate average, percentage over land and over ocean for the (2X2) SOM classes.

Class	Occ	D_o	N_w	*RR*	Land (%)	Ocean (%)
(1,1)	32.28	0.86	4.31	2.74	15.02	84.98
(1,2)	26.00	1.24	4.30	11.97	28.51	71.49
(2,1)	32.19	1.09	4.31	6.41	20.18	79.82
(2,2)	9.53	1.66	4.04	34.69	43.94	56.06

6.2.2 Case Study: Comparison Between Convective VPR Over Land and Ocean.

A brief comparison between the VPR over land and over ocean is done using the information that is available to us from the results of the SOM classification technique. The classification of convective rain type profiles for year 2000 using (2X2) the SOM classification algorithm over land and ocean are shown in Figure 6-3. This classification is also done using the data collected for the months of January, April, August, and November of year 2000 [Figure 6-4]. The SOM classes for the convective profiles over land have a higher reflectivity structure value and a higher storm top height than the convective profiles over the ocean in all the four classes. Alternatively we can say that the percentage of profiles with high reflectivity structure value and high storm top height is higher over land than over ocean. The same conclusion can be observed if the same analysis is applied using the data collected each month separately from January, April, August, and November of year 2000.

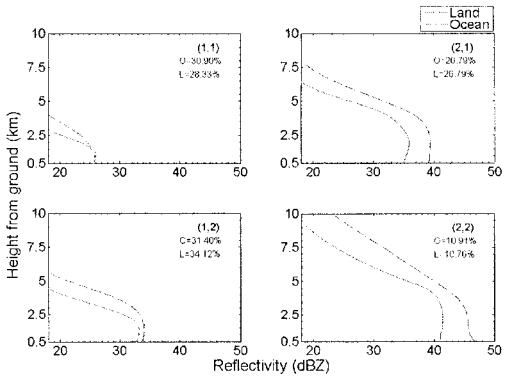

Figure 6-3. The (2X2) SOM classification results for the convective rain type reflectivity observation data collected over land and oceans. O is the total percentage of profiles over ocean and L is the total percentage of profiles over land.

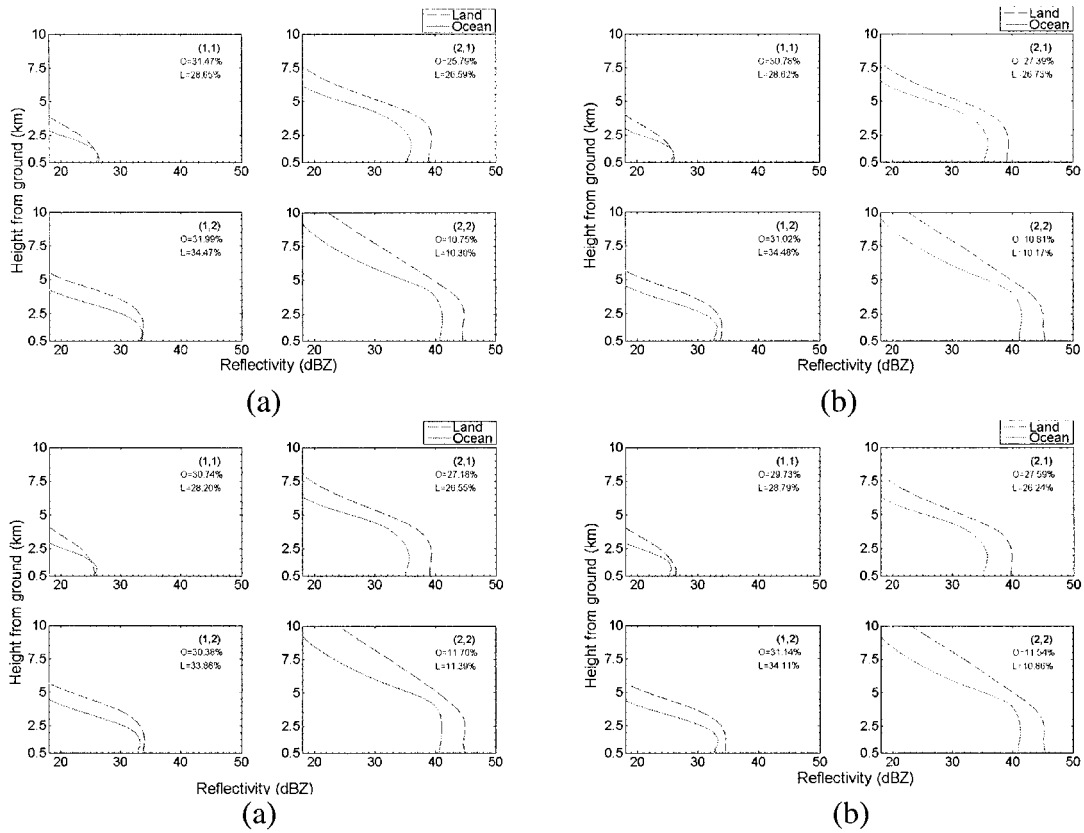

Figure 6-4. The (2X2) SOM classification results for the convective rain type reflectivity observation data collected over land and over oceans for the months of (a) January 2000, (b) April 2000, (c) August 2000, and (d) November 2000.

The average D_o value for the convective rain type reflectivity observation data over land is 1.21 mm while it is 1.08 mm over ocean. The average $\log(N_w)$ value for convective rain type reflectivity observation data over land is 4.21 while it is 4.30 over the ocean. In conclusion, the percentage of storms with a high reflectivity structure value and high storm top height over land is higher than the one over ocean.

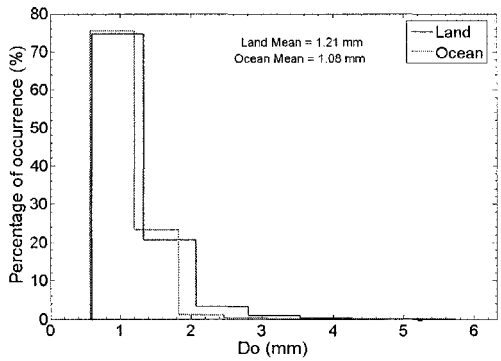

Figure 6-5. The histogram of D_o for the convective rain type reflectivity observation data over land and ocean for year 2000.

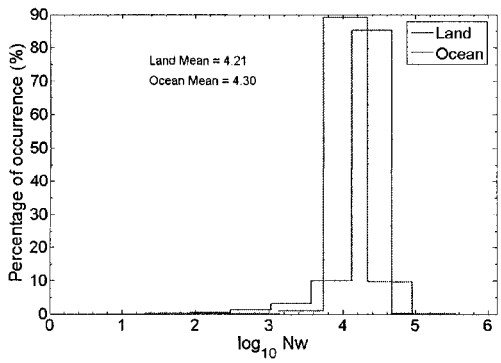

Figure 6-6. The histogram of $\log(N_w)$ for the convective rain type reflectivity observation data over land and ocean for year 2000.

6.2.3 Case Study: Comparison Between The Convective VPR over the Northern and Southern Hemispheres

A brief comparison between the VPR over the northern and over the southern hemispheres is done using information that is available to us using the results of the SOM classification. The classification of convective rain type profiles for the year 2000 using a (2X2) SOM over the northern and the southern hemispheres is shown in Figure 6-7. The results of the same classification are done using data collected each month separately from January, April, August, and November for year 2000 [Figure 6-8].

The comparison between the classes of the data over the northern and southern hemispheres indicates that there is not a large difference in the reflectivity structure. Most classes of the (2X2) SOM classification algorithm of convective rain type profiles over the northern hemisphere have a lower reflectivity value near the ground than the profiles over the southern hemispheres do. The height of storm top height for the northern hemisphere profiles is higher by a few hundred meters than the southern hemisphere profiles. These small differences in reflectivity structure may be due to the percentage of storms over land in the northern hemisphere, 24%, while it is 19% over the southern hemisphere. This can also describe the difference in storm top height between the northern and southern hemispheres data. The difference in reflectivity value near the ground between rain profiles over the northern and southern hemispheres may be due to the difference in average freezing height. The northern hemisphere average freezing height is equal to 3938 m while it is 3387 m over the southern hemisphere. This also may indicate differences in rainfall rate near the ground between the two cases. Figure 6-8 shows that there are seasonal differences between storms over the northern and southern

hemispheres. This is expected due to the big temperature differences between the northern and southern temperature during the summer and winter seasons.

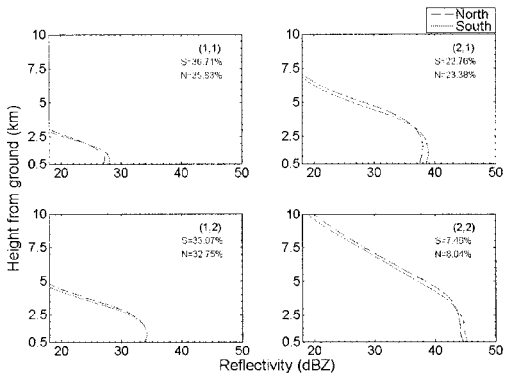

Figure 6-7. The (2X2) SOM classification results for the convective rain type reflectivity observation collected over the northern and southern hemispheres. S is the total percentage of the profiles over the southern hemisphere and N is the total percentage of the profiles over the northern hemisphere.

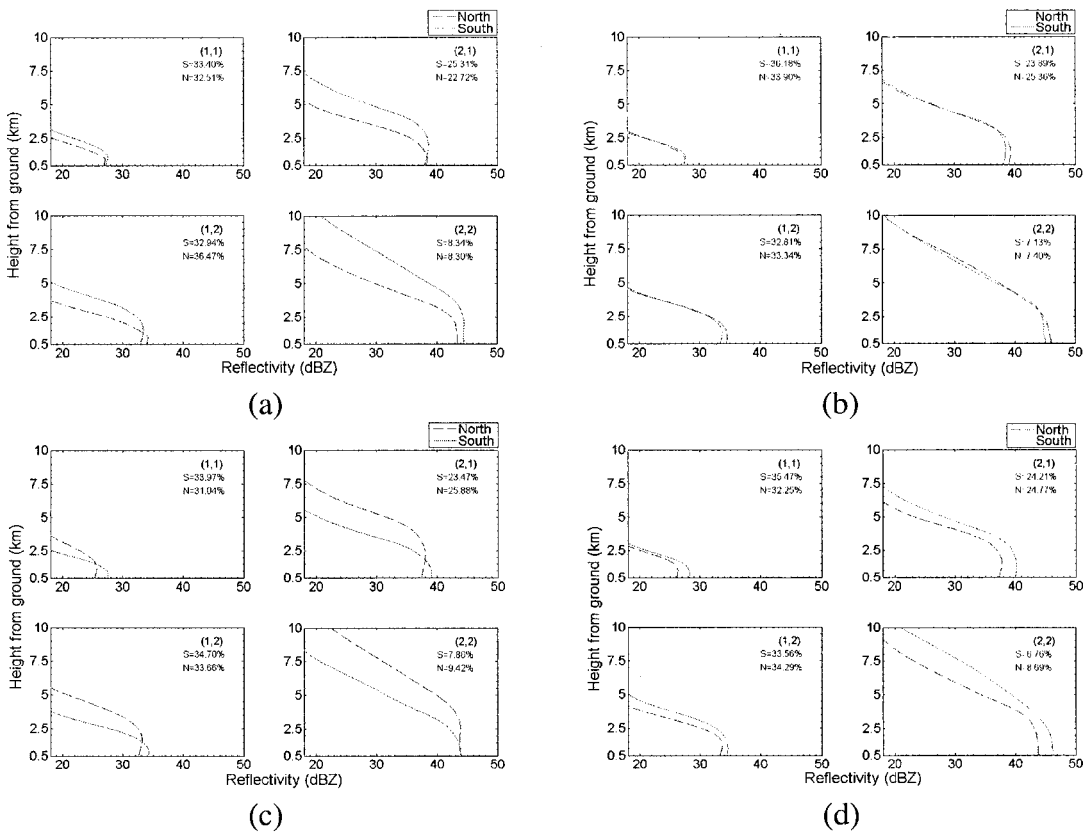

Figure 6-8. The (2X2) SOM classification results for the convective rain type reflectivity observation collected over the northern and southern hemispheres for the months of (a) January 2000, (b) April 2000, (c) August 2000, and (d) November 2000.

6.2.4 Case Study: Comparison Between Convective VPR Over East and West Pacific Ocean.

A brief comparison between the convective vertical profiles over the East and West Pacific Ocean is done using information that is available to us from the results of the SOM classification. The (2X2) SOM classification algorithm of the convective rain type VPR for the year 2000 over the East and West Pacific Ocean are shown in Figure 6-9. This classification is also done using the data collected each month separately from January, April, August, and November of year 2000 as shown in

Figure 5-14. The SOM classes for the convective profiles over the East and West Pacific Ocean have a very similar reflectivity structure. There is a small difference in the height of the storm top for the data from the year 2000 and each month between the East and West Pacific Ocean. The figures show that the East Pacific Ocean storms have a lower storm top height than the West Pacific Ocean storms. This is due to the fact that the East Pacific Ocean has a colder sea surface temperature than the West Pacific Ocean. The percentage of shallow precipitation, which is represented by class (1, 1) in Figure 6-9 for the East Pacific Ocean, is 31.4%, while it is 28.74% for the West Pacific Ocean. This finding agrees with the results found by Janowiak et al. in [69] and Berg in [12][70], where they found evidence that the East Pacific has shallower precipitation.

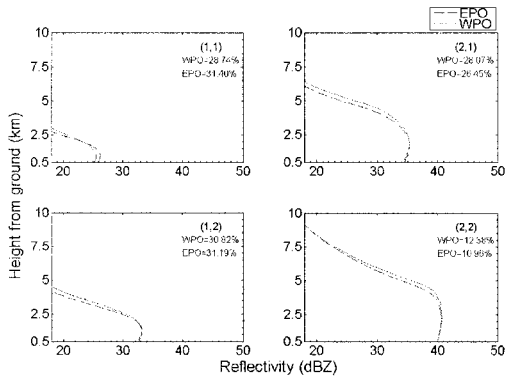

Figure 6-9. The (2X2) SOM classification results for the convective rain type reflectivity observation collected over the East and West Pacific Ocean. WPO is the total percentage of the profiles over the west Pacific Ocean and EPO is the total percentage of the profiles over the East Pacific Ocean.

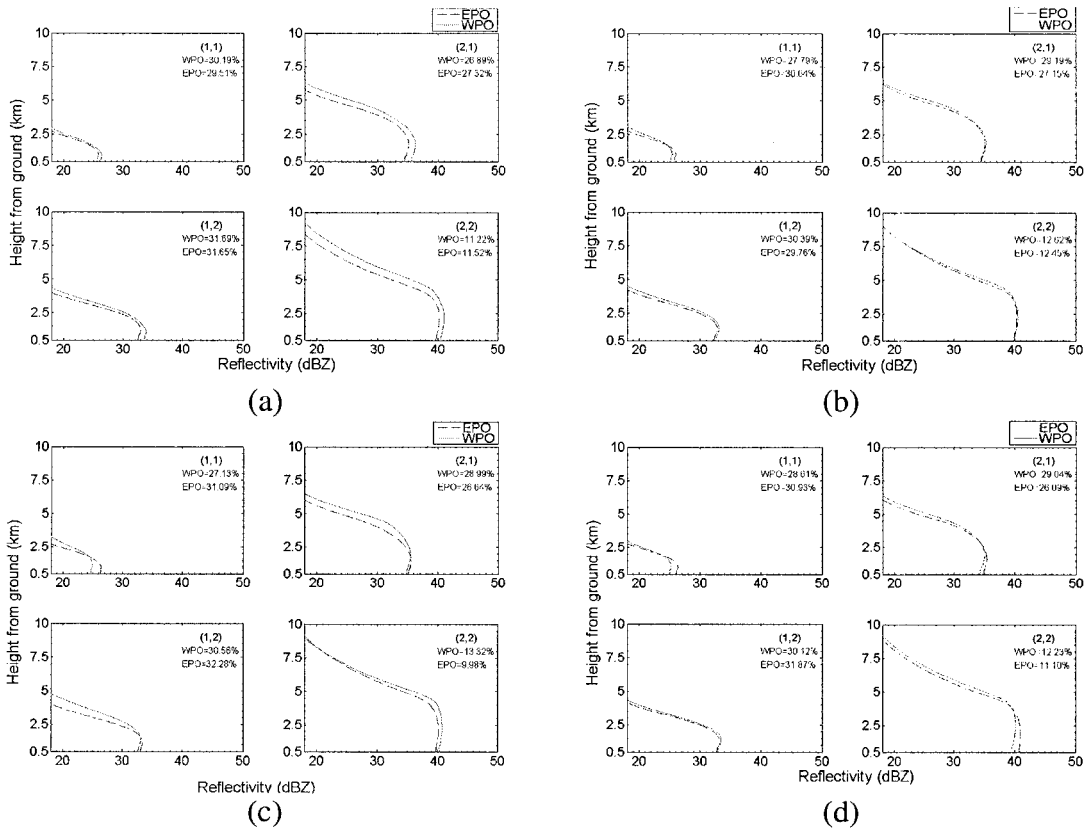

Figure 6-10. The (2X2) SOM classification results for the convective rain type reflectivity observation collected over the East and West Pacific Ocean for the months of (a) January 2000, (b) April 2000, (c) August 2000, and (d) November 2000.

6.3 CONCLUSION

Using convective rain type TRMM-PR data from across the Tropics for the year 2000, we have determined percentage of occurrences, the DSD parameters and the percentage of occurrences over land and ocean for the SOM classes. Each of these quantities is useful to large-scale studies of tropical precipitation and atmospheric circulation.

The percentage of occurrence for convective rain type profiles is 77% over ocean and 23% over land. Convective rain reflectivity structure behaves differently over land and ocean. Convective rain rates attain greater values over land, consistent with studies showing that convection over land is stronger on average than over ocean in terms of updraft strength, and reflectivity profiles. The convective rain reflectivity structure over ocean is a more uniform in term of seasonal cycle than over land. The comparison between the convective VPR over the northern and the southern hemispheres show obvious seasonal cycle. The comparison between the convective VPR over the east and the west Pacific Ocean show similar class structures around the year.

6.4 HURRICANE STRUCTURE USING SOM

Satellite-based retrievals offer a good source of hurricane observations over oceans. Using vertical structure of rain systems observed with the TRMM-PR, we attempt to investigate the properties of vertical profile rain data over different hurricane cases. Comparison is done with hurricane cases data collected over oceans. Figure 6-11 shows the plot of reflectivity observations at 2 km above ground for radar observations over hurricane storms that are listed in Table 6–2. These cases are collected from a 3-years period from August 22, 1998, to May 28, 2001. The hurricane reflectivity structure will be studied using the SOM classification result of BB region of stratiform rain type profiles and convective region profiles separately.

6.4.1 CASE STUDY: REFLECTIVITY STRUCTURE OF BB REGION AT HURRICANE PROFILES.

Figure 6-12 shows the (2X2) SOM for stratiform with BB rain type reflectivity observation collected for storms over hurricanes that are listed in Table 6–2 and compared with results of the SOM of data collected over oceans for the month of September for the year 2000. The percentage for hurricane data in class (1, 2) and (2, 2) is more than oceanic data. Figure 6-13 shows the (5X5) SOM classification classes for stratiform rain type with BB region reflectivity observation collected over hurricane regions and over oceans. This figure shows that the percentage for the high reflectivity structure for hurricane cases is more than for the ocean cases. Figure 6-14 (a)-(e) show the histogram of the bright band peak height from sea level, the storm top height, the reflectivity of BB peak, the BB thickness, and the BB sharpness index for the stratiform rain type with BB collected using TRMM-PR for hurricane data and oceanic data. The analysis demonstrates that the percentage of bright band reflectivity structure with high

reflectivity structure value for hurricane data is higher than for the oceanic data. The SOM classification result of near ground height hurricane reflectivity structure data are higher than the oceanic data. This gives an indication that the hurricane storms have more rainfall rate near the ground.

Table 6–2. List of hurricane cases used in this case study.

Case #	Hurricane Name	Date	Orbit	Scan #
1	Hurricane Bonnie	August 22, 1998	4224	5650-5850
2	Hurricane Alley	September 2, 1998	4391	2700-2900 3200-3400 3730-4000 4200-4420
3	Hurricane Georges	September 27, 1998	4792	3500-3700
4	Hurricane Mitch	October 27, 1998	5254	2900-3100
5	Hurricane Dennis	August 27, 1999	10055	3550-3700
6	Hurricane Floyd	September 13, 1999	10321	3600-3800
7	Hurricane Gert	September 16, 1999	10367	5950-6150
8	Hurricane Alberto	August 8, 2000	15522	5900-6100
9	Hurricane Florence	September 13, 2000	16094	6450-6650
10	Hurricane Keith	October 5, 2000	16435	5900-6050
11	Hurricane Adolph	May 28, 2001	20140	6150-6350

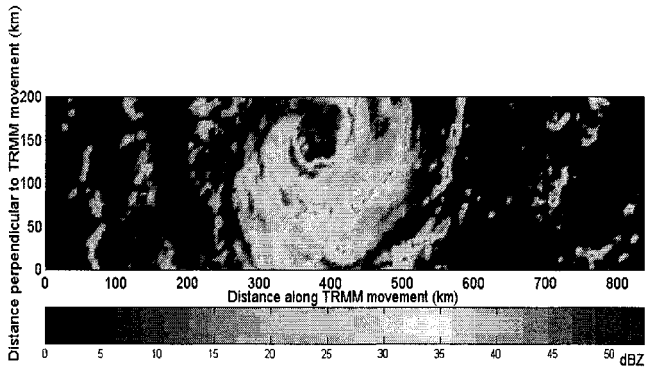

(a)

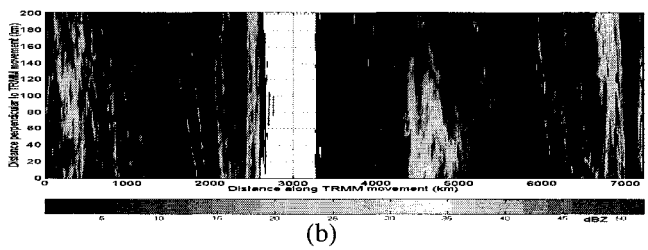

(b)

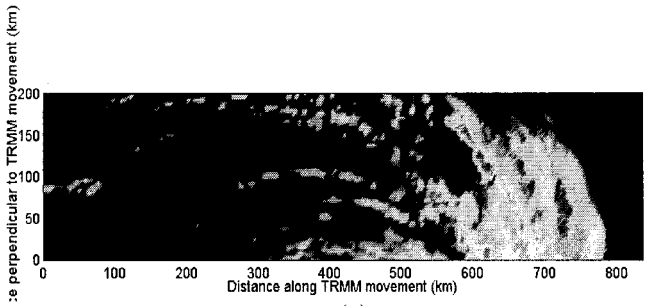

(c)

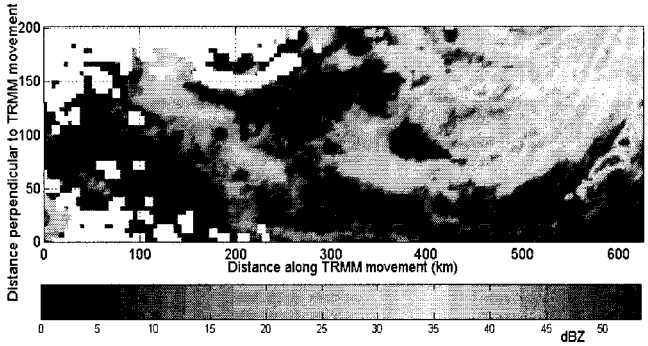

(d)

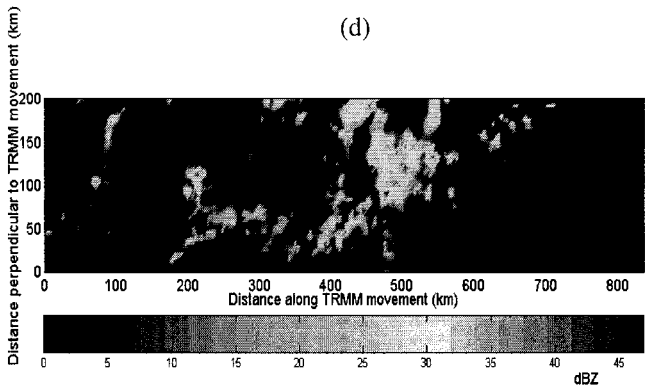

(e)

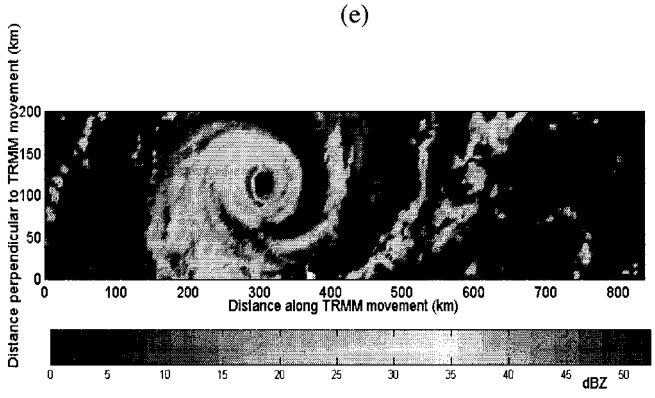

(f)

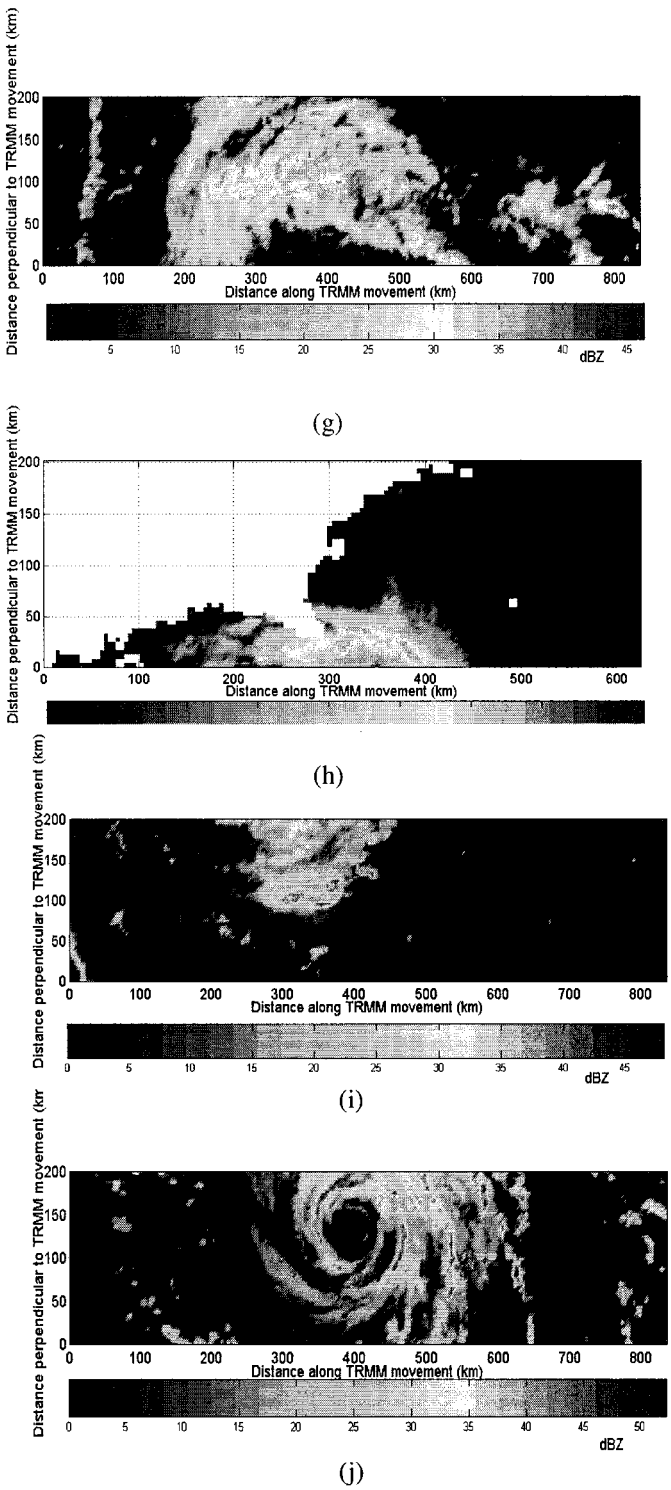

Figure 6-11. (a) – (j), The plot of TRMM-PR rain reflectivity at 2 km above ground for the hurricane cases 1 – 11 listed in Table 6–2.

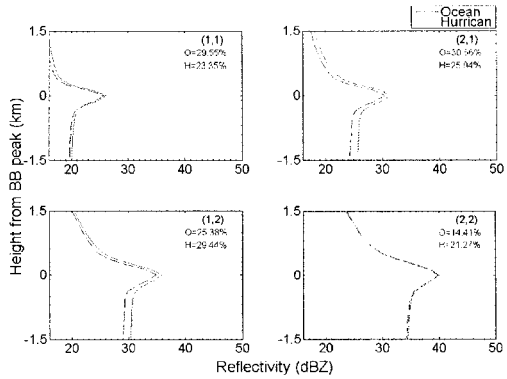

Figure 6-12. The (2X2) SOM classification results for stratiform with BB rain type reflectivity observation collected over hurricane (H) regions and over ocean (O).

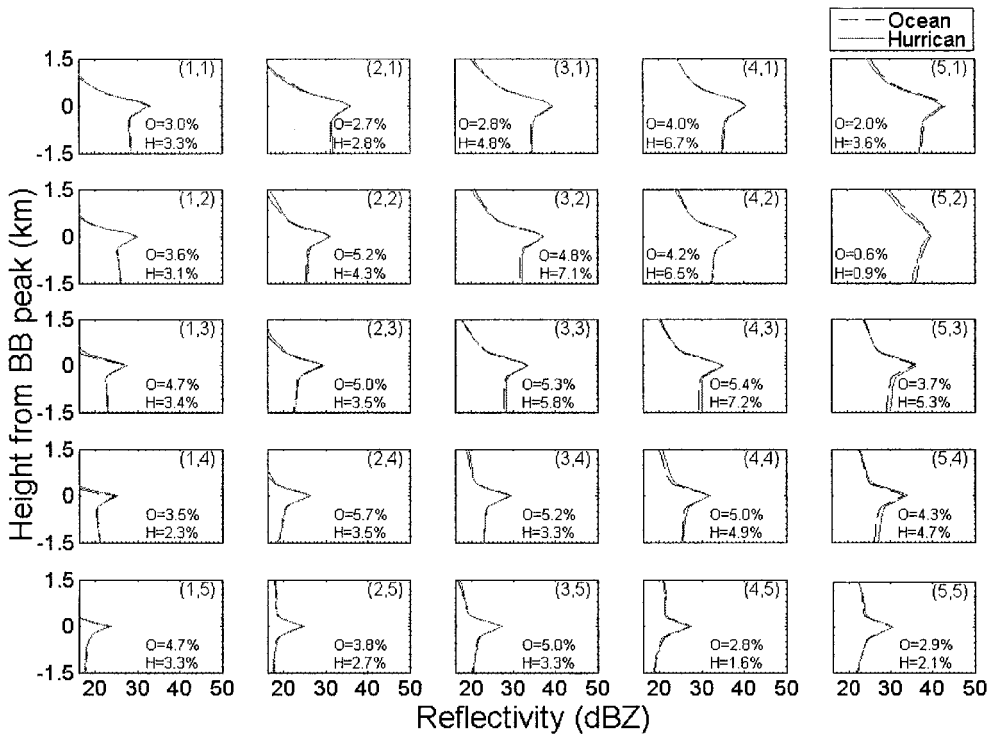

Figure 6-13. The (5X5) SOM classification results for stratiform with BB rain type reflectivity observation collected over hurricane (H) regions and over ocean (O).

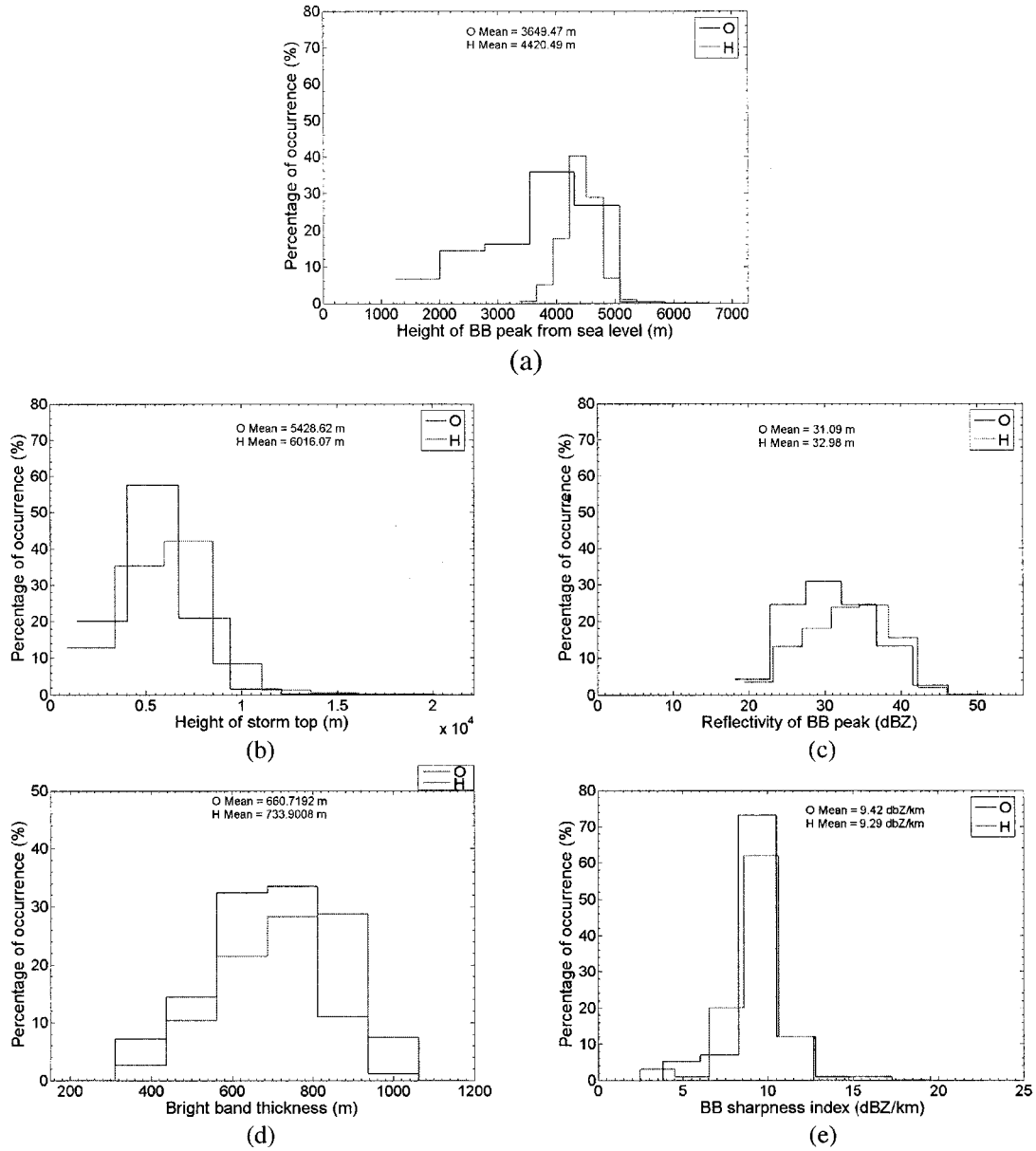

Figure 6-14. The histogram of stratiform rain type with BB profiles over hurrican cases (H) and over ocean , (O) of (a) the bright band peak height from sea level. (b) the storm top height. (c) the reflectivity of BB peak. (d) the BB thickness. (e) the BB sharpness index.

6.4.2 CASE STUDY: HURRICANE STORMS REFLECTIVITY STRUCTURE CONVECTIVE RAIN TYPE.

Figure 6-15 shows the (2X2) SOM for convective rain type reflectivity observation collected over hurricane regions and over oceans. The percentage of class (2, 1) and (2, 2) is more for hurricane cases listed in Table 6–2 than for ocean cases. Figure 6-16 shows the (4X4) SOM classification results for the convective rain type reflectivity observations collected over hurricane regions and over oceans. It shows that the percentage for high reflectivity structure for the hurricane cases is more than for the oceanic cases. It is also shows that reflectivity between 0.5 km to 2 km is higher in hurricane cases than the oceanic cases, which indicates a greater rainfall rate near the ground for hurricane cases. Figure 6-17 shows the histogram of D_o for convective storms over hurricane regions and over oceans. Figure 6-18 shows the histogram of N_w for convective storms over hurricane regions and over oceans. It appears that there are some differences in the reflectivity structure of the SOM near the ground which have a large effect on the rainfall rate between the two cases. There are small differences above and below the BB height between hurricane and oceans due to the high percentage of profiles with high reflectivity value in hurricane cases.

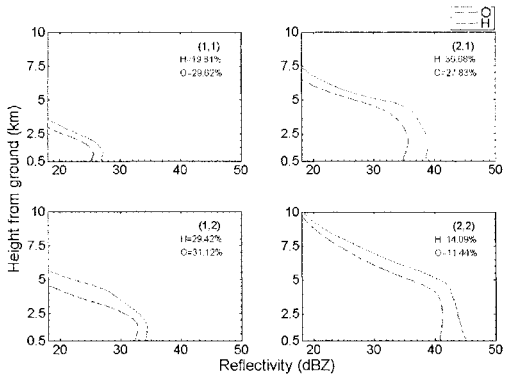

Figure 6-15. The (2X2) SOM classification results for convective rain type reflectivity observation collected over hurricane regions and over oceans. H is the total percentage of profiles over hurricane regions and O is the total percentage of profiles over oceans.

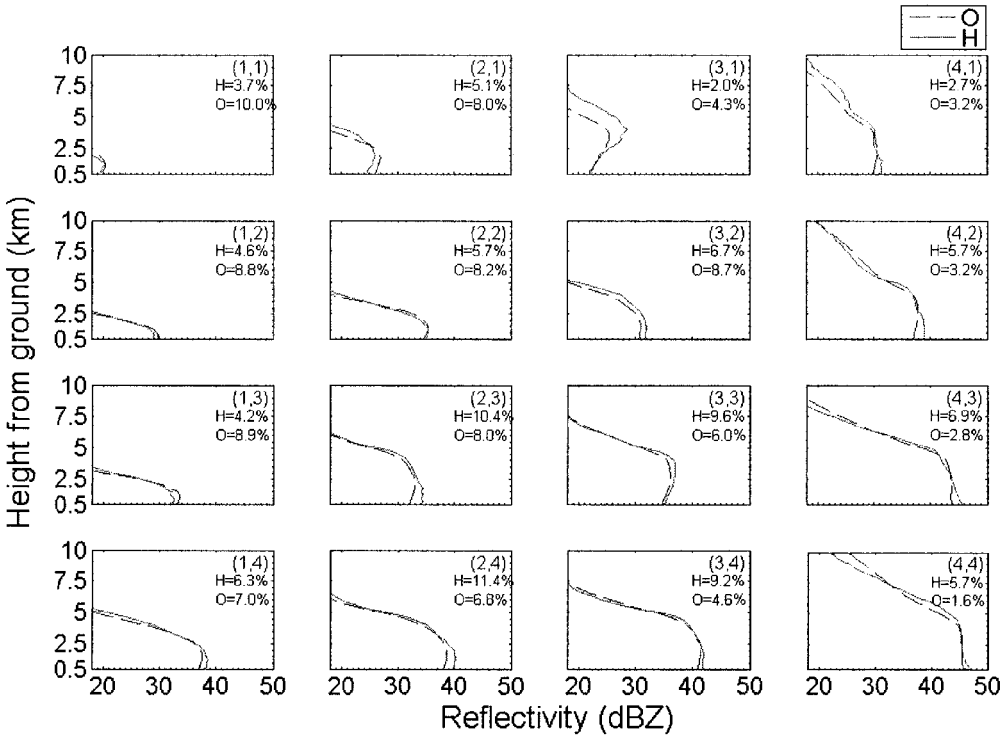

Figure 6-16. The (4X4) SOM classification result for convective rain type reflectivity observation collected over the hurricane region and over oceans. H is the total percentage of profiles over the hurricane regions and O is the total percentage of profiles over oceans.

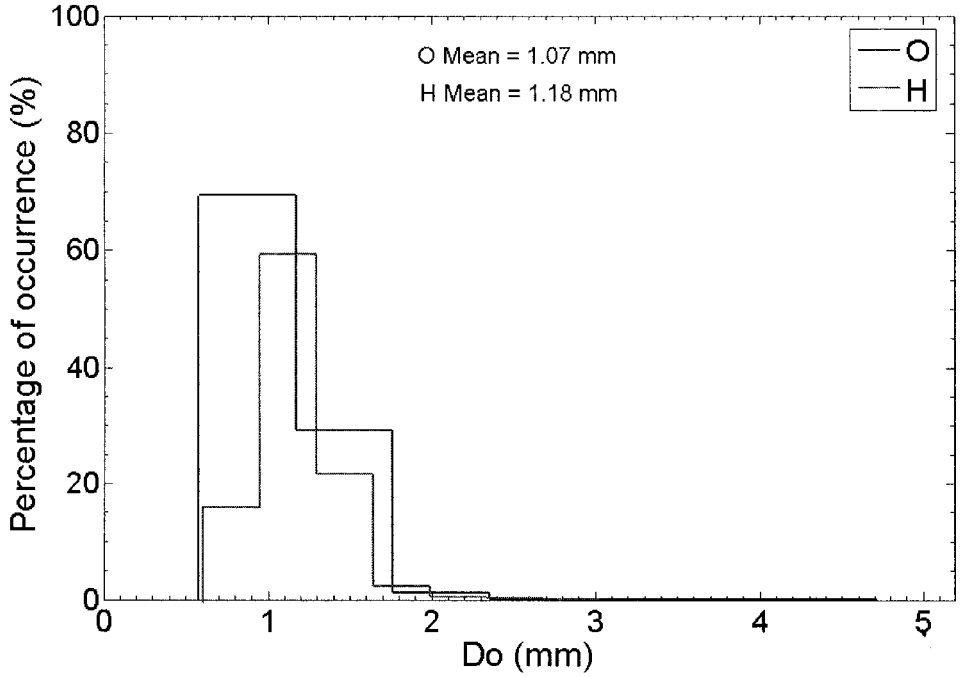

Figure 6-17. The histogram of D_o for convective storms over hurricane regions and over oceans.

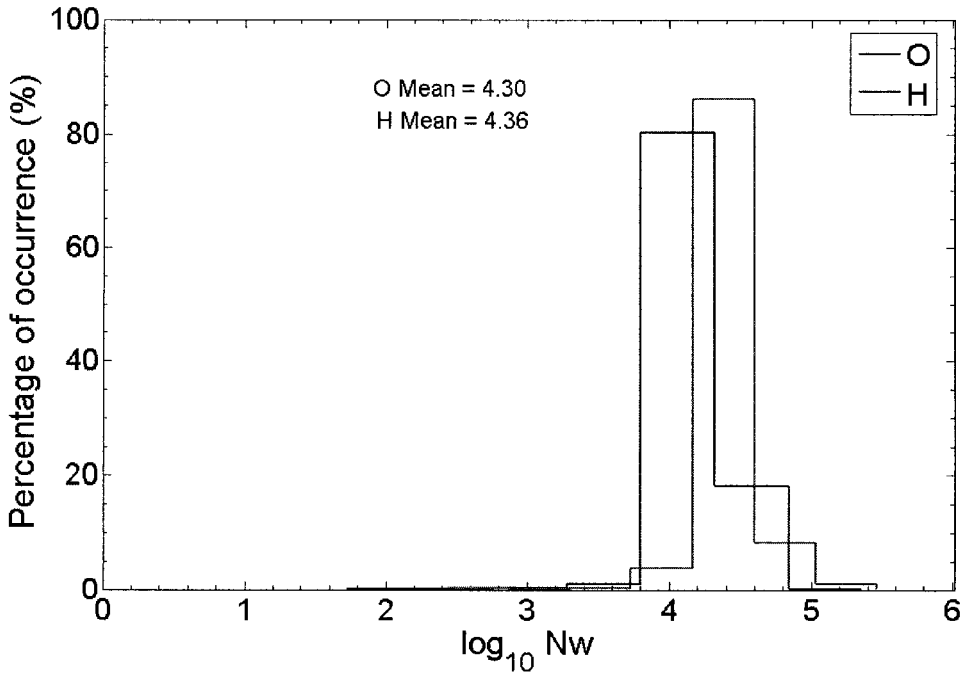

Figure 6-18. The histogram of $\log(N_w)$ for convective storms over hurricane regions and over oceans.

6.5 CONCLUSION

Studying the convective rain type profiles around the globe shows no seasonal difference. The comparison of the convective rain type for storms over land and over ocean indicates that the percentage of profiles with high reflectivity value and storm top height is larger over land than over ocean. This conclusion is the same for all seasons.

The comparison of the convective rain type for storms over the northern and southern hemispheres for the entire data set of year 2000 indicates no difference. There are significant seasonal differences between the northern and southern hemispheres due to the differences in the temperature of both seasons.

The comparison of the convective rain type for storms over the East and West Pacific Ocean indicates a small difference in the reflectivity structure of the SOM classes. Precipitation systems in the East Pacific were shallower than those in the West Pacific, and had a lower storm top height. This is due to the fact that the East Pacific Ocean has colder sea surface temperatures than the West Pacific Ocean.

In addition, the analysis demonstrates that the percentage of bright band reflectivity structure with high reflectivity structure value for hurricane data is larger than the ocean data. The SOM classification results of the hurricane reflectivity structure data are larger at the area near the ground height than the ocean data. This gives an indication that the hurricane storms have more rainfall rate near the ground.

The percentage for the high reflectivity structure for the hurricane cases is more than for the ocean cases. It also shows that reflectivity between 0.5 km to 2 km is higher in the hurricane cases than the profiles over the oceans which indicates a higher rainfall rate near the ground for the hurricane cases.

CHAPTER 7

ESTIMATION OF RAINDROP SIZE DISTRIBUTION FROM SPACE-BORNE RADAR OBSERVATIONS

7.1 INTRODUCTION

Specific attenuation in precipitation is mainly due to absorption at high frequencies and is relative to the volume of rain. The reflectivity of a rain profile is relative to the sixth power of raindrop sizes. A physical explanation of the variability in the $k-Z$ relation can be provided with the normalized drop size distributions. To retrieve the DSD parameters, the relation between specific attenuation and reflectivity is used. Using TRMM-PR observation, this chapter explains the method used to estimate the DSD parameters from the reflectivity and attenuation measurements.

The TRMM-PR-based DSD retrieval algorithms are used to generate monthly maps of the DSD around the globe. Preliminary analysis of the DSD is used to estimate the mean difference in D_o over land as well as over ocean, classified into convective/stratiform-type precipitation. The global distribution of DSD parameters is critically important for development of retrieval algorithms used by the Global Precipitation Mission Radiometers (GPM).

7.2 RAINDROP SIZE DISTRIBUTION (DSD)

The raindrop size distribution (DSD) plays an important role in defining the radar parameters such as the reflectivity factor (Z), the differential reflectivity (Z_{dr}) and the specific differential phase (k_{dp}) [61].

A Gamma model can describe the most variability in the DSD [60] and the DSD can take the following form:

$$N(D) = N_0 D^{\mu} \exp(-\Lambda D) \ \ mm^{-1}m^{-3} \tag{22}$$

where $N(D)$ is the distribution of raindrops per diameter interval D to $D + \Delta D$ (mm), $N_0\left(mm^{-1-\mu}m^{-3}\right)$ is the intercept parameter, μ is the shape parameter, and Λ is the slope of the exponential. The normalized and scaled Gamma DSD can be written as

$$N(D) = N_w f(\mu)\left(\frac{D}{D_0}\right)^{\mu} \exp(-\Lambda D) \tag{23}$$

where

$$f(\mu) = \frac{6(3.67+\mu)^{\mu+4}}{3.67^4\Gamma(\mu+4)} \tag{24}$$

where μ is the shape factor, and N_w is the equivalent intercept parameter of an exponential distribution, such that both the DSDs have the same water content. N_w has units of $mm^{-1}m^{-3}$. To provide a physical basis for the reflectivity rainfall relationship, the concept of normalized gamma DSD has been used [61][62]. In the next section, we will describe the algorithm for estimating a vertical profile of D_o and path averaged N_w from TRMM-PR parameters.

7.3 ESTIMATION OF RAINDROP SIZE DISTRIBUTION (DSD) PARAMETERS FROM TRMM-PR MEASUREMENTS

Typically, the relation between specific attenuation and reflectivity has been parameterized as a power law of the form:

$$k = \alpha Z^{\beta} \tag{25}$$

The parameters α and β can be vary depending on the DSD. The normalized attenuation and reflectivity can be related based on the concept of normalized DSD, as in [60][61] and the following:

$$\left(\frac{k}{N_w}\right) = \tilde{\alpha}\left(\frac{Z}{N_w}\right)^{\beta} \tag{26}$$

The parameter α is adjusted based on the measurement of the path-integrated attenuation (PIA) obtained using the surface cross-section as a data reference point, and is commonly known as the "α adjustment" method [63]. The Hitschfeld-Bordan method [64] is used if the surface reference is totally ignored and the $k-Z$ parameterization is taken as exact. It has been shown in [65] that the scatter plot of k/N_w versus Z/N_w at TRMM-PR frequency for widely varying DSD parameters ($3 \le \log(N_w) \le 5, 0.5 \le D_0 \le 3.5$ and $-1 \le \mu \le 5$) can be approximated by a straight line for $\log(k/N_w)$ versus $\log(Z/N_w)$ [Figure 7-1]. This justifies the parameterization given by (26), and equation (26) can be rewritten as

$$k = \tilde{\alpha}(N_w)^{1-\beta} Z^{\beta} = \alpha Z^{\beta} \tag{27}$$

Equation (27) shows that changes in α can be attributed to changes in N_w, where α and $\tilde{\alpha}$ are related by

$$\alpha = \tilde{\alpha}(N_w)^{1-\beta} \tag{28}$$

and

$$N_w = \left(\frac{\alpha}{\tilde{\alpha}}\right)^{\frac{1}{1-\beta}} \tag{29}$$

Equation 28 provides the physical basis for attributing changes in α to changes in N_w while keeping β fixed. The TRMM-PR uses the surface reference method to provide an estimate of the PIA. Subsequently, the PIA estimate is used to obtain an equivalent α that will be consistent with the estimate of the PIA from Hitschfeld-Bordan method and the prevailing vertical reflectivity profile [63]. To determine the attenuation correction, the TRMM program uses a weighted combination of the α adjustment procedure and Hitschfeld-Bordan algorithms [63][64]. When the surface reference is not reliable due to light rainfall, then the Hitschfeld-Bordan algorithm is used. TRMM uses a hybrid method between the two algorithms.

The attenuation correction starts with (α_{ini}) to estimate PIA. Subsequently, based on comparison with the surface reference technique, the α_{ini} is adjusted as [66]

$$\alpha_{adj} = \alpha_{ini}\varepsilon_0 \tag{30}$$

The final adjustment factor ε_f and the surface reference-based adjustment factor ε_0 are related by

$$\varepsilon_0 = 1 - \left[\frac{1-\varepsilon_f}{W}\right] \tag{31}$$

Where W is the weight factor [66].

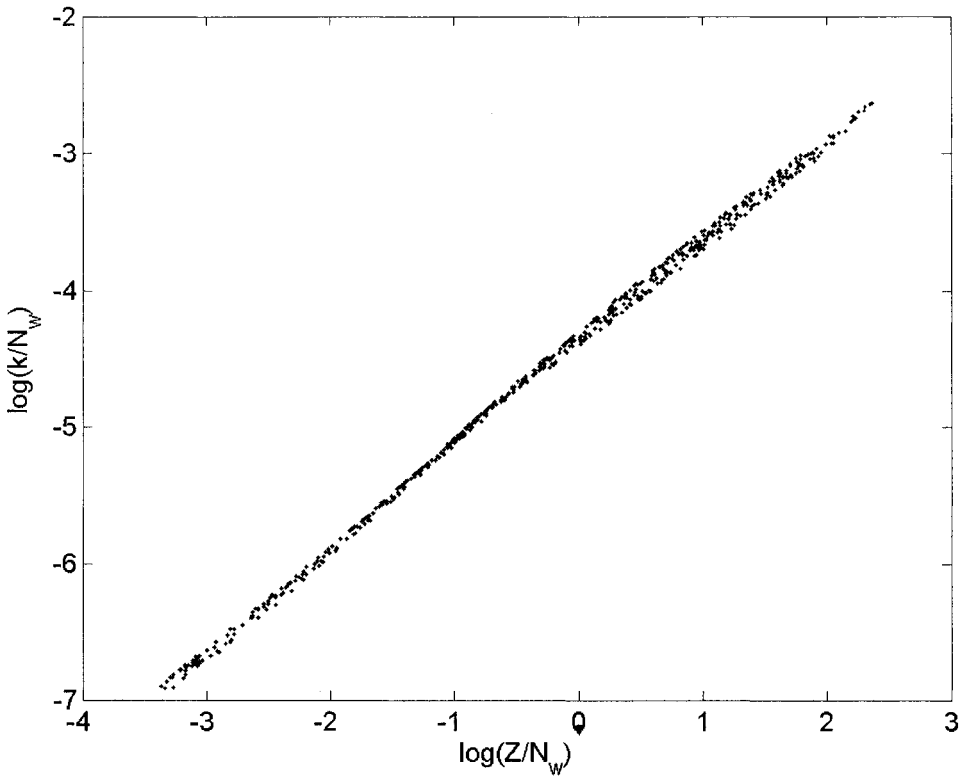

Figure 7-1 The scatter plot of k/N_w versus Z/N_w at TRMM-PR frequency for widely varying DSD parameters *(3≤log(Nw)≤5, 0.5≤D0≤3.5 and -1≤μ≤5)* can be approximated by a straight line for $\log(k/N_w)$ versus $\log(Z/N_w)$

Once α_{adj} is calculated then N_w can be retrieved from Equation (10). The median volume diameter, D_0, can be subsequently obtained as

$$D_0 \approx \left[\frac{Z}{N_w C}\right]^{\frac{1}{7}} \tag{32}$$

where C is given by

$$C = \frac{f(\mu)\Gamma(7+\mu)}{(3.67+\mu)^{7+\mu}} \tag{33}$$

The above equation assumes that reflectivity varies as D^6. However TRMM, operates at 13.8 GHz, and modeling the scattering without Rayleigh approximation yields

$$D_0 \approx \left[\frac{Z}{N_w C}\right]^{\frac{1}{7.5}} \tag{34}$$

which is used in this research. Meneghini et al. [67] show that the surface cross-section can be estimated to an accuracy of a fraction of a dB over an ocean, whereas the same varies by several dB over land. TRMM-PR uses a hybrid scheme to estimate the surface reference reflectivity [48][66], so that the PIA can be estimated to the best possible accuracy. In order to strike a compromise between the accuracy of the surface reference method and the Hitschfeld-Borden method, TRMM-PR algorithms use ε_f. Whenever the weight factor is close to zero, the surface reference is not relied upon significantly. If the SRT is unreliable, or if it is not used, then the PR does not provide independent estimates of the DSD parameters. In the absence of a reliable independent estimate of PIA, the PR algorithm uses k-Z relationships (one for stratiform rain and one for convective) that are based on surface disdrometer measurements from various locations within the TRMM coverage area.

7.4 DATA ANALYSIS OF DSD ON GLOBAL SCALE USING SOM

7.4.1 CASE STUDY: MONTHLY MAPS OF DSD PARAMETERS.

TRMM-PR observations to estimate the vertical profile of D_o and an average N_w estimate were described in the previous section. It was shown that the retrievals are based on results from the α adjustment procedure. However the α adjustment procedure based on the surface reference is most useful only in large attenuation scenarios. There are two ways to address this problem. One way is to use the ε_o value from the α adjustment procedure, whenever it is reliable, and use α_{ini} whenever the "α adjustment" procedure is

not reliable. This procedure was used by [65] to obtain global maps of DSD. It was shown in [65] that DSD retrievals using ε_f as a compromise between the a priori assumptions of α_{ini} and α_{adj} estimated from surface reference constraints compare well with ground radar observations. Therefore, as an alternative approach, ε_f can be used to generate the DSD estimates from PR.

Figure 7-2-Figure 7-25 show the global map of drop median diameter D_o evaluated at 2 km altitude and the global map for $\log(N_w)$ for all 12 months for year 2000. Each pixel in the plot is $0.5^\circ \times 0.5^\circ$ area, and therefore of fairly high resolution. The overlay shows the standard map of land/ocean boundaries. The plots are restricted to the latitudes of $\pm 37^\circ$, coinciding with the coverage of TRMM-PR. It can be seen from the year 2000 maps that large D_o occur over land compared to oceans, which has been known fairly well, attributed to the relative predominance of ice processes. Whenever D_o increases, N_w decreases as expected.

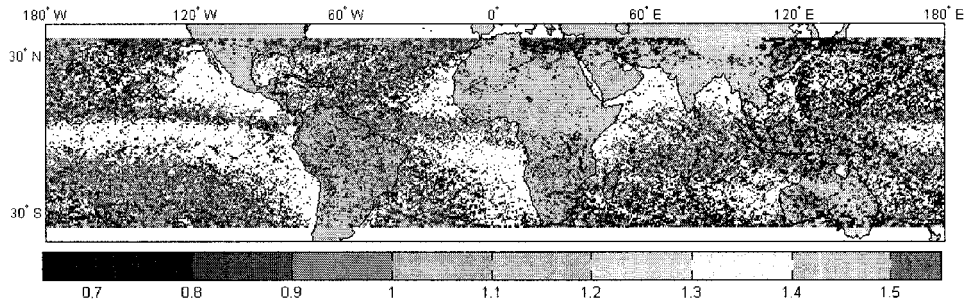

Figure 7-2. Global map of the estimated D_o (mm) evaluated at 2 km altitude, from TRMM-PR measurements, for data set of the month of January, 2000. The plots are restricted to the latitudes of ±37°, coinciding with the coverage of TRMM-PR. Each pixel in the plot is 0.5°X 0.5° area.

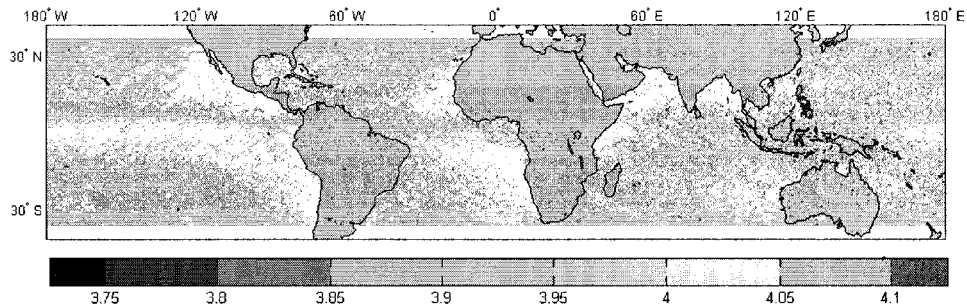

Figure 7-3. Global map of the average $\log(N_w)$ evaluated at 2 km altitude, from TRMM-PR measurements, for data set of the month of January, 2000. The plots are restricted to the latitudes of ±37°, coinciding with the coverage of TRMM-PR. Each pixel in the plot is 0.5°X 0.5° area.

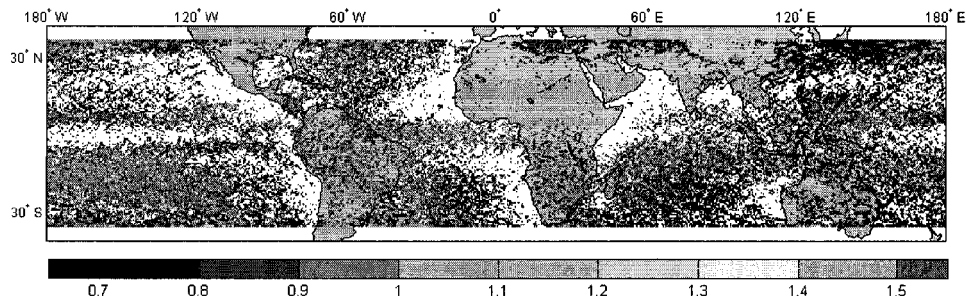

Figure 7-4. Global map of the estimated D_o (mm) evaluated at 2 km altitude, from TRMM-PR measurements, for data set of the month of February, 2000. The plots are restricted to the latitudes of ±37°, coinciding with the coverage of TRMM-PR. Each pixel in the plot is 0.5°X 0.5° area.

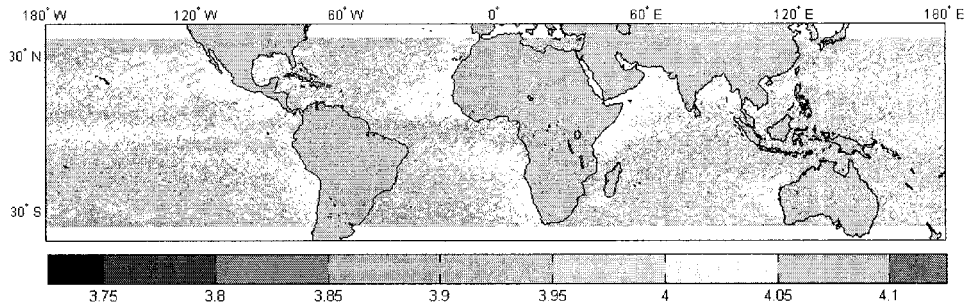

Figure 7-5. Global map of the average $\log(N_w)$ evaluated at 2 km altitude, from TRMM-PR measurements, for data set of the month of February, 2000. The plots are restricted to the latitudes of ±37°, coinciding with the coverage of TRMM-PR. Each pixel in the plot is 0.5°X 0.5° area.

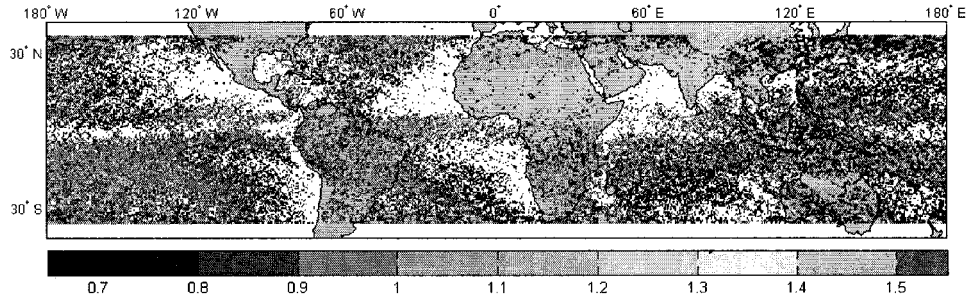

Figure 7-6. Global map of the estimated D_o (mm) evaluated at 2 km altitude, from TRMM-PR measurements, for data set of the month of March, 2000. The plots are restricted to the latitudes of ±37°, coinciding with the coverage of TRMM-PR. Each pixel in the plot is 0.5°X 0.5° area.

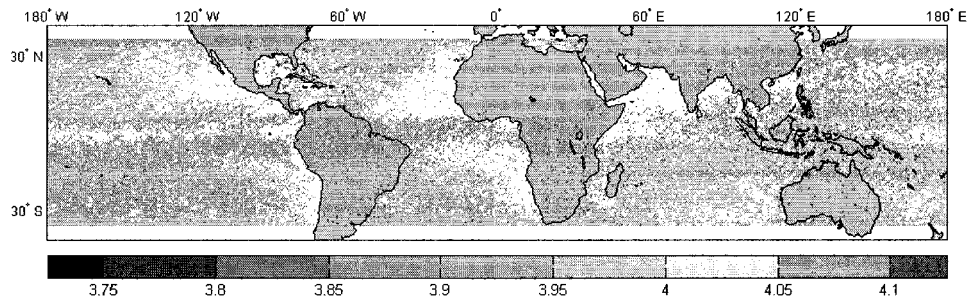

Figure 7-7. Global map of the average $\log(N_w)$ evaluated at 2 km altitude, from TRMM-PR measurements, for data set of the month of March, 2000. The plots are restricted to the latitudes of ±37°, coinciding with the coverage of TRMM-PR. Each pixel in the plot is 0.5°X 0.5° area.

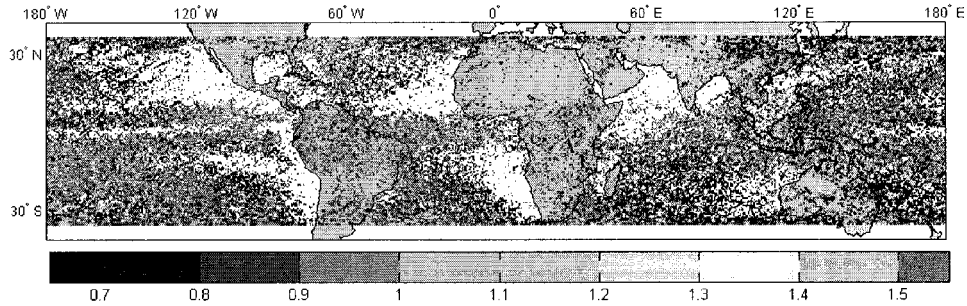

Figure 7-8. Global map of the estimated D_o (mm) evaluated at 2 km altitude, from TRMM-PR measurements, for data set of the month of April, 2000. The plots are restricted to the latitudes of ±37°, coinciding with the coverage of TRMM-PR. Each pixel in the plot is 0.5°X 0.5° area.

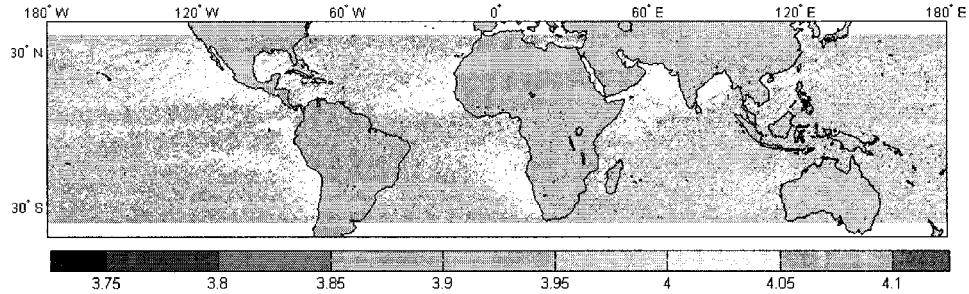

Figure 7-9. Global map of the average $\log(N_w)$ evaluated at 2 km altitude, from TRMM-PR measurements, for data set of the month of April, 2000. The plots are restricted to the latitudes of ±37°, coinciding with the coverage of TRMM-PR. Each pixel in the plot is 0.5°X 0.5° area.

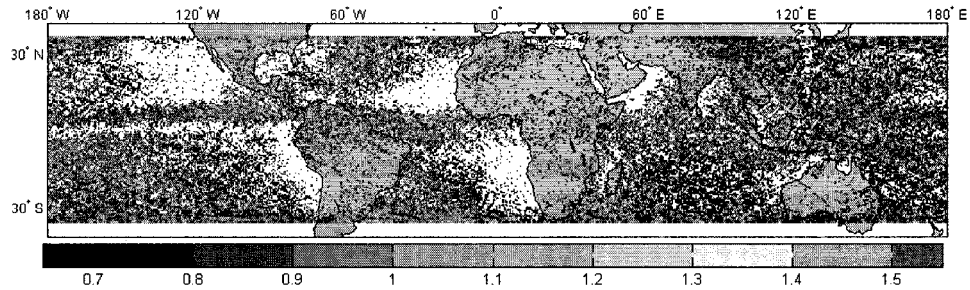

Figure 7-10. Global map of the estimated D_o (mm) evaluated at 2 km altitude, from TRMM-PR measurements, for data set of the month of May, 2000. The plots are restricted to the latitudes of ±37°, coinciding with the coverage of TRMM-PR. Each pixel in the plot is 0.5°X 0.5° area.

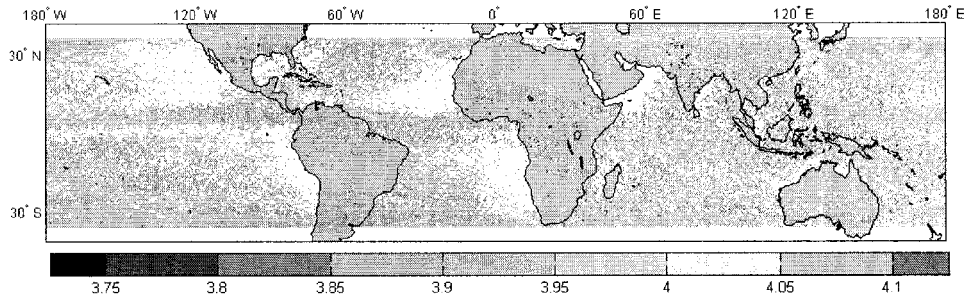

Figure 7-11. Global map of the average $\log(N_w)$ evaluated at 2 km altitude, from TRMM-PR measurements, for data set of the month of May, 2000. The plots are restricted to the latitudes of ±37°, coinciding with the coverage of TRMM-PR. Each pixel in the plot is 0.5°X 0.5° area.

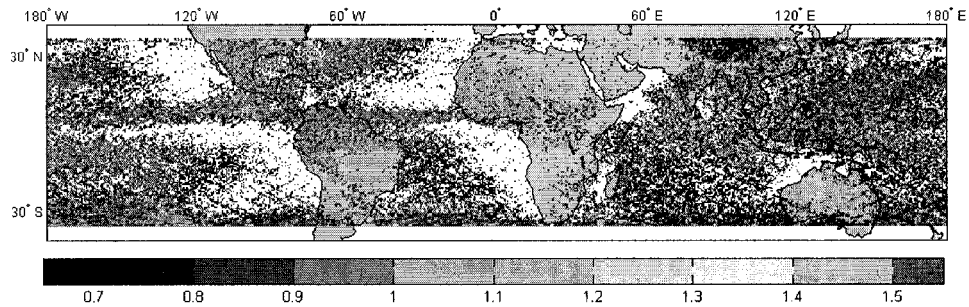

Figure 7-12. Global map of the estimated D_o (mm) evaluated at 2 km altitude, from TRMM-PR measurements, for data set of the month of Jun, 2000. The plots are restricted to the latitudes of ±37°, coinciding with the coverage of TRMM-PR. Each pixel in the plot is 0.5°X 0.5° area.

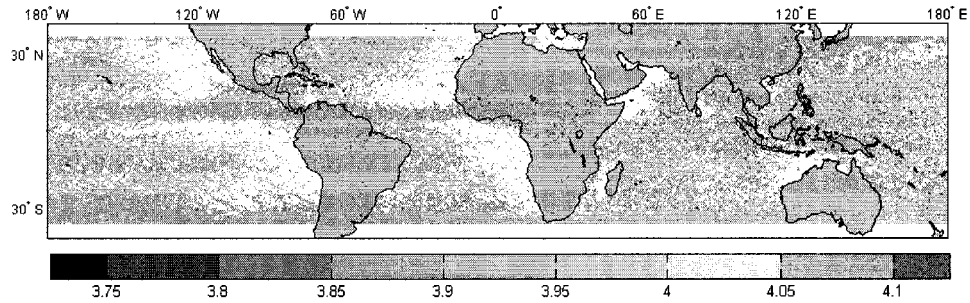

Figure 7-13. Global map of the average $\log(N_w)$ evaluated at 2 km altitude, from TRMM-PR measurements, for data set of the month of Jun, 2000. The plots are restricted to the latitudes of ±37°, coinciding with the coverage of TRMM-PR. Each pixel in the plot is 0.5°X 0.5° area.

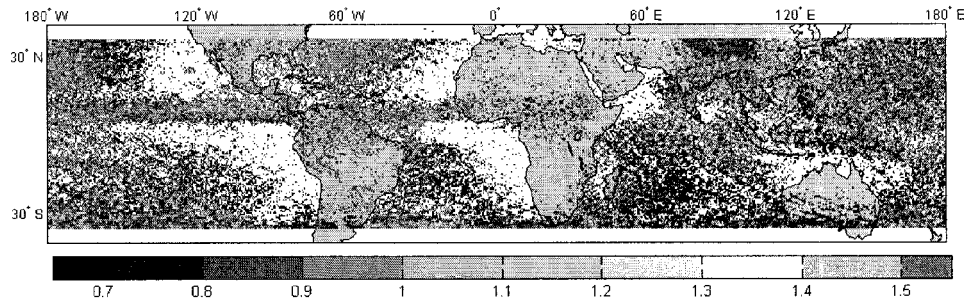

Figure 7-14. Global map of the estimated D_o (mm) evaluated at 2 km altitude, from TRMM-PR measurements, for data set of the month of July, 2000. The plots are restricted to the latitudes of ±37°, coinciding with the coverage of TRMM-PR. Each pixel in the plot is 0.5°X 0.5° area.

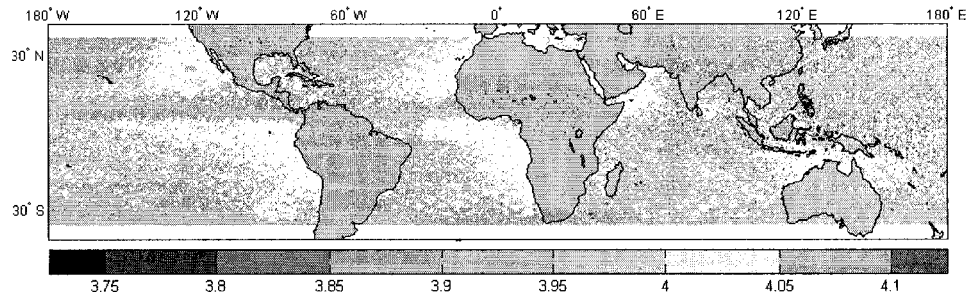

Figure 7-15. Global map of the average $\log(N_w)$ evaluated at 2 km altitude, from TRMM-PR measurements, for data set of the month of July, 2000. The plots are restricted to the latitudes of ±37°, coinciding with the coverage of TRMM-PR. Each pixel in the plot is 0.5°X 0.5° area.

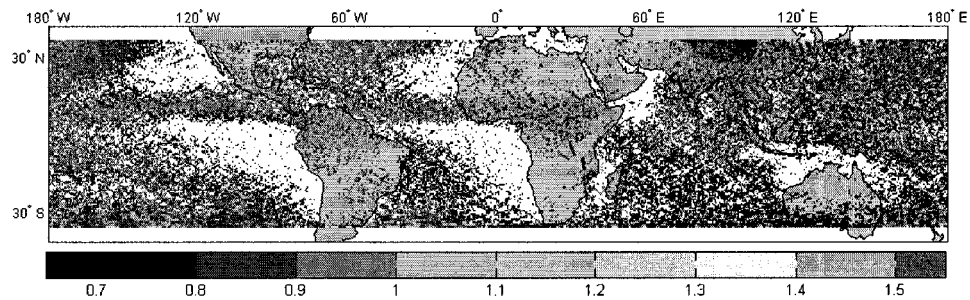

Figure 7-16. Global map of the estimated D_o (mm) evaluated at 2 km altitude, from TRMM-PR measurements, for data set of the month of August, 2000. The plots are restricted to the latitudes of ±37°, coinciding with the coverage of TRMM-PR. Each pixel in the plot is 0.5°X 0.5° area.

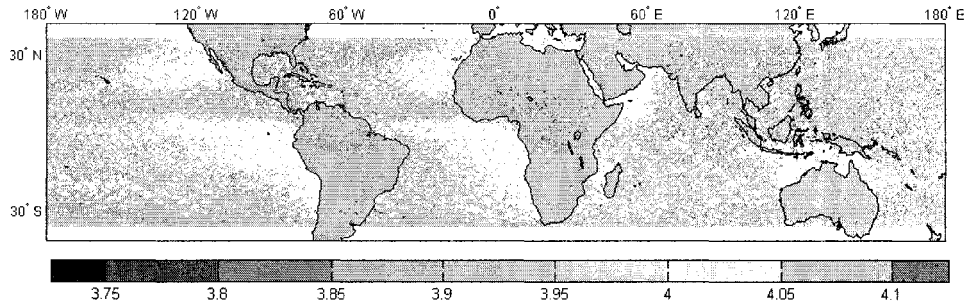

Figure 7-17. Global map of the average $\log(N_w)$ evaluated at 2 km altitude, from TRMM-PR measurements, for data set of the month of August, 2000. The plots are restricted to the latitudes of ±37°, coinciding with the coverage of TRMM-PR. Each pixel in the plot is 0.5°X 0.5° area.

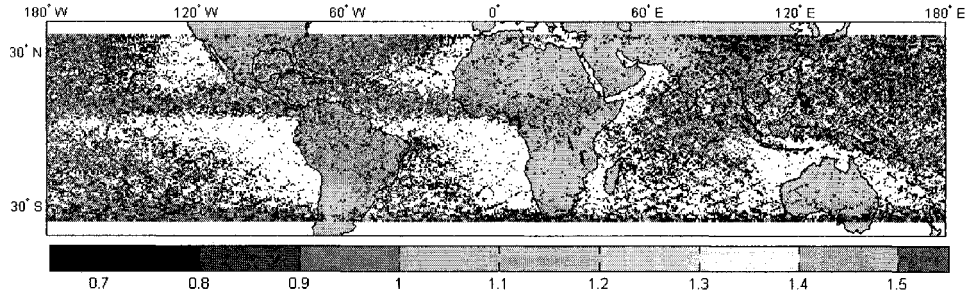

Figure 7-18. Global map of the estimated D_o (mm) evaluated at 2 km altitude, from TRMM-PR measurements, for data set of the month of September, 2000. The plots are restricted to the latitudes of ±37°, coinciding with the coverage of TRMM-PR. Each pixel in the plot is 0.5°X 0.5° area.

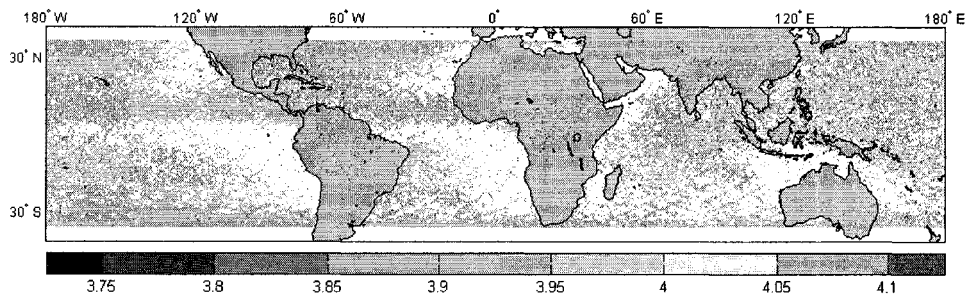

Figure 7-19. Global map of the average $\log(N_w)$ evaluated at 2 km altitude, from TRMM-PR measurements, for data set of the month of September, 2000. The plots are restricted to the latitudes of ±37°, coinciding with the coverage of TRMM-PR. Each pixel in the plot is 0.5°X 0.5° area.

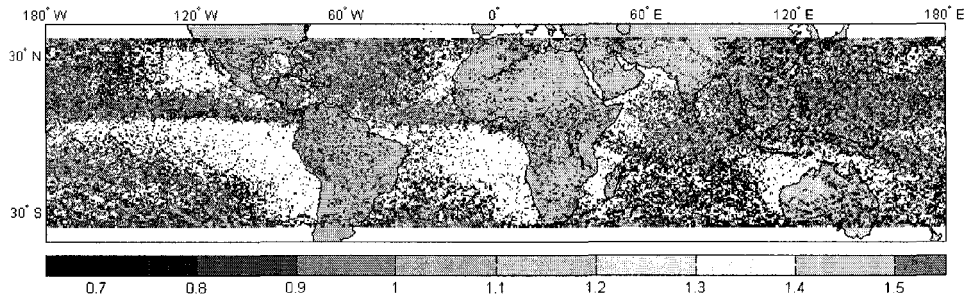

Figure 7-20. Global map of the estimated D_o (mm) evaluated at 2 km altitude, from TRMM-PR measurements, for data set of the month of October, 2000. The plots are restricted to the latitudes of ±37°, coinciding with the coverage of TRMM-PR. Each pixel in the plot is 0.5°X 0.5° area.

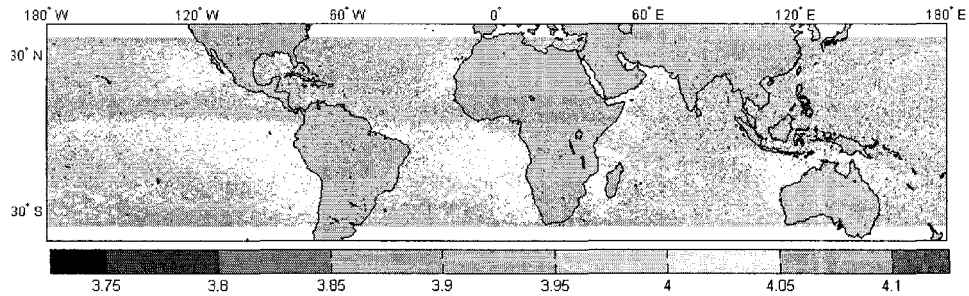

Figure 7-21. Global map of the average $\log(N_w)$ evaluated at 2 km altitude, from TRMM-PR measurements, for data set of the month of October, 2000. The plots are restricted to the latitudes of ±37°, coinciding with the coverage of TRMM-PR. Each pixel in the plot is 0.5°X 0.5° area.

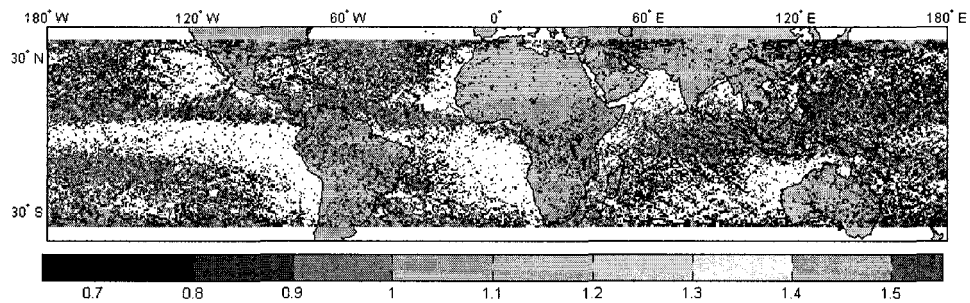

Figure 7-22. Global map of the estimated D_o (mm) evaluated at 2 km altitude, from TRMM-PR measurements, for data set of the month of November, 2000. The plots are restricted to the latitudes of ±37°, coinciding with the coverage of TRMM-PR. Each pixel in the plot is 0.5°X 0.5° area.

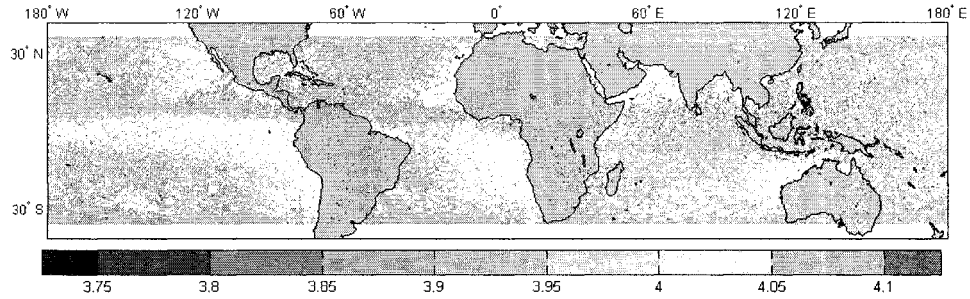

Figure 7-23. Global map of the average $\log(N_w)$ evaluated at 2 km altitude, from TRMM-PR measurements, for data set of the month of November, 2000. The plots are restricted to the latitudes of ±37°, coinciding with the coverage of TRMM-PR. Each pixel in the plot is 0.5°X 0.5° area.

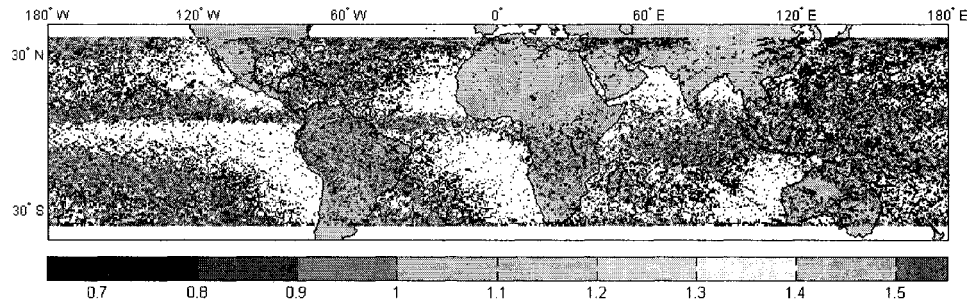

Figure 7-24. Global map of the estimated D_o (mm) evaluated at 2 km altitude, from TRMM-PR measurements, for data set of the month of December, 2000. The plots are restricted to the latitudes of ±37°, coinciding with the coverage of TRMM-PR. Each pixel in the plot is 0.5°X 0.5° area.

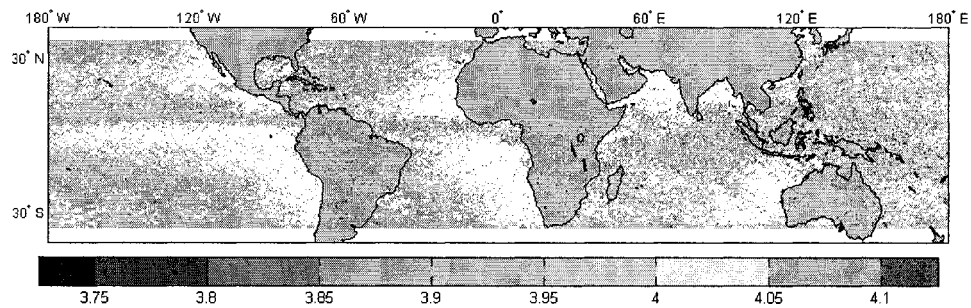

Figure 7-25. Global map of the average $\log(N_w)$ evaluated at 2 km altitude, from TRMM-PR measurements, for data set of the month of December, 2000. The plots are restricted to the latitudes of ±37°, coinciding with the coverage of TRMM-PR. Each pixel in the plot is 0.5°X 0.5° area.

7.4.2 Case Study: Global Maps of DSD Parameters for Year 2000.

Figure 7-26 shows the global map of drop median diameter D_o evaluated at 2 km altitude for the year 2000, whereas Figure 7-27 shows similar maps for $\log(N_w)$. Each pixel in the plot is $0.5^\circ \times 0.5^\circ$ area, and therefore of fairly high resolution. The overlay shows the standard map of land/ocean boundaries. The plots are restricted to the latitudes of $\pm 37^\circ$, coinciding with the coverage of TRMM-PR. It can be seen from the year 2000 maps that large D_o occur over land compared to oceans, which has been known fairly well, attributed to the relative predominance of ice processes. Whenever D_o increases, N_w decreases as expected. A detailed analysis of global DSD distribution is beyond the scope of this chapter, and the focus is on the methodology. In order to study the DSDs in the context of contribution to global rainfall product, an alternate DSD map is generated weighted by rainfall rate for year 2000. The rainfall weighted D_o and weighted value of average $\log(N_w)$ are shown in Figure 7-28 and Figure 7-29 for the same 2 km altitude. All the rest of the characteristics except rainfall weighting are same between all these figures. It can be seen that the weighting by rainfall produces higher values of D_o, as expected. Table I shows the average D_o at 2 km altitude over the TRMM observation area, separated into convective/stratiform as well as land/ocean. It appears from the table that D_o over land for convective storms is higher than that of ocean, while the values for stratiform are similar.

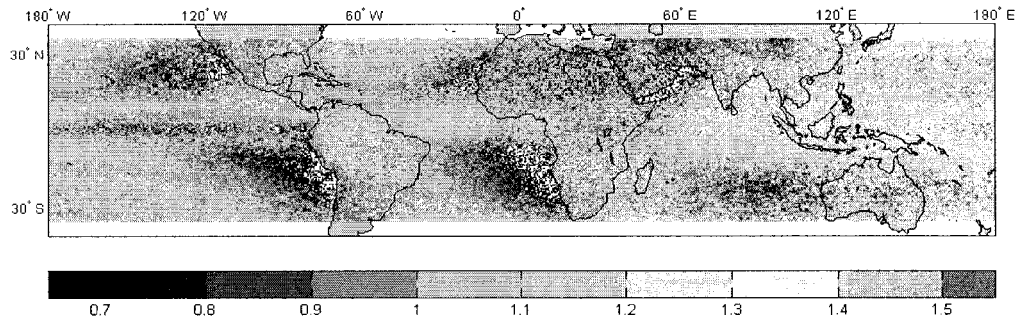

Figure 7-26. Global map of the estimated D_o (mm) evaluated at 2 km altitude, from TRMM-PR measurements, for data set of the year 2000. The plots are restricted to the latitudes of ±37°, coinciding with the coverage of TRMM-PR. Each pixel in the plot is 0.5°X 0.5° area.

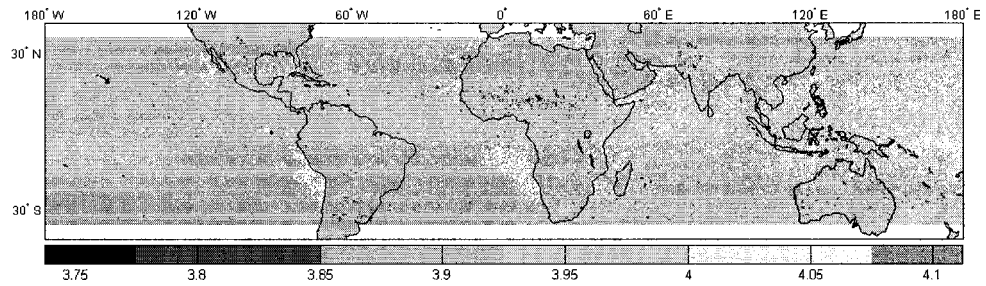

Figure 7-27. Global map of the average log(N_w) evaluated at 2 km altitude, from TRMM-PR measurements, for data set of the year 2000. The plots are restricted to the latitudes of ±37°, coinciding with the coverage of TRMM-PR. Each pixel in the plot is 0.5°X 0.5° area.

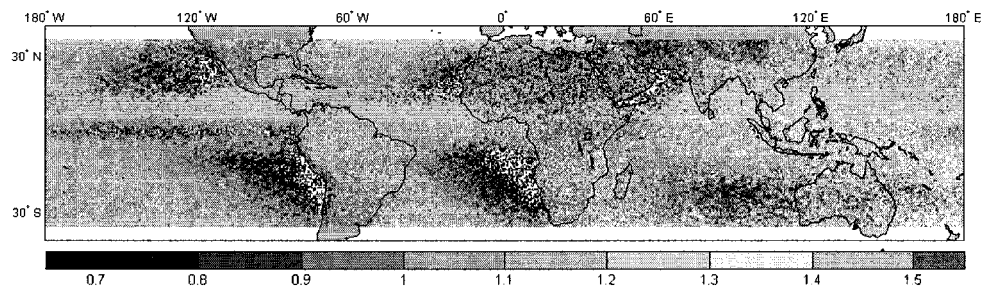

Figure 7-28, Global map of the rainfall weighted D_o (mm) evaluated at 2 km altitude, from TRMM-PR measurements, for data set of the year 2000. The plots are restricted to the latitudes of ±37°, coinciding with the coverage of TRMM-PR. Each pixel in the plot is 0.5°X 0.5° area.

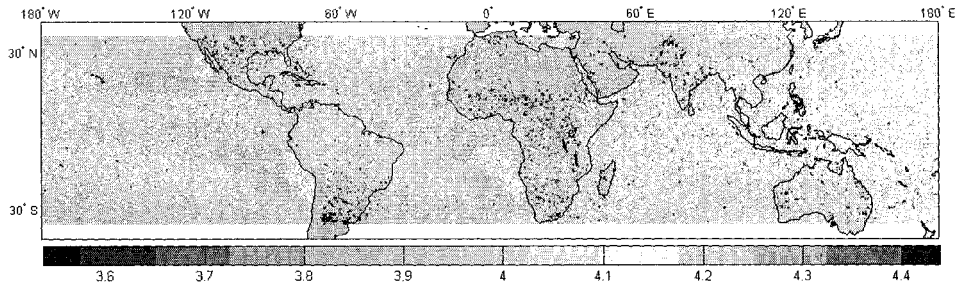

Figure 7-29. Global map of the weighted value of average $\log(N_w)$ evaluated at 2 km altitude, from TRMM-PR measurements, for data set of the year 2000. The plots are restricted to the latitudes of ±37°, coinciding with the coverage of TRMM-PR. Each pixel in the plot is 0.5°X 0.5° area.

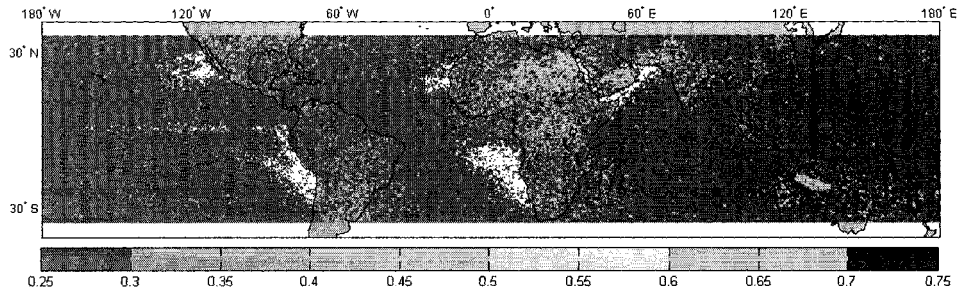

Figure 7-30. Global map of the STD of estimated D_o (mm) evaluated at 0.5°X 0.5° area and 2 km altitude, from TRMM-PR measurements, for data set of the year 2000. The plots are restricted to the latitudes of ±37°, coinciding with the coverage of TRMM-PR.

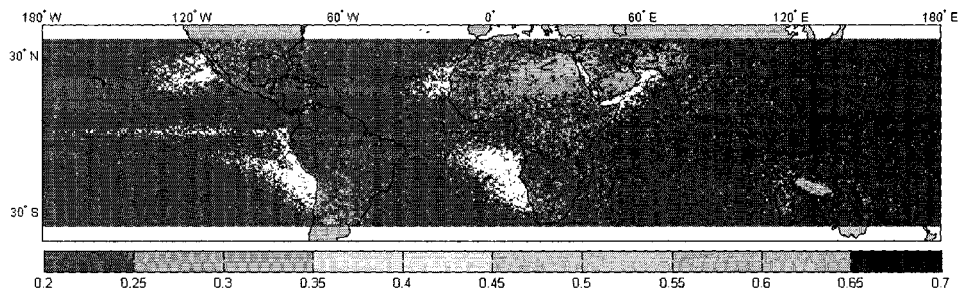

Figure 7-31 Global map of the STD of average $\log(N_w)$ evaluated at 0.5°X 0.5° area and 2 km altitude, from TRMM-PR measurements, for data set of the year 2000. The plots are restricted to the latitudes of ±37°, coinciding with the coverage of TRMM-PR.

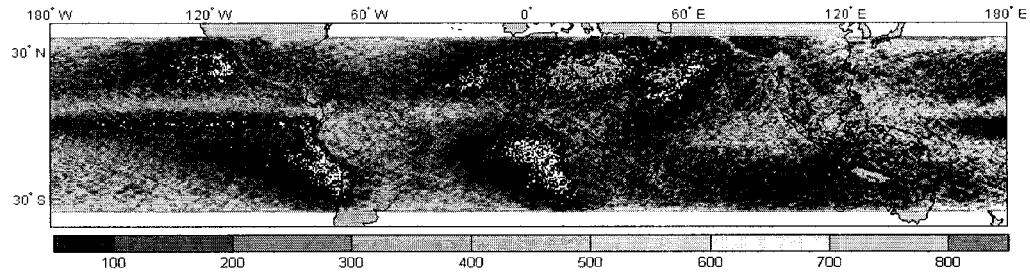

Figure 7-32 Global map of the number of profiles analyzed for DSD parameters calculations at each pixel of (0.5° X 0.5°) map for the year 2000. The plots are restricted to the latitudes of ±37°, coinciding with the coverage of TRMM-PR.

Table 7–1 The estimated D_o (mm) over the globe for the year 2000. D_o is evaluated at 2 km altitude, in units of mm. Land or ocean types are from TRMM-PR 1C-21 data product. Convective or stratiform types are from TRMM-PR 2A-23 data product. The percentage of convective rain type profiles is 16%, while it is 84% for stratiform rain type.

D_o	Convective	Stratiform	Total
Land	1.2086	0.9707	1.0136
Ocean	1.0653	0.9513	0.9693
Total	1.0998	0.9556	0.9791

Table 7–2. The average $\log(N_w)$ over the globe for the year 2000. N_w is evaluated at 2 km altitude, in units of mm. Land or ocean types are from TRMM-PR 1C-21 data product. Convective or stratiform types are from TRMM-PR 2A-23 data product. The percentage of convective rain type profiles is 16%, while it is 84% for stratiform rain type.

N_w	Convective	Stratiform	Total
Land	4.2053	3.8515	3.9153
Ocean	4.3029	3.8515	3.9229
Total	4.2796	3.8515	3.9214

7.4.3 Case Study: Monthly Maps of DSD Parameters using only α Adjustment.

It was shown that the retrievals of D_o and an average N_w are based on results from the α adjustment procedure. Due to the large data set for the year 2000, we have enough data to use only the α adjustment procedure. Figure 7-33 shows the global map of the drop median diameter D_o evaluated at 2 km altitude for the year 2000, whereas Figure 7-34 shows similar maps for $\log(N_w)$ using the α adjustment method. Each pixel in the plot is $0.5^\circ \times 0.5^\circ$ area. The overlay shows the standard map of land/ocean boundaries. The plots

are restricted to the latitudes of ±37°, coinciding with the coverage of TRMM-PR. It can be seen from the year 2000 maps that large D_o occurs mostly over land compared to ocean, which in this case is clearer than in the case of Figure 7-26. Whenever D_o increases, N_w decreases as expected. Table 7–3 shows the average D_o for the α adjustment profiles at 2 km altitude over the TRMM observation area, separated into convective/stratiform as well as land/ocean. It appears from the table that D_o using the α adjustment has a higher value than D_o at Table 7–1. This difference in D_o value is because the α adjustment profiles happened mostly at high rainfall rates storms.

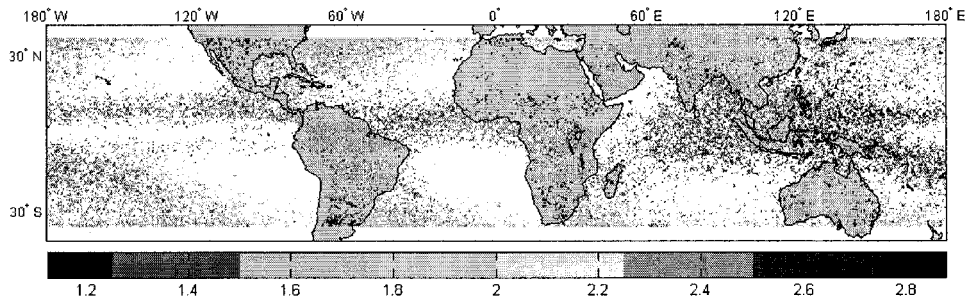

Figure 7-33. Global map of the estimated D_o (mm) evaluated at 2 km altitude, from TRMM-PR measurements, for data set of the year 2000 (using only data with α adjustment) . The plots are restricted to the latitudes of ±37°, coinciding with the coverage of TRMM-PR. Each pixel in the plot is 0.5°X 0.5° area.

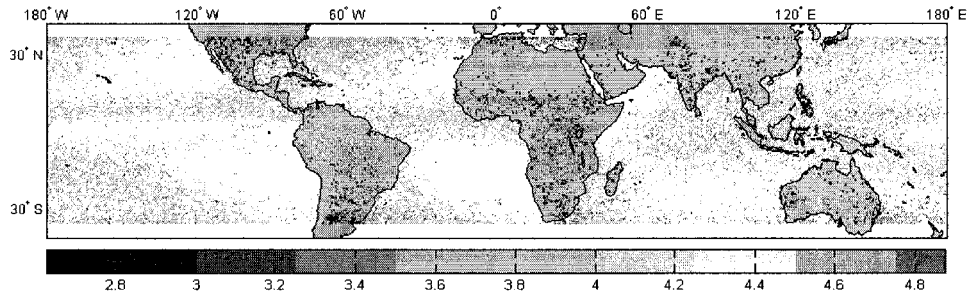

Figure 7-34. Global map of the average log(N_w) evaluated at 2 km altitude, from TRMM-PR measurements, for data set of year the 2000 (using only data with α adjustment). The plots are restricted to the latitudes of ±37°, coinciding with the coverage of TRMM-PR. Each pixel in the plot is 0.5°X 0.5° area.

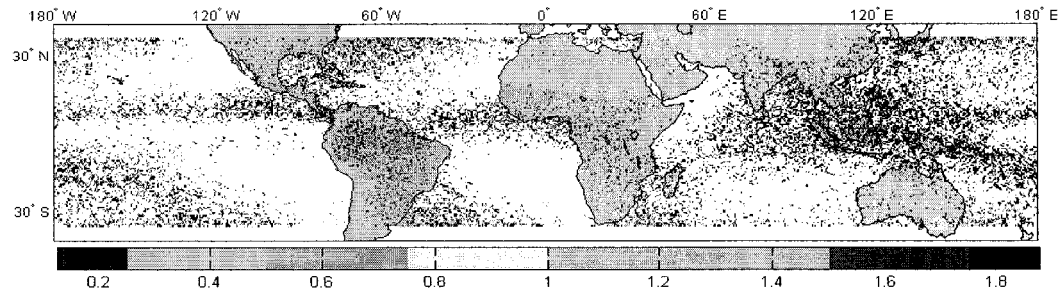

Figure 7-35 Global map of the STD of estimated D_o (mm) evaluated at 0.5°X 0.5° area and 2 km altitude, from TRMM-PR measurements, for data set of the year 2000 (using only data with α adjustment). The plots are restricted to the latitudes of ±37°, coinciding with the coverage of TRMM-PR.

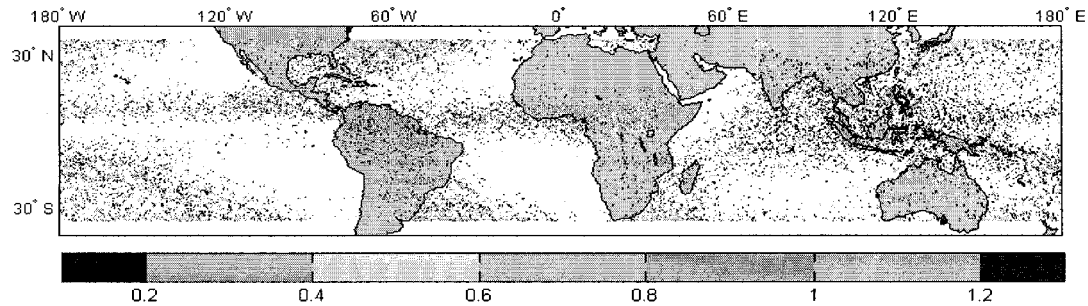

Figure 7-36. Global map of the STD of average log(N_w) evaluated at 0.5°X 0.5° area and 2 km altitude, from TRMM-PR measurements, for data set of the year 2000 (using only data with α adjustment). The plots are restricted to the latitudes of ±37°, coinciding with the coverage of TRMM-PR.

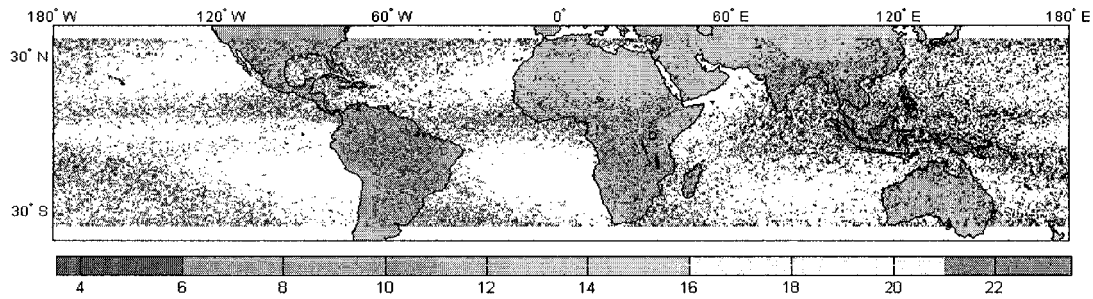

Figure 7-37. Global map of the number of profiles analyzed for DSD parameters calculation at each pixel of (0.5° X 0.5°) map for the year 2000 (using only data with α adjustment). The plots are restricted to the latitudes of ±37°, coinciding with the coverage of TRMM-PR.

Table 7–3. The estimated D_o (mm) over the globe for the year 2000. D_o evaluated at 2 km altitude, in units of mm. Land or ocean types are from TRMM-PR 1C-21 data product. Convective or stratiform types are from TRMM-PR 2A-23 data product. Convective profiles is 93% while stratiform profiles is 7% .

D_o	Convective	Stratiform	Total
Land	2.1789	1.9890	2.1758
Ocean	1.6322	1.7343	1.6405
Total	1.8052	1.7551	1.8021

Table 7–4. Average $\log(N_w)$ over globe for the year 2000. N_w samples are at 2 km altitude, in units of mm. Land or ocean types are from TRMM-PR 1C-21 data product. Convective or stratiform types are from TRMM-PR 2A-23 data product.

N_w	Convective	Stratiform	Total
Land	3.5658	3.7076	3.5682
Ocean	4.1746	3.7861	4.1428
Total	3.9835	3.7805	3.9710

7.5 SUMMARY AND CONCLUSION

The prevailing relationship between specific attenuation and reflectivity is used to retrieve the parameters of the DSD. The main use of the surface reference method in TRMM is to provide the "α adjustment." However, the α adjustment is only as good as the reliability of the surface reference technique. In order to accommodate the accuracy of the surface reference technique, the TRMM-PR uses a weighted application of "α adjustment." The TRMM-PR-based DSD retrieval algorithms are used to generate monthly maps of DSD around the globe. The knowledge of the natural distribution of DSD around the globe is important for various applications such as sensor development for satellite-borne radars, and has potential applications for radiometric retrievals. It was shown by Wilheit [57] that the DSD information is a major source of retrieval uncertainty, especially for moderate and high rainfall rates. The global maps presented in this chapter should be considered a demonstration of the methodology. These maps are potentially useful for developing a radiometer-based precipitation retrieval algorithm in the Global Precipitation Mission era.

CHAPTER 8

CONCLUSION AND FUTURE WORK

8.1 SUMMARY AND CONCLUSIONS

The following are the conclusions and the summary of this research:

- Precipitation type classification and bright band detection are two products produced by the TRMM-PR program. The precipitation type is currently classified as convective or stratiform based on the spatial variability of the TRMM precipitation radar reflectivity patterns as well as the presence of bright band. Alternative algorithms for rain type classification as well as bright band detection are developed based on the two-dimensional wavelet analysis. It is shown that the two-dimensional wavelet analysis-based algorithm performs better for bright band detection, especially for bright band low altitudes. A qualitative comparison for the rain type classification with simultaneous ground radar results shows the results of both the TRMM-PR algorithm and the proposed algorithm are compared well with the ground radar classification. A combination of the 2A-23 and 2D-WA decision is likely to produce better detection of bright band and rain type classification.
- An understanding of the vertical structure of precipitating systems is important because it implies differences in the rainfall. Extensive information about the type of storm is contained in the vertical structure. The classification of global precipitation radar profiles using the self-organizing maps (SOM) technique can be used to extend

rain type classification beyond the convective/stratiform rain type separation. The SOM technique is used as an analysis tool for generating hypotheses on the relationships, and eventually as a function of the vertical profile. Vertical profile of reflectivity observation obtained from TRMM-PR is classified with a SOM algorithm. The methodology is demonstrated by computing SOM for one year of TRMM radar data around the globe. The organization structure is visualized by the SOM method, and the organized structures are characterized in terms of the properties of the profiles of the radar reflectivity. Subsequently, the data are summarized in terms of centroid profiles that can be useful in comparing the vertical profiles of reflectivity from different regions around the globe as well as from different seasons. This classification may help us to understand the natural separation of the VPR of the data set in view of the current convective/stratiform rain type classification. The entire data set is classified using the SOM technique into classes that carry the themes of the average profiles of the stratiform rain type and the average profiles of the convective rain type. It is difficult to study those classes if each class consists of a percentage of stratiform and convective rain type. The SOM method is used to study the stratiform rain type and convective rain type profiles separately.

- A classification of vertical profiles of the bright band region of reflectivity from radar observation obtained by TRMM-PR using a self-organizing map is presented. The classification is used to build statistics of bright band profile characteristics in terms of bright band peak height, storm top height, bright band peak reflectivity, bright band thickness, and bright band sharpness index. The results presented in the research

show that while bright band height from sea level varies widely, the BB thickness and sharpness do not vary around the globe. There is no seasonal variation of the BB region profile. The height of the bright band may have a small effect on the reflectivity structure below BB peak height. There are small differences above BB height between land and ocean.

- Studying the convective rain type profiles around the globe shows that the percentage of strong convective storms over land is higher than the percentage of strong convective storms over ocean. The comparison of the convective rain type for storms over land and over oceans indicates that the percentage of profiles with high reflectivity value and storm top height is higher over land than over oceans. This conclusion is the same for all seasons. The results of the natural separation of (4X4) SOM for the VPR of year 2000 show that more than 50% of the total rain can fall in four classes out of the 16. The comparison of the convective rain type for storms over the northern and southern hemispheres for the entire data set for the year 2000 indicates no difference. There are significant seasonal differences between the northern and southern hemispheres that are obvious. The comparison of the convective rain type for storms over the East and West Pacific Ocean indicates a small difference in the reflectivity structure of their SOM classes. Precipitation systems in the East Pacific were shallower than those in the West Pacific, and had a lower storm top height. This is due to the fact that East Pacific Ocean has colder sea surface temperatures than the East Pacific Ocean.
- Reflectivity profiles of hurricanes were compared against generic oceanic storms. The analysis demonstrates that the percentage of bright band reflectivity structure with

high reflectivity structure value for hurricane data is higher than the generic oceanic data. The hurricane profiles have larger reflectivity near the sea level than the generic oceanic data. This indicates that the hurricane storms have a higher rainfall rate near the ground. The percentage for the high reflectivity structure for hurricane cases is more than for the oceanic cases.

- The prevailing relationship between specific attenuation and reflectivity is used to retrieve the parameters of the DSD. The main use of the surface reference method in TRMM is to provide the "α adjustment." However, the α adjustment is only as good as the reliability of the surface reference technique. In order to accommodate the accuracy of the surface reference technique, the TRMM-PR uses a weighted application of "α adjustment." The TRMM-PR-based DSD retrieval algorithms are used to generate monthly maps of DSD around the globe. The knowledge of the natural distribution of DSD around the globe is important for various applications such as sensor development for satellite-borne radars and has potential applications for radiometric retrievals. These maps are potentially useful for developing radiometer-based precipitation retrieval algorithms in the Global Precipitation Mission era. It can be seen from the year 2000 maps that large D_o occur over land compared to ocean attributed to the relative predominance of ice processes. Maps also show that whenever D_o increases, N_w decreases as expected.

8.2 SUGGESTIONS FOR FUTURE WORK

- The precipitation type classification and bright band detection may be improved using the 3D wavelet analysis transform. The 3D wavelet analysis transform can looks to

the 3D precipitation reflectivity structure instead of only analyzing one scan at a time using the 2D wavelet analysis transform.

- Adjust the thresholds of the wavelet analysis transform coefficients used in precipitation classification algorithm by using SOM classification results of precipitation profiles. The SOM classes of bright band may be used to simulate 3D precipitation reflectivity structure that can be used to calculate the wavelet coefficients of the bright band classes.
- Study the precipitation type classification and bright band detection using SOM technique. This can be done using neural network technique by training the neural network to recognize the SOM classes.
- Study the DSD parameters with regard to the similar SOM classes profiles of both ground and space-borne radar. This can be done by exporting the raindrop size distribution statistics deduced from polarimetric ground radars to the SOM classes obtained from the Tropical Rainfall Measuring Mission Precipitation Radar (TRMM-PR).

REFERENCES

[1] Varma, A. and G. Liu, Near-Global Climatology of the Satellite Pixel-Scale Horizontal Variability of Rainfall, Report Submitted to Monthly Weather Review – April 2004.

[2] Yunfei F., L. Yihua, G. Liu, and W. Qiang, Seasonal Characteristics of Precipitation in 1998 over East Asia as Derived from TRMM-PR, Adv. Atmos. Sci., 20, 511-529, 2003.

[3] Fujiyoshi, Y., T. Takasugi, Y. Gocho, and T. Takeda, Radar-echo structure of middle-level precipitating clouds and the change of raindrops-Processes of mixing of precipitation particles falling from generating cells, J. Meteor. Soc. Japan, 58, 203–216, 1980.

[4] Houze, R., Structures of atmospheric precipitation systems–A global survey, Radio Sci., 16, 671–689, 1981.

[5] Kummerow, C., and L. Giglio, A passive microwave technique for estimating rainfall and vertical structure information from space. Part I: Algorithm description, J. Appl. Meteor., 33, 3–18, 1994.

[6] Houghton, H. G., On precipitation mechanisms and their artificial modification, J. Appl. Meteor., 7, 851-859, 1968.

[7] Tokay, A., and D. Short, Evidence from tropical raindrop spectra of the origin of rain from stratiform and convective clouds, J. Appl. Meteor., 35, 355-371, 1996.

[8] Houze, R. A., Cloud clusters and large-scale vertical motions in the tropics, J. Meteor. Soc. Japan, 60, 396-409, 1982.

[9] Houze, R. A., Observed structure of mesoscale convective systems and implications for large-scale heating, Quart. J. Roy. Meteor. Soc., 115, 425-461, 1989.

[10] Johnson, R. H., and G. S. Young, Heat and moisture budgets of tropical mesoscale anvil clouds, J. Atmos. Sci., 40, 2138-2147, 1983.

[11] L'Ecuyer, T. S., C. Kummerow, and H. Masunaga, Relationships between the Microphysics of Precipitating Cloud Systems and Their Radar Reflectivity Patterns, 31st International Conference on Radar Meteorology, 2003.

[12] Berg, W., C. Kummerow, and C. A. Morales, Difference between east and west Pacific rainfall systems, J. Climate, 15, 3659-3672, 2002.

[13] Varma, A. K., R. M. Gairola, P. C. Pandey, and K. P. Singh, Use of TOPEX altimeter for the study of diurnal and spatial distribution of monsoon rainfall over the Bay of Bengal and the Arabian Sea, Rem. Sens. Environ., 77, 112-121, 2001.

[14] Pokhrel, S., A. K. Varma, R. M. Gairola, and V K. Agarwal, Distribution and intraseasonal variability of rain over Indian Oceanic region from Indian Remote Sensing Satellite IRS-P4 Multifrequency Scanning Microwave Radiometer, J. Geophys. Res., 2003.

[15] LeMone, M. A., and E. J. Zipser, Cumulonimbus vertical velocity events in GATE. Part I: Diameter, intensity and mass flux, J. Atmos. Sci., 37, 2444-2457, 1980.

[16] Jorgensen, D. P., and M A. LeMone, Vertical Velocity Characteristics of Oceanic Convection, J. Atmos. Sci., 621–640, 1989.

[17] Geerts, B., G. M. Heymsfield and L. Tian, High Resolution reflectivity profiles in various convectively generated precipitation systems, Preprints, 22nd Radar Meteor. Conf., Amer. Meteor. Soc., Montreal, 11-16 July, 1999.

[18] Geerts, B., and T. Dejene, The Regonal and Diurnal Variability of the Vertical Structure of Precepitation Systems in Africa based on TRMM-PRecepitation radar data, 31st International Conference on Radar Meteorology, 2003.

[19] Petersen, W. A., and S. A. Rutledge, Regional Variability in Tropical Convection: Observations from TRMM, J. of Climate, 14, 17, 3566–3586, 2001.

[20] Shin, D., G. R. North, K. P. Bowman, A Summary of Reflectivity Profiles from the First Year of TRMM Radar Data, J. of Climate, 13, 23, 4072–4086, 2000.

[21] Austin, P. M., and A. C. Bemis, A quantitative study of the bright band in radar precipitation echoes, J. Meteor., 7, 145–151, 1950.

[22] Houze, R. A., Stratiform precipitation in regions of convection: A meteorological paradox?, Bul. American Met. Soc., 78, 2179-2196, 1997.

[23] Chandrasekar, V., R. Meneghini, and I. Zawadzki, Global and Local Precipitation Measurements by Radar, Meteorological Monographs, 30, 215-215, 2003.

[24] Schumacher, C., and R. A. Houze, Stratiform rain in the tropics as seen by the TRMM Precipitation radar, J. Climate, 16, 1739-1756, 2003.

[25] Fabry, F., Vertical profiles of reflectivity and precipitation intensity. In Weather Radar Technology for Water Resources Management, UNESCO Press, 137-145, 1997.

[26] Boccippio, D. J., Archetype TRMM radar profiles Identified Through Cluster Analysis, 31st International Conference on Radar Meteorology, 2003.

[27] PR Instruction Manual (for Product Version 5) http://www.eorc.nasda.go.jp /TRMM/document/pr_manual/pr_manual2.pdf, 2004.

[28] TSDIS TRMM official web site http://tsdis02.nascom.nasa.gov, 2004.

[29] TRMM Satellite Validation Office http://trmm-fc.gsfc.nasa.gov/trmm_gv, 2004.

[30] TRMM Science Operations Plan, Executive summary. NASA TRMM Program, 1996.

[31] Simpson, J., TRMM: A Satellite Mission to Measure Tropical Rainfall, Report of the Science Steering Group, NASA, GSFC, Greenbelt, Maryland 20771, 94, 1988.

[32] Awaka, J., T. Iguchi, and K. Okamoto, Early results on rain type classification by the Tropical Rainfall Measuring Mission (TRMM) precipitation radar, Proc. 8th URSI Commission F Open Symp., Aveiro, Portugal, 143-146, 1998.

[33] Steiner, M., R. Houze, and S. Yuter, Climatological characterization of three-dimensional storm structure from operational radar and rain gauge data, J. Appl. Meteor., 34, 1978-2007, 1995.

[34] Mallat, S., A Wavelet Tour of signal Processing, Academic Press, 1998.

[35] Mallat, S. G., and S. Zhong, Complete signal representation with multiscale edges. Technical report, Courant Institute of Mathematical Sciences, 1989.

[36] Gerritsen, M., Designing an Effcient Solution Strategy for Fluid Flows, PhD dissertation, Stanford University, 1996.

[37] Mallat, S., and W. L. Hwang, Singularity detection and processing with wavelets, IEEE transactions on information theory, 38, 2, 617-643, 1992.

[38] Kohonen, T., Self-Organizing Maps. Springer, 3rd edition, 1997.

[39] Kaski, S., J. Kangas, and T. Kohonen, Bibliography of self-organizing map (SOM) papers: 1981–1997, Neural Computing Surveys, 1:102–350, 1998.

[40] Kohonen, T., E. Oja, O. Simula, A. Visa, and J. Kangas, Engineering applications of the self-organizing map, Proc. of the IEEE, 84, 10, 1358–84, 1996.

[41] Simula, O., and J. Kangas, Process monitoring and visualization using selforganizing maps, In A. B. Bulsari, editor, Neural Networks for Chemical Engineers, 371–384, 1995.

[42] Alhoniemi, E., Unsupervised pattern recognition methods for exploratory analysis of industrial process data, doctoral thesis, Helsinki University of Technology, 2002.

[43] Samad, T., and S. A. Harp, Self-Organization with Partial Data, Network, 3:205--212, IOP Publishing Ltd, 1992.

[44] Kohonen, T., Self-organizing maps: Optimization approaches, in Artificial Neural Networks, The Netherlands: Elsevier, 981–990, 1991.

[45] Kohonen, T., Things you haven't heard about the self-organizing map, Proc. ICNN, 1147-1156, 1993.

[46] Vesanto, J., J. Himberg, E. Alhoniemi, and J. Parhankangas, SOM Toolbox for Matlab 5, Tech. Rep. A57, Helsinki University of Technology, 2000.

[47] Mangiameli, P., S. K. Chen and D. West, A Comparison of SOM neural network and hierarchical clustering methods, European Journal of Operational Research, 93, 2, 6, 402-417, 1996.

[48] Iguchi, T., T. Kozu, R. Meneghini, J. Awaka, and K. Okamoto, Rain-profiling algorithm for the TRMM Precipitation radar, J. Appl. Meteor., 39, 2038–2052, 2000.

[49] Hair, J. F., Jr., R. E. Anderson, R. L. Tatham, and W. C. Black, Multivariate data analysis, Prentice-Hall, 5th edition, 1998.

[50] Fabry, F., and I. Zawadzki, Long-term radar observations of the melting layer of precipitation and their interpretation, J. Atmos. Sci., 52, 838–851, 1995.

[51] Smith, C. J., The reduction of errors caused by bright bands in quantitative rainfall measurements made using radar, J. Atmos. Oceanic Technol., 3, 129–141, 1986.

[52] Harrold, T. W., and P. G. Kitchingman, Measurement of surface rainfall using radar when the beam intersects the melting layer. Preprints, 16th Conf. on Radar Meteorology, Houston, TX, Amer. Meteor. Soc., 473–478, 1975.

[53] Cheng, M., and C. G. Collier, An objective method for recognizing and partially correcting brightband error in radar images, J. Appl. Meteor., 32, 1142–1149, 1993.

[54] Andrieu, H., and J. D. Creutin, Identification of vertical profiles of radar reflectivities for hydrological applications using an inverse method. Part I: Formulation, J. Appl. Meteor., 34, 225–239, 1995.

[55] Borga, M., E. N. Anagnostou, and W. F. Krajewski, A simulation approach for validation of a brightband correction method, J. Appl. Meteor., 36, 1507–1518, 1997.

[56] Sanchez-Diezma, R., I. Zawadzki, and D. Sempere-Torres, Identification of the bright band through the analysis of volumetric radar data. J, Geophys. Res., 105 (D2), 2225–2236, 2000.

[57] White, A. B., D. J. Gottas, E. T. Strem, F. M. Ralph, and P. J. Neiman, An automated brightband height detection algorithm for use with Doppler radar spectral moments, J. Atmos. Oceanic Technol., 19, 687–697, 2002.

[58] Marwitz, J., and J. Toth, The Front Range blizzard of 1990. Part I: Synoptic and mesoscale structure, Mon. Wea. Rev., 121, 402–415, 1993.

[59] Davies, A.G., Bright band correlations for layer precipitation; the comparison of Chilbolton radar data and Hardaker model output, Meteorological Office (Forecasting Research Division) Tech. Report No. 32, 1992.

[60] Ulbrich, C. W., Natural Variations in the analytical form of the drop size distribution, J. Climate Appl. Meteor, 22, 1764–1775, 1983.

[61] Bringi, V. N., and V. Chandrasekar, Polarimetric Doppler Weather Radar: Principles and Applications, Cambridge University Press, New York, 2001.

[62] Testud, J., S. Oury, R. Black, P. Amayenc, and X. Dou, The Concept of "Normalized" Distribution to Describe Raindrop Spectra: A Tool for Cloud Physics and Cloud Remote Sensing, J. Appl. Meteor, 40, 6, 1118–1140, 2000.

[63] Meneghini, R, and K. Nakamura, Range profiling of the rain rate by an airborne weather radar, J. Remote Sens. Environ., 31, 193-209, 1990.

[64] Hitschfeld, W., and J. Bordan, Errors Inherent in the radar Measurements of Rainfall at Attenuation Wavelength, J. Meteor, 11, 58–67, 1954.

[65] Chandrasekar, V., K. Mubarak and S. Lim, Estimation of Raindrop Size Distribution from TRMM Precipitation Radar Observations, Proc. IGARSS'03, 2003.

[66] Iguchi, T., R. Meneghini, Intercomparison of Single-Frequency Methods for Retrieving a Vertical Rain Profile from Airborne or Spaceborne Radar Data, J. Atmospheric and Oceanic Technology, 11, 1507–1516, 1994.

[67] Meneghini, R., T. Iguchi, T. Kozu, L. Liao, K. Okamoto, J.A. Jones, and J. Kwiatkowski, Use of the Surface Reference Technique for Path Attenuation Estimates from the TRMM Precipitation Radar, J. Applied Meteor., 39, 12, 2053-2070, 2000.

[68] Anagnostou, E., and C. Kummerow, Stratiform and Convective Classification of Rainfall Using SSM/I 85-GHz Brightness Temperature Observations, J. Atmos. And Oceanic Tech., 14, 570-575, 1997.

[69] Janowiak, J., P. Arkin, P. Xie, M. Morrissey, and D. Legates, An examination of the east Pacific ITCZ rainfall distribution, J. Climate, 8, 2810-2823,1995.

[70] Berg, W., Differences in satellite estimates of precipitation over the east Pacific, 10th Conf. on Satellite Meteorology and Oceanography, Long Beach, CA, Amer. Meteor. Soc., 375–377, 2000.

[71] Chandrasekar, V. and B. Zafar, Precipitation type determination from space-borne radar observation, IEEE Trans GRSS, 42, 2248-2253, 2004.

[72] Jain, A. K., and, R. C. Dubes, Algorithms for Clustering Data, Prentice Hall, Englewood Cliffs, NJ, 1988